The search for Higgs boson production in the four-jet channel at $192 < \sqrt{s} < 202$ GeV with the ALEPH detector at LEP

David Hugh Smith

December 2001

A thesis submitted for

the degree of Doctor of Philosophy

of the University of Glasgow

Department of Physics and Astronomy

ProQuest Number: 13833995

ProQuest 13833995

Abstract

A search for neutral Higgs boson production in e^+e^- collisions using data collected by the ALEPH detector at the LEP accelerator is presented. Approximately 413 pb^{-1} of data collected at centre of mass energies between 188.6 and 201.6 GeV during 1998 and 1999 is used. The selection of candidates is described and the results of the search are presented and interpreted. Particular attention is given to the selection of the final states with four hadronic jets.

No evidence of Higgs boson production is found. In the context of the Standard Model the lower limit on the Higgs boson mass is set at 105.2 GeV/c^2 at the 95% confidence level.

Declaration

Except where explicit reference is made to the work of others, this dissertation is the result of my own work. None of this material has been submitted for any other degree at the University of Glasgow or any other institution.

David Smith

Acknowledgements

Firstly, I would like to thank David Saxon for giving me the opportunity to study for my PhD at the University of Glasgow.

I would like to acknowledge my supervisors; Andy Halley and Peter Negus. Many thanks to Andy for the support he gave after I joined the Glasgow group and later during my stay in Geneva and CERN, and his patient help during the first year of my PhD. Peter later took on the role and to him I am also very grateful.

Special thanks are due to Pedro Teixeira-Dias, for being my 'unofficial' supervisor whilst at CERN and for the many, many hours of discussion and suggestions. Your help has been vital.

I would like to thank James Lynch for his enthusiasm and advice, and especially for his support while I was writing this thesis.

Thanks also to the Higgs Task Force and other members of the experiment, for making me welcome during my time with ALEPH, for their helpful advice, observations and collaboration.

Finally a big thank-you to my office mates and other friends from Glasgow, CERN and Geneva whom I have met over the last four years. I value your friendship greatly.

David Smith

Contents

List of Figures

9

List of Tables

Chapter 1

Introduction

1.1 Motivation

The topic of this thesis is the search for Higgs boson particles in data collected at a high energy electron positron collider. The current theory of fundamental particle interactions requires that a Higgs boson should exist. (This is discussed in more detail in Chapter 2). To date no Higgs bosons have ever been observed to exist in Nature. However, in other respects current models are in good agreement with observed phenomenon. Therefore the existence, or otherwise, of a Higgs boson is of huge significance to our understanding of Nature at a fundamental level.

1.2 Overview

The results detailed in this thesis were obtained with data collected by the ALEPH Collaboration using the LEP accelerator at CERN. CERN is the *The European Organisation for Nuclear Research* laboratory near Geneva in Switzerland. LEP is the Large Electron Positron collider, a very large circular machine built to accelerate electrons and positrons in opposite directions and to equal energies after which they are made to collide.

The period of LEP operation between the years 1990 and 1995 is known as LEP I, when each of the beams of electrons and positrons were accelerated to an energy of ~ 45 GeV. Thus the centre of mass energy ($\sqrt{s}$) of each electron-positron collision was

about 90 GeV, which is near the Z resonance peak. The aim was to produce and record a large number of Z boson decays to allow for precise measurements of the Z boson. In November 1995 $\sqrt{s}$ was raised to 130 GeV and 136 GeV and some data recorded. That period is sometimes called LEP 1.5.

Since 1996 to 2000 LEP has operated at higher energies. See table 1.1 for the centre of mass energies that LEP has achieved, and the size of the corresponding data sample that the ALEPH Collaboration recorded. Small data samples were still taken at the Z resonance each year, to facilitate detector calibration.

Year	Integrated Luminosity (pb^{-1})	Energy Range (GeV)
1995	5.7	130, 136
1996	11.1	161
1996	10.6	170,172
1997	7.1	130, 136
1997	57	181-184
1998	176	188.6
1999	237	~192-202
2000	216	~200-209

Table 1.1: Table of centre of mass energies at which LEP has operated at since LEP I and excluding small amounts of calibration data taken at the Z resonance each year. Also shown is the size of the data samples recorded by the ALEPH Collaboration at each energy or energy range.

There were two main reasons for the continual increase of beam energy at LEP II. Firstly was to enable study of the $W^{\pm}$ boson. To allow a pair of W^+, W^- bosons to be created $\sqrt{s} > 2m_w$ which is about 161 GeV. However a second reason for the rise in $\sqrt{s}$ is the search for previously unseen phenomena, which could include Higgs boson production.

1.2.1 More about LEP and the Experimental Detectors

The LEP was installed in a 26.7km circular horizontal tunnel (forming the so called LEP ring), buried between 50m and 175m underground. The ring is in fact inclined

slightly from the horizontal, forming a gradient of 1.42%, for engineering reasons. Nor is the ring completely circular. There are eight straight sections, each 500m long, and eight arcs with a radius of curvature of 3300m. The arcs contain the bending magnets while the straight sections house radio frequency accelerating cavities.

Construction of the machine started in September 1983, and was completed less than 6 years later in 1989. The machine was operational and able to deliver useful electron-positron collisions by the end of 1989. Figure 1.1 shows a pictorial representation of the underground LEP tunnel. There are eight access points equally spaced around the ring, referred to as points 1 to 8. The electron and positron beams are brought into collision at points 2,4,6 and 8 and in those locations large detectors are built to observe and record the results of the interactions.
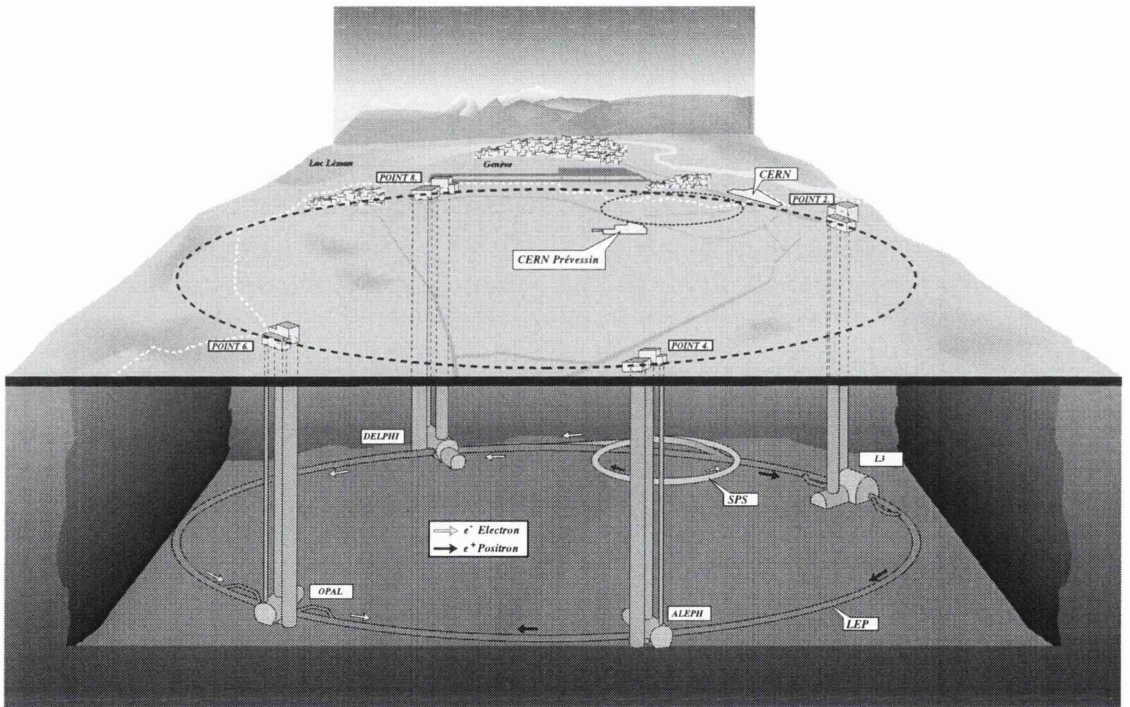
Figure 1.1: Pictorial impression of the LEP tunnel, showing the four associated experiments and their access tunnels to the surface.

The names of the experimental collaborations responsible for each detector are ALEPH, DELPHI, L3 and OPAL Collaborations. Each detector is usually simply referred to by the name of its collaboration, hence the data which will be used in this thesis were recorded by the ALEPH detector[1] during 1999. See, for example, the following references for details of the other LEP detectors; The DELPHI detector[2], the

L3 detector[3] and the OPAL detector[4].

1.2.2 LEP operation

Throughout the year LEP has not operated continuously, but has been shutdown during the Winter months. The increase in the beam energy seen since 1995 has required upgrades to the machine which were performed during the periods of shutdown.

Whilst in operation LEP depends on 3 other accelerators to fill (or inject) it with electrons and positrons. Once filled LEP is able to run with the beams in collision for a few hours. Once the beam current becomes too low, or the beams are completely lost the machine has to be refilled.

The injection sequence is shown in figure 1.2. Electrons are produced and accelerated to 200 MeV in a linear accelerator complex called the LIL. Positrons are created by allowing some of the electrons to pass through a fixed tungsten target. After, both electrons and positrons are accelerated to 600 MeV in another linear accelerator in the LIL. The leptons are stored and sorted into bunches in the Electron Positron Accumulator (EPA), ready for injection into the next stages.

From the EPA the electrons and positrons enter the Proton Synchrotron (PS) and are accelerated to 3.5 GeV, followed by transfer to the Super Proton Synchrotron (SPS) and acceleration to 22 GeV.

LEP receives the electrons and positrons at 22 GeV and must then accelerate them up to the required energy in a process called ramping. The two beams of electrons and positrons circulate in opposite directions, but share the same beam pipe. However the beams are kept separated until the beam energy is at (or very close to) the final beam energy. The particles are grouped into bunches that are about 2cm long, 190μm wide in the horizontal direction and 4μm wide in the vertical direction, when focused for interaction. In 1999 LEP ran with 4 bunches making up each beam. Bunches would cross every 22μs, during which an electron and positron could interact. Typically the beam current was up to 6mA, or 750μA per bunch, corresponding to 3.3×10^{12} particles in total.

The rate at which events from a given process are produced at the interaction points
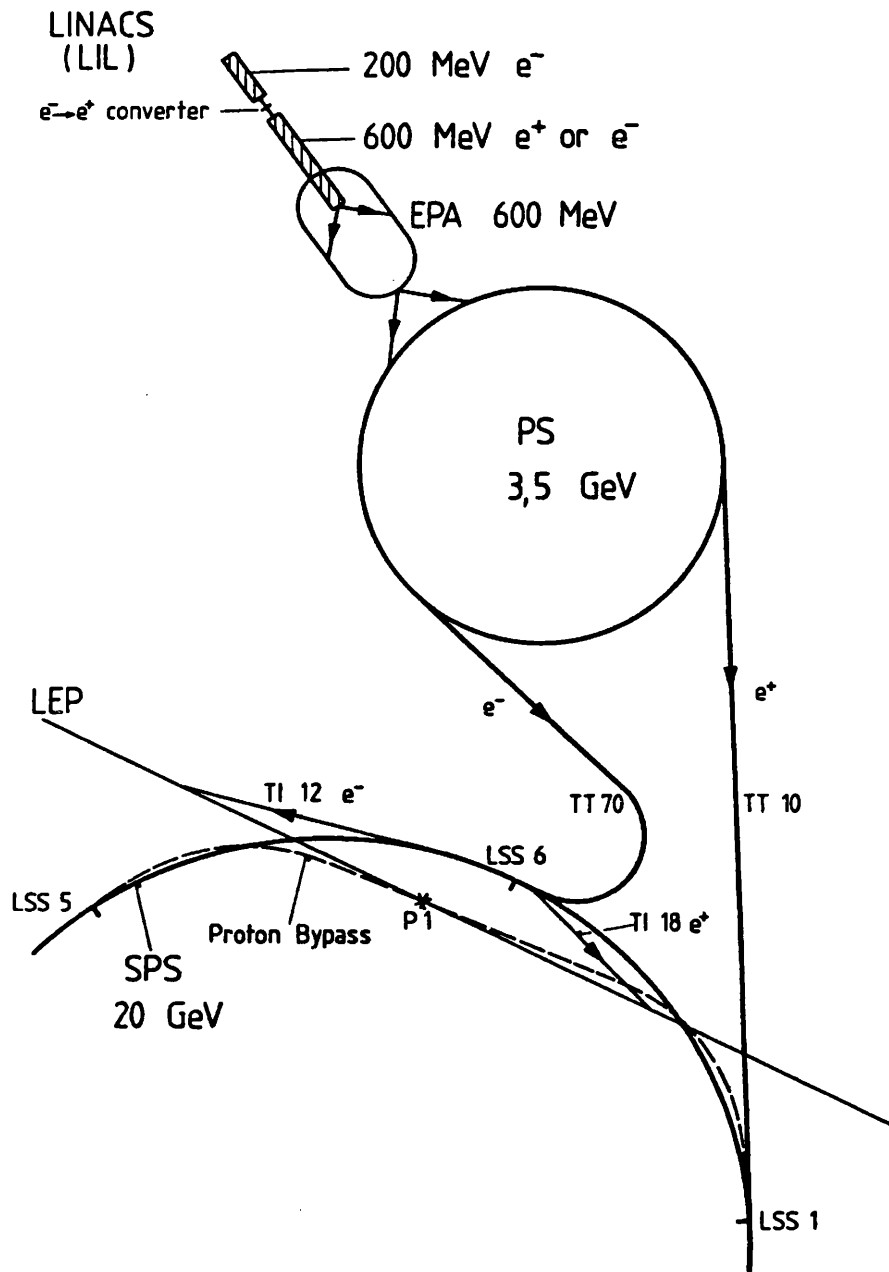
Figure 1.2:   The sequence of accelerators required for LEP injection.

is

$$\frac{dN}{dt} = \sigma\mathcal{L} \tag{1.1}$$

where σ is the interaction cross section for the process and $\mathcal{L}$ is the luminosity. In 1999 the peak luminosity seen was $1.1 \times 10^{32}\mathrm{cm}^{-2}\mathrm{s}^{-1}$.

1.2.3   The current state of LEP

LEP was finally disassembled after the physics run in 2000. The LEP tunnel will be used for the Large Hadron Collider, LHC, due to begin its physics programme in 2006.

Chapter 2

The theory of elementary particle interactions

2.1 A theoretical framework for particle interactions

The work documented in this thesis is performed within the context of the so-called Standard Model of Elementary Particle Interactions, or more simply *the Standard Model* (SM).

The Standard Model represents the current working model of the spectrum, properties and interactions of the most fundamental, indivisible, objects in the Universe. The Standard Model is the result of hundreds of years of work in Physics, although it owes most of its features to work performed in the last one hundred years. From the discovery of the electron by J. J. Thompson[5] in 1897 to that of the quark[6] in the 1960s, was the particle spectrum established which is now described by the Standard Model.

Despite the success of the Standard Model it is regarded as an incomplete picture of Nature. For this reason extensions to the Standard Model have been proposed and some of the work presented here will be concerned with the extended models known as the Minimal Supersymmetric extension of the Standard Model (MSSM).

In the following section the gross features of the SM and the MSSM are pointed out, together with points particularly relevant to the work contained in this thesis.

However the interested reader is urged to follow the cited references for a more complete discussion of the SM, the MSSM or other theories of particle interactions. A quantity of the material in this chapter was taken from [7].

2.2   The Standard Model

It has been found that the behaviour of the fundamental particles of Nature can be well described by a Quantum Field Theory (QFT). The Standard Model is a particular theory based on a QFT. The Standard Model describes the interactions of fields that represent the fundamental constituents of matter, *quarks* and *leptons*. Table 2.1 lists the known quarks and leptons. All these fermions have spin $\frac{1}{2}$. For reasons that are not known the quarks and leptons are each grouped together into families or generations. Experiment suggests that three generations exist[8] in Nature.

The Standard Model describes the interactions of the fermionic matter fields with bosonic fields. The bosonic fields arise as a result of local gauge symmetries within the model. Physically gauge bosons are associated to the bosonic fields. The gauge bosons are the force-carrying particles and have integer spin. By exchanging bosons the fermion matter particles experience a change in their momentum and hence interact.

The gauge bosons of the Standard Model are listed in table 2.2. To date four forces have been seen to act in Nature. They are the strong force, the weak force, the electromagnetic interaction and gravity. The names of three of the forces are also listed in table 2.2 and are identified with the gauge boson to which the propagation of the force is attributed. Quarks and electrically charged leptons may interact through the electro-magnetic force, while both quarks and leptons experience the weak force. Quarks alone are subject to the strong force.

No satisfactory description has been made of gravity at the quantum level. Gravity and the corresponding bosonic force carrier, the graviton, are excluded from the discussion in the rest of this thesis.

The original success of a QFT came with the development of Quantum Electro Dynamics (QED). QED describes the interactions of electrically charged particles via the exchange of photons and has been experimentally tested and verified to a precision

Quarks			
Particle Name	Symbol	Electric Charge (e)	Mass GeV/c^2
up	u	+2/3	0.0015 to 0.005
down	d	-1/3	0.003 to 0.009
charm	c	+2/3	1.1 to 1.4
strange	s	-1/3	0.060 to 0.170
top	t	+2/3	173.8 ± 5.2
bottom	b	-1/3	4.1 to 4.4

Leptons			
Particle Name	Symbol	Electric Charge (e)	Mass MeV/c^2
electron	e	-1	0.510999
electron neutrino	ν_e	0	< 0.000015
muon	μ	-1	105.658
muon neutrino	ν_μ	0	< 0.17
tau	τ	-1	$1777.05^{+0.29}_{-0.26}$
tau neutrino	ν_τ	0	< 18.2

Table 2.1: List of fermions described by the Standard Model. Each of the particles also has a corresponding antiparticle with opposite electric change.

of one part in 10^8.

The development of the weak force as a Quantum Field Theory and its unification with the electromagnetic force to form the electroweak force was a very important step. The QFT had allowed the unification of two seemingly separate forces to a new more fundamental force. The mathematical expression of the electroweak force was a great step forward in the construction of the SM.

The addition of the strong force, which is mediated by the exchange of the gluons completes the SM that is in use today. The strong force interacts with particles which

Gauge Bosons				
Force	Particle Name	Symbol	Electric Charge (e)	Mass GeV/c^2
Electroweak	Photon	γ	0	0
Electroweak	W boson	$W^\pm$	± 1	80.402 ± 0.020
Electroweak	Z boson	Z	0	91.187 ± 0.007
Strong	gluon	g	0	0

Table 2.2: The force-carrying gauge bosons of the Standard Model.

carry a charged referred to as colour, and for that reason the theory of the strong force is called Quantum ChromoDynamics (QCD).

2.2.1 Fundamental Particles and Gauge Symmetries

The interaction terms in the SM Lagrangian arise through requirement that the physical interpretation of the theory should not depend on the relative phase of the fermion wave-functions.

For example, consider a space-time independent transformation of a fermion field

$$\psi(x) \rightarrow e^{i\alpha}\psi(x) \tag{2.1}$$

where α is a real constant. If the Lagrangian for the free propagation of a particle with mass m,

$$\mathcal{L} = \bar{\psi}(i\gamma^\mu \partial_\mu - m)\psi \tag{2.2}$$

is to be invariant under such a transform then it follows that

$$\partial_\mu \psi \rightarrow e^{i\alpha}\partial_\mu \psi \tag{2.3}$$

and

$$\bar{\psi} \rightarrow e^{-i\alpha}\bar{\psi} \tag{2.4}$$

Such an invariance is known as a *global gauge* invariance. Noether's theorem[9] implies the existence of a conserved current for every continuous symmetry of a Lagrangian. Following from this the fundamental particles are said to possess conserved gauge charges.

If instead it is required that the Lagrangian must be also locally invariant, i.e.

$$\psi(x) \to e^{i\alpha(x)}\psi(x) \tag{2.5}$$

where $\alpha(x)$ is now dependent on space-time coordinates x then the transformation is said to be a *local gauge* transform. In the case of the local gauge transform the Lagrangian of equation (2.2) is not invariant. To gain invariance the partial derivative, ∂_μ must be replaced with another operator denoted D_μ such that

$$D_\mu\psi \to e^{-i\alpha(x)}D_\mu\psi \tag{2.6}$$

The operator D_μ is called the covariant derivative. It can be seen that in order to have the transformation properties of 2.6, D_μ must be constructed as

$$D_\mu = \partial_\mu - ieA_\mu \tag{2.7}$$

where A_μ is a vector field which transforms as

$$A_\mu \to A_\mu + \frac{1}{e}\partial_\mu\alpha. \tag{2.8}$$

So replacing ∂_μ with D_μ in 2.2

$$\mathcal{L} = \bar{\psi}(i\gamma^\mu\partial_\mu - m)\psi + e\bar{\psi}\gamma^\mu A_\mu\psi \tag{2.9}$$

which is now invariant under local gauge transformations. However as a consequence a vector field A_μ has been introduced into the Lagrangian. From the form of the last term it can be seen that the field A_μ will couple to the fermion fields.

The physical interpretation of requiring local gauge invariance is that a new particle has arisen that interacts with the fermions in the theory. The presence of the interaction (potential) term in the Lagrangian requires the addition of a corresponding kinetic term. In order to preserve the Lagrangian's gauge invariance the kinematic term is formed from the gauge invariant field strength tensor,

$$F_{\mu\nu} = \partial_\mu A_\nu - \partial_\nu A_\mu \tag{2.10}$$

yielding the Lagrangian

$$\mathcal{L} = \bar{\psi}(i\gamma^\mu\partial_\mu - m)\psi + e\bar{\psi}\gamma^\mu A_\mu\psi - \frac{1}{4}F^{\mu\nu}F_{\mu\nu}. \tag{2.11}$$

Equation 2.11 is that of QED, in which charged fermions interact via the exchange of a massless boson. In QED the charge is identified with electric charge and the exchange boson is the photon.

In the above example of QED, of particular interest is that requiring local gauge invariance lead naturally to the presence of a massless vector boson in the theory. The introduction of an explicit mass term for the vector boson in the Lagrangian ($\frac{1}{2}m^2 A_\mu A^\mu$) would violate gauge invariance.

2.2.2 The Higgs Mechanism

Generally a Quantum Field Theory may not give finite results when used as a physical model. However the QFTs that are locally gauge invariant have been found to be renormalizable. In particular the renormalizability of the theories means that they yield finite, calculable, predictions. Given this, plus the above description of the natural way in which the fermion fields are found to interact, makes the local gauge invariant QFT very attractive.

The main problem, as seen in the example of QED above is that local gauge invariance requires massless gauge bosons. Addition of explicit mass terms loose not just the local gauge invariance but the renormalizability of the theory as well. Massless gauge bosons are very much at odds with the observations of massive weak gauge bosons, the $W^\pm$ and Z^0. The weak force is known to operate only over short distances, which implies a massive force carrier. In addition the direct observation of massive weak bosons has enabled their mass to be measured to be in the order of $80 - 90$ GeV/c^2[10, 11].

A solution to the apparent inadequacy of massless gauge bosons is found in the Higgs Mechanism[12, 13]. The Higgs mechanism provides a way to generate masses for the gauge bosons while retaining the local gauge invariance of the theory.

The Higgs mechanism generates mass for the gauge bosons by means of spontaneous symmetry breaking. A given symmetry is said to be spontaneously broken if the vacuum does not possess the same symmetry as the Lagrangian. For example, consider a U(1) locally gauge invariant Lagrangian describing the interaction of a scalar field

$\phi(x)$ with a gauge field $A_\mu(x)$

$$\mathcal{L} = (D_\mu \phi)^\dagger (D_\mu \phi) - V(\phi) - \frac{1}{4} F_{\mu\nu} F^{\mu\nu} \tag{2.12}$$

where $\phi = \frac{1}{\sqrt{2}}(\phi_1 + i\phi_2)$, $D^\mu = \partial^\mu + ig A^\mu$ and the scalar potential $V(\phi)$ is described by $V(\phi) = \mu^2 \phi^\dagger \phi + \lambda(\phi^\dagger \phi)^2$ with $\lambda > 0$.
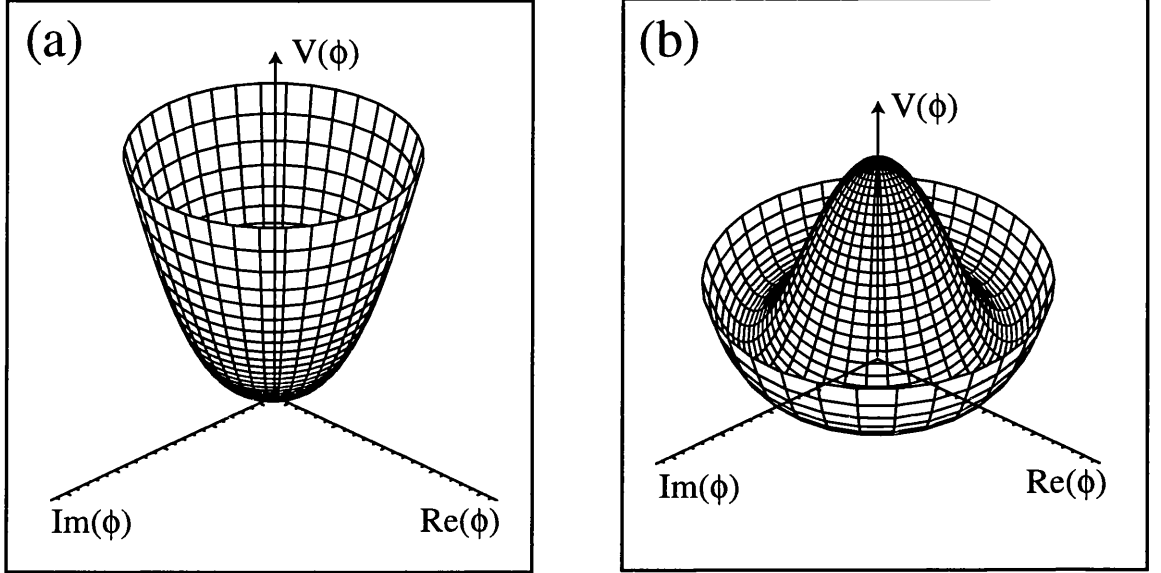
Figure 2.1: The potential $V(\phi) = \mu^2 \phi^\dagger \phi + \lambda(\phi^\dagger \phi)^2$ for (a) $\mu^2 > 0$ and (b) $\mu^2 < 0$.

Two possible solutions for the form of the scalar potential $V(\phi)$ exist. Choosing $\mu^2 > 0$ gives a minimum at $\phi_1 = \phi_2 = 0$, illustrated in figure 2.1a, while for the choice with $\mu^2 < 0$, $V(\phi)$ takes on the form depicted in figure 2.1b.

When $V(\phi)$ takes the form shown in 2.1b the minima form a ring situated at

$$|\phi|^2 = \phi_1^2 + \phi_2^2 = \frac{-\mu^2}{2\lambda} = \frac{\nu^2}{2} \tag{2.13}$$

The symmetry visible in the scalar potential of 2.1b is broken by making a specific choice of minimum. In the SM the gauge symmetry is said to be *spontaneously broken*. That is, the vacuum does not exhibit the gauge invariance which the Lagrangian possesses due to the vacuum having spontaneously adopted a specific ground state.

Returning to the example of the scalar field in the Lagrangian of equation (2.12), a ground state is chosen by translation. $\phi(x)$ may then be expanded about the vacuum, e.g. in terms of the fields h, ξ according to

$$\phi(x) = \frac{1}{\sqrt{2}} \exp\left(i\frac{\xi(x)}{\nu} \right) [\nu + h(x)] \tag{2.14}$$

the Lagrangian becomes

$$\mathcal{L}' = \frac{1}{2}(\partial_\mu h)^2 + \frac{1}{2}(\partial_\mu \xi)^2 + \mu^2 h^2 + g\nu A_\mu \partial^\mu \xi + \frac{1}{2}g^2 \nu^2 A_\mu A^\mu$$
$$- \frac{1}{4}F_{\mu\nu}F^{\mu\nu} + \text{Interaction terms...} \tag{2.15}$$

The Lagrangian $\mathcal{L}'$ is composed of a massless (ξ) and a massive scalar field (h) plus, crucially, a massive vector field A_μ.

For the Lagrangian $\mathcal{L}'$

$$m_\xi = 0,$$

$$m_h = \sqrt{-2\mu^2}, \tag{2.16}$$

$$m_A = g\nu.$$

A massive vector boson has been generated without spoiling the local gauge invariance of the Lagrangian. The Lagrangian also contains a massless field, ξ. In general ξ is an example of a Goldstone boson. Goldstone's theorem[14] states that the spontaneous breaking of a continuous global symmetry is always accompanied by one ore more massless scalar particles.

However in the context of a local gauge symmetry ξ does not correspond to a physical particle. Consider a particular gauge transform, $\alpha(x) = -\xi(x)/g\nu$ (known as the Unitary Gauge). Under the Unitary Gauge the fields become

$$\phi \to \phi'(x) = \phi(x)\exp\left(i\frac{\xi(x)}{\nu}\right) = \frac{1}{\sqrt{2}}(\nu + h(x))$$
$$A_\mu(x) \to A'_\mu(x) = A_\mu(x) - \frac{1}{g\nu}\partial_\mu \xi(x) \tag{2.17}$$

The terms in ξ and $\partial_\mu \xi$ cancel in the Lagrangian and so

$$\mathcal{L}'' = \frac{1}{2}(\partial_\mu h)^2 + \mu^2 h^2 + \frac{1}{2}g^2 \nu^2 A_\mu A^\mu - \frac{1}{4}F_{\mu\nu}F^{\mu\nu} \tag{2.18}$$

The Goldstone boson can be interpreted as a longitudinal polarisation degree of freedom for the massive gauge field A_μ. From 2.18 it can be seen that after spontaneous symmetry breaking the theory is left with a massive real scalar field $h(x)$ with mass $\sqrt{-2\mu^2}$ and a massive gauge field A_μ with mass $g\nu$.

2.2.3 The Electroweak Interaction

The electroweak model of Glashow[15], Salam[16] and Weinberg[17] is based on the symmetry group $SU(2)_L \otimes U(1)_Y$. Following from the case of QED in which

$$-iej_\mu^{\text{em}} A^\mu = -ie(\bar{\psi}\gamma_\mu Q\psi)A^\mu \tag{2.19}$$

where Q is the electric charge operator and j_μ^{em} represents the conserved electromagnetic current, it is found that the electroweak process requires two basic interactions. Firstly an iso-triplet of weak currents J_μ coupled to three vector bosons W_i^μ ($i = 1, 2, 3$).

$$-gJ_\mu W^\mu = -ig\bar{\chi}_L\gamma_\mu T W^\mu \chi_L \tag{2.20}$$

and secondly a weak hypercharge current coupled to a fourth vector boson B_μ,

$$\frac{-ig'}{2}J_\mu^Y B^\mu = -g'\bar{\psi}\gamma_\mu \frac{Y}{2} B^\mu \tag{2.21}$$

where the operators T and Y are the generators of the $SU(2)_L$ and $U(1)_Y$ groups of gauge transforms respectively, while g and g' are two coupling constants and χ_L is the left handed components of ψ. Taken together the transformations of the left handed and right handed components of ψ are

$$\begin{aligned} \chi_L &\rightarrow \chi_L' = e^{i\alpha(x)T + i\beta(x)Y}\chi_L \\ \psi_R &\rightarrow \psi_R' = e^{i\beta(x)Y}\psi_R \end{aligned} \tag{2.22}$$

where left handed fermions form isospin doublets χ_L and right handed fermions form iso-singlets ψ_R.

For example, in the first generation

$$\chi_L = \begin{pmatrix} \nu_e \\ e^- \end{pmatrix}_L \quad \text{with} \quad T = \frac{1}{2}, Y = -1$$

$$\psi_R = \bar{e}_R \quad \text{with} \quad T = 0, Y = -2 \tag{2.23}$$

$$\chi_L = \begin{pmatrix} u \\ d \end{pmatrix}_L \quad \text{with} \quad \psi_R = u_R, d_R$$

Imposing $SU(2)_L \otimes U(1)_Y$ invariance results in a Lagrangian of the form

$$\begin{aligned} \mathcal{L}_1 = &\bar{\chi}_L\gamma^\mu[i\partial_\mu - g\frac{1}{2}\tau W_\mu - g'(\frac{-1}{2})B_\mu]\chi_L \\ &+ \bar{e}_R\gamma^\mu[i\partial_\mu - g'(-1)B_\mu]e_R \\ &- \frac{1}{4}W_{\mu\nu}W^{\mu\nu} - \frac{1}{4}B_{\mu\nu}B^{\mu\nu} \end{aligned}$$

where τ are the Pauli spin matrices and the hypercharge values $Y_L = -1$, $Y_R = -2$ have been inserted. $\mathcal{L}_1$ embodies both the weak isospin and hypercharge interactions. The final two terms represent the kinematic energy and self coupling of the W_μ fields and the kinetic energy of the B_μ field.

The gauge symmetry of $\mathcal{L}_1$ is broken if a mass term for the boson or the fermion fields is introduced directly. To generate mass within the electroweak sector the Higgs mechanism is used. The Higgs mechanism is here formulated such that the $W^\pm$ and Z^0 bosons become massive while the photon remains massless. To achieve this, four real scalar fields ϕ_i are introduced by adding gauge invariant Lagrangian terms

$$\mathcal{L}_2 = |(i\partial_\mu - gTW_\mu - g'\frac{Y}{2}B_\mu)\phi|^2 - V(\phi) \tag{2.24}$$

to the electroweak Lagrangian $\mathcal{L}_1$, where the fields ϕ belong to a $SU(2)_L \otimes U(1)_Y$ multiplet and $|x|^2 = x^\dagger x$.

The minimal choice is to arrange the four fields in an isospin doublet with weak hypercharge $Y = +1$:

$$\phi = \begin{pmatrix} \phi^+ \\ \phi^0 \end{pmatrix} = \frac{1}{\sqrt{2}} \begin{pmatrix} \phi_1 + i\phi_2 \\ \phi_3 + i\phi_4 \end{pmatrix} \tag{2.25}$$

The Higgs potential is chosen such that

$$V(\phi) = \mu^2 \phi^\dagger \phi + \lambda(\phi^\dagger \phi)^2 \tag{2.26}$$

where, in the case of $\mu^2 < 0$ and $\lambda > 0$, this has a minimum at a finite value of $|\phi|$ defined by

$$|\phi|^2 = \frac{-\mu^2}{2\lambda} \neq 0. \tag{2.27}$$

The ground state chosen is degenerate and has no preferred direction in weak isospin space as a consequence of the $SU(2)_L$ symmetry. It is therefore possible to choose the value of the phase ϕ.

By choosing

$$\phi_0 = \frac{1}{\sqrt{2}} \begin{pmatrix} 0 \\ \nu \end{pmatrix} \tag{2.28}$$

the $U(1)_{em}$ symmetry is left unbroken. That is $Q\phi_0 = 0$ such that

$$\phi_0 \rightarrow \phi_0' = e^{i\alpha(x)Q}\phi_0 = \phi_0 \tag{2.29}$$

28

for any value of $\alpha(x)$.

The vacuum remains invariant under a $U(1)_{\text{em}}$ transform and the gauge boson associated with the electromagnetic force, the photon, remains massless. By expanding $\phi(x)$ about the chosen vacuum it is found that ϕ may be expressed in terms of the one remaining scalar field, which is here denoted as the Higgs field h:

$$\phi(x) = \frac{1}{\sqrt{2}} \begin{pmatrix} 0 \\ \nu + h(x) \end{pmatrix} \tag{2.30}$$

The massive gauge bosons are identified by substituting the vacuum expectation value ϕ_0 for $\phi(x)$ into the Lagrangian $\mathcal{L}_2$ giving:

$$(\frac{1}{2}\nu g)^2 W_\mu^+ W_\mu^- + \frac{1}{8}\nu^2 (W_\mu^3, B_\mu) \begin{pmatrix} g^2 & -gg' \\ -gg' & g'^2 \end{pmatrix} \begin{pmatrix} W^{\mu 3} \\ B^\mu \end{pmatrix} \tag{2.31}$$

where $W^\pm = \frac{1}{\sqrt{2}}(W^1 \mp W^2)$. The comparison of the first term with the expected form of a mass term for a charged boson, $m_W^2 W^+ W^-$, leads to the identification of the W boson mass as

$$m_W = \frac{1}{2}g\nu \tag{2.32}$$

The second term is off diagonal in the (W_μ^3, B_μ) basis. Diagonalisation of the 2x2 mass matrix yields

$$0 \left(g'W_\mu^3 + gB_\mu\right)^2 + \frac{1}{8}\nu^2 \left(gW_\mu^3 - g'B_\mu\right)^2 \tag{2.33}$$

These two orthogonal terms represent the physical fields A_μ and Z_μ with their respective masses m_A and m_Z given by comparison of the expected mass terms for neutral vector bosons $\frac{1}{2}m_A^2 A^2$ and $\frac{1}{2}m_Z^2 Z^2$.

$$A_\mu = \frac{g'W_\mu^3 + gB_\mu}{\sqrt{g^2 + g'^2}}$$

$$m_A = 0$$

$$Z_\mu = \frac{gW_\mu^3 - g'B_\mu}{\sqrt{g^2 + g'^2}} \tag{2.34}$$

$$m_Z = \frac{\nu}{2}\sqrt{g^2 + g'^2}.$$

This result may be recast in terms of θ_W by considering

$$\tan\theta_W = \frac{g'}{g}. \tag{2.35}$$

Thus:

$$A_\mu = \cos\theta_W B_\mu + \sin\theta_W W_\mu^3 \qquad (2.36)$$

and

$$Z_\mu = -\sin\theta_W B_\mu + \cos\theta_W W_\mu^3 \qquad (2.37)$$

and so

$$\frac{m_W}{m_Z} = \cos\theta_W \qquad (2.38)$$

The inequality $m_Z \neq m_W$ originates from the mixing between the W_μ^3 and B_μ fields. The application of the Higgs mechanism to the electroweak sector of the Standard Model has led to the generation of a massless photon, A_μ, and massive Z_μ and $W^\pm$ fields with $m_Z > m_W$. The relationship between m_Z and m_W is a prediction of the Standard Model and the Higgs sector as described here. Tests of this relationship form an indirect probe into the exact nature of the Higgs mechanism which is at work in the electroweak sector.

2.2.4 The Higgs boson and the fermions

As for the gauge bosons, addition of a fermion mass term, $-m\bar\psi\psi$, into the electroweak Lagrangian (equation 2.2.3) would result in loss of gauge invariance. However, the Higgs mechanism is also able to give mass to the leptons and quarks.

For example, considering the case of the electron, to generate the electron mass the following $SU(2)_L \otimes SU(1)_Y$ gauge invariant term is added to the Lagrangian,

$$\mathcal{L}_3 = -G_e \left[(\bar\nu_e \bar e)_L \begin{pmatrix} \phi^+ \\ \phi^0 \end{pmatrix} e_R + \bar e_R (\phi^-, \bar\phi^0) \begin{pmatrix} \nu_e \\ e \end{pmatrix}_L \right] \qquad (2.39)$$

where the Higgs doublet is found to have the exact $SU(2)_L \otimes U(1)_Y$ quantum numbers to couple to $\bar e_L e_R$. After spontaneous symmetry breaking takes place

$$\mathcal{L}'_3 = -\frac{G_e}{\sqrt{2}}\nu(\bar e_L e_R + \bar e_R e_L) - \frac{G_e}{\sqrt{2}}(\bar e_L e_R + \bar e_R e_L)h \qquad (2.40)$$

and substituting $m_e = G_e \nu / \sqrt{2}$ the Lagrangian term may be written as

$$\mathcal{L}'_3 = -m_e \bar e e - \frac{m_e}{\nu}\bar e e h. \qquad (2.41)$$

Thus the theory gains a mass term for the electron along with an electron-Higgs interaction term. The other leptons and the quarks may also gain mass through the Higgs mechanism. The strength of the interaction between the Higgs boson and each fermion is not predicted (i.e., G_e in the above was arbitrary). However, it can be seen that the fermion masses are directly proportional to the strength of their couplings to the Higgs boson.

2.3   The Strong Interaction

Quarks experience strong interactions while leptons do not. The part of the Standard Model describing strong interactions is a gauge field theory known as quantum chromo-dynamics (QCD) based on the non-Abelian group $SU(3)$. The corresponding strong gauge charge is referred to as colour and comes in three varieties (e.g., red, green and blue). Hence, for each quark flavour, there are three possible colours it may possess. The gauge bosons for the strong interaction are the gluons.

The first direct evidence for the gluon was found in three-jet events interpreted as hard gluon bremsstrahlung from one of the quarks leading to two quark jets and a gluon jet (i.e. $e^+e^- \rightarrow q\bar{q}g$)[18, 19, 20]. However, there is no evidence of free single quarks or gluons in Nature[21]. This observation supports a central feature of QCD, called confinement. Confinement refers to the fact that at small values of momentum transfer, Q^2 the QCD running coupling constant $\alpha_s(Q^2)$ becomes large. The complementary case is referred to as asymptotic freedom; At large values of Q^2, $\alpha_s(Q^2)$ tends to zero and QCD processes can be treated perturbatively, quarks behave as quasi-free particles. This leads to the existence of only colour-singlet objects in Nature and the fact that a non-colour singlet configuration of quarks will polarise the vacuum creating $q\bar{q}$ pairs until a system of colour-singlet objects is obtained.

2.4   The MSSM

In addition to the Standard Model interpretation of the Higgs sector, described in section 2.2.3, the Higgs sector is found to be richer in the context of the Minimal Supersymmetric extension of the Standard Model (MSSM) and is described briefly

here.

Supersymmetry is an attractive extension to the Standard Model. Supersymmetry (or SUSY) has been been extensively studied theoretically, and experimental evidence to test if this model may be realised in Nature has been sought. However, to date no experimental evidence has been found. The search continues and in this thesis the Higgs boson search results are also applied to the Higgs sector as found in the MSSM.

In supersymmetric models each matter fermion has a scalar SUSY partner and each gauge boson has a fermionic SUSY partner. The naming convention for the new scalar particles is simply to append an 's' (for scalar) to the front of the name of their Standard Model counterpart. The notation convention for all the new supersymmetric particles is that of a tilde above the letter used to denote the Standard Model equivalent. For example, the *selectron* ($\tilde{e}$), *smuon* ($\tilde{\mu}$) and *sneutrino* ($\tilde{\nu}$) or more generally a *slepton* ($\tilde{l}$). Alternatively there is the *stop* ($\tilde{t}$) and the *sbottom* ($\tilde{b}$), both examples of a *squark* ($\tilde{q}$). These are all *sfermions* ($\tilde{f}$). With the exception of the sneutrinos, there are two of each corresponding to the left-handed and right-handed states of the respective Standard Model particle. Thus the difference between a left-handed and right-handed sfermion is nothing to do with helicity (or chiral) states of the sfermions themselves (since they are scalar), but instead refers to the helicity states of their Standard Model superpartners. All the supersymmetric partners of the Standard Model particles are collectively known as *sparticles*.

In a SUSY theory there must be at least two Higgs doublets. This doubles the number of real degrees of freedom, with respect to the SM, to eight. After electroweak symmetry breaking, as in the Standard Model, three degrees of freedom become the longitudinal modes of the Z and $W^{\pm}$. Thus five, as opposed to just one in the SM, are left over and form new scalar bosons. So in SUSY theories there must be at least five Higgs bosons. Three are neutral, one positive and one negative.

The spin $\frac{1}{2}$ superpartners of the MSSM Higgs bosons are referred to as the *Higgsinos*. SUSY partners also exist for the Standard Model's gauge bosons. The naming convention for the fermionic partners of bosons is to add 'ino' to the end of the name of the Standard Model counterpart, replacing 'on' where it exists. Thus *photino* ($\tilde{\gamma}$), *zino* ($\tilde{Z}$), *wino* ($\tilde{W}^{\pm}$) and *gluino* ($\tilde{g}$), all of which are *gauginos*. However, the zino, wino and

Higgsinos are not mass eigenstates. The mass eigenstates are called the *neutralinos* (which are a mix of the zino and neutral higgsinos) and the *charginos* (which are a mix of the winos and charged higgsinos).

The five Higgs bosons of the MSSM are denoted, h, A, H and $H^{\pm}$. The h and H are CP-even while the A is CP-odd. The form of the Higgs potential is

$$V(\Phi_1, \Phi_2) = \lambda_1(\Phi_1^{\dagger}\Phi_1 - \nu_1^2)^2 + \lambda_2(\Phi_2^{\dagger}\Phi_2 - \nu_2^2)^2$$
$$+ \lambda_3[(\Phi_1^{\dagger}\Phi_1 - \nu_1^2) + (\Phi_2^{\dagger}\Phi_2 - \nu_2^2)]^2$$
$$+ \lambda_4[(\Phi_1^{\dagger}\Phi_1)(\Phi_2^{\dagger}\Phi_2) - (\Phi_1^{\dagger}\Phi_2)(\Phi_2^{\dagger}\Phi_1)]$$
$$+ \lambda_5[Re(\Phi_1^{\dagger}\Phi_2) - \nu_1\nu_2]^2$$
$$+ \lambda_6[Im(\Phi_1^{\dagger}\Phi_2)]^2$$

where λ_i are real parameters and Φ_1 and Φ_2 denote two complex fields.

$$\langle\Phi_1\rangle = \begin{pmatrix} \phi_1^{0*} \\ -\phi_1^{-} \end{pmatrix}, \quad Y = -1$$
$$\langle\Phi_2\rangle = \begin{pmatrix} \phi_2^{+} \\ \phi_2^{0} \end{pmatrix}, \quad Y = 1 \tag{2.42}$$

Both Φ_1 and Φ_2 form a doublet under $SU(2)_L$ with opposite hypercharge. If the parameters λ_i are not negative then the following minima for the potentials are found

$$\langle\Phi_1\rangle = \begin{pmatrix} 0 \\ \nu_1 \end{pmatrix}, \quad \langle\Phi_2\rangle = \begin{pmatrix} 0 \\ \nu_2 \end{pmatrix} \tag{2.43}$$

where ν_1 and ν_2 are the vacuum expectation values of the Higgs fields. (They are related to the W mass via $m_W^2 = g^2(\nu_1^2 + \nu_2^2)/2$).

Once the Goldstone bosons have been removed five physical states arise. The MSSM Higgs sector is described by six independent parameters. The four Higgs boson masses, the ratio of vacuum expectation values:

$$\frac{\nu_1}{\nu_2} = \tan\beta \tag{2.44}$$

and α, a mixing angle in the CP-even sector. The physical Higgs states in the charged sector are

$$H^{\pm} = -\Phi_1^{\pm}\sin\beta + \Phi_2^{\pm}\cos\beta \tag{2.45}$$

with a mass $m_{H^{\pm}}^2 = \lambda_4(\nu_1^2 + \nu_2^2)$. The CP-odd sector has one boson, A,

$$A = \sqrt{2}(-Im(\Phi_1^0)\sin\beta + Im(\Phi_2^0)\cos\beta) \tag{2.46}$$

with a mass $m_A^2 = \lambda_6(\nu_1^2 + \nu_2^2)$. In the CP-even sector two physical Higgs scalars mix through the following mass squared matrix

$$\mathcal{M} = \begin{pmatrix} 4\nu_1^2(\lambda_1 + \lambda_3) + \nu_2^2\lambda_5 & (4\lambda_3 + \lambda_5)\nu_1\nu_2 \\ (4\lambda_3 + \lambda_5)\nu_1\nu_2 & 4\nu_2^2(\lambda_2 + \lambda_3) + \nu_1^2\lambda_5 \end{pmatrix} \tag{2.47}$$

with the physical mass eigenstates

$$H^0 = \sqrt{2}[(Re(\Phi_1^0) - \nu_1)\cos\alpha + (Re(\Phi_2^0)\nu_2)\sin\alpha]$$
$$h^0 = \sqrt{2}[-(Re(\Phi_1^0) - \nu_1)\sin\alpha + (Re(\Phi_2^0) - \nu_2)\cos\alpha] \tag{2.48}$$

and corresponding masses

$$m_{H^0,h^0}^2 = \frac{1}{2}[\mathcal{M}_{11} + \mathcal{M}_{22} \pm \sqrt{(\mathcal{M}_{11} - \mathcal{M}_{22})^2 + 4\mathcal{M}_{12}^2}]. \tag{2.49}$$

The sixth free parameter, the mixing angle of the CP-even fields α, is obtained from

$$\sin(2\alpha) = \frac{2\mathcal{M}_{12}}{\sqrt{(\mathcal{M}_{11} - \mathcal{M}_{22})^2 + 4\mathcal{M}_{12}^2}}$$
$$\cos(2\alpha) = \frac{\mathcal{M}_{11} - \mathcal{M}_{22}}{\sqrt{(\mathcal{M}_{11} - \mathcal{M}_{22})^2 + 4\mathcal{M}_{12}^2}} \tag{2.50}$$

The couplings of the Higgs bosons to gauge bosons and fermions determine production cross sections as well as decay rates.

The production cross sections for the processes $e^+e^- \rightarrow hZ$ and $e^+e^- \rightarrow hA$ are

$$\sigma(e^+e^- \rightarrow hZ) = \sin^2(\beta - \alpha)\sigma_{SM}$$
$$\sigma(e^+e^- \rightarrow hA) = \cos^2(\beta - \alpha)\bar{\lambda}\sigma_{SM} \tag{2.51}$$

The factor $\bar{\lambda}$ is a phase space factor, while σ_{SM} is the cross section for the $e^+e^- \rightarrow hZ$ process within the Standard Model.

2.5 Higgs Boson Phenomenology

This section presents the phenomenological issues relevant to the Higgs boson searches at LEP II. The interaction of the Higgs boson with the other particles of the Standard Model may be described fully as a function of the Higgs boson mass. Therefore, for a given Higgs boson mass, all relevant processes (e.g., production cross sections and decay branching ratios) of the Higgs boson may be determined. The results of these calculations are used to provide a framework for developing direct Higgs boson searches and interpreting the results of searches.

2.5.1   Constraints on the Higgs boson mass

Although the Higgs boson mass is a free parameter in the Standard Model, it may be constrained by both theoretical and experimental methods. Theoretical arguments based on the self-consistency of the Standard Model may be used to derive upper bounds on the mass of the Higgs boson while experimental results from electroweak data and direct searches may be used to set indirect and direct mass bounds, respectively.

Theoretical arguments based on unitarity may be used to place upper bounds on the mass of the Higgs boson. The absence of a fundamental scalar field, the Higgs field, causes the amplitude for longitudinally polarised WW scattering to diverge quadratically in energy when calculated perturbatively[22]. This ultimately leads to the violation of unitarity. The inclusion of the Higgs boson in the theory suppresses this behaviour and unitarity remains unviolated provided that the Higgs boson has a mass less than ~ 1 TeV/c^2.

The mass of the Higgs boson may also be constrained by precision measurements of electroweak data[10]. Electroweak processes are sensitive to the mass of the Higgs boson. The Higgs enters through higher order loop diagrams. The mass of the Higgs boson may be constrained by comparing the experimental measurements obtained from electroweak data to the predictions given for various Higgs boson masses. Similar methods were successfully used to constrain the mass of the top quark before its discovery in 1995[23, 24]. Precision electroweak measurements have been combined by the **LEP** Electroweak Working Group with a global fit to these data, performed as a function of the Higgs boson mass. The results of the fit, expressed in the form $\Delta\chi^2 = \chi^2 - \chi^2_{min}$, are shown in figure 2.2. The resulting fit determines the mass of the Higgs boson to be in the range

$$m_{\mathrm{h}} = 60^{+52}_{-29} \text{ GeV}/c^2 \qquad (2.52)$$

while masses above 165 GeV/c^2 are excluded at the 95% confidence level[10]. However it should be noted that as noted in the cited source, the fit is very sensitive to the coupling constant α input into the fit. Using an alternative value gave $m_{\mathrm{h}} = 88^{+60}_{-37}$ GeV/c^2 an upper limit at the 95% confidence level of 206 GeV/c^2.

Direct searches for the Higgs boson by the four experiments at the **LEP** collider
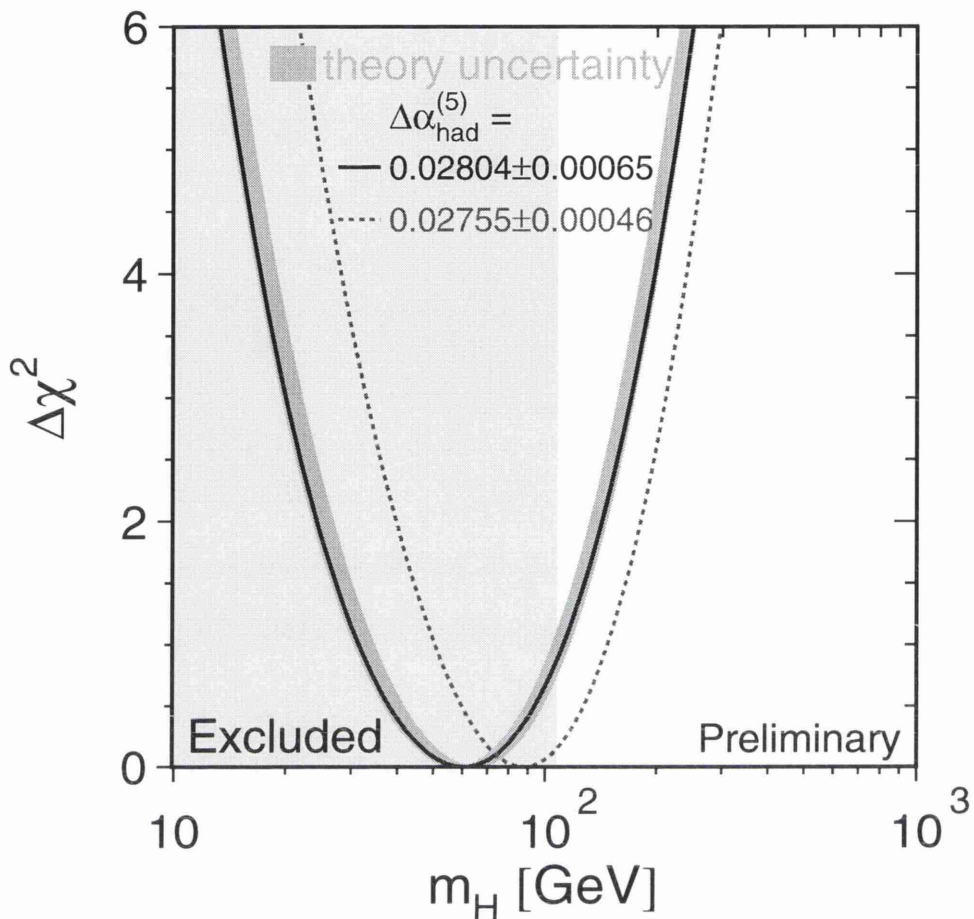
Figure 2.2: $\Delta\chi^2 = \chi^2 - \chi^2_{min}$ against m_h, from [10].

provide stringent lower bounds on the mass of the Higgs boson. The combination of the data from all four **LEP** experiments with centre of mass energies up to 202 GeV by the **LEP** Higgs Working Group leads to an exclusion of a Standard Model Higgs boson with mass below 107.9 GeV/c^2 at the 95% confidence level[26].

2.5.2 Higgs Boson production at LEP II

The dominant production mechanisms for the Higgs boson at **LEP II** are the Higgsstrahlung and boson-fusion processes, figure 2.3. Direct Higgs production via

$$\text{e}^+\text{e}^- \rightarrow h \tag{2.53}$$

is suppressed due to the very small electron mass and thus small eeh coupling term.

36
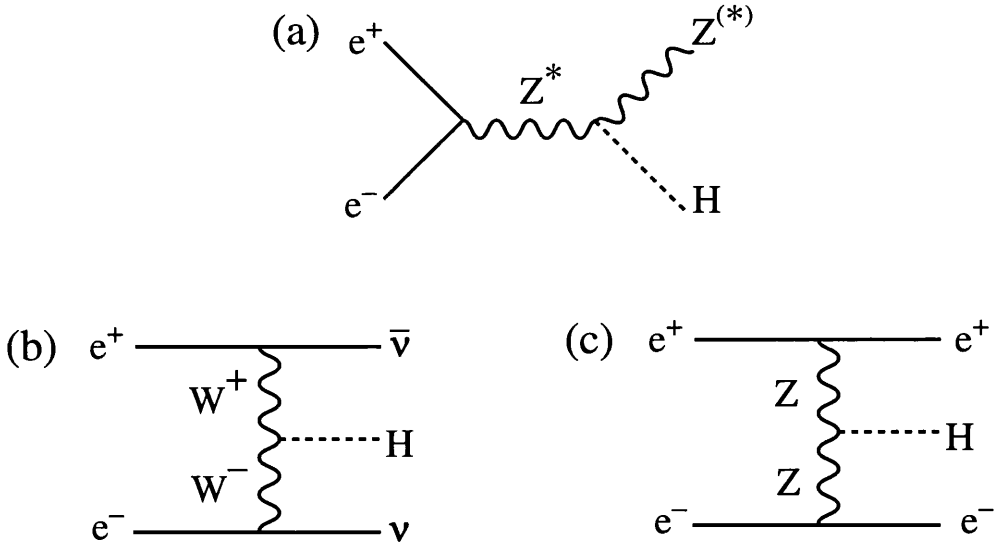
Figure 2.3:   Higgs boson production mechanisms within the Standard Model relevant to LEP II. (a) Higgsstrahlung, (b) W^+W^- fusion and (c) ZZ fusion.

The Higgsstrahlung process in which the Higgs boson is radiated from a virtual Z with the final observed Z returning to a mass value close to its pole mass provides the majority of the Higgs production cross section. However the cross section for the Higgsstrahlung process falls sharply as the hypothetical Higgs mass reaches and exceeds threshold

$$m_{\text{thresh}} = \sqrt{s} - m_Z \qquad (2.54)$$

in which case the final state Z boson is required to be off shell. In the region of kinematic threshold the WW and ZZ fusion processes, also shown in figure 2.3, contribute a larger fraction of the total Higgs boson production cross section. The Higgs production cross section for $\sqrt{s} = 199.5$ GeV is shown in figure 2.4. The corresponding kinematic limit is 108.3 GeV/c^2 and indeed a rapid decrease in the hZ production cross section can be seen around that mass.

2.5.3   Higgs Boson decay

The methods used to attempt to detect the Higgs boson at LEP are directly related to the expected decays of the Higgs boson system. It is vital to understand the expected signatures from the various types of decay which could be present in an event which contained a Higgs boson decay.
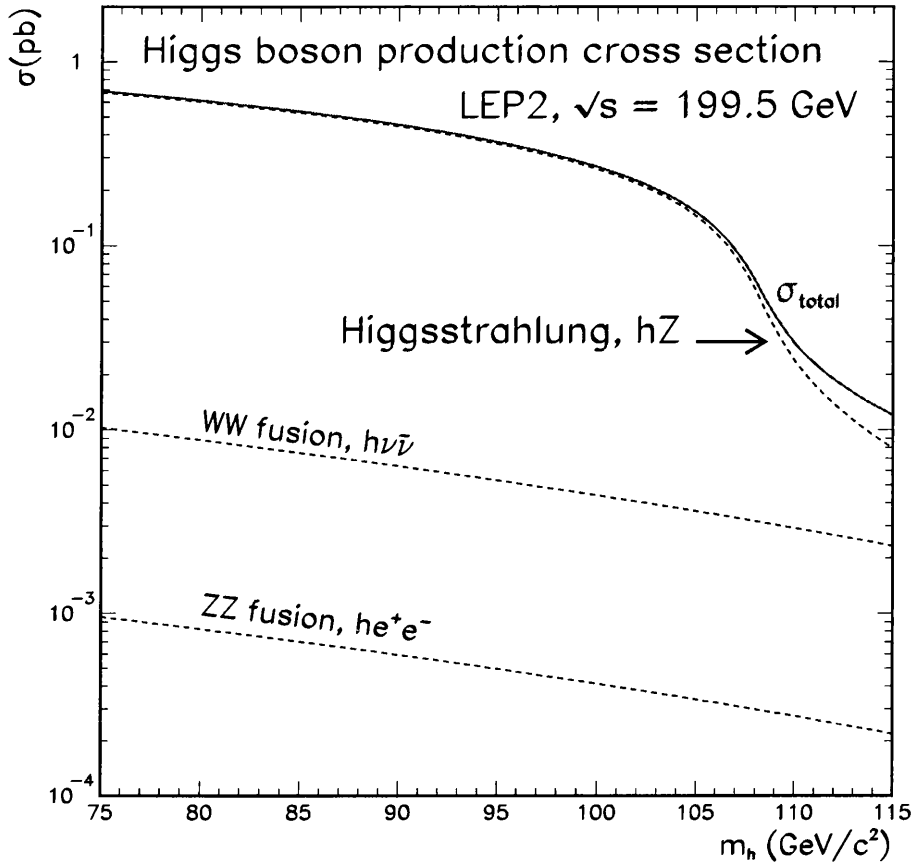
Figure 2.4: The evolution of the cross section for Higgs boson production in the Standard Model at $\sqrt{s} = 199.5$ GeV. The cross sections were calculated using the HZHA03[29, 30] generator.

The Higgs decay width is predicted to be very narrow, ~ 3 MeV/c^2, for a Higgs boson of mass 100 GeV/c^2[28]. The width of the Higgs boson is therefore expected to be too small to be resolved experimentally. The main decay modes of the Higgs boson in the mass ranges relevant to LEP II are shown in table 2.3.

Decay Mode	Branching Fraction (%)
$b\bar{b}$	82.1
$\tau^+\tau^-$	7.9
other $f\bar{f}$ or gg	9.2

Table 2.3: The significant decay modes of the Standard Model Higgs boson, for an assumed Higgs boson mass of 100 GeV/c^2.

The partial decay width of the Higgs boson to fermions is given by

$$\Gamma(h \to f\bar{f}) = \frac{N_c g^2 m_f^2}{32\pi m_W^2}(\beta^2 m_h) \qquad (2.55)$$

where $N_c = 1$ for leptons and 3 for quarks and $\beta = 1 - 4m_f^2/m_h^2$. The partial width is proportional to the square of the fermion mass when $m_h \gg m_f$ and so in the LEP II region it is expected that of all the fermions the Higgs boson would decay most strongly to the heaviest that is kinematically available (i.e. the b quark). The partial width of the decay to gauge bosons is suppressed for Higgs boson masses in the range $m_h < 2m_W$ and as such the fermionic decay $h \to b\bar{b}$ dominates.

The Higgs branching ratios for each final state as a function of Higgs boson mass are shown in figure 2.5.
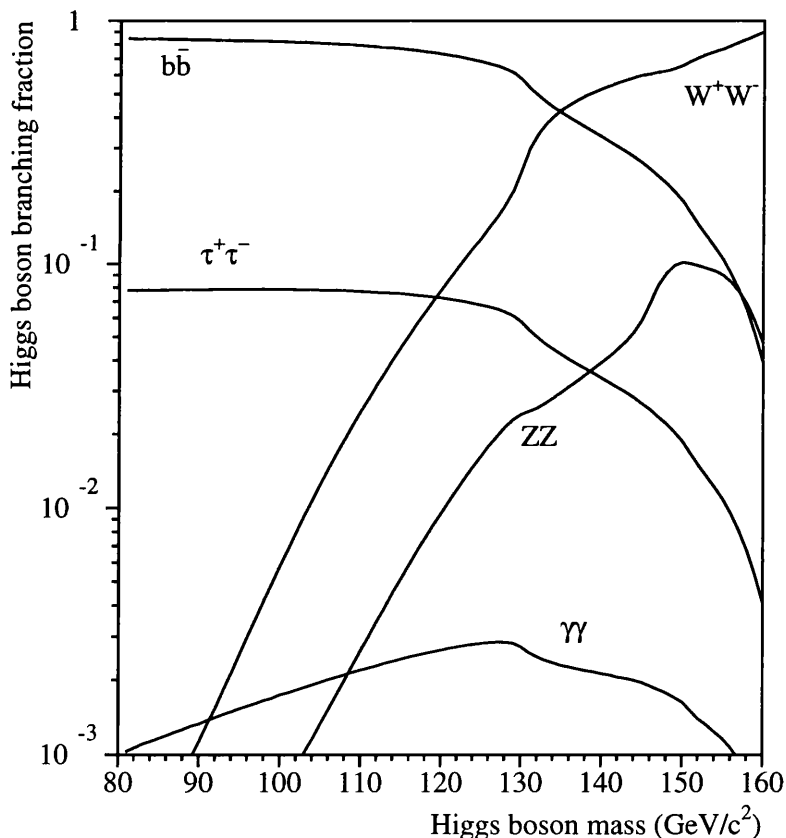
Figure 2.5:   The branching fractions of several possible Higgs boson decays, obtained in the Standard Model.

For $m_h \sim 100$ GeV/c^2 the $b\bar{b}$ decay is dominant while $\tau^+\tau^-$ makes up the single

next largest decay. The Higgs boson search strategy at LEP is to focus on distinctive Higgsstrahlung final state topologies which are defined by considering the possible decay modes of the Higgs and Z bosons. The topologies considered are four-jets ($b\bar{b}q\bar{q}$), missing energy ($h\nu\bar{\nu}$), tau final states ($h\tau^+\tau^- + \tau^+\tau^-q\bar{q}$) and the leptonic final state ($h\ell^+\ell^-$, where $\ell = e, \mu$). These channels are described in more detail in chapter 7. The relative amount of signal each final state will receive from Higgsstrahlung decays can be found by considering the Higgs decay branching ratio (e.g., table 2.3) and the Z decay branching ratio (see table 2.5). Thus for $m_h = 100 \text{ GeV}/c^2$, assuming the SM, the relative amount of Higgsstrahlung to be expected in each final state is shown in table 2.4.

Topology	Higgsstrahlung Branching Fraction (%)
Four-jets	63.8
Missing Energy	20.0
Tau final states	8.9
Leptonic final state	6.7

Table 2.4: Fraction of Higgsstrahlung decays that will fall into each characteristic final state, for an assumed SM Higgs boson mass of 100 GeV/c^2.

2.6 Background Processes

There exist several processes within the Standard Model which may mimic a Higgs boson signal. Therefore these processes present a background for any search for a possible Higgs boson signal. It is imperative that the backgrounds are correctly understood and minimised within each individual search channel.

The backgrounds originate from numerous processes each of which may result in a final state that on an individual event by event basis may be identical to the result of a decay involving a Higgs boson. The Standard Model background processes can be broken down into two distinct groups, the two fermion (section 2.6.1) and four fermion processes (section 2.6.2 - 2.6.5).

With the exception of $\tau^+\tau^-\ell^+\ell^-$ all the decay channels treated at LEP are multi-

hadronic in nature and so only multi-hadronic background processes are relevant in those cases.

There follows a brief description of the background processes which are relevant to the Higgs searches performed at LEP II.

2.6.1   Two Fermion Process

The two fermion process is the production of a $q\bar{q}$ pair from a Z^* boson or a virtual photon. The Z^* boson may be produced nearly on shell, by the emission of an energetic Initial State Radiation (ISR) photon. (See figure 2.6a for the Feynman diagram). For the events that do have an energetic ISR photon present, the photon often escapes detection by travelling along the beam pipe approximately collinear with one of the original annihilation electrons. Events that had an energetic but undetected ISR photon are characterised by a visible energy below $\sqrt{s}$ and an imbalance in the total momentum along the direction of the incoming annihilation electrons.

It is possible for the two fermion process to appear four fermion like by the radiation of one or two gluons in the final state.

2.6.2   Two Photon Process

The two photon or $\gamma\gamma$ process refers to events in which virtual photons from the initial state e^+e^- form a fermion-antifermion pair. This process, shown in figure 2.6b, represents a four fermion final state as the original e^+e^- are still present. The majority of these events are classed as *untagged*, where the final state e^+e^- escape detection by continuing down the beam pipe after interacting.

The two photon process is relevant in the case where the fermion pair produced is $q\bar{q}$ or $\tau^+\tau^-$. The high interaction cross section for this process is compensated by the low visible mass and particle multiplicity which make the large majority of two photon interactions distinct from the expected signal final states. The two photon process is of most importance when considering a search for the $h\nu\bar{\nu}$ final state.

2.6.3 The W$^+$W$^-$ Process

The pair production of W$^\pm$ bosons occurs mostly via one of three processes, the graphs for which are shown in figure 2.6c. As the W can decay to cs, ud or $\ell\nu$ (where $\ell = e, \mu$ or τ) these processes can produce final states with leptons and jets and is a source of c quark jets which may be misidentified as b jets (see section 4.3.1). However, the lack of b jets from W decays (at tree level) suppresses the majority of the WW background.

2.6.4 The ZZ Process

The ZZ Process refers to several reactions which may produce four fermion final states. The decay modes of the Z boson (see table 2.5) allow this decay process to form multiple final states which overlap with different Higgs boson signals. The ZZ background process shown in figure 2.6d presents a major challenge for the Higgs boson searches. It may produce final states with b$\bar{\text{b}}$ and $\tau^+\tau^-$ pairs which are effectively indistinguishable from Higgsstrahlung final states, for $m_\text{h} \sim m_\text{Z}$. As a result the ZZ process is often referred to as an irreducible source of background.

Decay Products	Branching Ratio (%)
q$\bar{\text{q}}$ (b$\bar{\text{b}}$)	69.9 (15.2)
$\nu\bar{\nu}$	20
charged leptons ($\ell^+\ell^-$)	10

Table 2.5: Approximate branching fractions fractions for the decay of the Z boson.

2.6.5 The single W and Z processes

The production of a single $W^\pm$ via $e^+e^- \rightarrow W^\pm e\nu_e$ (denoted Weν) and single Z bosons via $e^+e^- \rightarrow Ze^+e^-$ (denoted Zee) are other four fermion final states. Their production processes are shown in figures 2.6e and 2.6f respectively.

A characteristic which is common to both the Zee and Weν processes is the typical escape of one of the initial e$^+$e$^-$ pair down the beam pipe. The events therefore have a large component of missing longitudinal momentum which may be used to identify them as background events. The events are also characterised by a visible mass which
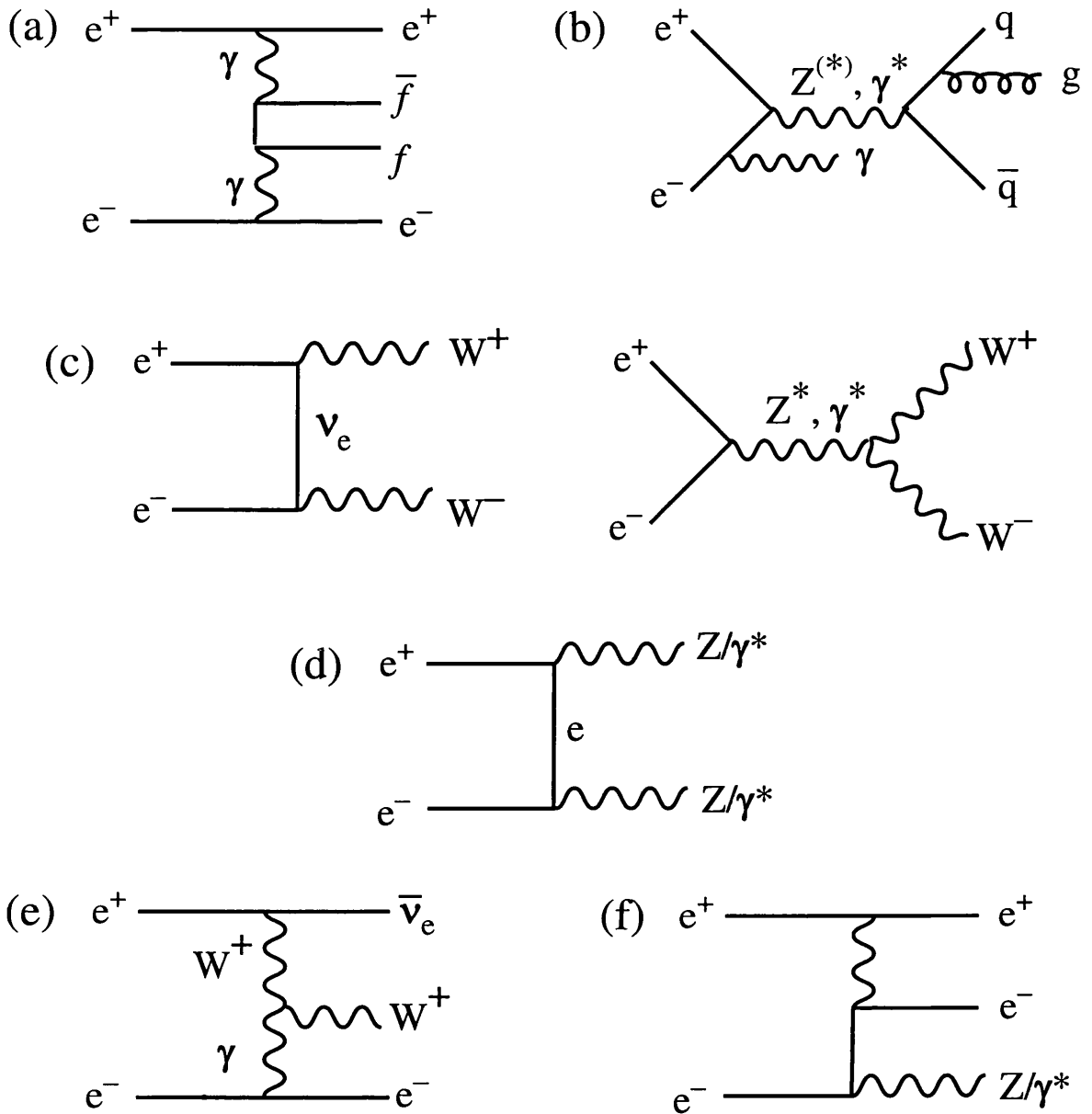
Figure 2.6: Feynman graphs: The background processes in the search for Higgs bosons.

is near that of the produced W or Z boson. In many signal channels, for instance the $e^+e^- \rightarrow Z^* \rightarrow hZ \rightarrow b\bar{b}q\bar{q}$ the visible mass is near the centre of mass energy.

The production of single Z bosons is also possible via the $e^+e^- \rightarrow Z\nu\bar{\nu}$ process which follows exactly that of Higgs production via WW fusion but with the Z boson substituted for the Higgs boson. However, single Z production has a very low cross section reducing the impact of the background on Higgs boson searches. The cross sections of some background process at $\sqrt{s} = 199.5$ GeV are summarised in table 2.6.

43

Background Process	Cross-section (pb^{-1})
ZZ	2.86
WW	17.38
$q\bar{q}$	87.09
Zee	8.32
Weν	0.795
Z$\nu\bar{\nu}$	0.015

Table 2.6: The cross-sections for several background processes, at $\sqrt{s} = 199.5$ GeV.

2.7 Background treatment

Each background process will contribute to the search for Higgs signals but with varying importance between the final states. The degree to which the background is considered important is a product of both the production cross section and the overlap of the event characteristics between the given background and the Higgs signal hypothesis for the specific channel.

Each search channel first applies a loose pre-selection to the data to eliminate unmodelled backgrounds and the majority of the most distinguishable background sources. The application of pre-selection cuts also allows a comparison of data and the Monte Carlo simulated data to determine the accuracy of the simulation. Then follows a tighter selection in which it is attempted to maximise the power of the analysis to distinguish between a Higgs boson signal and background.

Chapter 3

Experimental Apparatus

The **ALEPH** (Apparatus for LEp PHysics) detector[1] is one of the four **LEP** detectors and was designed to study all types of Standard Model processes at **LEP** without restricting searches for new physics. The detector is located at point number four of the **LEP** ring, in a cavern 143m underground. The **ALEPH** detector is approximately a cylinder of length and diameter 12m, with the axis of the cylinder aligned along the beam axis.

The **ALEPH** coordinate reference system is defined as: the z direction is along the beam direction, positive in the direction travelled by electrons. The x direction is horizontal and points towards the centre of the **LEP** ring. The y direction points upwards, but deviates slightly from the vertical since **LEP** does not lie completely in the horizontal plane. Cylindrical polar coordinates (r, ϕ, z) are often used, along with θ, the polar angle.

A diagram illustrating the **ALEPH** detector in a cut-through view is shown in figure 3.1. The overall design is that of a number of sub-detectors arranged as a series of layers, centred on the electron-positron interaction point (IP) and aligned along the direction of the beam.

In the following sections the **ALEPH** subdetectors are described, together with some typical performance figures. Afterwards some aspects of data processing are discussed.

Vertex Detector

Inner Tracking Chamber

Time Projection Chamber

Electromagnetic Calorimeter

Superconducting Magnet Coil

Hadron Calorimeter

Muon Chambers

Luminosity Monitors
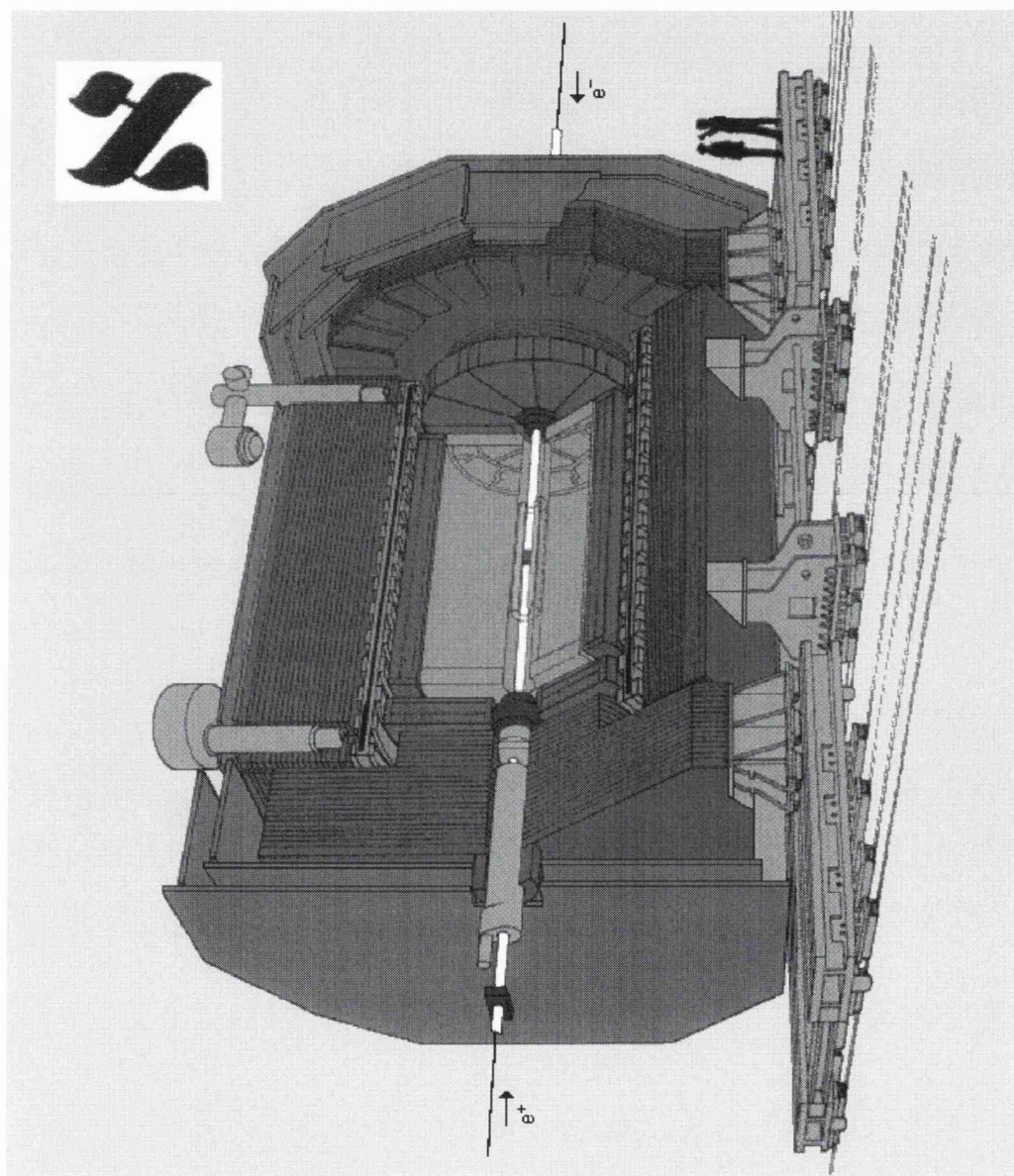
The ALEPH Detector

Figure 3.1: A drawing of the ALEPH detector, showing pictorially a cut through section.

3.1 The Silicon Strip Vertex Detector

The innermost subdetector of ALEPH is the silicon strip vertex detector, called the VDET. Its purpose is to detect the passage of charged particles passing through its

active area and to provide three dimensional information about points lying on the trajectory of the charged particles.

The VDET is situated close to the interaction point for two reasons. Firstly to minimise the amount of material traversed by particles produced at the IP before measurement. Secondly, since the trajectory of charged particles are also measured at larger radial distances by other tracking detectors (see subsections 3.2 and 3.3) a measurement close to the particle production point gives a much longer lever arm for the track reconstruction. In this way the tracks of charged particles may be accurately extrapolated back to the interaction point, allowing the direct reconstruction of the primary vertex (i.e., the precise position of the IP) event by event. Hence the need to reduce multiple coulomb scattering which could otherwise degrade the extrapolation.

An accurate knowledge of the paths of charged particles close to the IP is especially important in identifying secondary vertices, which may be displaced from the IP by only a few hundred microns. Physically secondary vertices may occur through the production and subsequent decay of relatively long lived particles. Of particular interest are hadrons which contain b quarks (B-hadrons) which can give rise to secondary vertices displaced from the IP by up to several millimetres. The VDET is of special importance to b-physics in general and in particular to the searches and studies presented in this thesis (see section 2.5). Due to the increase in precision which the VDET brings to charged particle tracking, it is a vital component of the detector on which the Higgs boson search relies.

The design of the VDET approximates that of two concentric cylinders, with their z axis lying along the beam. The surface of each cylinder is formed by faces. The active area of the faces extend to ±20cm in z about the interaction point. The outer layer consists of fifteen faces and the inner nine faces. The two layers lie at distances of approximately 63mm and 110mm from the beam line. Each face consists of two VDET modules stuck together. The two modules have independent readout electronics situated at the ends of the face.

Each module consists of three silicon detector wafers. The wafers are double sided, the inner side providing the z readout and the outer the $r\phi$ readout. Each wafer is a rectangle, approximately 50 x 65mm and 300μm thick. On the wafers silicon strips run

parallel to the beam axis on the azimuthal, ϕ, readout side and at right angles to the beam for the z side. The fixed position of the wafer in space provides the r coordinate. The strip pitch for the $r\phi$ and z sides is 25μm and 50μm respectively.

Each strip works as a reverse biased p-n diode. The presence of ionising radiation through the bulk of the silicon gives rise to electron-hole pairs. These pairs drift apart under the influence of the applied electric field. They are collected at electrodes, giving rise to a pulse proportional to the amount of ionisation present. Due to capacitive coupling between the strips a signal is observed on several adjacent strips. For this reason not every strip is readout, but only every other strip. Thus the readout pitch, is 50μm and 100μm in ϕ and z respectively.

Figure 3.2$left$ shows a drawing of the mechanical arrangement of the VDET, while figure 3.2$right$ shows the back and front of a VDET face.

The measured performance of the VDET is shown in figure 3.3. The hit resolution on the ϕ side is about 10μm, whilst the z resolution at 90 degrees is slightly larger, $\sim 15\mu$m. The acceptance of tracks goes down to $|\cos\theta| < 0.95$.
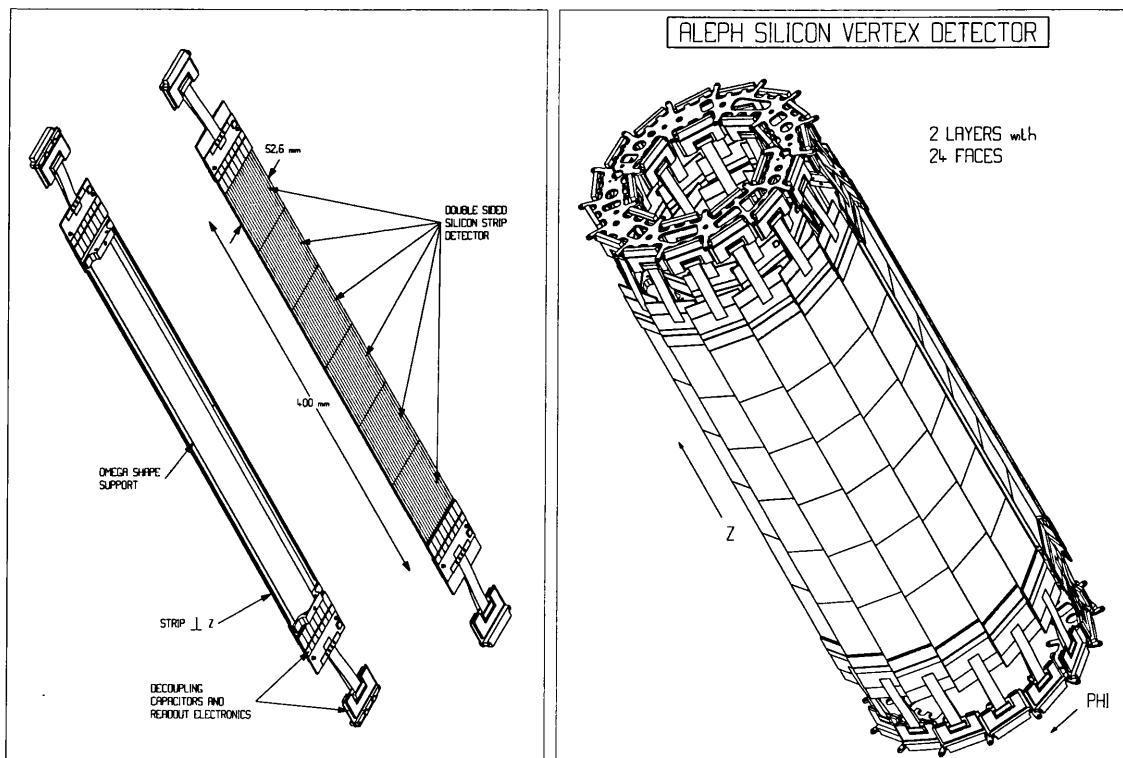
Figure 3.2: *(left)* Drawing of one face of the VDET detector *(right)* The ALEPH VDET. Taken from reference [31].

Resolution vs. cos(θ)
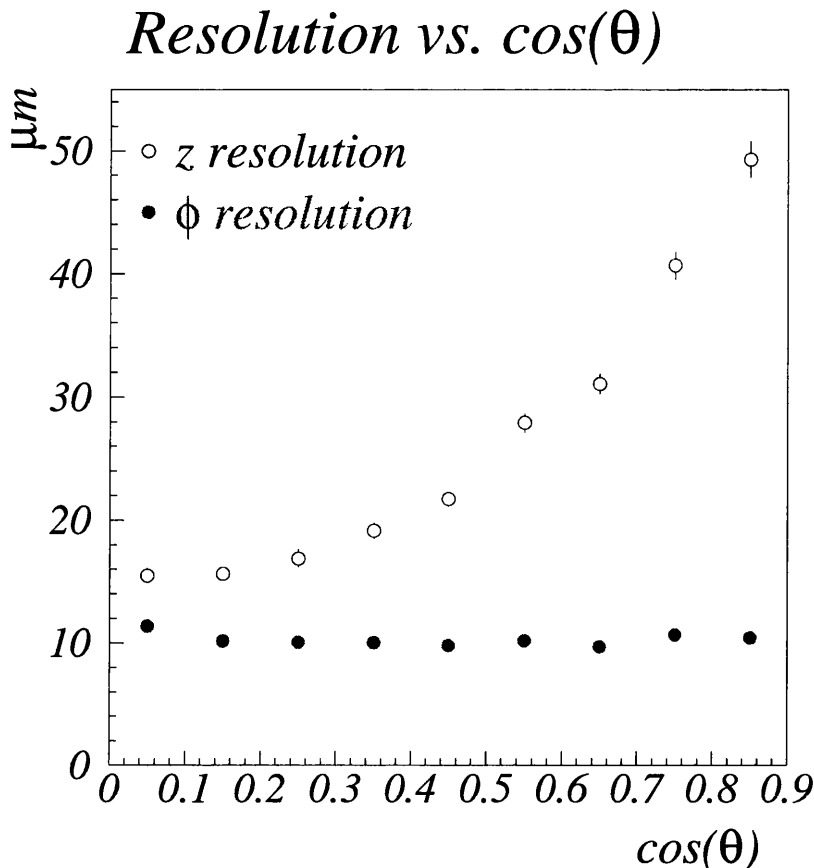
Figure 3.3: Hit resolution of the VDET in the z and ϕ directions against $\cos\theta$. Taken from reference [31].

3.2 The Inner Tracking Chamber

The Inner Tracking Chamber is known as the ITC. It is a cylindrical multiwire drift chamber of active length 2m. The chamber's long axis is placed along the beamline and is centred on the interaction point. In the radial region between 160mm and 260mm from the beam line the device is sensitive to the passage of ionising particles and able to provide three dimensional hit points for tracking.

The primary purpose of the ITC is to provide tracking information to the level 1 trigger. It is the only tracking information available to the first level trigger. The suitability of the ITC for selecting events to record is due to the fast readout and processing of information from the chamber. All information required by the trigger is available from the ITC within $3\mu s$ of a beam crossing.

3.2.1 Construction of the ITC

The active volume of the ITC is filled with a gaseous mixture, 80% argon and 20% carbon dioxide. Between the two endplates of the cylinder forming the ITC are strung many thin wires running parallel to the beam line.

An ionising particle traversing the volume may be detected as it passes through a *drift cell*. A drift cell is formed by six wires, called field wires, which are arranged in a hexagonal shape. At the centre of the hexagon is a sense wire. By holding the field wires at ground potential and placing a positive potential on the sense wire a hexagonal drift cell is formed.

In total there are 960 sense wires arranged in 8 concentric layers. Within each layer the hexagonal cells form a close-packed structure, so that four of the six field wires for each cell are shared with the neighbouring two. There are 96 cells per layer in the four inner layers and 144 cells in the outer four. Consequently the cell size and therefore the maximum drift distance varies layer by layer. The cells in the fourth layer have the largest maximum drift distance and those in the fifth the shortest. Keeping the maximum drift distance small makes the readout of the ITC fast, the maximum and minimum drift distances being 6.5mm and 4.7mm respectively.

Figure 3.4 shows pictorially the hexagonal cell structure of two adjacent layers. In between each layer and the next is a protective wire mesh to limit the damage in case a wire breaks.

Since the drift velocity of electrons within the drift cell is known the drift time and wire position can be used to calculate an $r\phi$ coordinate. Each layer is staggered by half a cell width. This is to resolve the $r\phi$ left-right ambiguity which arises because a cell is only able to provide the distance over which the electrons travelled to the sense wire and not the direction. In order to obtain the z coordinate the difference in time at which the pulse arrives at the either end of sense wire is measured.

3.2.2 Performance of the ITC

A track from the interaction point with $|\cos\theta| < 0.97$ will pass through all layers. Thus up to eight three dimensional tracking points are available. The resolution in $r\phi$ depends upon where in a cell a track passes, while the z resolution varies strongly

with sense wire pulse height. Averaged over a typical data sample, the $r\phi$ resolution is found to be 150μm while that in z is 5cm.
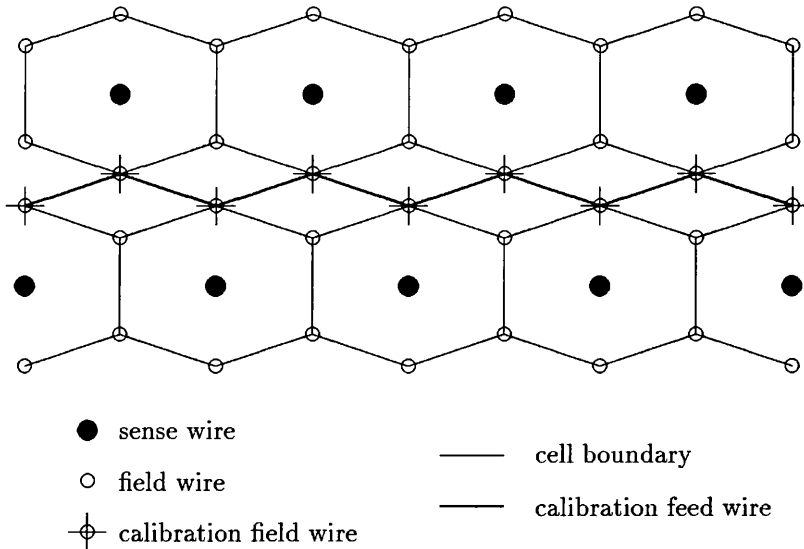
Figure 3.4: Arrangement of the ITC wires. Taken from reference [31].

3.3   The Time Projection Chamber

The Time Projection Chamber, or TPC, is the central tracking subdetector of **ALEPH**. The TPC consists of (see Figure 3.5) two hollow cylinders, centred on the interaction point, the long axis lies along the beam line. The ends of the TPC are sealed by end plates. The beam pipe and inner detectors fit inside the smaller cylinder. The active region of the TPC is the volume enclosed between the inner and outer cylinder walls. The enclosed volume is divided into two halves by a central membrane that lies in the plane of the end plates.

Tracking is achieved by setting up a uniform electric field running from the end plates to the central membrane, together with the parallel magnetic field provided by the **ALEPH** solenoid. The end plates are maintained at ground potential while the central membrane is lowered to a large ($\sim$-27kV) negative potential. The volume of the TPC is filled with a gaseous mixture of 91% argon and 9% methane, held slightly above atmospheric pressure. The gas filled region is called the drift volume. The passage of charged particles through the drift volume liberate atomic electrons by ionising the
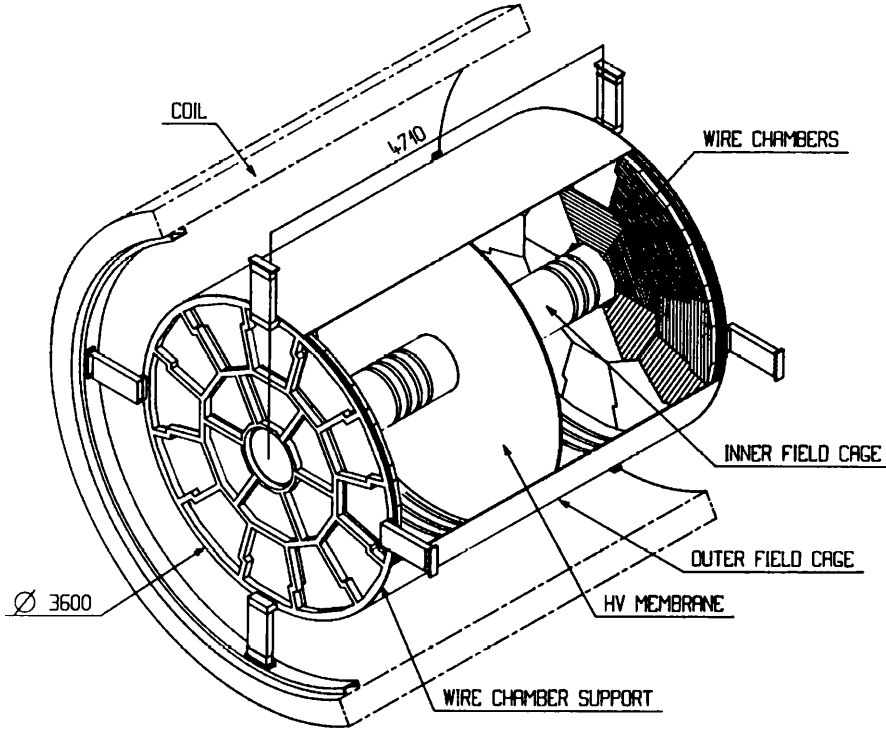
Figure 3.5: View of a section through the TPC. Taken from reference [31].

gas. The electrons drift towards the end plates under the influence of the electric field. The motion of an electron describes a tight helix, spiralling along the direction of the magnetic field. Effectively the presence of uniform parallel electric and magnetic fields limit the radial diffusion of the electron clusters whilst they drift.

At the TPC end plates are located three wire grids. (See figure 3.6) An electron drifting from the drift volume first encounters the Gating grid, which will be discussed shortly. Followed by the cathode grid, which is grounded. Finally the electrons are collected at the sense wires, maintained at ~ 1300V. The sense and field wires form conventional multiwire proportional chambers with the addition of cathode pads. Electrons are collected on the anode sense wires, where the electron clusters undergo gas amplification. The strong electric field around the thin sense wires cause an electron avalanche by means of secondary ionisation of the gas around the wire by the drifting electrons. A signal is induced on the nearby cathode pads by capacitive coupling and this signal is used to provide $r\phi$ position information for the electron cluster. The z coordinate of the original ionisation in the TPC is calculated from the arrival time of the signal on the pad and the known drift velocity of electrons in the gas mixture.
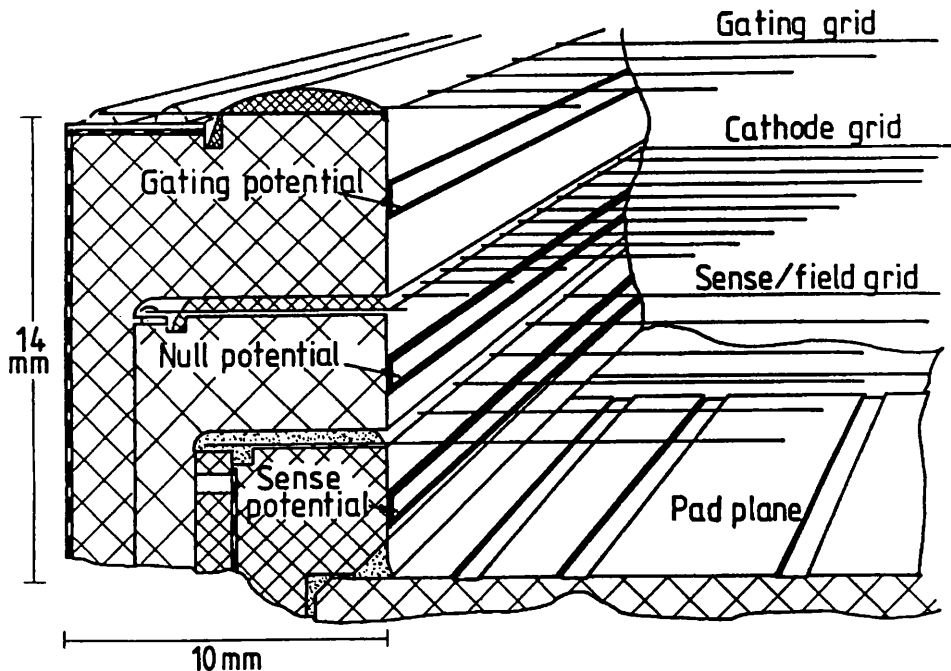
Figure 3.6: Some of the instrumentation on the TPC end plate. Taken from reference [31].

The anode wires themselves provide, separately, pulse height, time and wire number. The track fits are performed using the three dimensional points provided by the information from the pads. Once tracks have been fitted to the coordinates, pulses on the wires are associated to tracks. The pulse height is used to calculate dE/dx for the track. In figure 3.7 can be seen how dE/dx is used in particle identification. Figure 3.7 shows the measured dE/dx against particle momentum for a sample of about 40,000 tracks. Each track was required to have at least 150 dE/dx measurements. The fitted parametrisation is shown for electrons, muons, pions, kaons and protons. The right figure shows the average dE/dx separation in standard deviations between different particle types as a function of momentum. Thus the TPC provides both tracking and particle identification information. The TPC spatial resolution of the $r\phi$ coordinate can reach $160\mu m$ and 0.8mm in z.

3.3.1 TPC Gating

The electron clusters from the TPC drift volume are detected at the anode wires by gas amplification, resulting in many positive ions being created at the end plates. Under the influence of the electric field these ions will move into the drift volume and the
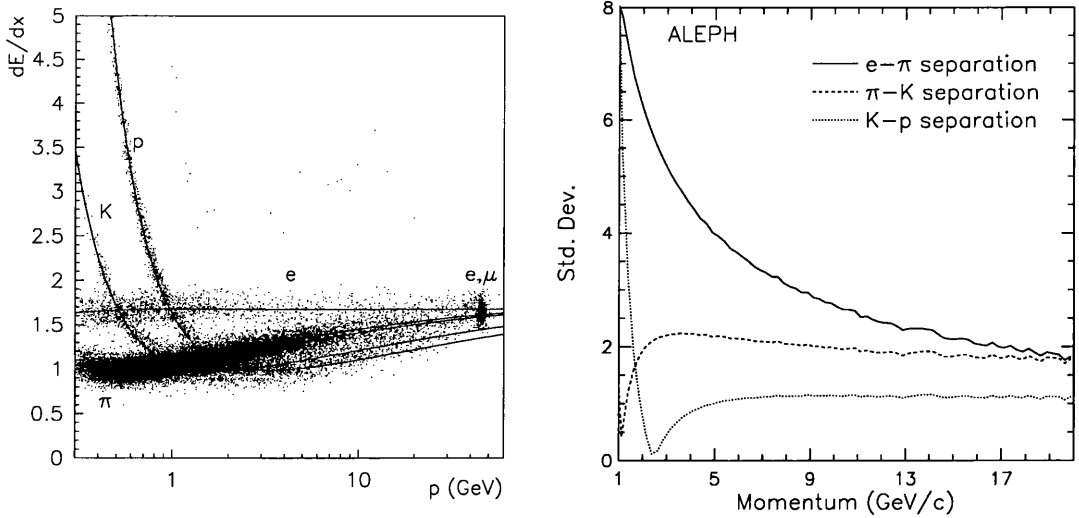
Figure 3.7: The left figure shows the measured dE/dx versus particle momentum. The right figure shows the average dE/dx separation in standard deviations between different particle types as a function of momentum. Taken from [32].

resulting space charge will create local distortions in the electric field. Field distortions lead to a reduced resolution on track hits and for this reason a system is implemented to prevent positive space charge from building up. The system is called the TPC Gating.

The Gating grid is the name of the grid of wires placed between the cathode grid and the TPC drift volume. The Gating grid may be said to be open or closed. In the open state the wires of the grid are held at the local equipotential. This causes no perturbation to the local electric field and thus is transparent to the passage of the charged ions. To close the grid an offset is added to the potential of each wire, of alternately positive and negative sign, resulting in a dipole field between the gating wires. When the gate is closed positive ions are prevented from entering the drift volume of the TPC and are collected at one of the cathode wires of the gating grid.

Since the closed Gating grid reduces the transmission of drift electrons from the drift volume to the sense wires it is desirable to keep the Gating open during readout. The opening and closing of the Gate is synchronised with the beam crossing signal and subsequent first level trigger decision.

3.4 Track Reconstruction

The data from all three tracking detectors is used to reconstruct the passage of charged particles. The reconstructed path is called a *track*. Track reconstructed begins in the TPC. Hits in neighbouring layers are joined together to form segments. Segments are joined together under the hypothesis that the track should form a helix. The track is then extrapolated into the ITC and VDET. Hits in those detectors which are consistent with belonging to the extrapolated track are associated to the track. An overall fit is then performed, taking into account the errors on the hits in the three detectors, to provide a reconstructed track and associated track fit error. Table 3.1 summarises the momentum resolution achieved using differing numbers of detectors. The events being fitted were $Z^0 \rightarrow \mu^+\mu^-$ events.

Tracking Detector	σ_p/p^2 $(\mathrm{GeV}/c)^{-1}$
TPC	1.2×10^{-3}
TPC + ITC	0.8×10^{-3}
TPC, ITC + VDET	0.6×10^{-3}

Table 3.1: The momentum resolution σ_p/p^2 , where p is the momentum, achieved with the ALEPH tracking detectors. Taken from reference [32].

3.4.1 The Electromagnetic Calorimeter

The purpose of the ALEPH Electromagnetic Calorimeter, or ECAL, is to measure the energy of electrons, positrons and photons in an event. Signals from the ECAL are also available to the trigger system.

The term Electromagnetic is used here to describe these particles, in the sense that they interact with the matter in the calorimeter by the exchange of photons. The active area of the ECAL detector covers $3.9\pi sr$ of the solid angle around the interaction point. The good coverage and large number of readout channels also enable an effective identification of electrons from other particles to be made.

ECAL is essentially a piece of material of large total radiation length instrumented with detectors to measure the energy content of electromagnetic showers. Specifically
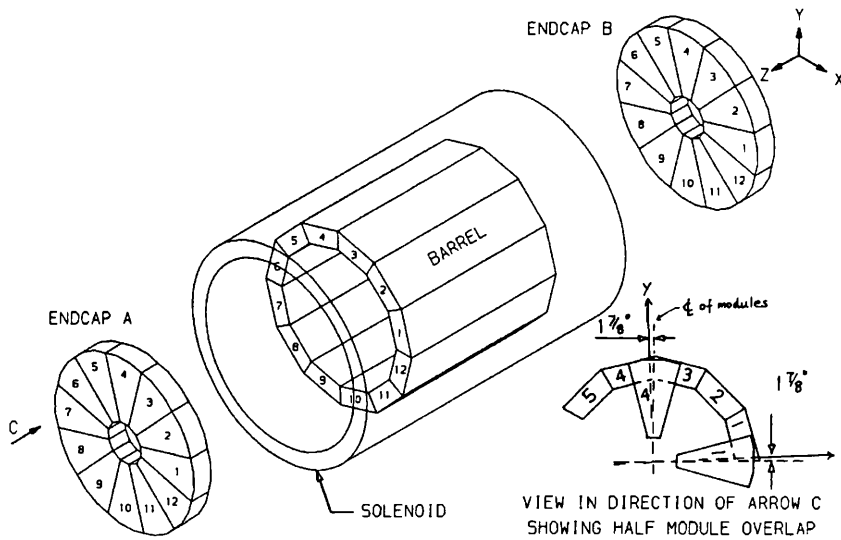
Figure 3.8: Design of the ECAL. Taken from [31].

the ECAL is of a barrel and endcap design. (See figure 3.8). The barrel section has inner radius of 184.7mm and outer radius 225.4mm. The detectors TPC, ITC and VDET sit inside the calorimeter while the magnetic solenoid surrounds it. The shower material is lead which used for its short radiation length, $\chi_0 = 5.6$mm. The total thickness of lead used is about $22\chi_0$, which is chosen such that over 98% of the energy of a 50 GeV electron is contained within the lead.

The barrel and two endcaps sections of the ECAL are further subdivided. Each section is divided in ϕ into 12 modules. Thus each module subtends an angle of 30 degrees in ϕ about the z axis. The details of the construction of the modules in the endcaps differs from those in the barrel because of engineering limitations imposed by the different geometric orientation. However the modules are all of the same basic operation and specification.

Each module consists of 45 layers of lead stacked together. In between each layer is a gas wire-chamber. A typical arrangement of a small portion of a layer within a module is pictured in Fig 3.9. A gas mixture of 80% xenon and 20% carbon dioxide fills each gas tight module. Charged particles from electromagnetic showers ionise this gas mixture. The ionisation is detected in the wire-chamber. Electrons undergo gas amplification around the anode wires, inducing an electric pulse which is read out on

56
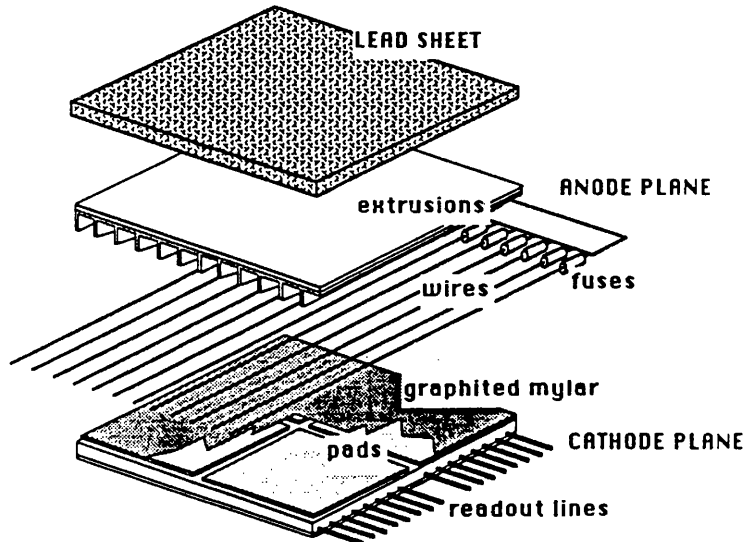
Figure 3.9: Construction of an ECAL layer. Taken from reference [31].

the anode plane for the whole layer of the module. A more granular signal is available from the cathode plane, which is segmented into pads. Adjacent layers in the lead stack are grouped together to form three storeys. Within a story pads next to each other, but in different layers, are connected and readout as one to form a tower. All the towers point toward the interaction point and have a cross section of ~ 30x30mm^2 along the tower axis. In total there are 73,728 towers in the whole ECAL each read out in three storeys. This large number of channels enables the calorimeter to achieve good spatial resolution and shower profile measurement as well as calorimetry.

The energy resolution of the ECAL has been studied using Bhabha scattered electrons, comparing their measured ECAL energy with the track momentum or beam energy. The resolution has been parametrised as[32]:

$$\frac{\sigma(E)}{E} = \frac{0.18}{\sqrt{E}} + 0.009. \tag{3.1}$$

Where E is the energy of the electron, measured in GeV.

3.4.2 The Hadronic Calorimeter and Muon Chambers

The hadron calorimeter, or HCAL, is used to measure the energy of hadronic particles in events. The HCAL is also part of the system used to identify μ leptons, either by

their hit pattern or by acting as a veto for dedicated muon detectors which surround the hadron calorimeter.

The HCAL is composed of instrumented layers of iron. The incoming hadrons will interact with the nucleons present in the iron atoms via the strong force, producing showers of lower energy particles. Iron was chosen so that the total nuclear interaction length is sufficient to contain most of the energy from penetrating hadrons. The HCAL is ~ 7.16 interaction lengths in depth at normal incidence. Instrumentation is by way of plastic streamer tubes. The tubes are coated with graphite and contain eight wire counter cells. The tube layers are readout with pad electrodes that give an integrated energy measurement. Additionally the iron of the HCAL forms the return yoke for the magnetic flux of the ALEPH solenoid, which is placed inbetween the ECAL and HCAL.

The construction is of a barrel section and two endcaps. The muon chambers surround the outside of the barrel and endcaps. The HCAL barrel is made from 12 modules and each endcap from 6 petals. The whole HCAL is rotated 32.7mrad with respect to the ECAL to avoid overlapping uninstrumented (crack) regions. A module consists of 23 layers of iron. The inner 22 layers are 5cm thick and the final one 10cm thick. There is a space of 2.2cm between each layer. The instrumentation is inserted in the gap between the layers and also placed in front of the first layer. The construction of the module and petals are broadly similar. The number of layers in the end caps is reduced to 16 in the region where the barrel touches the endcap. The barrel modules are 724cm long.

The energy resolution is obtained by studying pions at normal incidence, and is given by [32]:

$$\frac{\sigma(E)}{E} = \frac{0.84}{\sqrt{E}}. \tag{3.2}$$

Where E is the energy of the pion, measured in GeV.

Muons leave a characteristic signal in the HCAL, a single trail of hits with no shower development. Outside the HCAL are two further planes of streamer tubes, known as muon chambers, which act as tracking detectors for muons. In the barrel section they are radially separated by 0.5m, which enables track segments to be measured with an accuracy of 10-15mrad.

3.4.3 The Luminosity Monitors

An accurate determination of the integrated luminosity received from the **LEP** collider is required in order for **ALEPH** to be able to measure absolute cross sections for given reactions.

The instantaneous luminosity is defined as the ratio of the rate of $e^+e^- \rightarrow e^+e^-$ (Bhabha) interactions to the theoretical cross-section for this process, which is well known. The integrated luminosity is defined as the ratio of the number of Bhabha events in a certain time to the cross section.

The cross section for Bhabha scattering is strongly peaked at polar angles close to the beam pipe, so to aid the cross section measurement three specialist calorimeters are installed close to the beam line.

The Luminosity Calorimeter (LCAL) is a lead-wire sampling calorimeter, similar in construction to the ECAL. The LCAL consists of two detectors covering a region with radii between 10 and 52cm at ± 2.62m from the IP, covering a polar angle as low as ~ 2.6 degrees. The luminosity is measured by counting Bhabha events which have the characteristic signature of symmetric back-to-back energy deposits. LCAL provides the primary luminosity measurement for **ALEPH** at **LEP II**.

The Solid State Luminosity Calorimeter (SiCAL) extends the coverage down to a polar angle of ~ 1.4 degrees. SiCAL consists of two detectors on either side of the IP that are constructed from 12 tungsten sheets separated by silicon pads. SiCAL provided the primary luminosity measurement for **LEP I**. However, at the beginning of **LEP II** low angle tungsten shielding was installed to protect the central trackers from increased beam related background. This shielding obscures part of SiCAL, adding an extra source of systematic uncertainty in the luminosity measurement. In **LEP II** SiCAL is used only to extend the coverage of the overall **ALEPH** calorimetry.

The Bhabha Calorimeter (BCAL) has two modules located 7.7m from the IP, each consisting of 12 tungsten-scintillator layers. The rate of Bhabha events is much higher in BCAL due to its position, allowing higher statistical precision on the luminosity measurement. However, its position also places it close to a **LEP** focusing quadrapole magnet, making it more sensitive to beam related backgrounds. Consequently the BCAL luminosity measurement has to be calibrated with LCAL. BCAL is therefore

used to provide an instantaneous luminosity measurement and also to monitor the background conditions while the detector is in operation.

3.5 Event Processing

3.5.1 The Trigger

Bunch crossings occur approximately every $22\mu s$, giving a possible interaction rate of up to 45kHz. However the ALEPH data acquisition system could not read out and record events at such a high rate. However, of all the bunch crossings only a small fraction represent interesting interactions. Most of the time the crossings do not result in electron position reactions, but instead scatter into the detector off-momentum beam particles or particles which have interacted with gas molecules in the accelerator.

The reduce the amount of data which needs to be recorded and keep only events which are likely to be of interest a *trigger* system is used. The ALEPH trigger system consists and two *levels* of hardwired logic and one level implemented in software. The trigger systems use signals derived from various ALEPH subdetectors and result in a binary *yes* or *no* decision. See table 3.2.

Name of Stage	Decision Time	Maximum Rate (Hz)	Subdetectors used
Level 1	$5\mu s$	~ 10	ITC, ECAL, HCAL, LCAL
Level 2	$50\mu s$	~ 5	TPC, ECAL, HCAL, LCAL
Level 3	$\sim 50ms$	1-3	All subdetectors

Table 3.2: The 3 levels of the ALEPH trigger along with typical trigger output rates.

After each beam crossing the event is first considered by the level 1 trigger. If the event is not accepted the detector is reset, in preparation for the next beam crossing. In particular the level 1 trigger determines whether to hold the TPC gating grid open (see section 3.3.1), to allow the TPC to be readout. If an event is selected detector readout continues and the results are used by the level 2 trigger. The level 2 trigger is similar to the first level trigger, but TPC tracking information from charged particles is substituted for the ITC hit patterns used in the level 1 trigger. Finally events which

are accepted are fully readout. However before the event information is recorded to disc the final, level 3 trigger, is used to further reduce to amount of information stored.

3.5.2 Event Reconstruction

The group of events that are taken from the same LEP fill are further subdivided by ALEPH into smaller, more manageable chunks called *runs*. A run is finished when any of the following occur; Two hours worth of data are collected, 600 MB of disc storage is consumed by the current run, the LEP fill finishes or whenever the operator overseeing ALEPH manually requests a run change.

As soon as a complete run has been taken the events in that run are reconstructed fully. This is done using the Facility for ALeph COmputing and Networking (FAL-CON), by running the ALEPH program JULIA (Job to Understand Lep Interactions in ALEPH[38]). JULIA converts the signals supplied by the all the subdetectors into physically meaningful information. Specifically JULIA:

- Reconstructs charged tracks.
- Calculates their dE/dx from the TPC wire information.
- Reconstructs the primary vertex and V^0 candidates.
- Clusters calorimeter energy deposits and performs an energy flow analysis.
- Identifies electrons, muons and photons.

A V^0 is a generic term for a hypothetical neutral particle, the presence of which is inferred when two charged tracks are seen to originate from a common vertex away from the primary vertex. Physically a V^0 could be a relatively long lived but unstable particle such as a K^0 or Λ. An energy flow algorithm is an analysis which uses information in an event to form a better representation of the stable particles which were present in the detector.

3.5.3 Energy Flow

The analyses described in this thesis use the results of an energy flow algorithm. It is described briefly here. The energy flow algorithm as described in [32] is used, which

takes track and calorimeter information to reconstruct a set of energy flow *objects* for use in physics analyses. The overall energy resolution is improved by making use of as much information as possible to identify different particles. This includes track momenta, the TPC dE/dx information, the shape of the showers deposited in the calorimeters and the muon chamber information.

The energy flow algorithm proceeds like this; in the first stage, a selection of charged tracks and calorimeter clusters is made. The tracks must originate from a cylinder of length 20 cm and radius 2 cm round the interaction point, to reject tracks unlikely to have originated from the primary vertex. After this, charged particle tracks are extrapolated to the calorimeters and groups of topologically connected tracks and clusters (or *calorimeter objects*) are formed. All charged particle tracks coming from the nominal interaction point are assumed to be pions. Charged particle tracks identified as electrons are removed from the calorimeter object along with the energy contained in the associated ECAL towers. If the difference between the track momentum and the ECAL energy is more than three times the expected resolution, electron bremsstrahlung is assumed to have occurred and is counted as neutral ECAL energy. Charged particle tracks identified as muons are removed from the calorimeter object along with a maximum of 1 GeV from the associated ECAL cluster, if any, and a maximum of 400 MeV per plane fired around the muon track for any corresponding HCAL clusters. Photons and π^0s are counted as neutral ECAL energy and removed from the calorimeter object list. Finally, the remaining calorimeter objects are assumed to be charged or neutral hadrons.

The result of the energy flow algorithm is a list of energy flow objects, which are treated as representations of particles by analyses. Each energy flow object has an associated tag to identify its type. It may be classed as electron, muon, photon or charged or neutral hadron.

3.6 Monte Carlo Simulation

The production of simulated events by Monte Carlo techniques is essential for many analyses, and has been used extensively for the work in this thesis.

The stages involved in the production of Monte Carlo data, as used by ALEPH is usually a three step process. The first process is comprised of several actions, performed together in one computer program.

The underlying event is generated using perturbative calculations. This is also sometimes called the hard event, since the particles involved are of high energy. The resulting particles from the final state may then have gluon bremsstrahlung added before the free quark or gluons are hadronised due to the effects of QCD confinement. Confinement is the process by which the colour carrying quarks are transformed into a series of lower energy, colour neutral, hadrons. Confinement is not rigorously understood so it is performed with a phenomenological model like JETSET[33] or HERWIG[34].

The above is the first step in Monte Carlo generation and the result is recorded in an ALEPH format called KINGAL[35], which is common no matter what process is being simulated. The KINGAL data contains the identity and 4-momentum of all the particles before they are considered to have interacted with the ALEPH detector.

The next stage is the detector simulation which is performed with the GALEPH[36] program. GALEPH simulates the interaction of the KINGAL level particles with the material of the detector (using the GEANT 3[37] package). GALEPH also simulates the digitisation of signals recorded in active, instrumented, regions of the detector. GALEPH also handles the decay of long lived particles which may decay inside the detector. The response of the detector should be as close to reality as possible, so effects such as dead readout channels, electronic noise in the readout and various detection efficiencies are all modelled. Since these effects change over time, Monte Carlo is produced for a given detector *geometry*, which relates to any time dependent aspect of the ALEPH detector. Therefore Monte Carlo is produced for a given period, usually a specified year of detector operation.

The result of GALEPH is recorded in the same format as the data from the real ALEPH detector, but with the additional information of the *true* identity and 4-momentum of all the particles in the event, the so-called truth information.

The final stage of Monte Carlo production is the application of JULIA[38], as in the case for real data from the detector. The resulting Monte Carlo data can also be used

in the same way as real data, with additionally the availability of the truth information. Great care is taken to ensure the Monte Carlo resembles the data as closely as possible or that known differences are accounted for.

The Monte Carlo data containing Higgs bosons used in this thesis were generated using the HZHA03[29, 30] generator, and the confinement of quarks carried out using JETSET. For other processes the generators used are noted, see section 8.1.1.

3.7 The ALPHA Analysis Framework

In order to present a common method of accessing the data recorded by the **ALEPH** detector an *analysis framework*, ALPHA[39], is available. It makes objects such as energy flow objects, JULIA tracks and clusters, or truth information from Monte Carlo available in a uniform way. Alternatively all the raw event information is also available. Details such as reading in and unpacking all the data for each event are handled by ALPHA. Typically an analysis, including those discussed in this thesis, use ALPHA to produce a more compact representation of interesting events, which are further processed as a part of the particular physics analysis.

Chapter 4

Identification of B hadrons

4.1 Introduction

The Higgs bosons which could be produced at LEP would decay mostly to b quarks. There are expected to be many events from background processes which are consistent with a Higgs boson topology. However there are far fewer background events that are also expected to contain B hadrons. Therefore it is of great importance to be able to identify events in which B hadrons have been produced and decayed. The process of identifying events likely to have contained B hadrons is called b-tagging. Several methods for performing b-tagging exist. All make use of the properties of B-hadrons which can distinguish them experimentally from hadrons not containing b quarks. Especially useful are the relatively large lifetime of B hadrons and their large rest mass.

Particle Name	Mass (GeV/c^2)	Lifetime (ps)
B^0	5.2794 ± 0.0005	1.540 ± 0.024
D^0	1.8645 ± 0.0005	0.4126 ± 0.0028

Table 4.1: The rest mass and mean lifetime of the B^0 and D^0 mesons.

It can be seen in Table 4.1 that the mass and lifetime of the bottom B^0 meson are much larger than that of the charmed D^0 meson. The B tag used by the ALEPH Collaboration for the Higgs boson search is a combination of methods which rely on the large mass and lifetime of B hadrons. The methods employed by the b tag which is

used in this work are the following:

- Track impact parameter with respect to the calculated interaction point.
- Reconstruction of secondary vertices
- Identified electrons or muons with large p_T.
- The variables Boosted sphericity and sum of p_T^2, which describe the shape of a jet.
- Track multiplicity normalised by a factor of 1 over the log of the energy of the jet.

The single most powerful method in use in ALEPH is the impact parameter technique. Most of the work described in this chapter is a method to improve the performance of the existing impact parameter based b-tag. However, firstly the procedure of jet clustering will be introduced followed by short descriptions of the above method of b-tagging. Jet clustering is used in all the b tagging methods to be described here and also in the Higgs boson search analyses which will be described in chapters 6 and 7.

4.2 Jet finding

A jet is defined as a group of reconstructed particles in an event. In the b tagging methods which follow a jet clustering technique is used. The aim of the jet clustering is to divide all the particles in an event into jets. Each jet is considered to be associated to the hadronisation and decay of a quark produced at the e^+e^- annihilation event. Here we describe the algorithm to cluster the observed charged and neutral particles into jets:

The invariant mass of all pairs of particles is calculated. The four-momenta of the two particles with the lowest invariant mass is then combined into a new pseudo-particle, which replaces the two original particles. This process is repeated – treating pseudo-particles and particles on an equal footing – until no more pairs can be found with scaled invariant mass y_{ij} (or clustering metric) lower than a specified cutoff value, y_{cut}:

$$y_{ij} = \frac{m_{ij}^2}{E_{\text{vis}}^2}, \tag{4.1}$$

where m_{ij} is the invariant mass of particles ij and E_{vis} is the visible energy of the event. The jets are then the particles remaining at the end of this process, be they original or newly formed pseudo-particles.

In the following we will make use of the so-called DURHAM and JADE jet clustering algorithms [44, 45]. In the DURHAM algorithm the invariant mass m_{ij} is defined as

$$m_{ij}^2 = 2\min(E_i^2, E_j^2)(1 - \cos\theta_{ij}) \tag{4.2}$$

whereas the JADE algorithm term is

$$m_{ij}^2 = 2E_i E_j (1 - \cos\theta_{ij}) \tag{4.3}$$

It should be noted that the number of jets found by the jet finder is not fixed by the cutoff value y_{cut} and will vary from event to event. Sometimes it is convenient to stop the clustering iterations when a given number of jets is reached (e.g., four jets in the case of $\text{hZ} \to \text{b}\bar{\text{b}}\text{q}\bar{\text{q}}$ hypothesis).

Both of the b-tagging methods to be discussed next rely on having clustered jets to work with.

4.3   b-tagging methods

4.3.1   b-tagging using track impact parameters

The impact parameter method relies on the small but measurable lifetime of the B hadrons produced via hadronisation from b quarks. The B hadron will typically travel a few millimetres in the detector before decaying to charged and neutral decay products. The tracks recorded from the charged decay products may be seen to have a small impact parameter with respect to the interaction point of the e^+e^- for the event. The program commonly used by the ALEPH Collaboration to b tag with track impact parameters is called QIPBTAG[40].

It is important to note that QIPBTAG makes no use of the constraint that the decay products of the B hadron should originate from a single secondary vertex in space. In this way the method is sensitive to any tracks originating from particles with lifetime. B hadrons will often decay via charmed hadrons which also posses a small lifetime, possibly giving rise to a tertiary vertex. By not assuming a rigid secondary vertex topology QIPBTAG retains sensitivity for cascaded decays with lifetime. (This is also why it is more difficult to distinguish a c-jet from a b-jet than with other, lighter, flavours). The first stage of the impact parameter based tag is to calculate a signed impact parameter and associated error for each track in an event.

To find the impact parameter an estimate of the location of the primary vertex, the e^+e^- interaction point, is required. To calculate if the measured impact parameter is statistically significant an estimate of the error on the primary vertex is also needed.

A dedicated procedure is employed to find the primary interaction point on an event by event basis. The approximate region in space of the interaction point during the period that the run was recorded is called the luminous region. The luminous region is the starting point for a more accurate determination for the primary vertex position for each event. The method used makes use of the reconstructed tracks in an event while remaining insensitive to lifetime in any of the particles produced. A full description of the primary vertex finding may be found in [41].

The size of the impact parameter is defined for each track as the track's distance of closest approach to the primary vertex. In addition the concept of signing the impact parameter is introduced. Signing the impact parameter adds more physical information:

The B hadron's decay products are constrained to have originated from a point which lies along the path that the original B hadron has travelling along. An estimate of the B hadron's 3 vector is made. It is assumed that the b quark (and B hadron) were produced at the primary interaction point. For each track the point of closest approach along the B hadron's flight axis is found. If that point lies in front of the primary interaction point, along the direction of B hadron flight, the sign of the track's impact parameter is chosen to be positive and negative otherwise.

Tracks which originated from the interaction point, but have non zero impact pa-

rameter due to detector resolution will not have a favoured sign. Tracks which did originate from the decay of particles with lifetime will tend to have positively signed impact parameters. Increasing the accuracy of the B hadron flight direction estimate will reduce sample contamination. Fewer tracks from particles with lifetime will enter the negatively signed impact parameter sample.

The final output of the QIPBTAG algorithm is $\mathcal{P}_{jet}$ for each jet. $\mathcal{P}_{jet}$ is a variable which tends to 0 for a b-like jet, and ranges between 0 and 1 for a light flavoured jet.

4.3.2   Secondary vertex reconstruction

Another approach to b-tagging is to explicitly reconstruct a secondary vertex. The tracks in the jet which come from the b-hadron's decay will all originate from a point, which in general will be displaced relative to the primary vertex of the event. The measurement of how well the tracks in a jet may be fitted to a double vertex hypothesis as opposed to a single vertex hypothesis (expressed as a $\Delta\chi^2$) can be used to identify jets with a significantly displaced secondary vertex. In addition, information is available on the decay length and direction of flight of the b-hadron. The program used by the ALEPH Collaboration to search for secondary vertices is called QVSRCH. A detailed description of QVSRCH is available in [42].

4.3.3   Leptons with large transverse momentum

The B meson may decay via the weak force and give rise to a charged lepton and neutrino in the decay chain, the so called semi-leptonic decay. The B meson will decay giving rise to either an electron or muon in $\sim 21\%$ of decays. The charged lepton will be generally be produced with a large momentum transverse to the direction of the jet axis due to the difference in mass between the B hadron and the lepton. By making use of specialised electron and muon identification a tag on B hadrons can be made. The method is limited by the relatively small decay branching fraction which lead to the more easily identifiable charged leptons.

4.3.4 Scaled jet charged-multiplicity

The number of charged particle tracks in an event is called the charged multiplicity. The average charged multiplicity of all events has a dependence on ln(E) where E is the energy of the collision in the centre of mass frame. In addition to the energy dependence the average number of charged tracks observed from the hadronisation and subsequent decay products of b quarks is larger than that for lighter quarks. Therefore the charged-multiplicity of each jet normalised by $\ln(E_{jet})$ may discriminate between b jets and jets from lighter flavoured quarks.

4.3.5 Jet shape variables

Two further variables are defined which show discrimination between b quark jets and other jets. The variables rely on the kinematics of the decays of B hadrons, which have a relatively large rest mass. The following variables are defined for each jet in an event using the reconstructed tracks associated with each jet in turn.

$$\sum p_T^2 = \sum_{i=1}^{i=N} p_{i\|}^2 \qquad (4.4)$$

where N is the number of tracks in the jet.

Boosted sphericity, is defined as the sphericity of the jet in the rest frame of the jet (assumed to be the rest frame of the b quark).

4.3.6 Neural Net b tagger

An artificial neural network known as the neural net b-tagger (NNBTAG[43]) is used to combine the available b tagging methods, for optimum performance. NNBTAG combines the variables described above to allow discrimination between light flavoured jets and b jets. In Table 4.2 are listed the input variables of the neural network.

4.4 QIPBTAG improvements

Jet clustering is important for b-tagging. The tag is constructed jet by jet and relies on having a physically meaningful clustering to work with. Explicitly the clustering

	Variable name
1	$\mathcal{P}_{jet}$ (QIPBTAG)
2	$\Delta\chi^2$ (QVSRCH BTAG)
3	Largest p_T of identified leptons
4	Boosted sphericity of jet
5	Sum of p_T^2 of all particles in the jet
6	Jet multiplicity / $\ln E_{jet}$

Table 4.2: The six inputs used for per-jet b-tagging by the neural network b-tagger.

should ensure that decay products from each distinct b-hadron be grouped together in separate jets. In addition to track association the jet cluster axis is also used. In particular the jet axis is important for the impact parameter b-tagger described in Section 4.3.1. To gain better performance account is taken of tracking resolution effects by signing the impact parameter. The finite tracking resolution on fragmentation tracks from the interaction point are expected to be the main contribution to tracks with negative impact parameter. Once signed, the impact parameter distribution allows the calculation of jet probabilities to take into account the unavoidable component due to tracks that originated from the primary vertex. It is noted that in the signing scheme described the jet axis is being used as an approximation for the b-hadron flight direction.

4.4.1 B hadron flight estimate

In the following subsections possible improvements to b-tagging with impact parameters are investigated. Alternative estimators of the b-hadron flight direction, other than the jet axis are tested. For the tests fully reconstructed simulated signal data was used. The sample size was 10k events with h and Z bosons decaying to four quarks. The Higgs boson mass assumed in the simulation was $m_h=80$ GeV/c^2.

Estimator using subjet axis

We consider an event in which jet clustering has already been performed. In order to better estimate the B-hadron direction one would want to identify only those tracks within a jet that came from the b decay.

To obtain such a subset of tracks from a jet it is proposed to repeat the application of the clustering algorithm on just the tracks in the jet. The clustering cutoff y_{cut} should be tuned such that it stops when the smallest invariant mass is approximately that of an average B-hadron, which is ~ 5.3 GeV/c^2. The resulting small clusters of tracks is termed *subjets*.

To investigate the effect of subjet treatment Monte Carlo studies were performed. In the studies hZ $\rightarrow$ b$\bar{\text{b}}$q$\bar{\text{q}}$ events were clustered to give four jets using the DURHAM jet metric, hereafter called the original jets. For each of the original jets another jet finding was performed, this time with a fixed y_{cut} value. The result is a number of subjets, which in total make up the whole of the original jet. The momentum of the most energetic subjet is chosen as an estimate of the b-hadron flight direction. The choice of subjet is motivated by the nature of the b fragmentation. The current b-quark fragmentation models predict the momentum spectrum of the b-hadron as a function of that of the b-quark. An example is the Peterson function [46]. The experimental results [47] are in good agreement with the Peterson model and favour a *hard* fragmentation of the b-quark. Thus the b-decay products are likely to be found in a hard core of the jet.

The distribution of the angle between the true b-hadron direction and the original jet axis $\Delta\theta$ may be found for the simulated data and is shown as a reference in all the plots in Figure 4.1. For comparison, the distributions are also shown using the subjet axis instead of the original jet axis. In order to optimise the match between the true flight direction and the subjet axis, a range of subjet sizes were investigated.

It can be seen in Figure 4.1 that using the subjet estimator changes the distribution of flight estimate. The distribution evolves over the range of y_{cut}. For very small values of the cutoff few tracks are clustered, and a large number of subjets result. Physically the tracks from the decay of the b-hadron are being split up between different clusters. For these very small subjets the estimate is clearly worse than the performance obtained
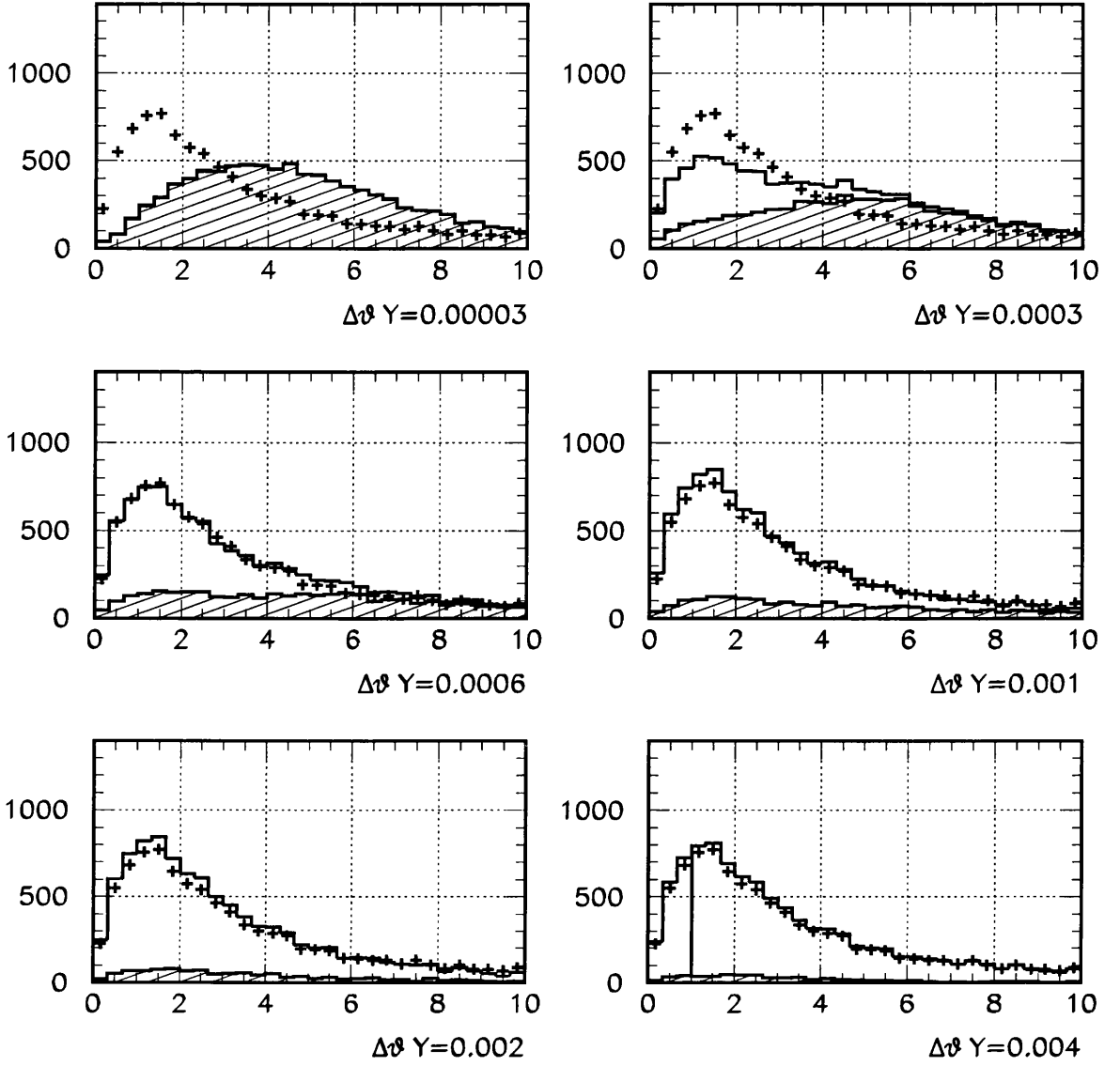
Figure 4.1: Distributions comparing performance of subjets for a range of y_{cut} values. Crosses are the reference and show the original performance. The histogram shows the performance of the new method and is divided in two components, hatched and clear. The hatched component of the histogram is from jets where more than one subjet was found. The clear component is from jets were only one subjet was found.

with the original jet axis. With increasing y_{cut} it can be seen that, as expected, fewer subjets are found within the original jet. The peak of the distribution moves to lower $\Delta\theta$ and the performance approaches that of the original jets.

For $0.0006 < y_{cut} < 0.004$ the average of the subjet peak coincides with that for the original jets, but the peak itself is enhanced. An enhancement to the peak at small $\Delta\theta$ indicates an improvement in the estimate of b-hadron flight direction. The best

73
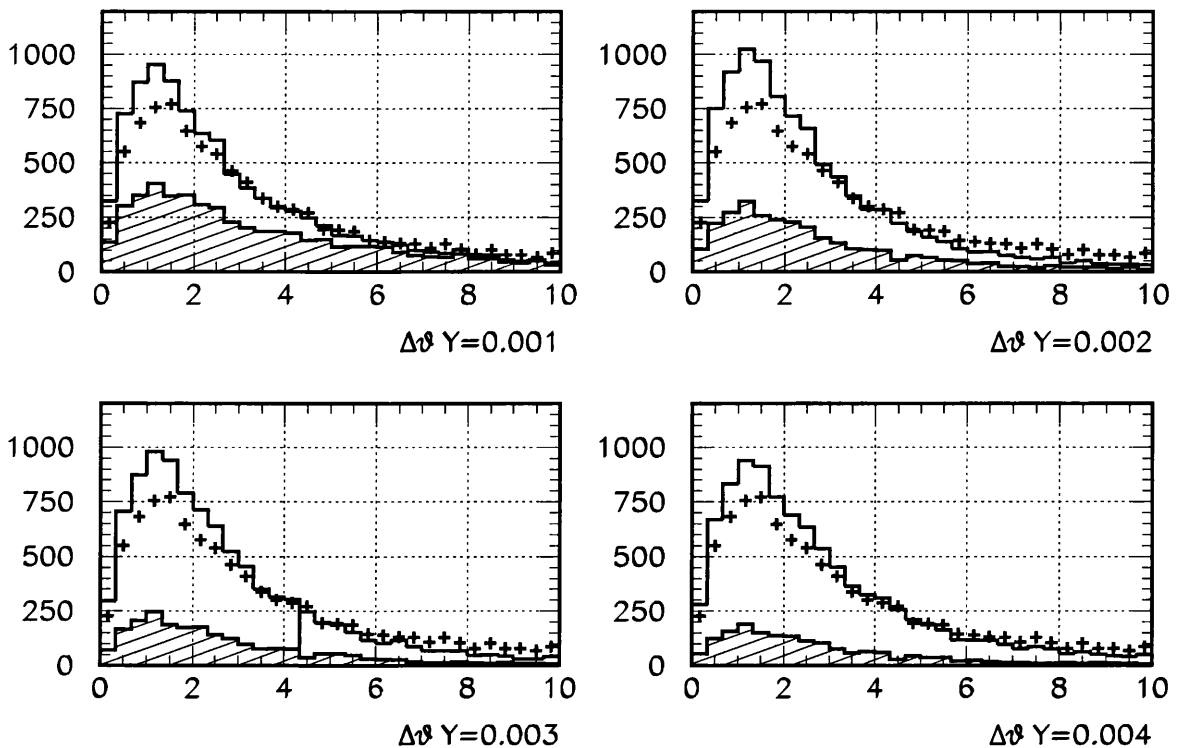
Figure 4.2: Distributions of $\Delta\theta$ comparing the performance of subjets and original jets, when using the JADE algorithm for subjet clustering.

performance is found to occur at $y_{cut} = 0.002$.

Figure 4.2 shows similar data, but using the JADE algorithm for subjet finding. The enhancement in the peak at small $\Delta\theta$ is striking as is the depletion of the tail of the distribution. Figure 4.2 indicates that subjets obtained with the JADE algorithm with $y_{cut} = 0.002$ provide the best estimate of the b-hadron flight direction of the methods tested. Therefore a $y_{cut} = 0.002$ is adopted for all the studies that follow.

Estimator using reconstructed secondary vertices

The other method investigated relies on a search for secondary vertices within a jet. The standard ALEPH algorithm, QVSRCH is used to do this [42]. It determines a list of tracks likely to belong to the secondary vertex, a b-tag variable based on the improvement in fit obtained by introducing the secondary vertex, and the coordinates and associated errors of the reconstructed secondary vertex.

The vector defined by the primary interaction vertex and the reconstructed secondary vertex provides an estimate of the b-flight direction. As with the subjets it

is necessary to tune selection parameters. Good estimates are required and since by construction a vertex candidate is always found, some way of discriminating on the quality of vertex is needed.

As an error estimate on the vertex position is available, the so-called *vertex significance* is used to identify likely candidates. This variable is defined as the flight length over its estimated error:

$$S_{\mathrm{vtx}} = \frac{L}{\sigma} \qquad (4.5)$$

In addition to S_{vtx} the total energy of charged tracks associated to the reconstructed secondary vertex E_{vtx} was also considered. E_{vtx} may be used to eliminate vertices where it is likely that many of the b-decay tracks are not associated to the secondary vertex. This may occur for vertices that are close to the interaction point, where decay tracks are confused with fragmentation tracks from the b-quark, or when the jet clustering has resulted in the splitting of b-hadron decay tracks between jets. In these cases the vertex coordinates are unlikely to be precise.

Distributions of S_{vtx} and E_{vtx} for various flavours of jets are shown in Figure 4.3. In order to obtain a good b-hadron flight estimate quality cuts are applied to the secondary vertex using S_{vtx} and E_{vtx}. In the case where the secondary vertex passed, the vector pointing from the interaction point to the secondary vertex is used as the b-hadron flight estimate. If the quality cuts are failed then the estimate from the original jet axis is used instead.

In order to optimise the quality selection a range of cuts on the vertex significance S_{vtx} were tried. The value giving the distribution of flight estimators closest to the true b-hadron flight direction was found to be 6.5.

The quality cut on the vertex energy E_{vtx} was then introduced, to reduce the number of vertex estimates with large $\Delta\theta$ (that is to reduce the number of poor estimates of the b-hadron direction). See Figure 4.4 for two illustrative plots.

A scan over several values of the minimum required vertex energy (5, 10, 15 and 20 GeV) determined that $E_{\mathrm{vtx}} > 15$ GeV is optimal together with a decrease of S_{vtx} to 6.0.
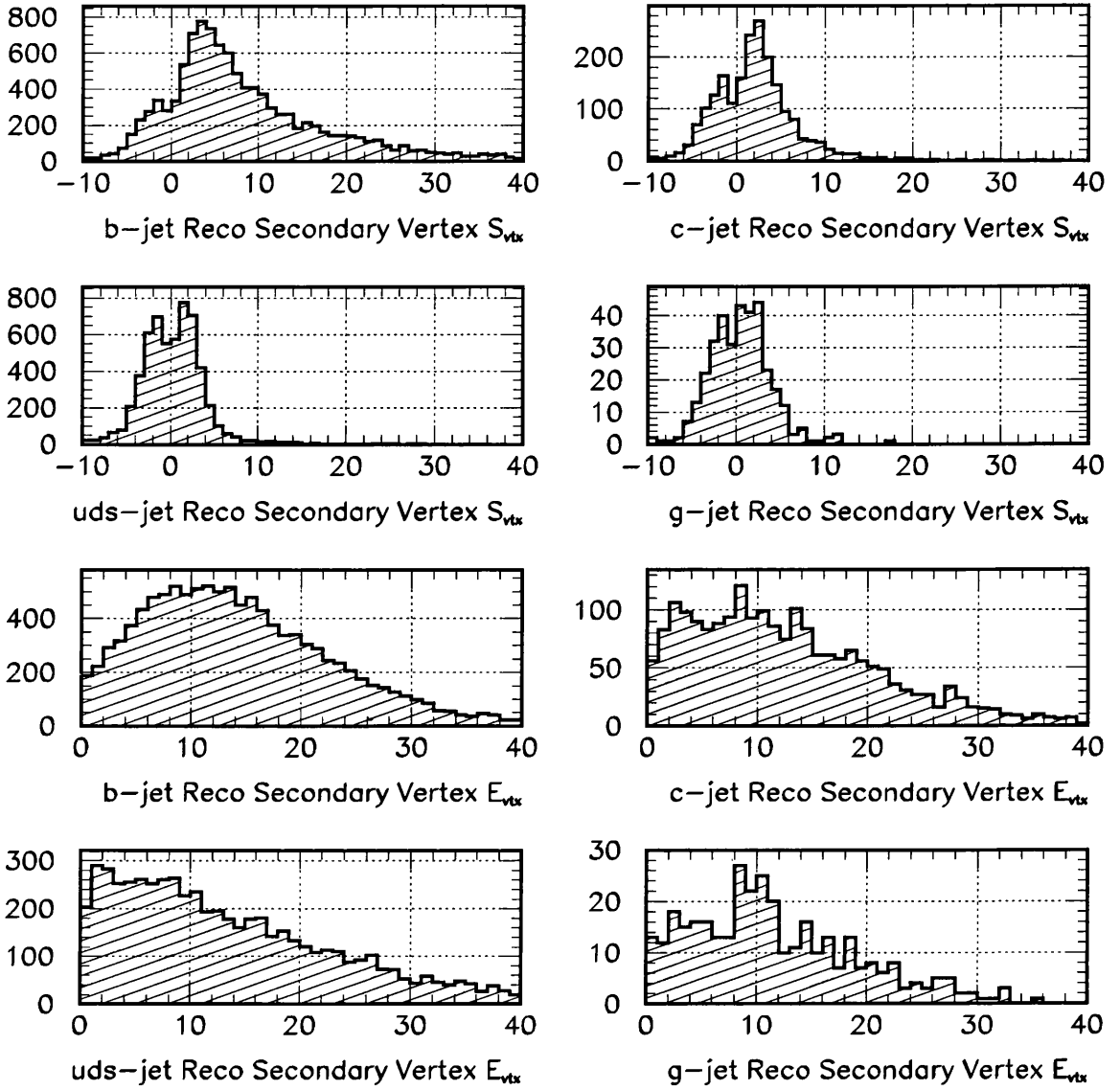
Figure 4.3: Distributions of the two variables S_{vtx} and E_{vtx}. The distributions are grouped into two sets of four, according to the flavour of the jet. *Top*: Secondary vertex significance S_{vtx}. *Bottom*: Energy associated to the secondary vertex E_{vtx}.

Using a combined method

In the above, two methods have been identified of obtaining an improved estimate for the b-hadron flight vector. The two methods are now combined to improve the average estimate further.

In the combined approach secondary vertices selected by the algorithm described in Section 4.4.1 are used as the flight vector estimate. If no such secondary vertex is found within a jet, the estimate from the JADE subjet axis (Section 4.4.1) is used

76
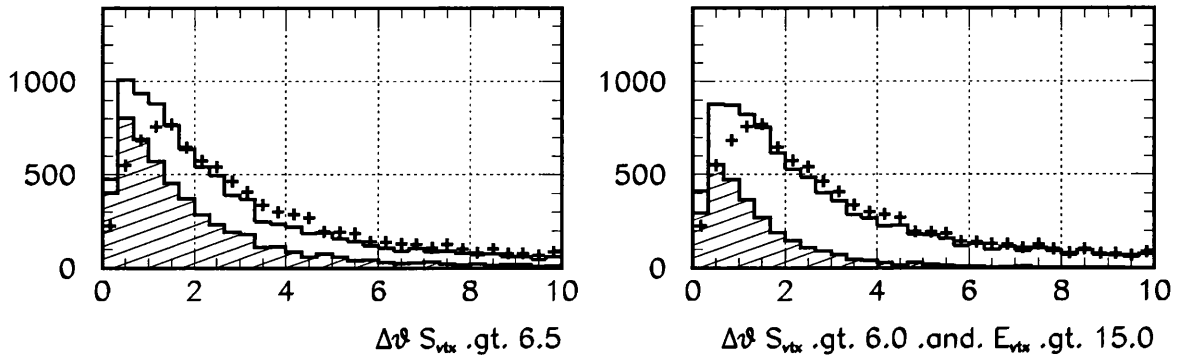
Figure 4.4: Distributions of $\Delta\theta$ when using b-hadron flight estimates derived from reconstructed secondary vertices. The two plots are for vertices selected according to two different sets of quality cuts. *Left*: $S_{vtx} > 6.5$, *Right*: $S_{vtx} > 6.0$ and $E_{vtx} > 15$ GeV. The shaded areas represent vertices, while the clear area indicates that the vertex failed selection and that the original jet estimate was used instead. The distribution with crosses is obtained when using only the original jet estimator.
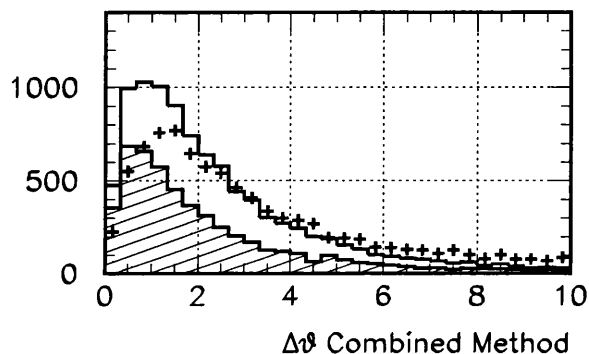
Figure 4.5: Distribution of $\Delta\theta$ for the combined approach to estimating b-hadron flight direction.

instead. The resulting $\Delta\theta$ distribution is shown in Figure 4.5.

4.4.2 Performance on simulated events

It has been shown that improvement in the estimate of the b-hadron flight direction can be achieved over that obtained from the original DURHAM jet axis. As these are the jets used in the current Higgs boson analyses to perform b-tagging, it follows that improvements in the tagging with better flight estimates should result in an increased efficiency for selecting possible Higgs boson signal events.

In order to test the effect on the b-tagger's ability to find b-quark jets against lighter-quark jets an evaluation of the tagger alone was performed. The test relies on

the comparison of the b efficiency against the efficiency for rejection of other flavours. The jets presented are from simulated signal events.

The improved b-tagging is also tested in the context of a Higgs boson event selection. For this the cut-based analysis of the four-jet channel, $hZ \rightarrow b\bar{b}q\bar{q}$ was chosen. (The selection is described in later in section 6). For the test using the Higgs selection simulated signal and background events are used. The input Higgs boson mass in the signal was $m_h = 85 \text{ GeV}/c^2$.

In the standard four-jet event selection an artificial neural network b-tagger is used for optimal efficiency. Although the most discriminating of the six input variables (see Table 4.2) is the impact parameter-based $\mathcal{P}_{jet}$ variable the neural network complicates testing. For an initial test it was felt that the necessary retraining that should be performed would not be justified. Instead, for the purposes of the tests the analysis was performed four times.

- The original $\mathcal{P}_{jet}$ is used in the neural network b-tagger, as in the standard analysis.

- The original $\mathcal{P}_{jet}$ is used by itself for b-tagging, instead of using the NN b-tagger output.

- The improved $\mathcal{P}_{jet}$ is used in the neural network b-tagger.

- The improved $\mathcal{P}_{jet}$ is used by itself for b-tagging, instead of using the NN b-tagger output.

In this way a comparison is possible between the two instances in which the impact parameter b-tagger was used alone, without the complicating issue of neural network retraining. Valuable information is still obtained by comparing the two neural networks analyses. However results for the modified tagger in this situation are unlikely to be optimal.

In the following subsections two sets of results are presented. One for each of the two different methods of performing the improved flight estimate. The sections are labelled as *Method A* and *Method B*, according to the definition

- **Method A**: Using the reconstructed secondary vertices described in Section 4.4.1 as the only alternative to the original jet axis. Recall that in accordance with the description given in that section the original jet axis is used in preference to poor vertices.

- **Method B**: The combined method described in Section 4.4.1 was tested. In this arrangement poor secondary vertices are replaced not with the original jet axis but with an energetic subjet axis.

Method A

The result of the tag performance can be seen in Figure 4.6. For a perfect tagger a curve is expected that approaches a b efficiency, ϵ_b of 1 for a light jet rejection, $1 - \epsilon_{udscg}$ of 1. That is, for improved performance the curve moves to the top right of the plot. It can be seen that the impact parameter b-tag does improve at high rejection region above ~95%. However the neural net response is indeterminate, indeed showing a degraded response in places.

The Higgs boson four-jet analysis result is shown in Figure 4.7. The channel signal selection efficiency, ϵ_{4jet} is shown in percent and the expected number of background events is normalised for an integrated luminosity of 57.0 pb^{-1}.

An improved analysis approaches low background for high efficiency, at the bottom right. It can be clearly seen that the impact parameter tagger has an improved relative performance of up to ~8% for fixed signal selection efficiency. The neural network shows little change from standard behaviour.

Method B

Using the combined approach described in Section 4.4.1 the b-jet tagging performance curve shown in Figure 4.8 is obtained. It can be seen that the modified impact parameter tag performs better over the range shown. Similarly the neural network b-tagger has higher efficiency for b-jet identification over much of the range. The corresponding four-jet analysis in Figure 4.9 reflects the positive performance increases seen in the jet by jet tag curve. The background has been reduced in both impact parameter b-tag
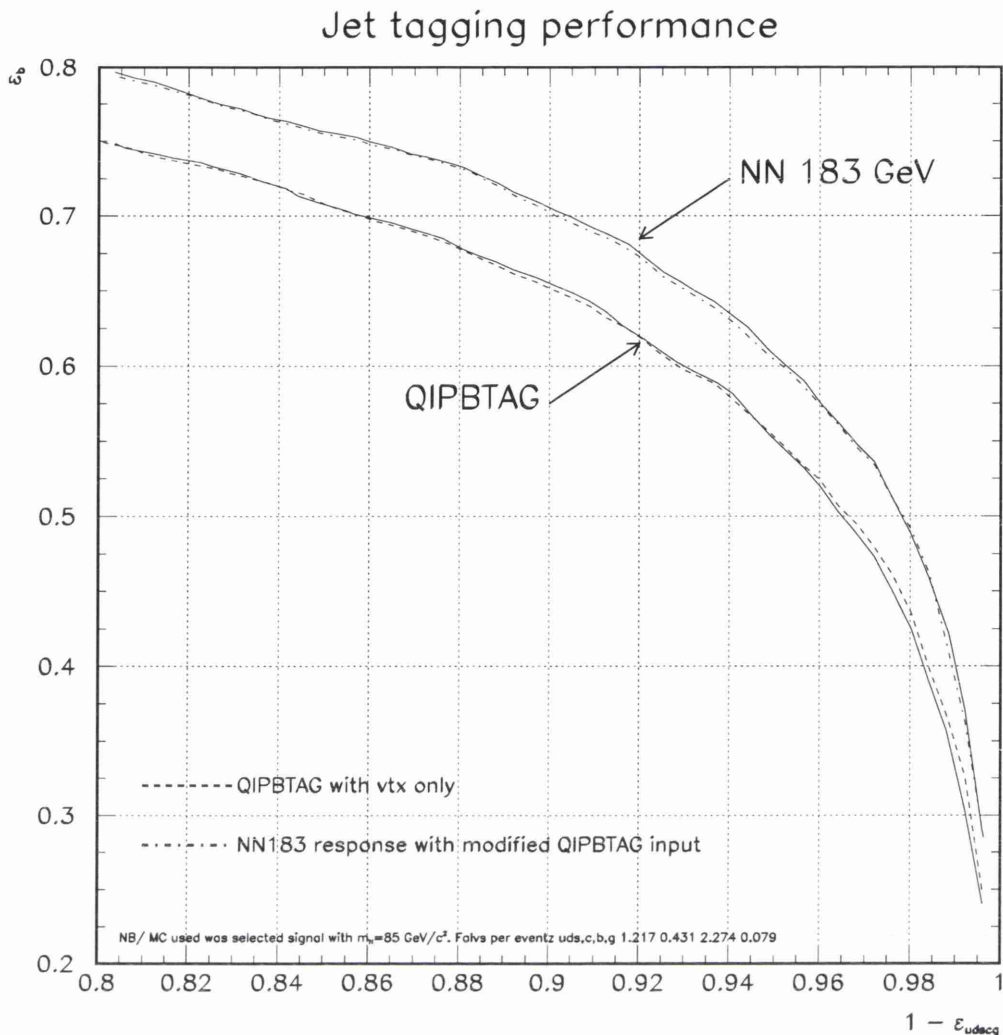
Figure 4.6: *Performance curve* for the b-tagging of jets.

and neural network analysis by ~5% for fixed signal selection efficiency.

4.4.3 Summary of observed changes in performance

Two new methods were described and are seen to give better estimates of the B hadron direction than using the jet axis obtained with the standard jet clustering algorithm.

Using the best new estimator (Method B) as an input to the calculation of the jet probability $\mathcal{P}_{jet}$ (using the QIPBTAG algorithm) resulted in an absolute improvement of 2-3% in the efficiency for tagging b-jets, for a fixed light jet rejection. The modified $\mathcal{P}_{jet}$ was used in three different contexts; An hZ $\rightarrow$ b$\bar{\text{b}}$q$\bar{\text{q}}$ event selection, to select b-quark jets directly and as an input to an existing pretrained b-tagging neural network.

In the context of a Higgs boson selection the results show a ~ 5% relative reduction in background for a given signal efficiency. The increase in the neural network b-tagging
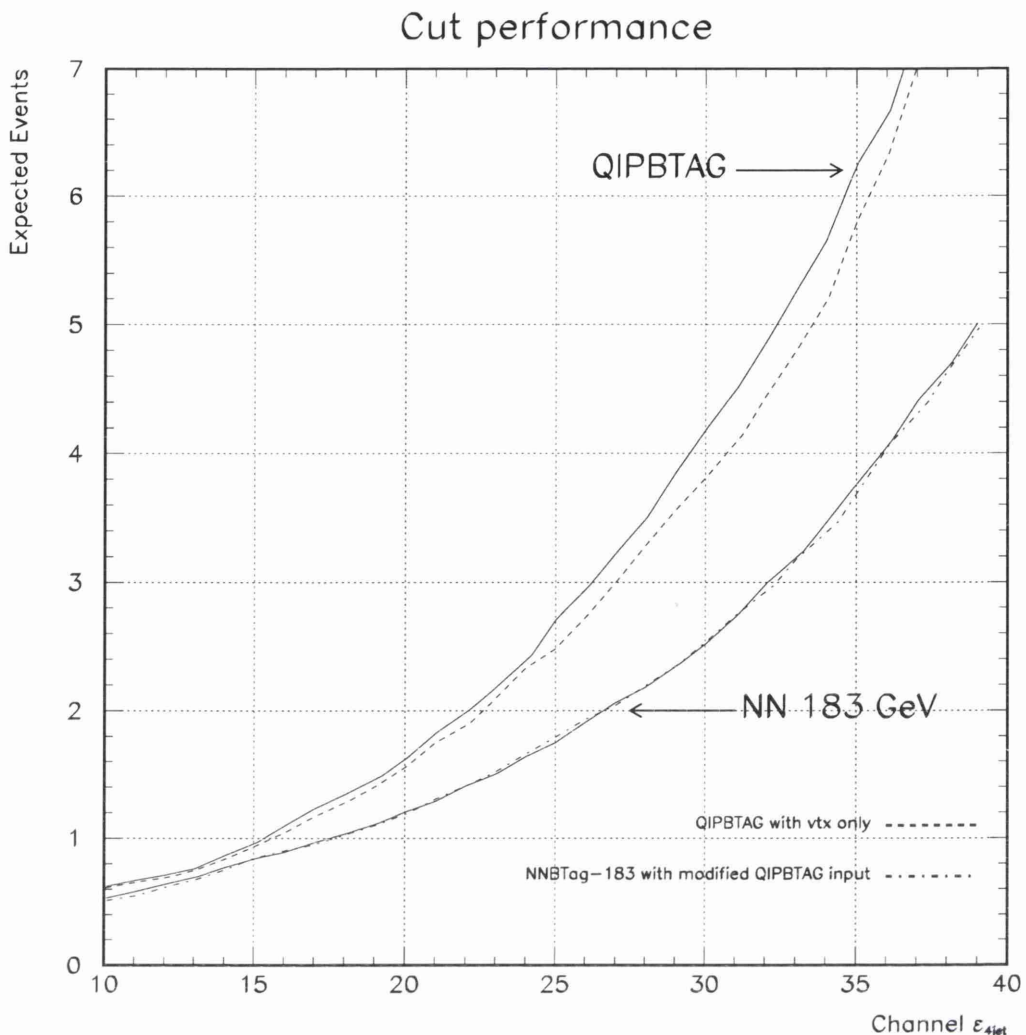
Cut performance

Figure 4.7: Performance of the Higgs boson four-jet selection.

performance is expected to be enhanced after the neural network is retrained using the modified $\mathcal{P}_{jet}$ variable.

4.4.4 Modifications adopted for a general implementation

In order to turn the proposed changes into a scheme which could be used by any group in the ALEPH Collaboration some further additions were made:

• Identified charged tracks from the decay of the short lived neutral particles K_s and λ are grouped together in the jet clustering stage to prevent the unphysical splitting of the decay products between jets.

• The clustering procedure for generating subjets was changed to use a cutoff in terms of $m_{ij} = 6.7$ GeV/c^2 instead of a y_{cut}. The use of an explicit mass removed a

81
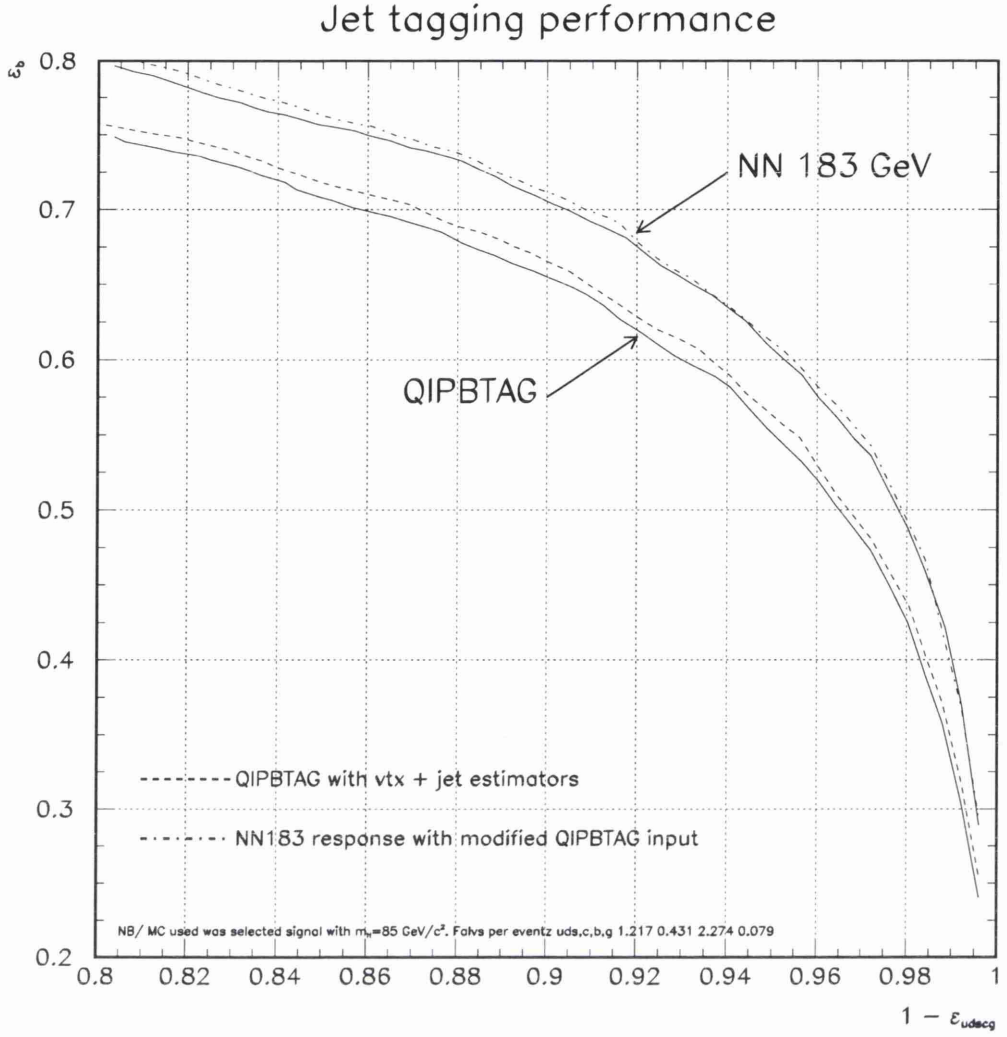
Figure 4.8: *Performance curve* for the b-tagging of jets.

dependence on E_{vis}, which could be very different in different analysis contexts.

• The subjet clustering was restricted to use only particles that make an angle of less than 30 degrees to the jet axis. The B hadron decay tracks are likely to lie in the centre of the jet.

• The subjet with the larger momentum (rather than energy) is chosen, to be consistent with the physical motivation from the Peterson function.

The selection of secondary vertices is unchanged, as is the combination method. However an extra quality cut is required if a subjet it to be used. The subjet is required to have a mass larger than 2 GeV/c^2, motivated by the mass of typical B hadrons ~ 5.3 GeV/c^2. If the chosen subjet fails the quality cut the original jet axis is used.
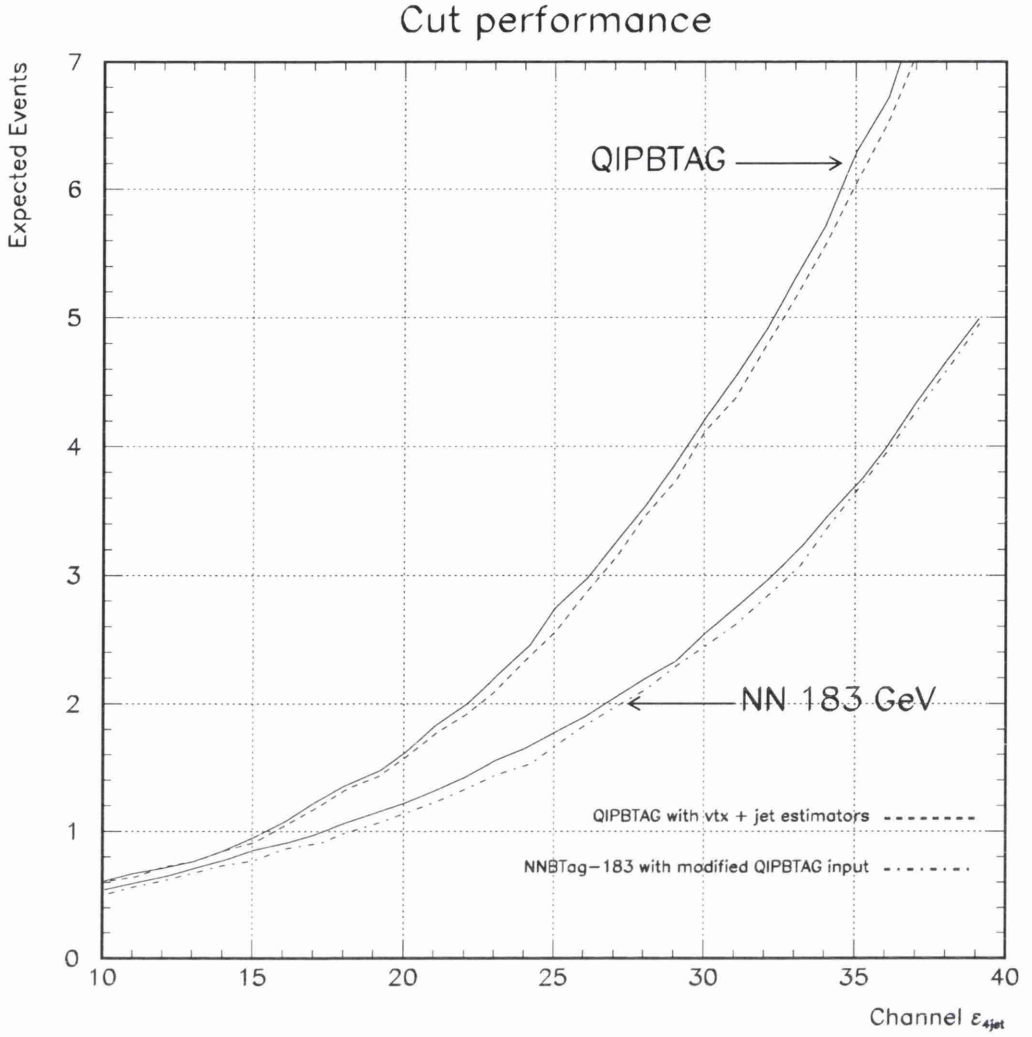
Figure 4.9: Performance of the Higgs boson four-jet selection.

A performance plot of the final scheme is shown in Figure 4.10. The dashed lines show the performance of the modified scheme. The calculation was made using simulated ZZ events, with a selection to choose four jet events. The jets were then tagged one by one. The generator information was used to assign the true flavour of the quark which led to the jet. Figure 4.10 (top plot) shows the efficiency of b jets selection against rejection of u,d or s jets and separately the b jet selection again charm jet rejection (lower pair). Figure 4.10 (bottom plot) shows the difference between the solid and dashed lines in the two pairs of curves from the upper plot. B jet selection against u,d or s jets shows the larger $\Delta\epsilon_b$.
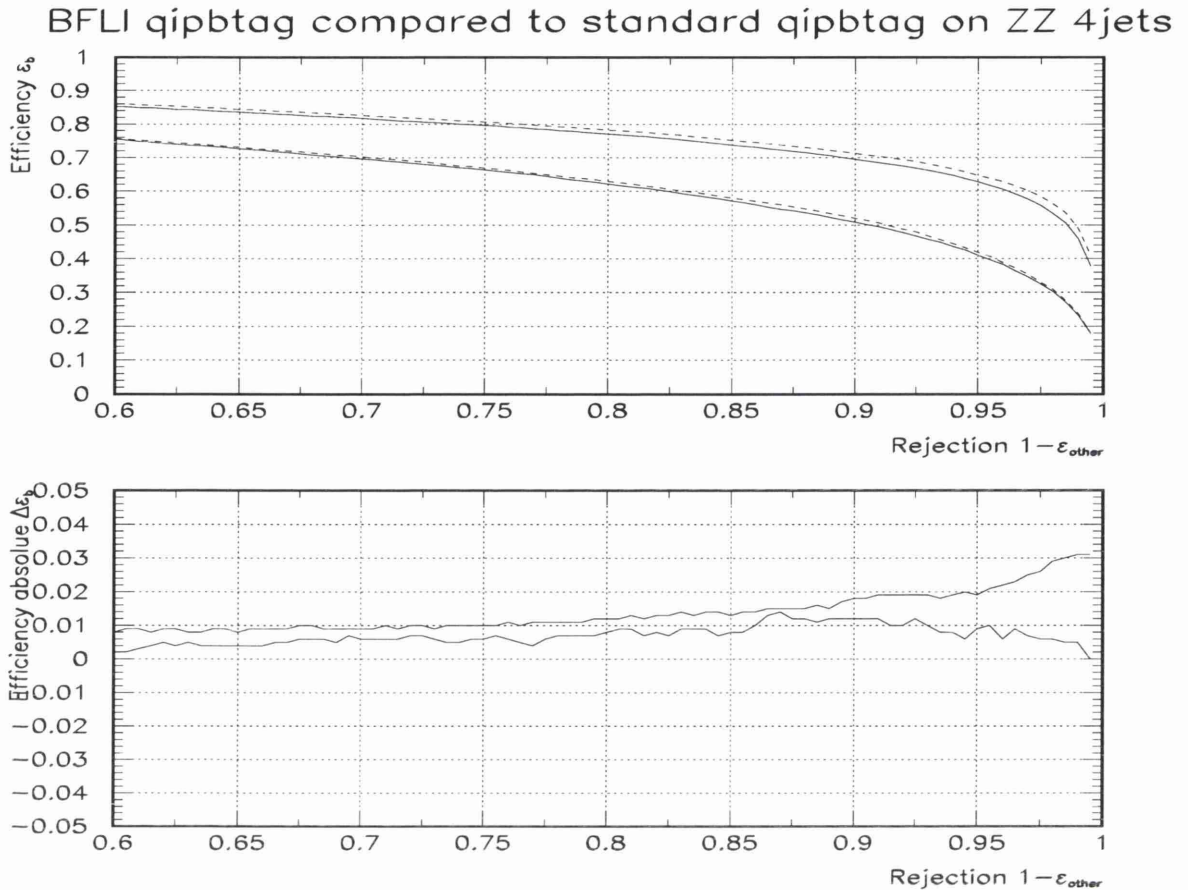
Figure 4.10: Performance enhancement in b tagging, determined from ZZ Monte Carlo events.

4.4.5 Systematic checks

Before the modified b tagging scheme was widely used it was important to understand if the method carried extra systematic uncertainties. An investigation was made into possible systematic problems with the modified b tag.

4.4.6 Comparison of real and simulated data

All of the performance studies that were done rely on accurate modelling by the Monte Carlo simulation of the underlying B-hadron production, decay and hadronisation. It is of great importance to verify agreement in between data and MC for variables used. Distributions of basic quantities were checked first followed by the overall rates of estimator use and finally b tag output. In all distributions shown below the solid histogram is the calculated rate from simulation with the observation rendered as points with associated statistical error.
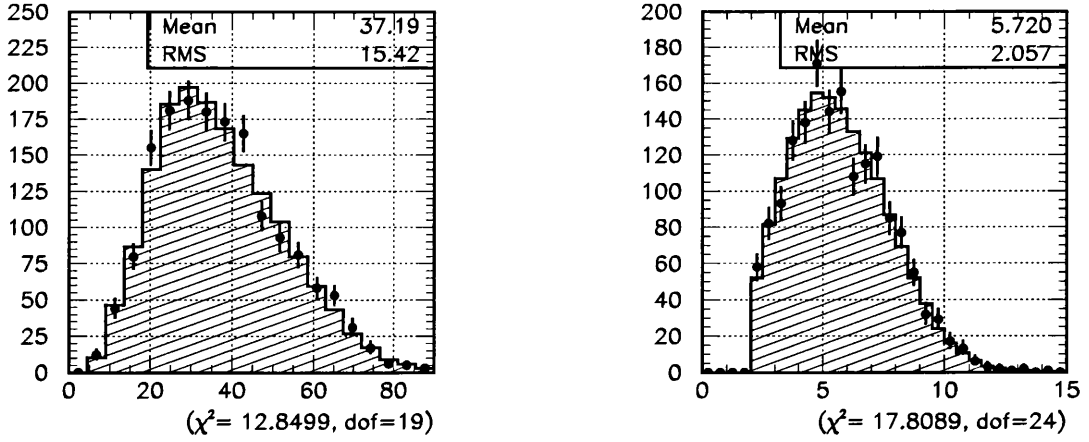
Figure 4.11: Distributions of momentum and mass of subjets. *Left:* Subjet momentum in GeV/c. *Right:* Subjet mass in GeV/c^2.

In Figure 4.11 the distribution of subjet momentum and mass is shown for the MC simulated events together with measured values from the data taken at 188.6 GeV. Events are required to pass the Higgs four jet preselection. The MC consists of the standard model processes expected to have non vanishing selection efficiency. Processes contributing are $q\bar{q}gg$, $q\bar{q}q\bar{q}$, WW and ZZ pair production, which have been added in the appropriate proportions in the histogram according to their production cross section and selection efficiency.

The process of quark to hadron formation, hadronisation, is not well understood. The MC simulation uses empirically determined functions with parameters tuned to observation. In particular the B-hadron momentum with respect to the original b-quark momentum is modelled by the Peterson fragmentation function [46]. The function has one free parameter, ϵ_b, previously tuned to observation [47]. Given that the process of subjet finding will be sensitive to the momentum of the B-hadron it is important to compare the momentum spectrum of the subjet between simulation and data. The distribution is shown in Figure 4.11(*left*). It may be seen that the agreement is good. Figure 4.11(*right*) shows the subjet mass distribution. The mass is cut at 2 GeV/c^2 which is why there is a sharp cut off in the distribution. Again the agreement is good, with the mode and mean of the subjet mass distribution near the B hadron mass of ~ 5.3 GeV/c^2.

Figure 4.12 shows the difference in angle between the subjet axis and the jet axis.

85
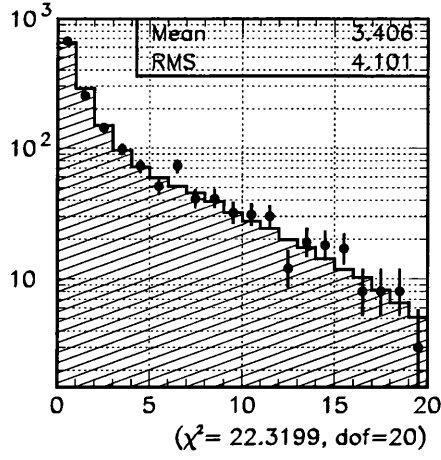
Figure 4.12: Angle between the subjet axis and the jet axis in degrees.

Shown are cases where the subjet is used as the estimate for the B hadron flight direction. In other words the angular difference is the size of the correction upon the jet axis which was the original estimate. It is noted that the data/MC agreement is good, and that while the mean angular difference is only 3.4 degrees there is a tail of events extending up to at least twenty degrees.
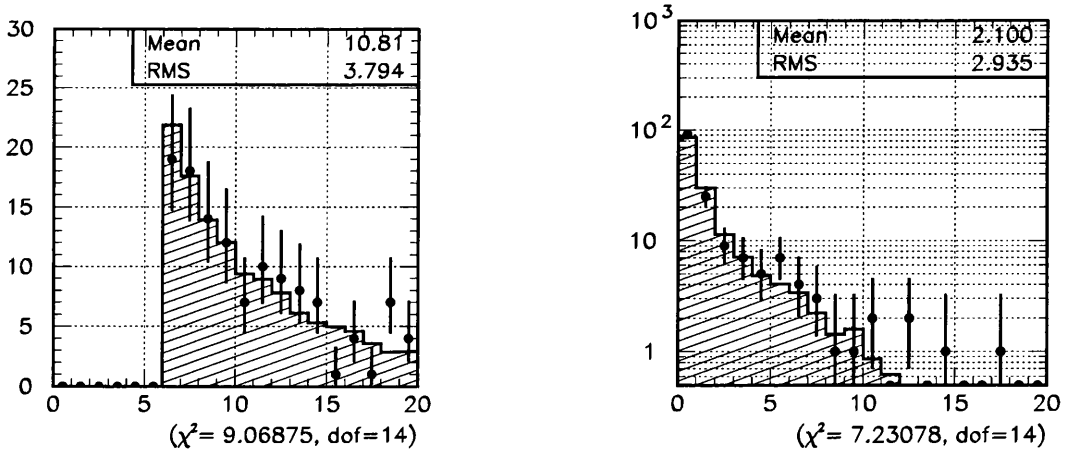
Figure 4.13: *Left:* Subjet significance. *Right:* Angle between vertex estimate and original jet axis (in degrees).

In cases where a secondary vertex is used rather than the subjet, the agreement between data and MC for the secondary vertex significance is shown in Figure 4.13(*left*). Since only the cases where the secondary vertex estimate is used the distribution is cut off below a significance of 6.0. It can be seen that the agreement is good. In Figure 4.13 *Right* the difference in angle between the vertex estimate and the jet axis is shown.

Again the agreement between data and MC is good and it is interesting to compare it to the corresponding plot for subjets. Comparing with Figure 4.12(*right*) it can been that the average angular correction to the jet axis estimate is somewhat smaller for the vertex estimator at 2.1 degrees compared to 3.4 degrees for subjets. Also there are few cases where the vertex estimator is more than 10 degrees from the jet axis whereas there are still a significant number of events using the subjet estimator that have a correction as large as 20 degrees. This suggests that the subjets will make the largest different to the eventual tagging performance.
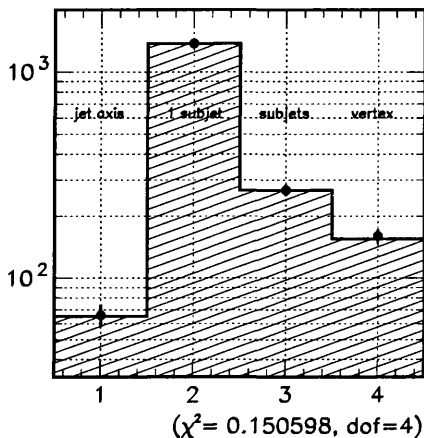
Figure 4.14:   The number of times each type of estimator is used for the most b-like jet in each event.

Figure 4.14 shows the overall number of times different types of estimator are used in tagging the most b like jet. The four bins correspond to

(1) jet axis is used.

(2) subjet is used. In this case only one jet could be formed from the core tracks and so there is no ambiguity in the definition of the subjet. If all the tracks in a jet are within the 30 degree core then the subjet formed will have the same axis as the jet.

(3) subjet is used. However more than one jet was formed from the core tracks and the one with the largest momentum was chosen as the subjet.

(4) A secondary vertex was found that passes the cuts. The vector from primary interaction point to secondary vertex is used as the B hadron flight direction. Agreement between data and MC is very good.

4.4.7 Smearing the Monte Carlo
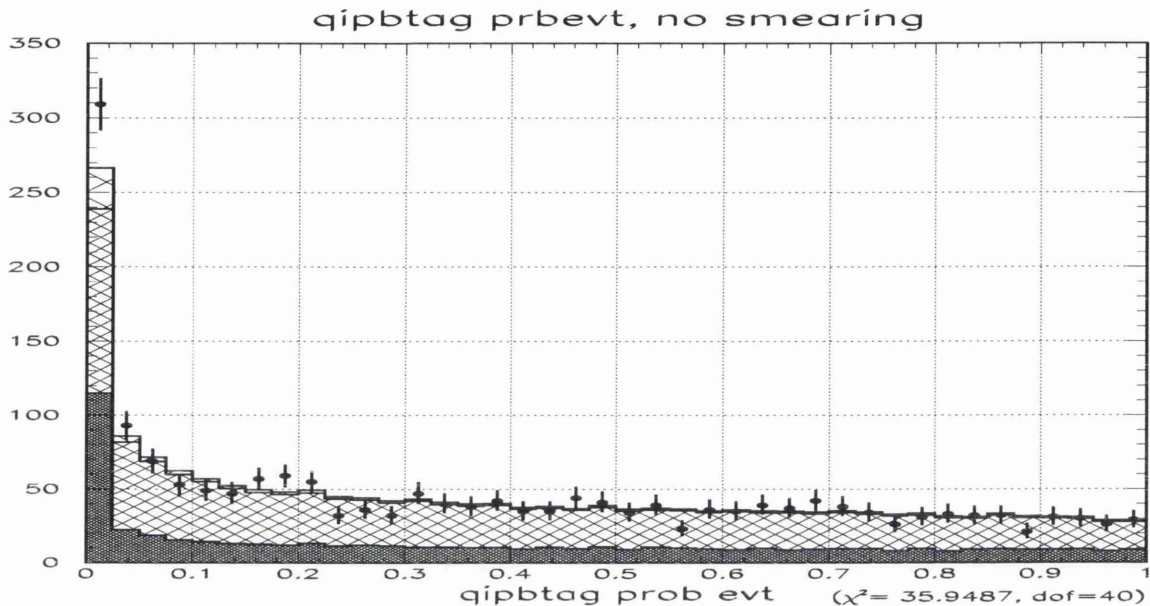
Figure 4.15:   The overall distribution of event b taggs, data recorded at 188.6 GeV data. The solid histogram is the MC prediction broken down by process, dark solid is qqg, heavy hatched WW and light hatched ZZ pairs.

In the 188.6 GeV data an excess of candidates in the four jet analysis were observed. The number of expected events was determined from MC studies which indicated that 19 events from background processes should be expected in a sample the same size as the measured data set. However 25 candidates are observed. The possibility that the difference between the observation and expectation could be caused by a systematic uncertainty in the simulation of the b-tagging was examined.

The overall agreement of the b-tag is evaluated in Figure 4.15. In the plot values tending towards 0 indicate a b rich event. It can be seen that there is an excess of events in data at a very small b-tag value. Since this is where Higgs search analysis are designed to select b-like events it is important to check if a possible b-tag systematic could be responsible for the excess in the number of observed events.

An algorithm had previously been developed to improve the agreement between MC and data by smearing basic track parameters in the simulated events. This was tuned to obtain MC to data agreement in the calibration data set taken at the Z peak, 91.2 GeV. The Z peak data have the advantage of being independent from the high energy data and in addition is free from any expectation of a Higgs boson signal. The Z peak MC had the parameters describing the point of closest approach of the fitted track helixes to the interaction point smeared in such a way as to produce agreement in the overall b-tag. However this resulted in over smearing of the track parameters, and so the use of the smearing was purely of use as a systematic check.

When the smearing was applied to the high energy MC events the b-tag distribution in Figure 4.16 was obtained. It can be seen that the smearing made the b-like region agree between data and MC. When the expected background was worked out from the smeared MC an expected background of 20 events was found (to be compared to 25 events observed). In conclusion, b-tag systematic uncertainty alone could not be expected to account for the observed excess of events.
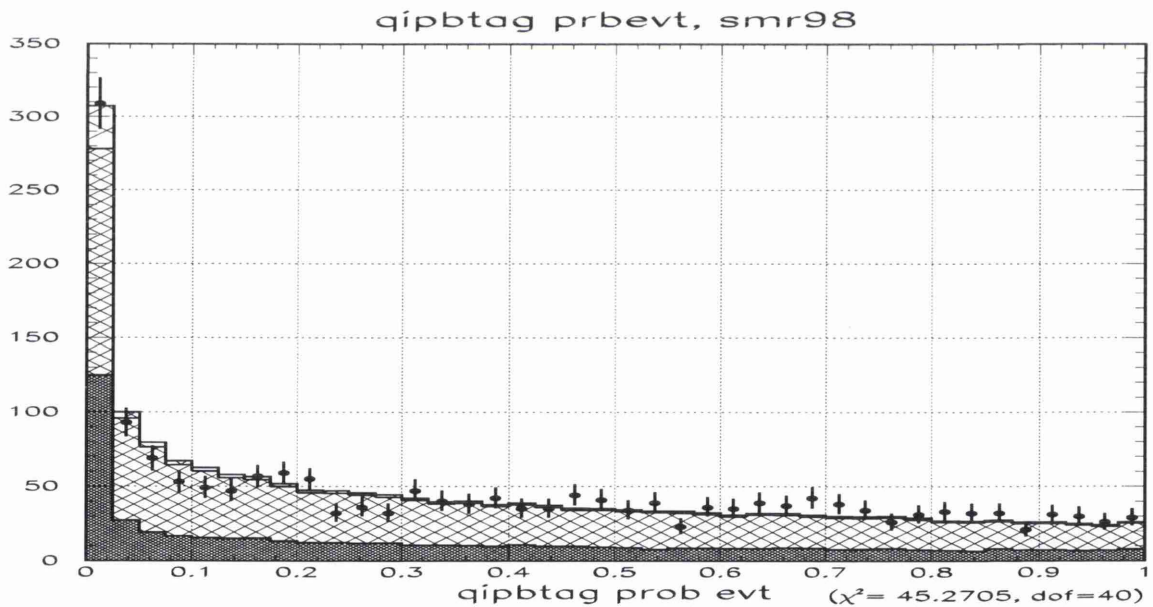
Figure 4.16: The overall distribution of event b taggs, data recorded at 188.6 GeV data. The solid histogram is the smeared MC prediction broken down by process, dark solid is qqg, heavy hatched WW and light hatched ZZ pairs.

Chapter 5

Interpreting results in the search for Higgs bosons

The purpose of the work presented in this thesis is to detect or rule out measurable production of Higgs bosons in the data events recorded. If no Higgs bosons can be found the data are used to set a lower limit on the Higgs boson mass. A Higgs boson with mass equal to or greater than the lower mass limit could exist and be compatible with the data recorded.

Conversely if many events that are compatible with Higgs boson production are observed it is no longer sensible to set a lower limit, but rather declare that an observation of the Higgs boson has been made. Since the beginning of LEP II each year of running has enabled the lower limit on the Higgs boson mass to be raised by a few GeV/c^2. Therefore the search is always looking for Higgs boson production where the Higgs boson mass is very near the limit of detectability. It is therefore most likely that if a Higgs boson is observed it will be observed in only a very small number of events. It is important to ascertain whether known background processes could have resulted in a similar observation by chance alone.

In this chapter a method is first described for assigning a quantifiable result to the data, describing how compatible they are with the Higgs boson production hypothesis. Since background and Higgs boson signal events may appear similar one also needs to know how typical the result is for background with and without signal. Two probabilities will be defined to make the distinction. One will measure the probability that

the observed events are due to background processes only. The other will similarly quantify how probable it is that the observed events are due to the sum of background and Higgs boson producing processes. Finally a description is given of how quantified results are used to decide if Higgs boson production has been observed, or otherwise set a lower limit on the Higgs boson mass. The inputs for the calculations motivate much of the work which is described in following chapters.

5.1 The estimator

The estimator is the name given to the quantity which represents the result of the analysis of all of the data. Generally the estimator depends upon the Higgs boson mass hypothesis. For a given Higgs boson mass, m_h, it is a number which represents how 'signal-like' the result is. The estimator is denoted by Q. The estimator used in the work presented here has the form:

$$Q(m_h) = \frac{\mathcal{L}_{s+b}(m_h)}{\mathcal{L}_b(m_h)} \tag{5.1}$$

where $\mathcal{L}_{s+b}$ and $\mathcal{L}_b$ are two likelihood functions. $Q(m_h)$ is called the likelihood ratio[25]. For a search result that is most compatible with background plus signal, $\mathcal{L}_{s+b}$ becomes large and $\mathcal{L}_b$ small. Therefore Q > 1 indicates a signal-like result and Q < 1 a background-like result. For historical reasons the quantity $-2\ln(Q)$ is most often used. Therefore for a given m_h:

- $-2\ln(Q) < 0$ indicates a result favouring the signal + background hypothesis.
- $-2\ln(Q) > 0$ indicates a result favouring a background-only hypothesis.

5.2 The likelihood functions

The likelihood functions in the likelihood ratio (equation 5.1) have the form:

$$\mathcal{L}_{\text{s+b}} = \prod_{i=1}^{N} \frac{\exp[-(s_i(m_{\text{h}}) + b_i)](s_i(m_{\text{h}}) + b_i)^{n_i}}{n_i!} \times \prod_{j=1}^{n_i} \frac{s_i(m_{\text{h}})S_i(m_{\text{h}}, m_{ij}) + b_i B_i(m_{ij})}{s_i(m_{\text{h}}) + b_i}$$

$$(5.2)$$

$$\mathcal{L}_{\text{b}} = \mathcal{L}_{\text{s+b}}\Big|_{\text{s}=0} \tag{5.3}$$

where N is the number of statistically independent contributions to the final result, each referred to as a search channel. s_i, b_i and n_i are the expected number of signal events, expected number of background events and the observed number of events in the ith channel respectively. The total expected signal and background are therefore $s = \sum_{i=1}^{N} s_i$ and $b = \sum_{i=1}^{N} b_i$. m_{ij} is a discriminating variable corresponding to observed event j in channel i. (For instance, this discriminating variable could be the reconstructed Higgs mass). S_i and B_i are probability density functions. $S_i(m_{\text{h}}, x)\,\mathrm{d}x$ ($B_i(x)\,\mathrm{d}x$) is the probability of observing a signal (background) event with a discriminating variable with a value between x and $x + \mathrm{d}x$.

The likelihood defined by equation 5.2 is seen to be made from two distinct components. The first is a Poisson term, the probability of observing n_i events from a distribution with mean $s_i + b_i$.

$$\mathcal{P} = \frac{\exp[-(s_i(m_{\text{h}}) + b_i)](s_i(m_{\text{h}}) + b_i)^{n_i}}{n_i!} \tag{5.4}$$

The second term is the probability density of obtaining a candidate with discriminating variable m_{ij}, from a sample with s_i signal and b_i background events expected to be present.

$$\rho(m_{ij}) = \frac{s_i(m_{\text{h}})S_i(m_{\text{h}}, m_{ij}) + b_i B_i(m_{ij})}{s_i(m_{\text{h}}) + b_i} \tag{5.5}$$

In this way it can be understood that the likelihoods are a measure of the favourability of the candidates to originate from a distribution of s signal events and b background events.

The likelihood ratio (estimator) may be written more simply as:

$$Q(m_{\mathrm{h}}) = \prod_{i=1}^{N} \mathrm{e}^{-\mathrm{s}_i} \prod_{j=1}^{n_i} \left[1 + \frac{\mathrm{s}_i \mathrm{S}_i(m_{\mathrm{h}}, m_{ij})}{\mathrm{b}_i \mathrm{B}_i(m_{ij})} \right] \tag{5.6}$$

and hence:

$$-2\ln(Q) = 2\mathrm{s} \; - \; 2 \sum_{i=1}^{N} \sum_{j=1}^{n_i} \ln \left[1 + \frac{\mathrm{s}_i \mathrm{S}_i(m_{\mathrm{h}}, m_{ij})}{\mathrm{b}_i \mathrm{B}_i(m_{ij})} \right] \tag{5.7}$$

5.3   Confidence in a hypothesis

The likelihood ratio gives a quantifiable measure of the compatibility of the observation with the presence of a Higgs boson signal with a hypothetical mass m_{h}. The observation may be classified as signal-like or background-like depending on the sign of $-2\ln(Q)$. However by itself the Estimator provides no measure of the confidence in the distinction between background only and background plus signal. For instance, with a small number of signal events expected it could be possible for the number of observed events to fluctuate upwards to more than the number expected. The estimator value found could be very compatible with the background + signal hypothesis, when in fact only background processes were contributing.

In order to obtain a measure of confidence, probability density functions of $-2\ln(Q)$ are required. Many simulated *experiments* with background-only or background + signal are made. (Here an experiment is taken to mean the collection of measurements from all N channels). The simulated experiments are called Toy Monte Carlo (Toy MC). Each Toy MC experiment is generated according to Poisson distributions and the expected numbers of signal and background in each channel. Each experiment also has a vector of discriminating variables generated according to the corresponding probability density functions. For each experiment $-2\ln(Q)$ is calculated. The distribution of $-2\ln(Q)$ found for all the Toy MC experiments with only background (background
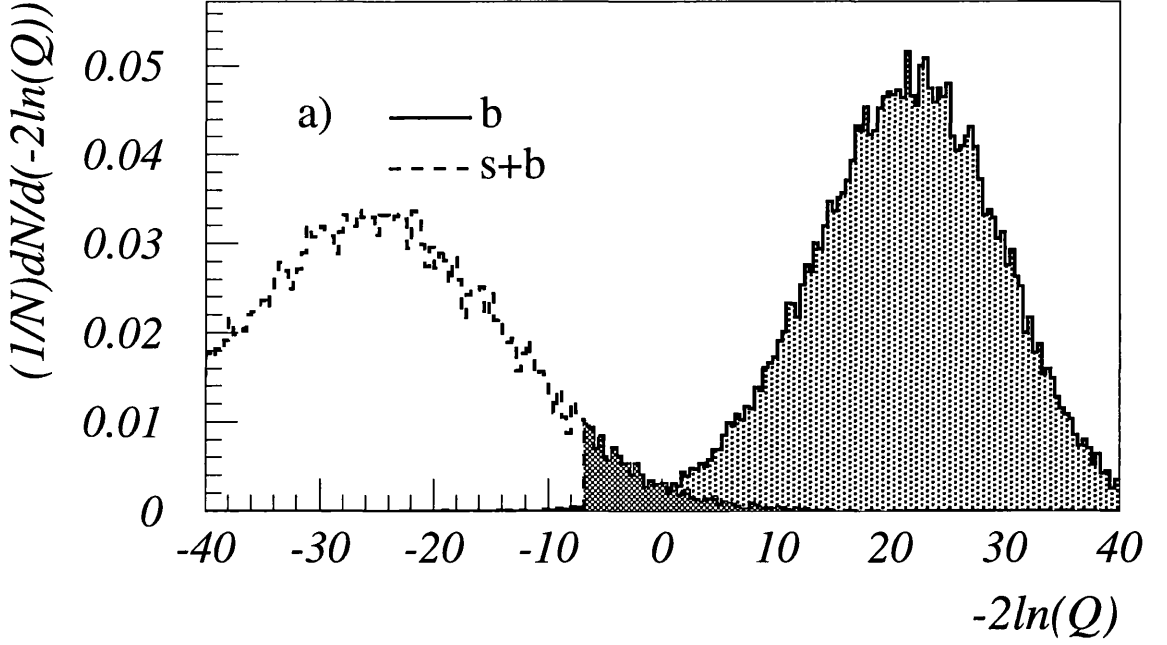
Figure 5.1: Distributions of $-2\ln(Q)$ obtained from many Toy MC experiments. The solid (dashed) distribution are those estimators obtained when the Toy MC experiments contain only background (background + signal) events. The two distributions describe the probability density functions ρ_b and ρ_{s+b} respectively. The example shown here is taken from [26].

and signal) present is used to define ρ_b (ρ_{s+b}). Figure 5.1 illustrates the results of the many Toy MC experiments, and the two probability density functions ρ_b and ρ_{s+b}.

Two confidence levels are then defined in the following way:

$$\mathrm{CL_b}(m_h) = \int_{x_0(m_h)}^{\infty} \rho_b(m_h, x) \; \mathrm{d}x \tag{5.8}$$

$$\mathrm{CL_{s+b}}(m_h) = \int_{x_0(m_h)}^{\infty} \rho_{s+b}(m_h, x) \; \mathrm{d}x \tag{5.9}$$

where $x_0(m_h) = -2\ln(Q)$ is the value obtained in the real experiment. It can be seen that $\mathrm{CL_b}$ is the fraction of times the estimator is expected to be more background-like than that observed when only background is present. Similarly $\mathrm{CL_{s+b}}$ is the fraction of times the estimator is expected to be more background-like than that observed when background and signal are present.

In order to measure the intrinsic performance of the search, two further quantities are also defined, $\langle \mathrm{CL_b} \rangle$ and $\langle \mathrm{CL_{s+b}} \rangle$.

$$\langle \mathrm{CL_b} \rangle = \overline{\mathrm{CL_b}} \;\Big|_{\text{background only}} \qquad (5.10)$$

$$\langle \mathrm{CL_{s+b}} \rangle = \overline{\mathrm{CL_{s+b}}} \;\Big|_{\text{background only}} \qquad (5.11)$$

$\langle \mathrm{CL_b} \rangle$ and $\langle \mathrm{CL_{s+b}} \rangle$ are defined to be the median value of $\mathrm{CL_b}$ and $\mathrm{CL_{s+b}}$ when x_0 is chosen according to ρ_b, the probability density of estimators when only background is present. As expected $\langle \mathrm{CL_b} \rangle = 0.5$.

5.4 Confidence in the background only hypothesis

The goal of the search is to detect or rule out measurable production of Higgs bosons in the recorded data sample. With $\mathrm{CL_b}$ the question may be answered. $\mathrm{CL_b}$ measures the confidence in the background-only hypothesis. Significant deviation away from the expected value of 0.5 indicates excess or deficit in data with respect to the expected background contribution. If a significant excess is seen $(1 - \mathrm{CL_b}) \to 0$, and a possible discovery may have been observed.

5.5 Setting a lower Higgs boson mass limit

In absence of significant deviation away from the background-only hypothesis the search should set a lower limit on the Higgs boson mass. In order to do this a measure of the confidence in the signal hypothesis is desired. $\mathrm{CL_{s+b}}$ is the confidence in the signal + background hypothesis, and an example easily demonstrates why this is not a useful quantity for setting a mass limit; If a very large Higgs boson mass hypothesis is considered such that $s(m_\mathrm{h}) \to 0$ then $\mathrm{CL_{s+b}} \simeq \mathrm{CL_b}$. If $\mathrm{CL_b}$ fluctuates to a low value and $\mathrm{CL_{s+b}}$ is used, an artificially high limit may be set.

In order to avoid this problem, the confidence level in the signal hypothesis has been estimated in two different ways. The two confidence levels are denoted by $\mathrm{CL_s}$ and
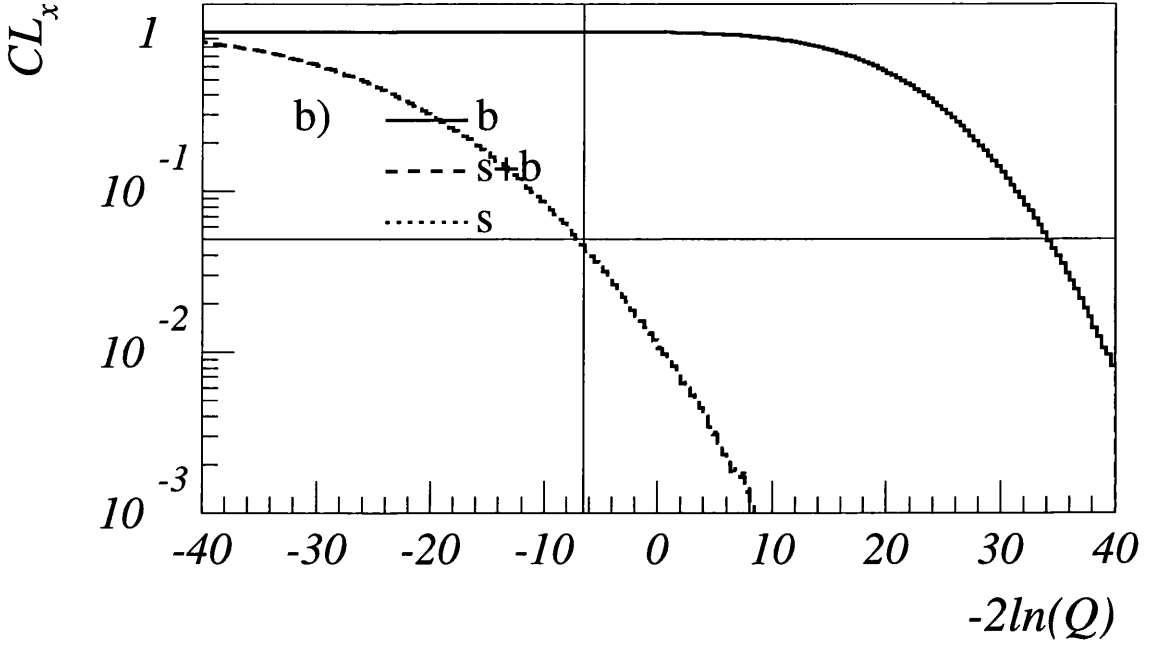
Figure 5.2: CL_b, CL_{s+b} and CL_s against $-2\ln(Q)$ for an example value of m_h. (In the plot CL_{s+b} and CL_s lie almost on top of each other). The example shown here is taken from [26].

CL_{SE} which are defined as:

$$CL_s = \frac{CL_{s+b}}{CL_b} \qquad (5.12)$$

$$CL_{SE} = CL_{s+b} + (1 - CL_b) \exp[-s] \qquad (5.13)$$

It can be seen that both CL_s and CL_{SE} are essentially CL_{s+b} normalised in some way by CL_b. CL_s shown in equation 5.12 is used by the **LEP** Working Group for Higgs boson searches. Consequently limits set with the combination of **LEP** data are found using using CL_s. However the **ALEPH** Collaboration uses CL_{SE}. CL_{SE} is also called the *signal estimator* and is described in [27]. The signal estimator method was found to perform better than CL_s when limit setting.

Figure 5.2 shows CL_b, CL_{s+b} and CL_s plotted against $-2\ln(Q)$. The ρ_b and ρ_{s+b} from which the confidence levels are derived are the same as in Figure 5.1. It can be seen that in this case $CL_s \simeq CL_{s+b}$, which is a consequence of the good separa-

tion of ρ_{s+b} and ρ_b.

A lower Higgs boson mass limit at 95% CL is set by finding the lowest m_h for which CL_{SE} (or CL_s) exceeds 5%.

Chapter 6

The hZ to four jets event selection

The ALEPH Collaboration adopted two parallel analyses for searching for hZ $\rightarrow$ four jets. One is based on an artificial neural network and the other analysis is based on a series of cuts on event variables.

The aim of the four-jet event selection is to maximise the selection efficiency for a Higgs boson signal whilst minimising the selection of background processes. The analysis used to select candidate events for hZ $\rightarrow$ b$\bar{\text{b}}$q$\bar{\text{q}}$ using cuts is described here[48]. The analysis to select the four-jet events from the MSSM process hA $\rightarrow$ b$\bar{\text{b}}$b$\bar{\text{b}}$ is not considered here, but a description may be found in section 7.4.

In addition to the event selection the four jet analysis also performs a second task. The selection calculates a measure of the Higgs boson mass for each candidate event. The Higgs mass found on an event by event basis is called the reconstructed Higgs boson mass and is denoted by m_{reco}. m_{reco} is used as the single discriminating variable of selected four-jet events. (See section 5.2 for an explanation of the use of discriminating variables).

Real data used in this chapter are from the database collected by the ALEPH Collaboration in 1999 at $\sqrt{s}$ =192,196,200 and 202 GeV. Unless otherwise stated the Higgs boson mass used in simulated signal examples is $m_{\text{h}} = 105$ GeV/c^2 at $\sqrt{s} = 201.6$ GeV.

6.1   Preselection

The first part of the selection is called the preselection and is designed to select events with characteristics common to multi-jet events. The most identifiable characteristics

of multi-jet events are a large number of energetic charged particles. An event with a large number of charged particles is called a multi-hadronic event. The preselection is composed of several cuts, the first of which are aimed at the selection of multi-hadronic events. Specifically, multi-hadronic events are selected by imposing a cut on the number and total energy of good charged tracks. A good charged track has a specific meaning. Firstly it means that the track has been reconstructed by using at least 4 TPC coordinates and that it has $|\cos(\theta)| < 0.95$. Secondly it means that the charged track is consistent with originating from the interaction point, enforced by requiring:

$$|\text{D0}| < 2 \text{ cm} \tag{6.1}$$

$$|\text{Z0}| < 10 \text{ cm} \tag{6.2}$$

where D0 is the distance of closest approach of a track to the interaction point in the $r - \phi$ projection, and Z0 is the distance of closest approach in the z direction.

To be selected as a multi-hadronic event the event must contain at least 8 good charged tracks, the total measured energy of which must be at least $0.1\sqrt{s}$. All of the simulated $\text{hZ} \rightarrow \text{b}\bar{\text{b}}\text{q}\bar{\text{q}}$ Higgs boson events satisfy the cuts for multi-hadronic events.

After the multi-hadronic selection four jets are made from the particles in the event using the DURHAM[45] jet clustering algorithm. The y_{34} transition value is then taken as a measure of how well the event fits the four jet topology. A larger y_{34} value indicates that the four jets found are more energetic or isolated (see equation 4.2). Therefore an event with a large y_{34} value may be said to be more four-jet like. In figure 6.1 the distribution of y_{34} values for data and for a simulated Higgs boson signal are compared. A cut requiring $y_{34} > 0.004$ retains 95.8% of the four-jet Higgs boson events.

Events passing the preselection described until now may have a good four jet topology. However the sample also includes a large number of radiative returns and two photon events.

A multi-hadronic radiative return to the Z pole corresponds to the reaction $\text{e}^+\text{e}^- \rightarrow \text{Z}(\gamma) \rightarrow \text{q}\bar{\text{q}}(\gamma)$. A radiative event is one in which a photon of around 70 GeV is emitted from the initial state leaving an e^+e^- system with centre of mass energy of $\sim m_Z$. The e^+e^- system subsequently annihilates mostly to two fermions via the Z boson. The
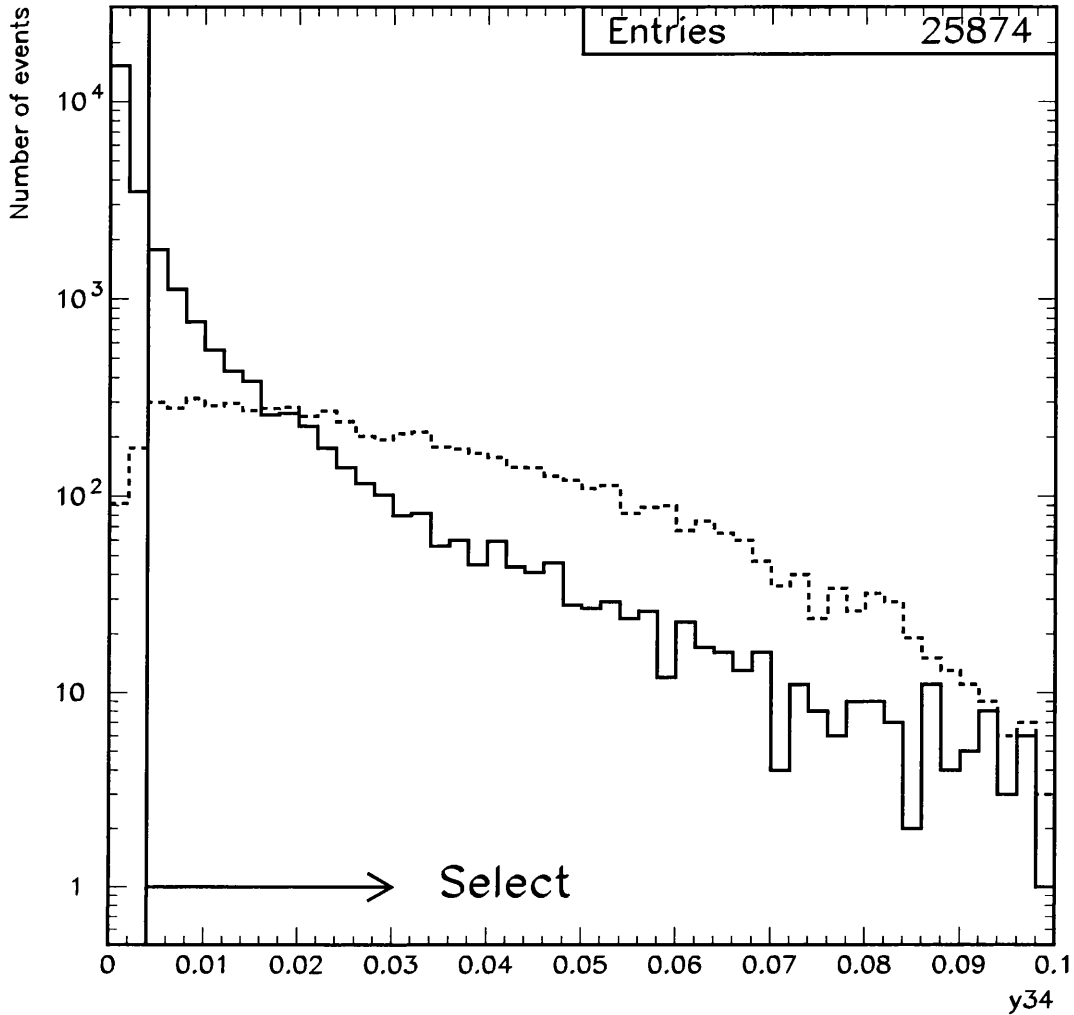
Figure 6.1: The distribution of y_{34} in the data (solid) and simulated Higgs boson signal (dashed) after the multi-hadronic selection. The normalisation of the plot is arbitrary. The vertical line indicates the y_{34} value of 0.004.

initial state photon may or may not be observed within the detector but in any case leaves a characteristic signature.

The two photon $(\gamma\gamma)$ events are the name given to the reaction $e^+e^- \rightarrow e^+e^-q\bar{q}$. They typically have a low visible mass.

To remove the radiative return and two photon events further cuts are made. $\overrightarrow{P_{vis}}$ is defined as the sum of the momentum of all particles measured in the event, E_{vis} is defined as the sum of the energy of all the particles measured in the event. It follows that the visible mass, M_{vis} is $M_{vis} = \sqrt{E_{vis}^2 - |\overrightarrow{P_{vis}}|^2}$ and p_z is the z component of $\overrightarrow{P_{vis}}$.

100

The first of the anti-radiative and anti-two photon cuts ensures that M_{vis} is larger than 90 GeV/c^2 and additionally that p_z is reasonably close to zero. It is required that:

$$|p_z| < 1.5(M_{vis} - 90) \qquad (6.3)$$

Applying inequality 6.3 removes events with visible mass less than 90 GeV/c^2 and events with larger visible mass but which are unbalanced. The hypothesis is that a radiative photon has escaped detection at small θ along the beam pipe. Figure 6.2 shows the ($|p_z|$, M_{vis}) plane together with the projection onto the M_{vis} axis before and after inequality 6.3 is applied. Also labelled are regions of interest on the M_{vis} plot. The two-photon, radiative returns and full energy annihilation events are peaked at distinctly different values of M_{vis}.
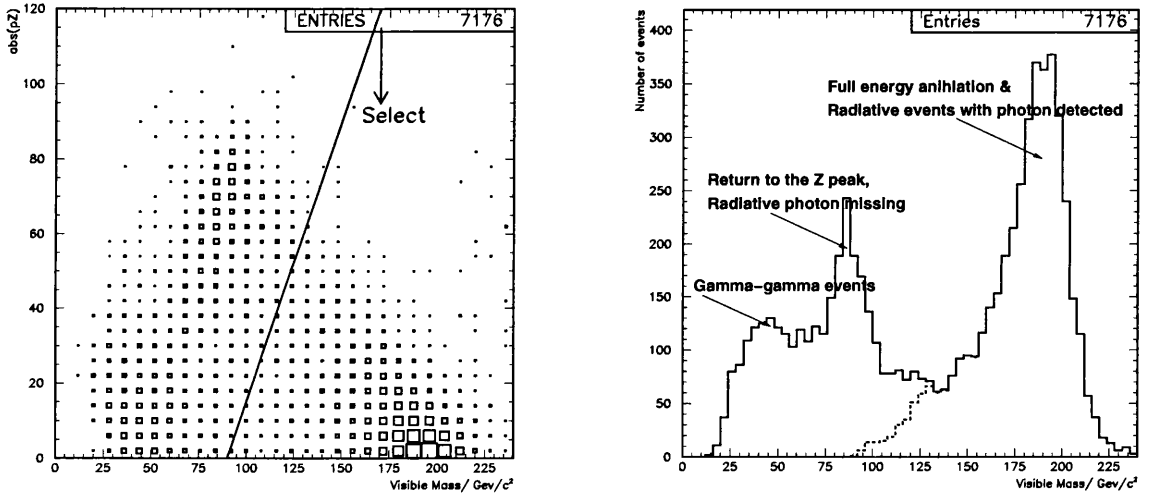
Figure 6.2: Left hand side: the distribution of $|p_z|$ against M_{vis} in the data. The diagonal line indicates the value of ($|p_z|$, M_{vis}) cut. Right hand side: the distribution of M_{vis} from events before (solid) and after (dashed) the ($|p_z|$, M_{vis}) cut is applied.

To remove radiative return events where the initial state photon is measured inside the detector a search for photons is performed. An initial state photon may also may have converted in the detector material to give an e^+e^- pair, so the search also looks for electrons and positrons. The candidate tracks found by the search are called electromagnetic objects, and the energy of the objects is the electromagnetic energy. The electromagnetic objects will have been clustered into some of the jets. The hypothesis

is that if there was a high energy photon the electromagnetic energy fraction of the jet into which it was clustered will be high.

To identify events likely to have contained a radiated photon the following procedure is adopted: for each jet the largest fraction of electromagnetic energy found within a $1°$ cone of any particle in the jet is calculated. x_γ is then the largest of the four fractions in the event. Radiative events are then rejected by requiring that:

$$x_\gamma < 0.8 \qquad (6.4)$$

Figure 6.3 shows a plot of x_γ and the distribution of M_{vis} before and after the inequality 6.4 is required. The calculation of M_{vis} for the radiative return events removed included the initial state photon, and so they have a similar distribution of M_{vis} as events with no radiation in the initial state. Indeed it can be seen that as expected the shape of the M_{vis} distribution is largely unchanged by the x_γ requirement.
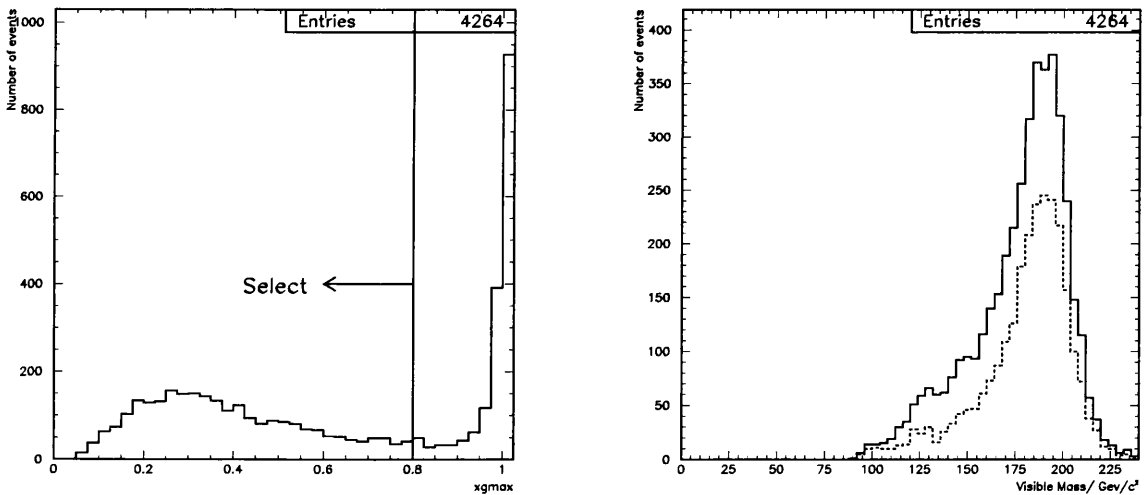
Figure 6.3:   Left hand side: the distribution of x_γ in the data. The vertical line indicates the cut. Right hand side: the distribution of M_{vis} from events before (solid) and after (dashed) applying the cut on x_γ.

Each jet is required to contain at least one charged track. Figure 6.4 shows the relative data and a signal rate for the minimum number of charged tracks in any jet.
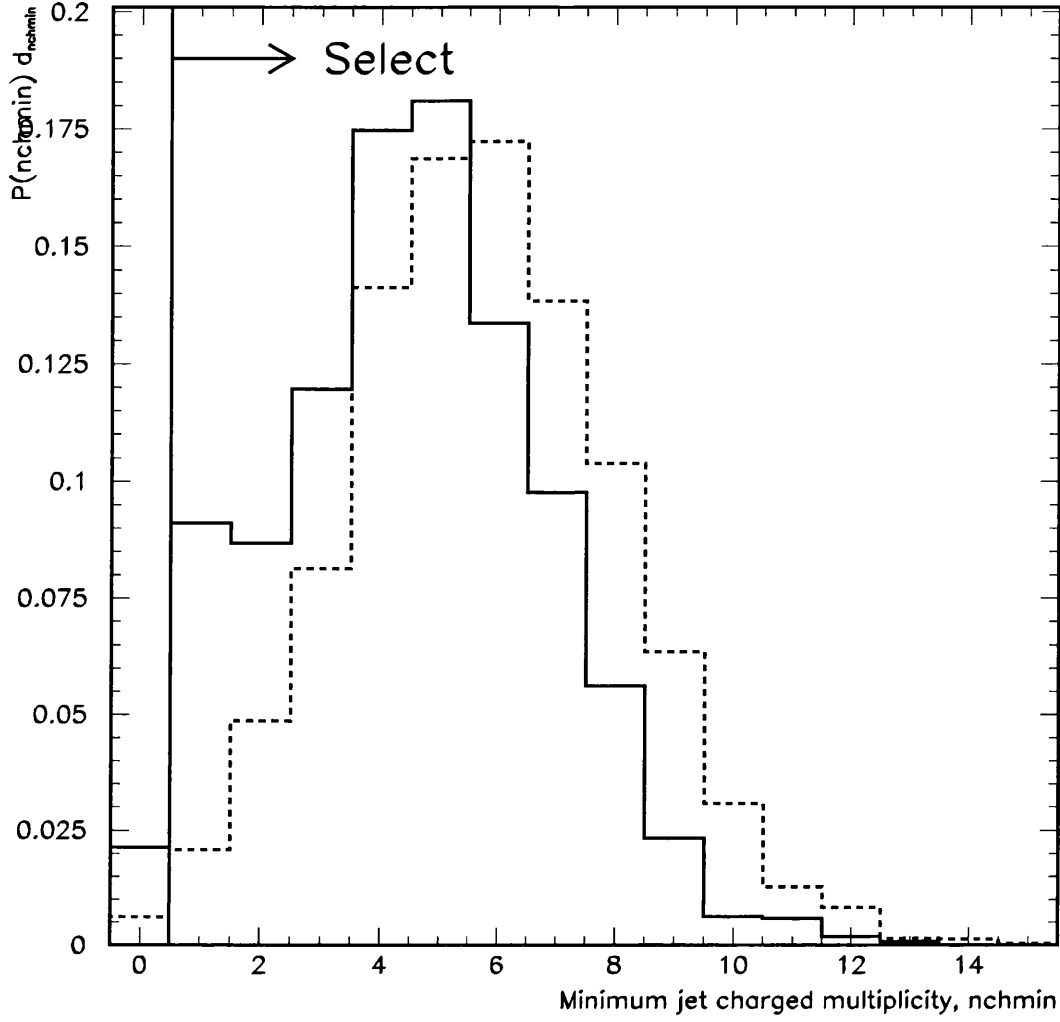
Figure 6.4: The minimum jet charged multiplicity in data (solid) and simulated Higgs boson events (dashed). The plots are normalised to unit area.

6.2 Event selection

The criteria described up to this point constitute the four-jet preselection. The sample of events retained by the selection will contain many four-jet like topologies arising from four-fermion reactions:

$$e^+e^- \rightarrow WW, ZZ \rightarrow \text{four jets} \qquad (6.5)$$

as well as the so-called QCD background:

$$e^+e^- \rightarrow q\bar{q}g \rightarrow \text{four jets} \qquad (6.6)$$

103

The event selection cuts are designed to reduce these backgrounds.

The two fermion final state $q\bar{q}g$ is where a gluon is radiated from a quark in the final state. Events from the $q\bar{q}g$ process frequently have the topology of one jet recoiling against three others. Conversely the hZ signal is typically planar. To make use of the distinctive topology of the unwanted $q\bar{q}g$ events the quantity Θ is considered, where Θ is the sum of the four smallest jet-jet angles. The quantity Θ is plotted in figure 6.5.
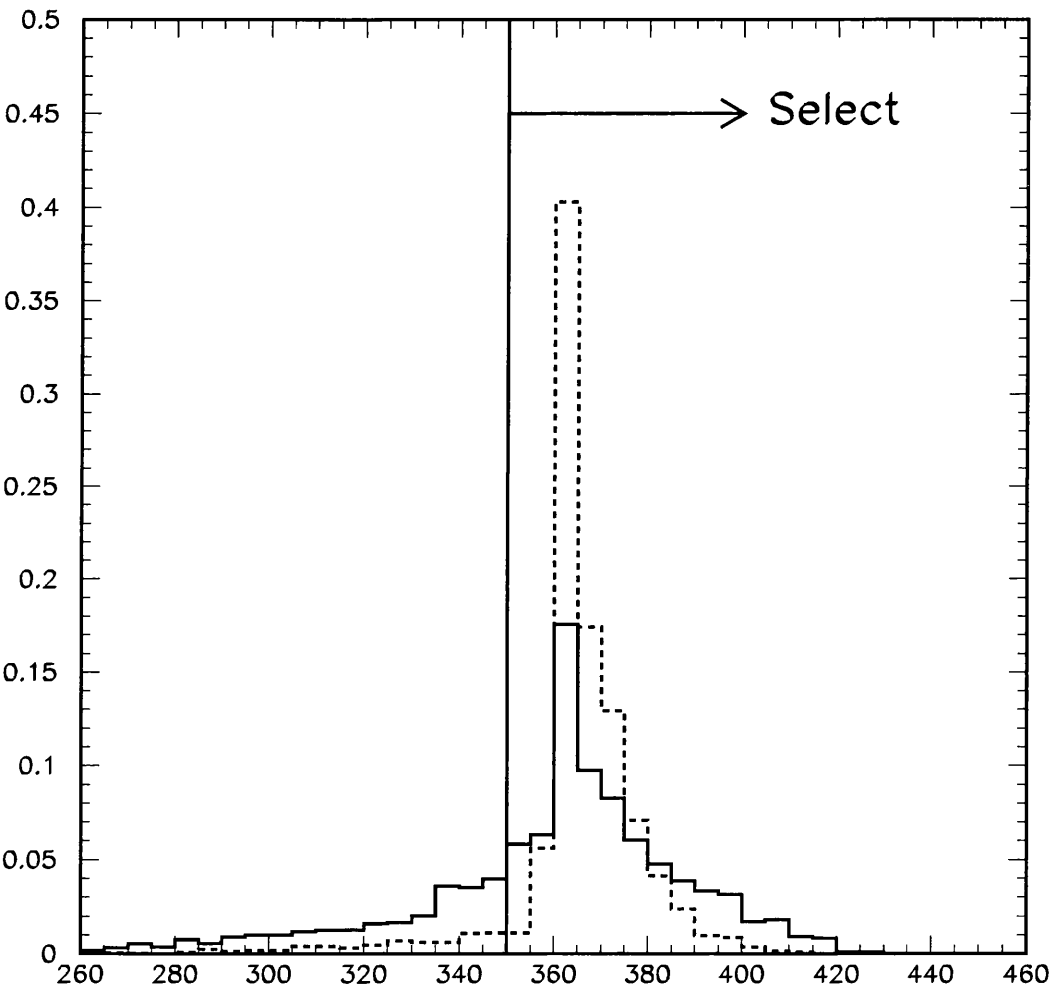
Figure 6.5:   Distribution of the Θ variable for data (solid) and simulated Higgs boson signal (dashed). Both histograms are normalised to unit area.

$$\Theta > 350° \tag{6.7}$$

The inequality 6.7 is required and has the effect of rejecting jets in the configuration depicted in figure 6.6. An example of a real data event with a Θ value of 309 is shown in
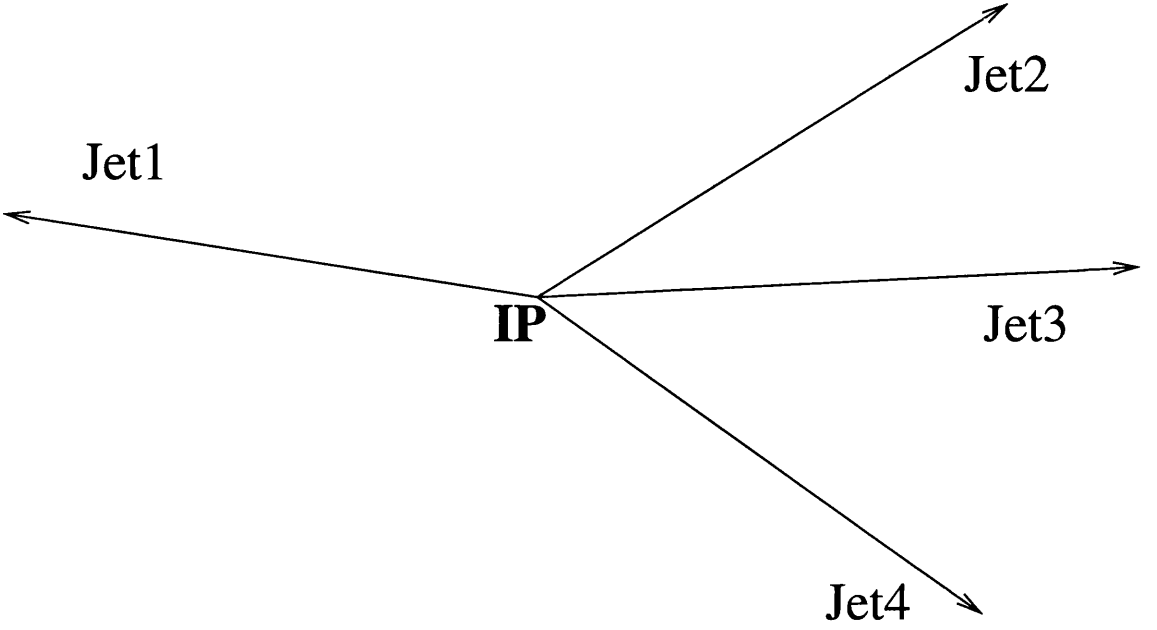
Figure 6.6: Figurative diagram showing typical $q\bar{q}g$ like topology, to be rejected with a cut on Θ.

figure 6.7. The event shown was recorded at $\sqrt{s} = 201.6$ GeV. The event has a visible mass of 176 GeV/c^2 but a Θ value of 309°, far below the requirement of 350°. The hypothesis is that the event originates when two gluons are radiated from quarks in the final state. Possible reactions include: $e^+e^- \rightarrow Z^* \rightarrow q\bar{q}gg/q\bar{q}q\bar{q}$, i.e., two quark decay of the Z^* with two gluons radiated in the final state or one gluon radiated followed by $g \rightarrow q\bar{q}$, which is called gluon splitting.

The region of most interest for the Standard Model Higgs search is from the kinematic threshold $m_h \sim \sqrt{s} - m_Z$ to about 10 GeV/c^2 below. Masses below this range are excluded by previous searches. Due to the proximity of the Higgs boson mass to threshold the decay products of each boson in $e^+e^- \rightarrow hZ$, are expected be produced approximately back-to-back in the laboratory frame. A distinct topology of two pairs of near back-to-back jets is therefore expected. The variable γ is defined to identify a back-to-back topology. γ is defined as:

$$\gamma = \min(\cos\theta_{ij} + \cos\theta_{kl}) \tag{6.8}$$

where the indexes i, j, k, l represent each of the four jets in turn. γ is the sum of the two cosines of the angle between each pair of jets. Of the three possible ways of choosing
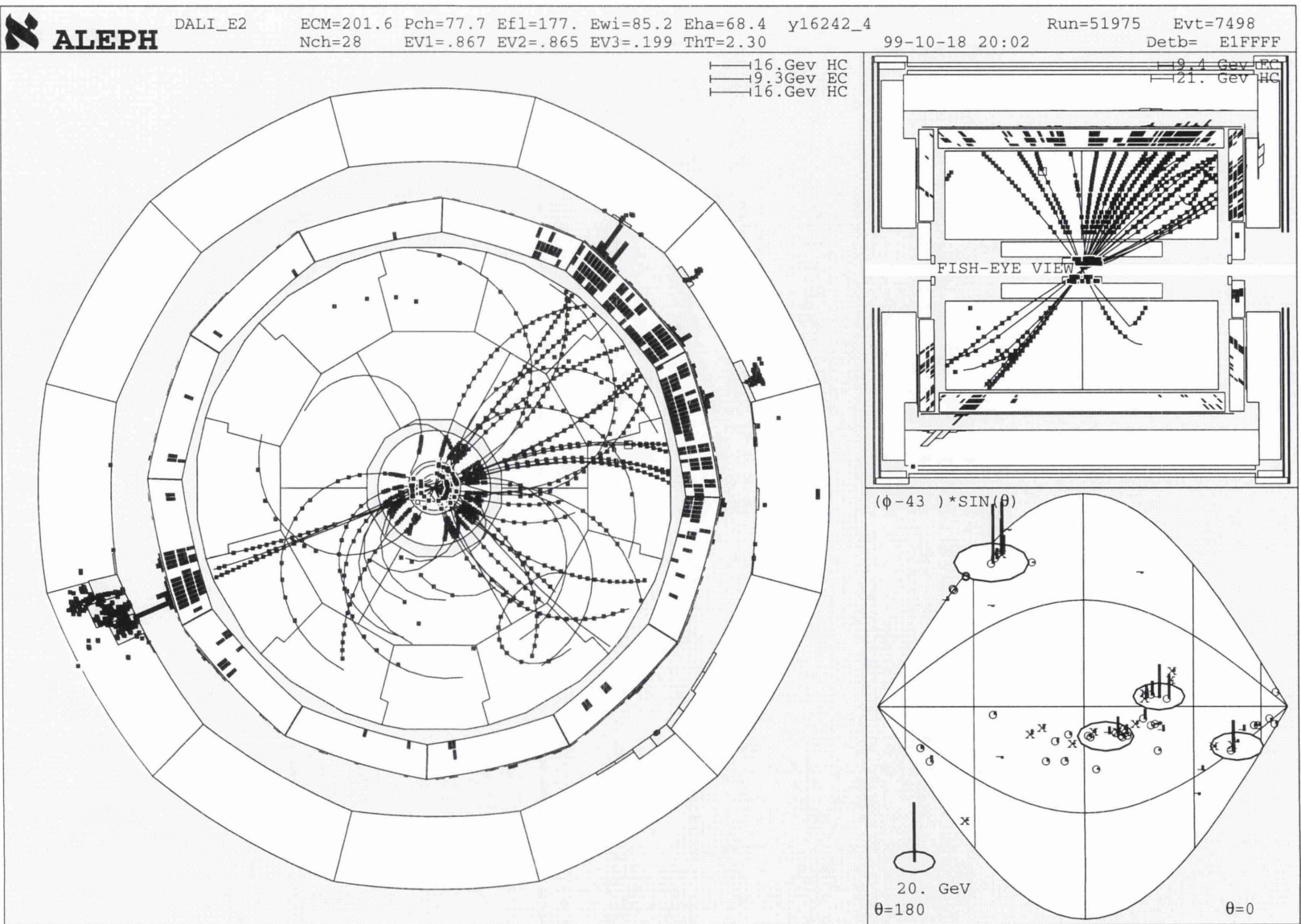
Figure 6.7: Event display of a real data event, exemplifying the background-like topology sketched in fig 6.6. Θ for this event is found to be 309°.

a pair of jets from the four in the event, the one which gives the smallest value of the cosine sum is taken. For two pairs of back-to-back jets γ tends to -2. In figure 6.8 is shown the distribution of γ in data and two simulated Higgs boson samples. The Higgs boson mass is different in the two samples, $m_h = 85\ \text{GeV}/c^2$ and $m_h = 105\ \text{GeV}/c^2$. Both of the Higgs boson samples are simulated at $\sqrt{s} = 201.6\ \text{GeV}$, therefore the kinematic limit for Higgs boson production is $110.4\ \text{GeV}/c^2$. For the sample with $m_h = 85\ \text{GeV}/c^2$, the distribution of γ is seen to peak a away from -2. While for the sample with $m_h = 105\ \text{GeV}/c^2$, γ is much more strongly peaked towards -2 as is expected from the proximity to the kinematic threshold.

Due to the strong dependence of the γ variable on the Higgs boson mass the cut requirement is not chosen as the optimum value for a Higgs boson mass very close to threshold. However, it is important to retain efficiency for the lower mass Higgs hypothesis as that mass range is important in the context of the MSSM. It is required that:

$$\gamma < -1.3 \tag{6.9}$$

Inequality 6.9 ensures that some selection efficiency is retained for lighter Higgs bosons. Figure 6.9 shows a real data event recorded at $\sqrt{s} = 201.6\ \text{GeV}$. The event has a visible mass of $183\ \text{GeV}/c^2$ and a γ value of -0.76, above the cut value of -1.3 which is imposed. In figure 6.9 there is an arrangement of jets that gives two dijet invariant masses of $78.4\ \text{GeV}/c^2$ and $82.89\ \text{GeV}/c^2$. The largest jet b-tag is 0.09, which indicates that none of the jets are likely to be b-jets. Consequently the most likely hypothesis is that the event is $e^+e^- \rightarrow W^+W^- \rightarrow q\bar{q}q\bar{q}$.

6.2.1 Two selection branches

The event selection is divided into a series of cuts designed to select $hZ \rightarrow b\bar{b}q\bar{q}$ (two b), and $hZ \rightarrow b\bar{b}b\bar{b}$ (four b) signal events. The two sets of cuts are parallel to each other and so form two branches. Events that pass at least one of these branches are selected. The scheme is shown in the form of a flow diagram in figure 6.10.
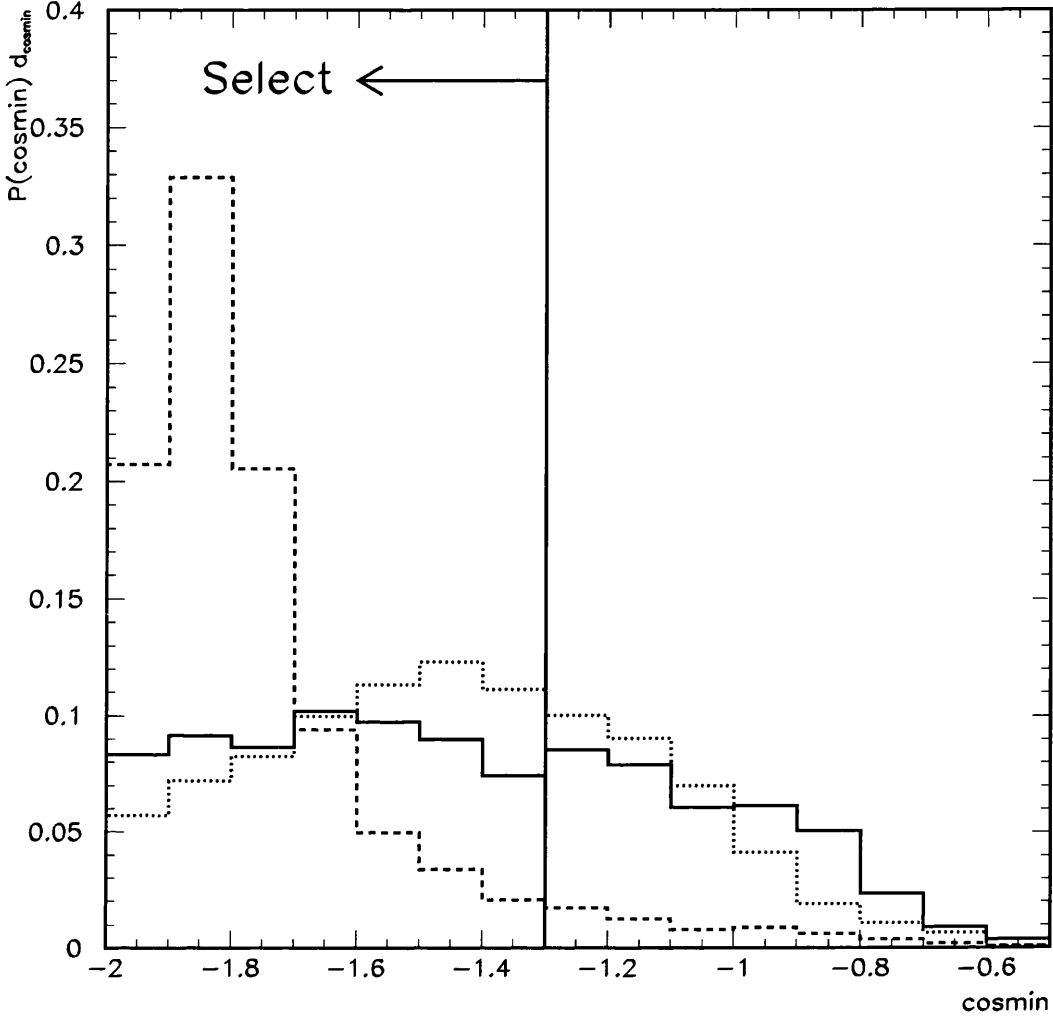
Figure 6.8: The distribution of the γ variable in data (solid) and two simulated Higgs boson samples. The dotted plot is that obtained from a $m_h = 85$ GeV/c^2 Higgs boson sample, while the dashed is from a sample in which $m_h = 105$ GeV/c^2.

6.2.2 The two b branch

Five cuts form the $b\bar{b}q\bar{q}$ branch. Firstly the y_{34} requirement for the event is tightened so that:

$$y_{34} > 0.008 \tag{6.10}$$

The tighter y_{34} cut is imposed to ensure that the four jets are very well isolated. The four remaining cuts of the two b branch use variables which depend upon the *pairing choice*. The pairing choice refers to the degree of freedom available by defining
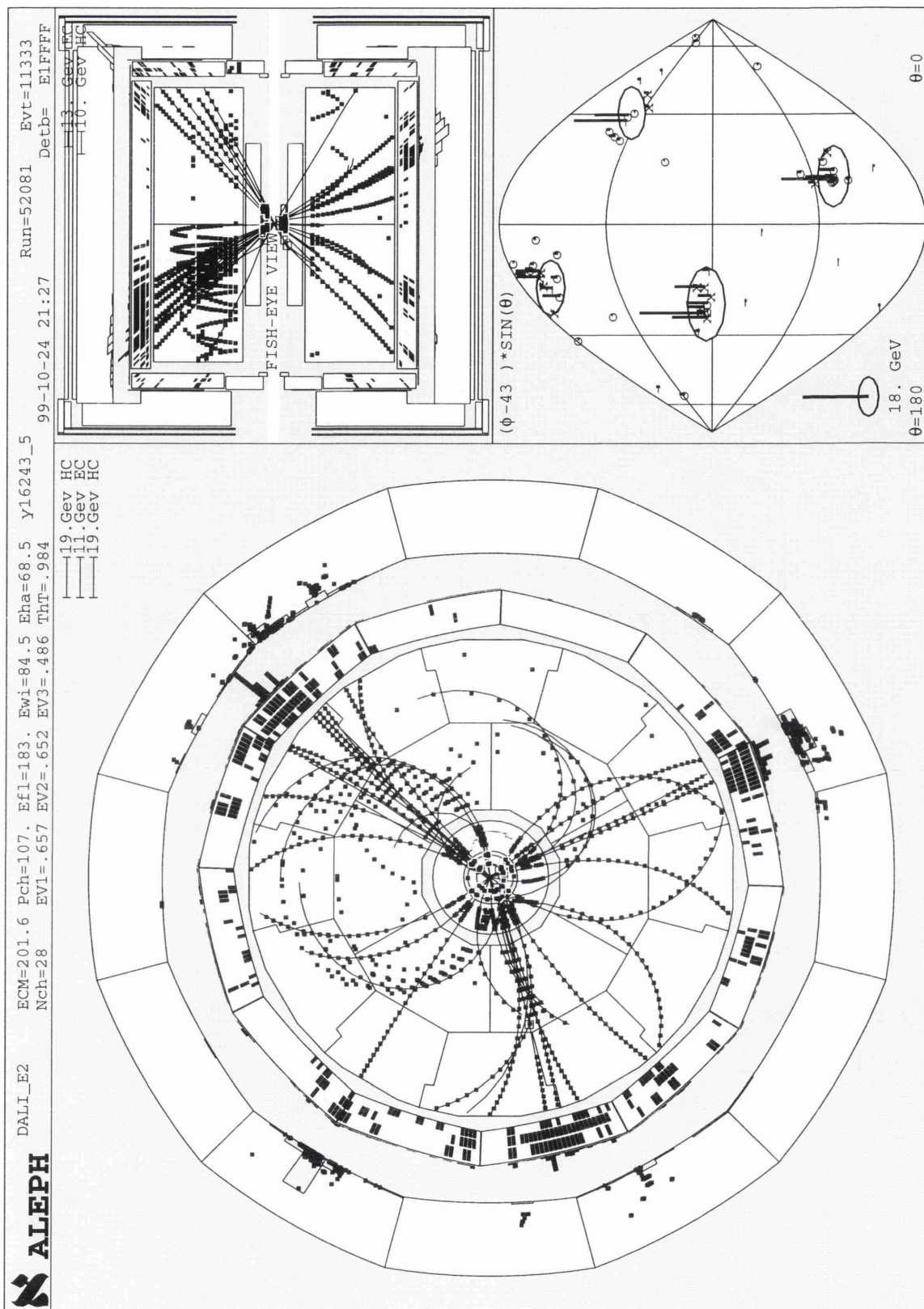
Figure 6.9: Event display of a real data event. γ for this event was found to be -0.76.

which two jets originated from the (assumed) Higgs boson decay and consequently
which two originated from the associated Z boson decay. In each event there are three

109

EVENTS

Four jet preselection

Selection

Selection with:
Θ, γ

Two b selection

Four b selection

SELECTED EVENTS
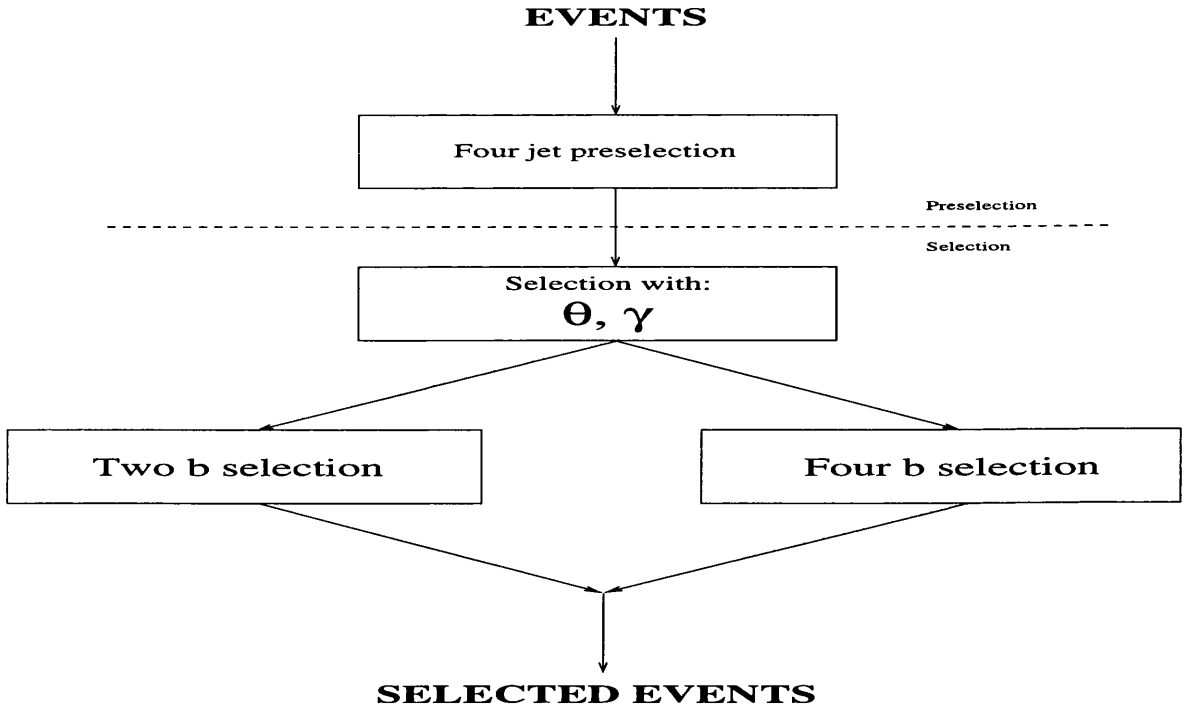
Figure 6.10: Schematic depiction of the two branch structure in the four jets selection.

ways of choosing two pairs of jets. One of the pair must be assigned to either the Higgs boson or Z boson, the other pair is then defined as originating from the other boson. Therefore there are six pairing configurations available for each event. Pairing-dependent variables may take different values for each of the six pairing choices.

The next two selection cuts are made on the measured value of the mass of the Higgs and Z bosons. The mass of each boson is taken as the fitted mass of the pair of jets associated to it, ie. the dijet mass. In order to improve the mass resolution the measured values of 4-momentum of the jets are replaced with values obtained by performing a 4C fit. The four fit constraints are that of energy and 3 momentum conservation. The constraints are imposed by varying the measured energy and 3 momentum of the jets with regard to their experimental uncertainty.

By convention the pair of jets associated to the Z boson are labelled 1,2 and those associated with the Higgs boson are labelled 3,4. Hence m_{12} and m_{34} are, respectively the invariant mass of the Z and Higgs bosons after the 4C fit. The distribution of m_{12} and m_{34} in data events is shown in figure 6.11. All six combinations per event are included in the figure and hence the distribution is identical for both m_{12} and m_{34}.
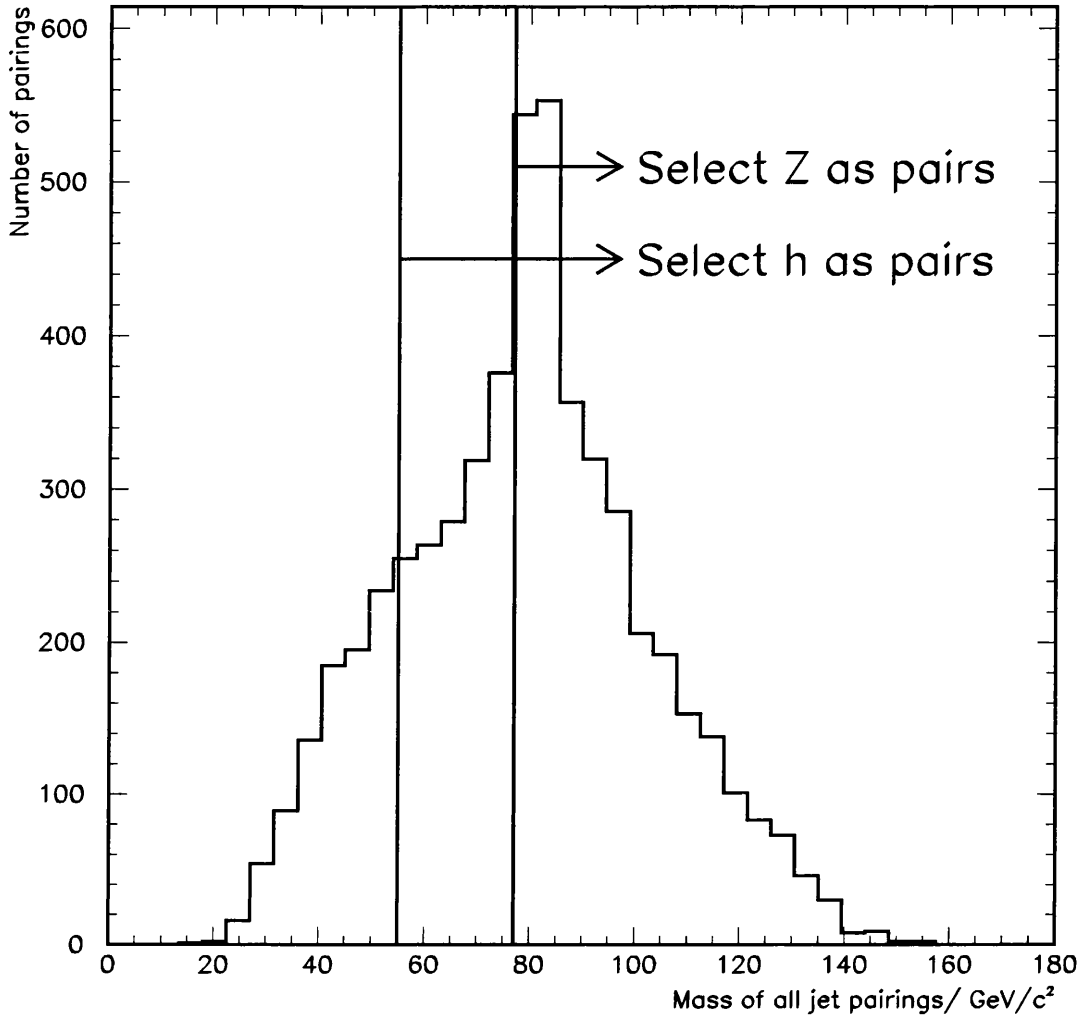
Figure 6.11: Mass plot showing the distribution of the dijet invariant mass of all pairing choices per event.

The following mass cuts are imposed:

$$m_{12} > 77 \text{ GeV}/c^2 \qquad (6.11)$$

$$m_{34} > 55 \text{ GeV}/c^2 \qquad (6.12)$$

The mass cuts 6.11 and 6.12 are motivated by the measured mass of the Z boson and the lower mass bound for the Higgs boson that was set at **LEP I**. The position of the two cuts are indicated in figure 6.11. After the cuts are imposed the mass distributions for m_{12} and m_{34} are shown in figure 6.12. Now only the pairing choices in each event for which both the mass cuts 6.11 and 6.12 are satisfied are included. Therefore the

111

distributions of m_{12} and m_{34} are no longer identical.
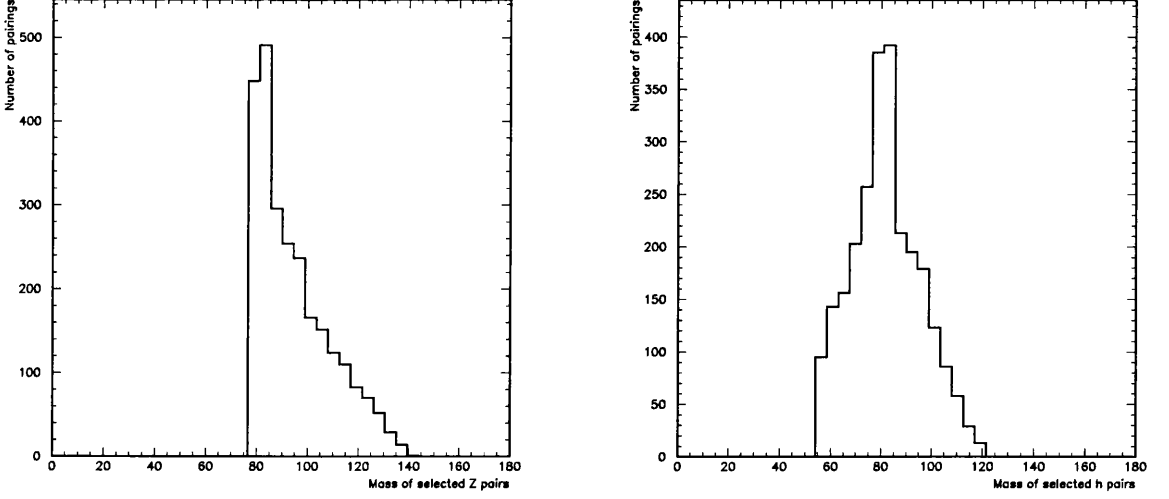
Figure 6.12: Left hand side: The distribution of m_{12}, the reconstructed mass of the Z boson. Right hand side: The distribution of m_{34}, the reconstructed mass of the Higgs boson.

The final two cuts of the two b branch are based upon the b-tag information of the two jets associated to the decay of the Higgs boson. Each jet is b-tagged using the six variable neural net b-tagger described in section 4.3.6. The neural net outputs are denoted by η_3,η_4, corresponding to the numbering scheme for the jets associated to the Higgs boson. Two cuts are then imposed:

$$\min(\eta_3, \eta_4) > 0.35 \tag{6.13}$$

$$(1 - \eta_3)(1 - \eta_4) < 4.8 \times 10^{-3} \tag{6.14}$$

The two b-tag distributions before the cuts 6.13 and 6.14, are shown in figure 6.13. Both data and signal are plotted, with the corresponding position of the cuts indicated. The signal events can be seen to clearly extend into the b-like regions in both plots.

6.2.3 The four b branch

In about 20% of the four-jet hZ decays the Z boson decays to b quarks, in addition to the Higgs boson. The resulting distinctive signature of four b jets in an event may be selected with high purity. The aim of the four b branch is to increase the overall
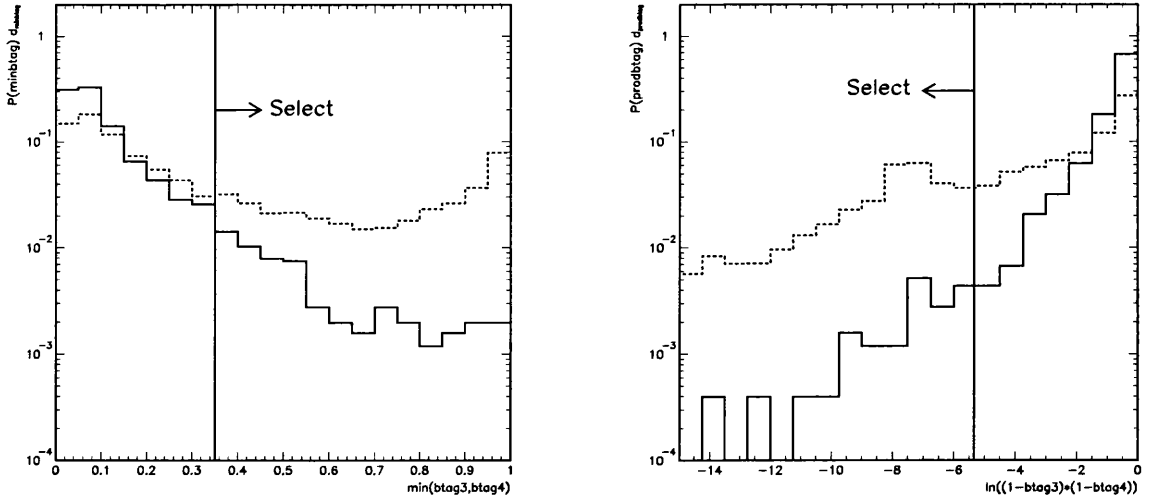
Figure 6.13: Left hand side: Distribution of $\min(\eta_3, \eta_4)$. Right hand side: Distribution of $\ln(1 - \eta_3)(1 - \eta_4)$. Solid histogram are data, the dotted is simulated Higgs boson signal.

signal selection efficiency by making use of a high purity selection designed for the four b final state.

There is only one cut in the four b branch:

$$9.5y_{34} + \sum_{i=1}^{4} \eta_i > 3.2 \qquad (6.15)$$

The left hand side of inequality 6.15 is a linear discriminant, and does not depend on the jet pairing choice. Events in which the four jets are found to be very b-like and for which y_{34} indicates that the jets are well separated are more likely to be selected. Figure 6.14 shows the cut in the plane of $(\sum_{i=1}^{4} \eta_i, 9.5y_{34})$ for both data and a Higgs boson signal.

In figure 6.14 the further to the right, and the further to the top an event falls the more four b-like it is. It can be clearly seen that a sizeable fraction of the signal events extend into the selected region. The events selected by cut 6.15 are identified as those containing four b jets. Little background contributes to the region. The main sources of background in the four b branch is from $q\bar{q}g$ with gluon splitting resulting in a four b final state, and an irreducible component from the process $e^+e^- \rightarrow ZZ \rightarrow b\bar{b}b\bar{b}$.
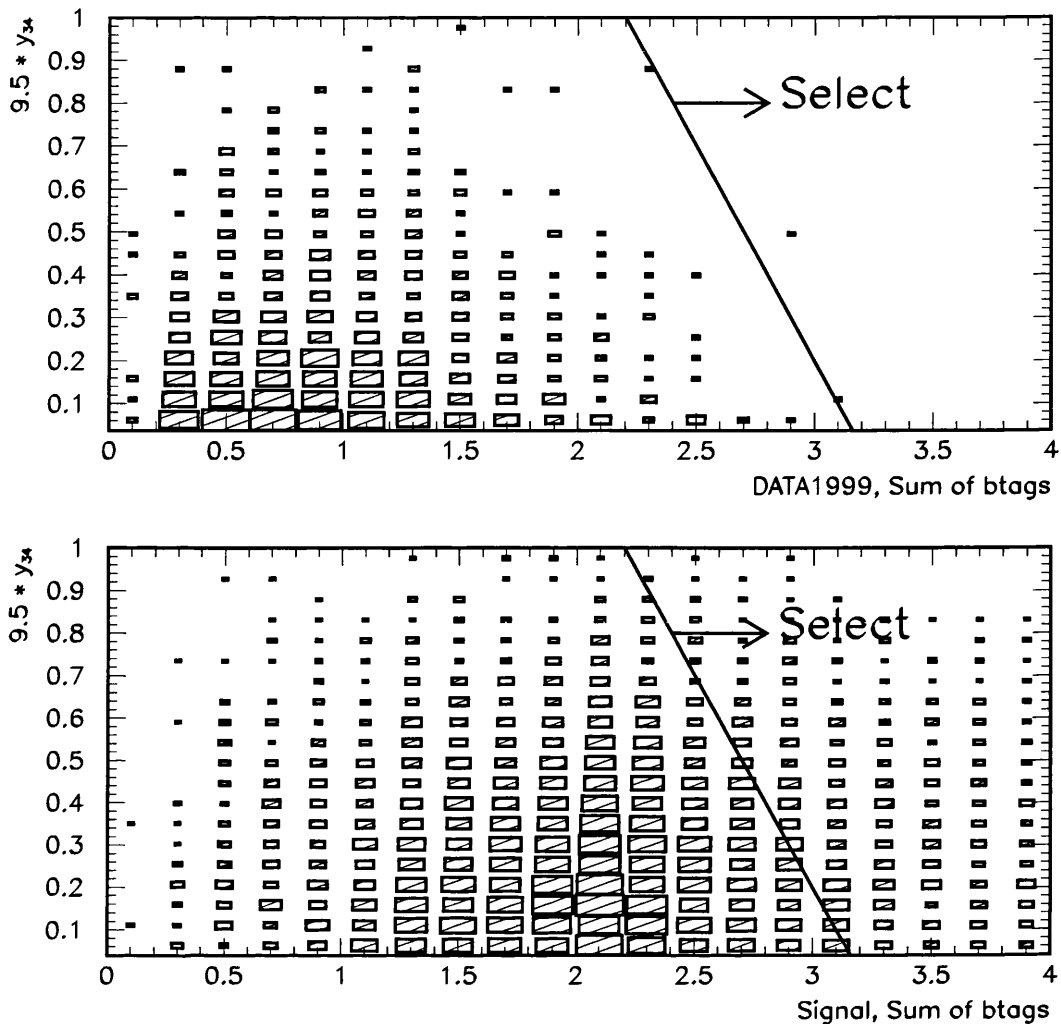
Figure 6.14: Plot showing the plane of the four b branch cut. Top: Data. Bottom: Simulated Higgs boson signal.

6.3 Pairing choice

An event is selected if at least one jet pairing choice passes all cuts. For events passing the four b branch all six pairings are selected as equation 6.15 does not depend on the pairing choice for the event. For events passing only the two b branch fewer than six combinations are likely to be chosen.

Table 6.1 indicates the number of data events passing cuts at three different points in the analysis as described so far. The points are: after all the cuts discussed previous to the two b branch described in section 6.2.2, the number after the two b branch and

after the four b branch described in 6.2.3. A more detailed count of events passing cuts at different points in the analysis can be found in table 6.5.

It can be seen that 1169 data events enter the two branches of the analysis. The total number of events selected by the analysis is the sum of the two exclusive counts plus the overlap, thus 20 events in total pass at least one of the branches and are therefore hZ candidates.

Entering branches	Selected two b only	Selected four b only	Pass Both
1169	19	0	1

Table 6.1: Number of events in the data that pass various different stages of the four jet selection.

For the 1168 data events not selected by the four b branch the number of pairings in each event as selected by the two b branch are shown in table 6.2.

Combinations selected	0	1	2	3	4	5	6
Number of events	1149	17	2	0	0	0	0

Table 6.2: Final number of events, not selected by the four b branch which have 0 to 6 combinations selected by the two b branch.

Once an event is selected a reconstructed Higgs boson mass is assigned to it. The reconstructed mass is used later, in addition to the total number of candidates selected, to help discriminate between the background-only and the signal + background hypotheses.

In order to compute the reconstructed Higgs boson mass for an event a jet pairing choice must be made. For events with only one selected pairing there is no choice, but otherwise a pairing method is used to choose one of the selected pairings. The reconstructed mass is defined as:

$$m_{reco} = m_{12} + m_{34} - 91.2 \text{ GeV}/c^2 \qquad (6.16)$$

where m_{12} is the dijet invariant mass assigned to the Z boson and m_{34} that assigned to the Higgs boson. Simulation has shown that by summing the reconstructed mass of the h and Z bosons and then subtracting the known mass of the Z boson a better

resolution on the Higgs boson mass is achieved. The reason for this is believed to be incorrect track assignment to jets in the jet clustering. To first order incorrect track assignment lowers the measured mass of one boson and increases the mass of the other by an equal amount, the effect is therefore reduced in the value of the sum of m_{12} and m_{34}.

Since the reconstructed mass involves only the sum of m_{12} and m_{34} their value may be swapped and the same reconstructed mass obtained. There are thus only 3 possible reconstructed masses for any event in which all 6 combinations are considered.

The method used to choose a jet pairing is to find the measured decay angles, θ_d, for the two bosons, assuming each valid combination in turn. θ_d is measured in the rest frame of the boson and is the angle between one decay jet and the momentum axis of the boson in the laboratory frame.

The configuration chosen is the one which yields $|\theta_d|$ for either boson which is least likely to be obtained from an incorrect pairing choice in signal or any combination in a background event[49]. Two probability density functions, fig 6.15, are used. One for the Z boson and one for the Higgs boson. The pairing yielding the highest probability value for either the Z or the Higgs boson is chosen.

6.4   Overlaps between four-jet and other final state selections

The hZ cuts selection, as described in this section is not used in isolation, but as one of four analyses to select common final states of hZ decay. The other three analyses are the leptonic final state, missing energy and final states with taus, see section 2.5.3 for some possible Higgs boson decay modes. It is important to eliminate selection overlaps in data. In order to do this the final candidate list is produced by running the analyses in a predetermined order, the four jets selection last. An event selected by a preceding selection may not be selected by a later one.

It was found that 1 of the 20 events selected from the data by the four-jet analysis was also selected by the $X\tau^+\tau^-$ analysis, see section 7.3. Since the four jet search is performed after all others in the ordered approach the candidate is not counted as a
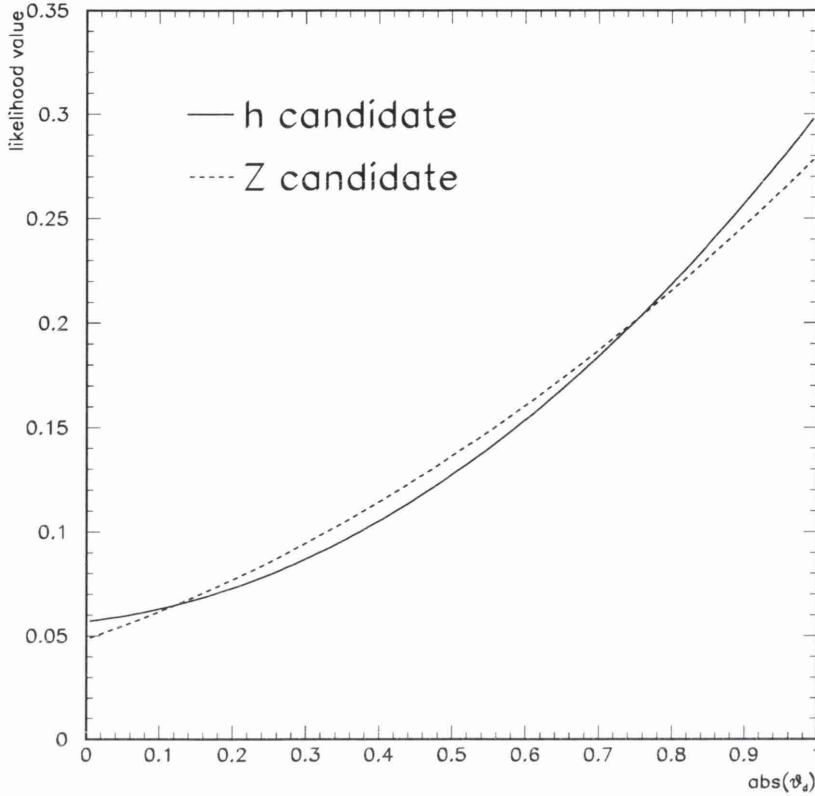
Figure 6.15: The probability density functions used in the pairing choice[49]. In selected events with more than one valid combination the combination which maximises the likelihood for either the Higgs or the Z boson is chosen.

four-jet event. Some details of the candidate are listed in table 6.3.

Lost to Finale State	ALEPH Run number	ALEPH event number
$X\tau^+\tau^-$	51422	3541

Table 6.3: Some details of the event selected by both the $X\tau\tau$ and the four-jet event selections.

The overlaps between final states are very small, and so when dealing with simulated events the overlaps are generally treated conservatively rather than rigorously. When performing Higgs boson signal selection studies only simulated signal events corresponding to the particular final state selection in question are used. In this way the signal efficiency may be slightly underestimated, as the selection may have a non zero selection efficiency for other signal final states.

In order to be conservative with the background estimates overlaps are generally

not considered, thus possibly slightly overestimating the expected background. One exception, which is treated rigorously is the overlap between the four-jet and $h\ell^+\ell^-$ event selections.

The hll analysis is designed to select the final state in which the Z boson decays to electrons or muons (see section 7.1). The four-jet analysis incorporates the hll selection and requires that an event is *not* selected also as an hll candidate.

The effect of rejecting hll candidates on the performance of the four-jet analysis is very small. In table 6.4 the impact on the four-jet analysis at an early stage of the selection is shown.

	Expected background	Observed
Without hll anti cut	2652.5	2526
With hll anti cut	2643.5	2515

Table 6.4: The impact of the anti-hll cut on the four-jet selection at preselection level. The effect is seen to be very small, a decrease in efficiency of 0.3% relative to that without the cut.

6.5 Comparison of data and Monte Carlo

It is important to verify that the simulated data used model the observed data well. To check the simulated data many data to Monte Carlo comparisons were made. Some of the distributions checked are shown in figures 6.19 to 6.29. In all the distributions checked the simulated data were found to model the observed data well.

Table 6.5 compares the expected number of selected events from background processes against the observed number of selected events from the data at various parts of the four-jet analysis. Agreement between the two is reasonably good.

6.6 Optimisation of cut values

The four-jet cut selection is optimised at a given Higgs boson mass. Once the signal mass is chosen the background selection efficiency is minimised as a function of the signal selection efficiency. The performance of the analysis is a function of the values

Cut name										
Multi hadronic	X	X	X	X	X	X	X	X	X	X
$y_{34} > 0.004$		X	X	X	X	X	X	X	X	X
$|p_z| > 1.5(M_{vis} - 90)$			X	X	X	X	X	X	X	X
xgmax < 0.8				X	X	X	X	X	X	X
anti-hll					X	X	X	X	X	X
nchmin > 0						X	X	X	X	X
JAS $> 350°$							X	X	X	X
COSMIN < -1.3								X	X	X
$y_{34} > 0.008$									X	
$9.5y_{34} + \sum_{i=1}^{4} \mathrm{NN}_i > 3.2$										X
Expected	–	–	–	2701.9	2693.0	2643.5	1981.8	1224.0	979.0	5.14
Observed	25874	7176	4264	2581	2570	2515	1858	1161	910	1

Table 6.5: The observed number of candidates in the data compared with the expected number of events from background process simulation, for various combinations of applied cuts.

of all the cuts. The set of cut values which give the lowest background for a given signal selection efficiency could in principal be determined with a search of the N dimension space formed by all N cut variables. However, it is not possible to do a complete scan in a reasonable amount of time and optimising some cuts will lead to an analysis for which the signal selection efficiency is a strong function of the Higgs boson mass. Away from the optimisation mass the signal efficiency could fall sharply. While some mass dependence is inevitable it is desirable to retain substantial signal efficiency over a wide range of signal mass. Consequently only four of the selection cuts are searched exhaustively. The others are set according to standard ALEPH definitions, (e.g., the multi-hadronic requirement) and others by optimisation by dedicated investigations. The four cuts which are scanned are:

- m_{12}

- $\min(\eta_3, \eta_4)$

- $(1 - \eta_3)(1 - \eta_4)$

- $9.5y_{34} + \sum_{i=1}^{4} \eta_i$

Each cut is varied between set boundaries and takes discrete values separated by equally sized values chosen to yield a desired number of steps. The scan results in a 4

dimensional grid of points in the space defined by the 4 cuts variables. For each point the signal and background selection efficiency on simulated events is found. Signal efficiency bins are defined, each 1% in width and for each bin the point in the scan yielding the lowest background efficiency is recorded.

The selection is said to be optimised at the $\sqrt{s}$ and m_h used in the simulated events. The set of points from the optimisation form the so-called performance curve. The performance curve obtained with backgrounds and signal at $\sqrt{s} = 199.5$ GeV and $m_h = 106.5$ GeV/c^2 is shown in figure 6.16.
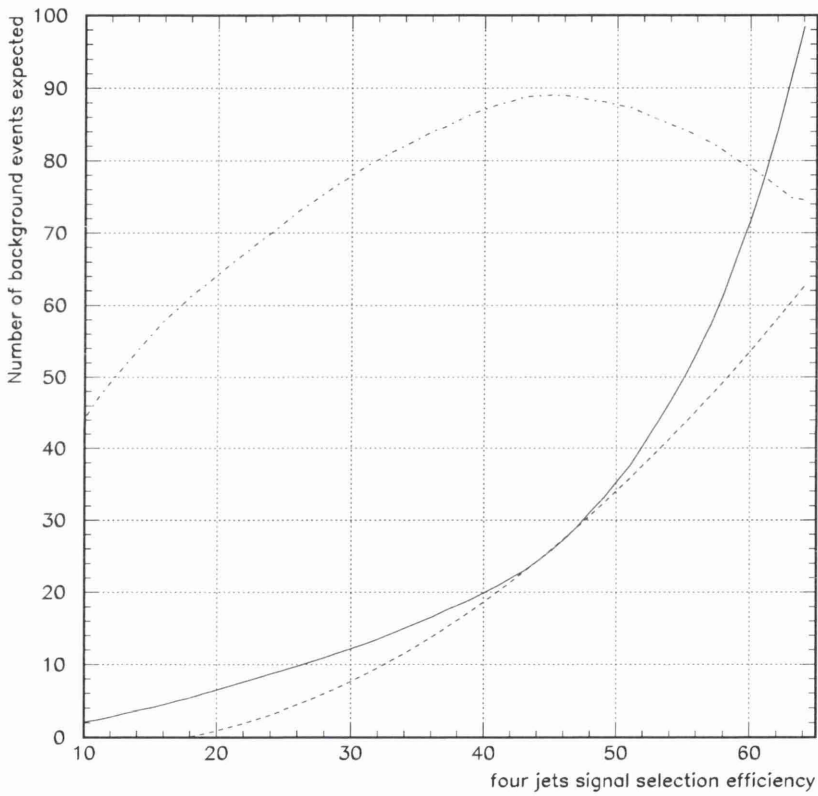
Figure 6.16:   The performance curve, shown in solid line, obtained at $\sqrt{s} = 199.5$ GeV, and $m_h = 106.5$ GeV/c^2. The expected background numbers are normalised for an integrated luminosity of 168 pb^{-1}. The broken lines are illustrative estimates: The dash-dotted line gives an estimate of the sensitivity (with arbitrary normalisation) of the selection along the performance curve. The dotted line is a line showing the performance which would yield a constant sensitivity value.

Figure 6.16 shows the expected number of background events against Higgs boson selection efficiency. It was obtained by scanning the three b-tag cuts and the cut on

the reconstructed Z mass. The background is plotted against the four-jet selection efficiency $\mathcal{E}$, so that the expected number of signal events, s

$$s = \sigma_{\text{hZ}} \text{BR}(\text{hZ} \to \text{four jets})\mathcal{E}. \tag{6.17}$$

where σ_{hZ} is the hZ production cross section and $\text{BR}(\text{hZ} \to \text{four jets})$ is the four-jet branching ratio.

6.7 Working point determination

The performance curve yields the optimum choice of cuts in terms of background efficiency for any desired signal selection efficiency. However the selection efficiency to be used, known as the working point, is not determined by the selection cut optimisation procedure.

The dashed and dash-dotted curve in figure 6.16 are included for information only and are not part of the procedure used to find the working point. However it can be instructive to consider them. The dash-dotted curve shows the function $s/f(s+b)$ with arbitrary normalisation. Here $f(s+b) \sim \sqrt{s+b}$ for large $b+s$, and is the expected Poisson error on the observation of $b+s$ events. Thus the dash-dotted curve is an estimate of the sensitivity of the selection, based on expected event counts only.

The dashed curve is a contour of equal $s/f(s+b)$, the contour indicating the value equal to the highest value of the sensitivity estimate obtained along the performance curve. The dashed curve gives an indication of the number of background events which would be required at any signal selection efficiency to equal the highest sensitivity seen.

The above illustrates why the choice of working point is important. Considerable variation of the sensitivity estimate is seen across the signal selection efficiency range. In order to rigorously determine the working point the full calculation of $\langle \text{CL}_{\text{SE}} \rangle$ (see Chapter 5) is performed. When $\langle \text{CL}_{\text{SE}} \rangle$ is calculated, using a given signal efficiency point, against Higgs boson mass hypothesis the mass at which $\langle \text{CL}_{\text{SE}} \rangle$ exceeds 5% gives the expected sensitivity of the analysis to a Higgs boson. Thus the working point is determined by choosing a Higgs boson mass near the expected limit, and finding $\langle \text{CL}_{\text{SE}} \rangle$ against selection efficiency. The selection efficiency which minimises

$\langle \mathrm{CL_{SE}} \rangle$ will give the highest expected limit in the absence of signal and is used as the working point.

The calculation requires the performance curve from the event selection optimisation and also the probability density functions (pdfs) S_i and B_i which describe the background and signal distributions in m_{reco} as a function of selection efficiency. Figure 6.17 shows examples of the background and signal pdfs for three different selection efficiencies each.
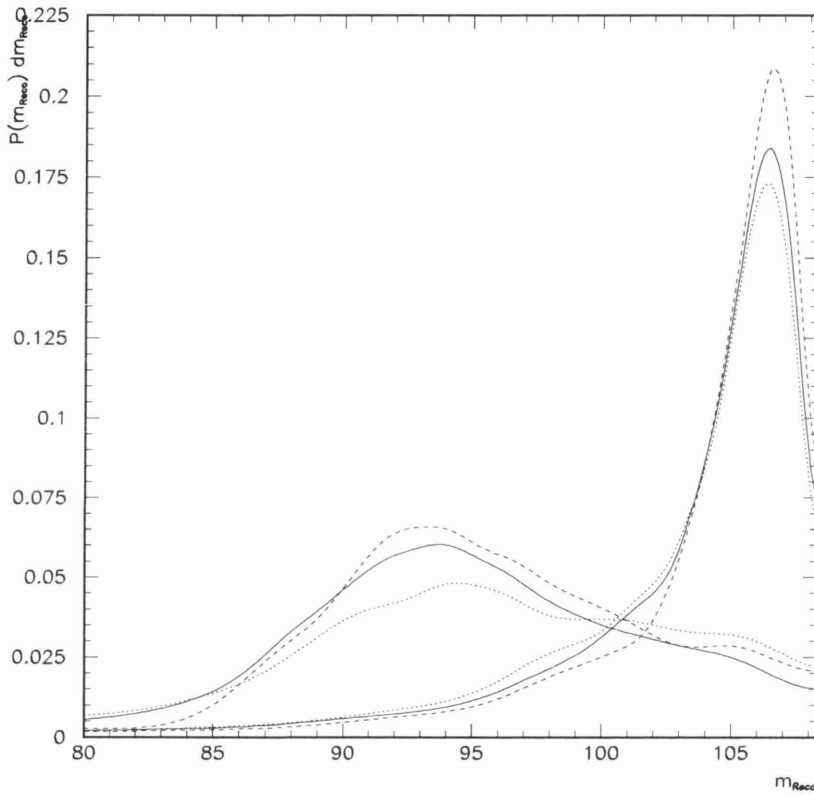
Figure 6.17:   The probability density functions describing the probability to find a candidate from background or signal with a given range of reconstructed mass, m_{reco}. The signal used has a mass of $m_h = 106.5$ GeV/c^2 and both background and signal were generated at $\sqrt{s} = 199.5$ GeV. The three sets of curves for the signal peak around 106.5 GeV/c^2 while those of background peak at a somewhat lower mass near m_Z. The two *solid* curves are for a selection efficiency of 40% while the *dashed* (*dotted*) curves were obtained with a selection efficiency of 20% (55%).

The result of the calculations of $\langle \mathrm{CL_{SE}} \rangle$ are shown in figure 6.18, and includes one set of results where m_{reco} is used as a discriminating variable and one where only the expected signal and backgrounds counts are used. There is a clear overall lowering of
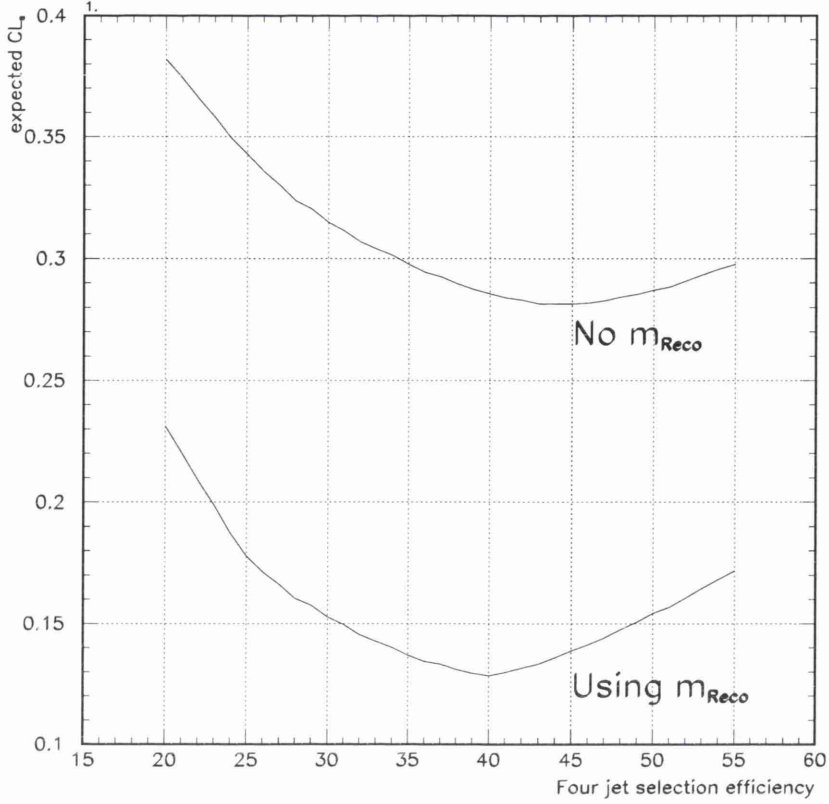
Figure 6.18: The result of the calculation for $\langle \mathrm{CL_{SE}} \rangle$ for two cases: using only the expected signal and background rates (labelled *No m_{reco}*) and in addition using m_{reco} as a discriminating variable (labelled *Using m_{reco}*).

$\langle \mathrm{CL_{SE}} \rangle$ at all efficiencies when the use of m_{reco} is introduced. This indicates that the sensitivity to discriminate between the b and s+b hypotheses is substantially improved by the use of m_{reco}.

When the full calculation of $\langle \mathrm{CL_{SE}} \rangle$ is performed including the use of a discriminating variable the working point is found to be 40%.
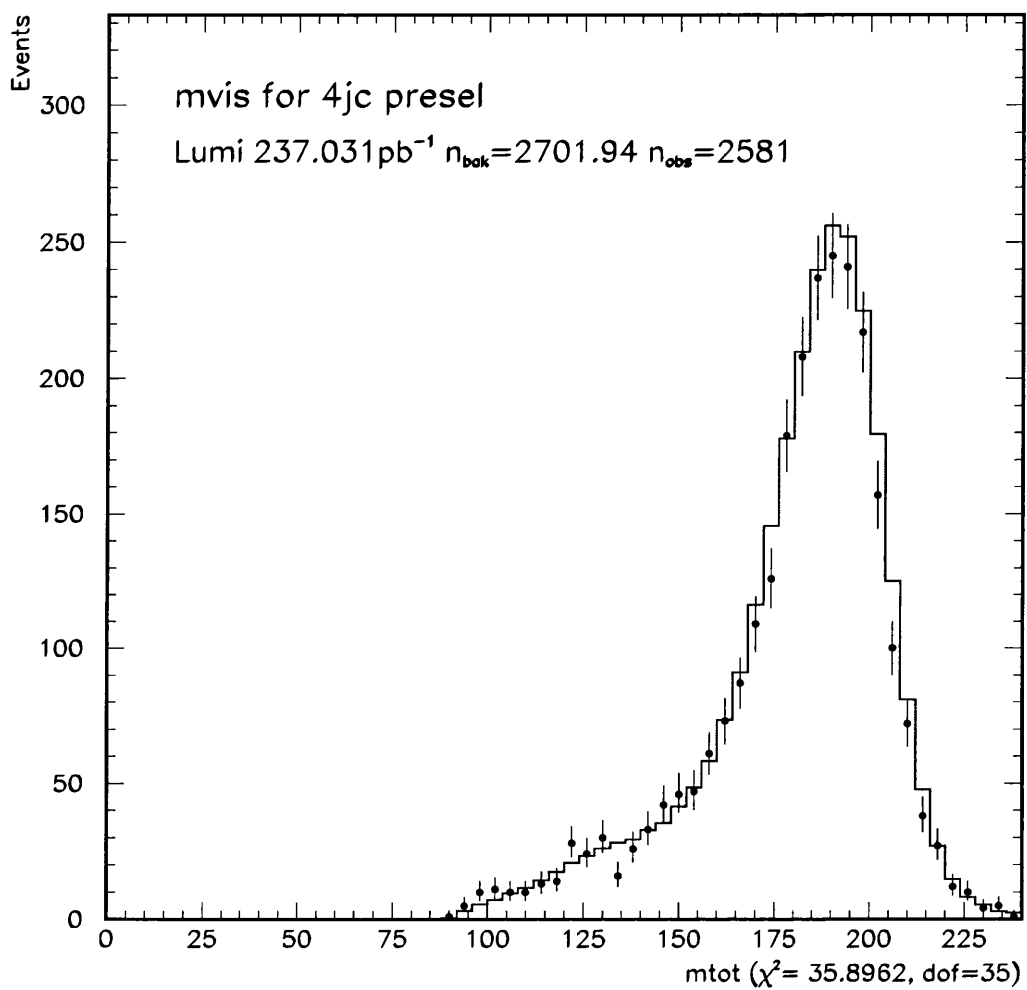
Figure 6.19: The distribution of total visible mass in the data (points) and simulated background components (solid).
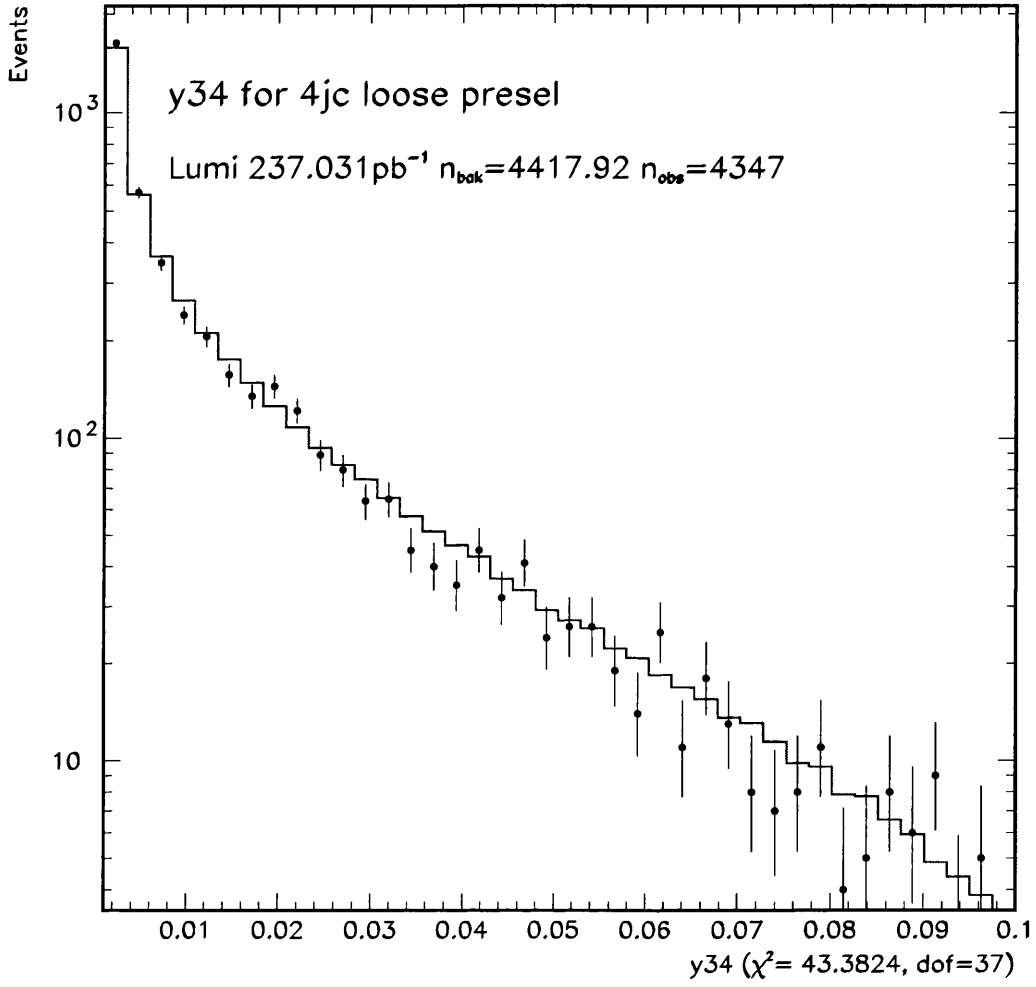
Figure 6.20: The distribution of y_{34} in the data (points) and simulated background components (solid).
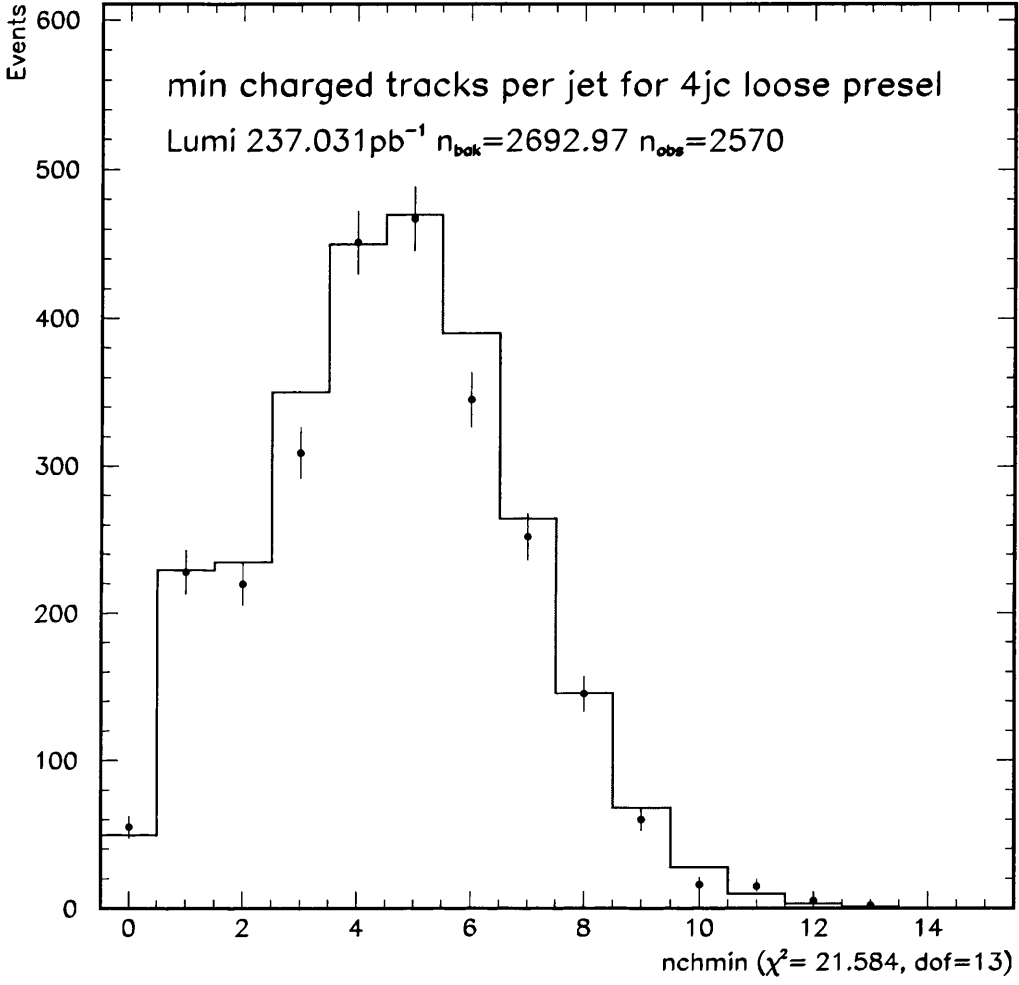
Figure 6.21: The distribution of the minimum number of good charged tracks in any jet per event in the data (points) and simulated background components (solid).
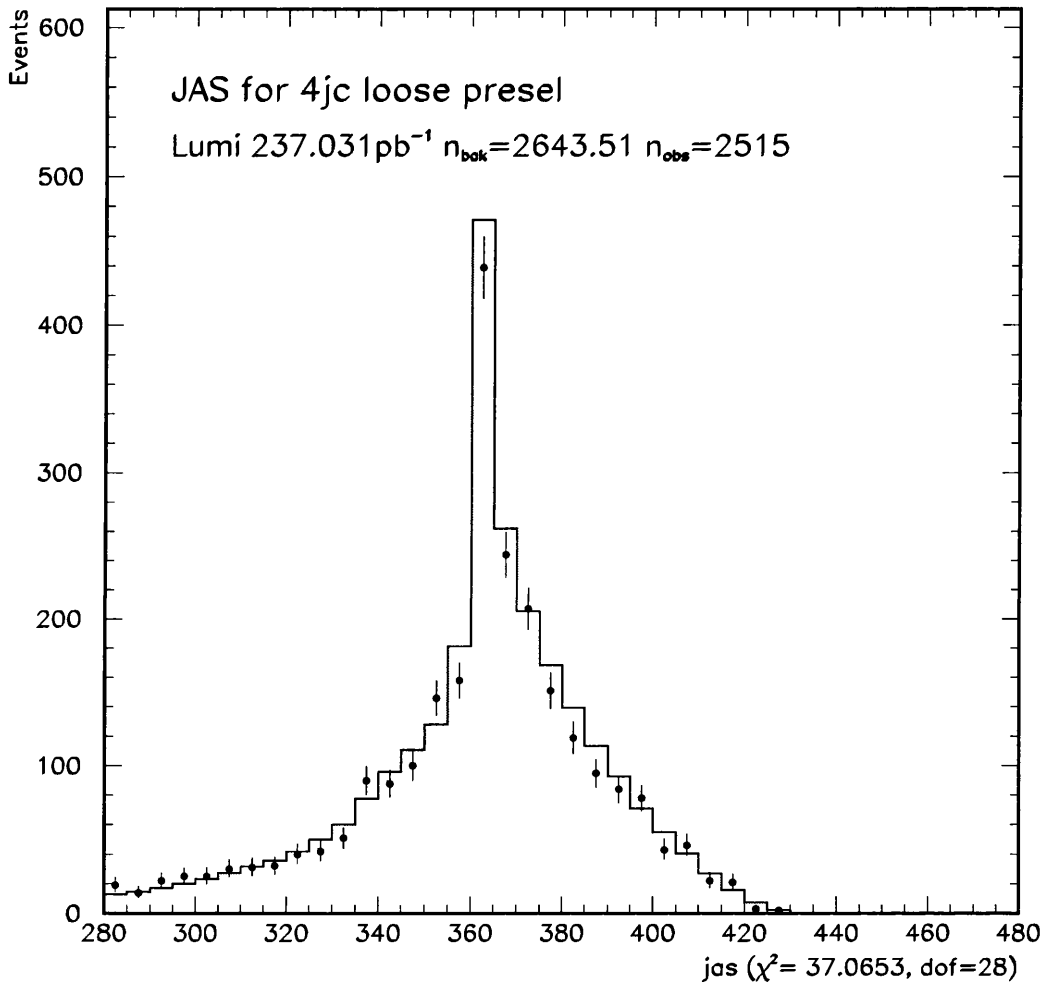
Figure 6.22: The distribution of Θ in the data (points) and simulated background components (solid).
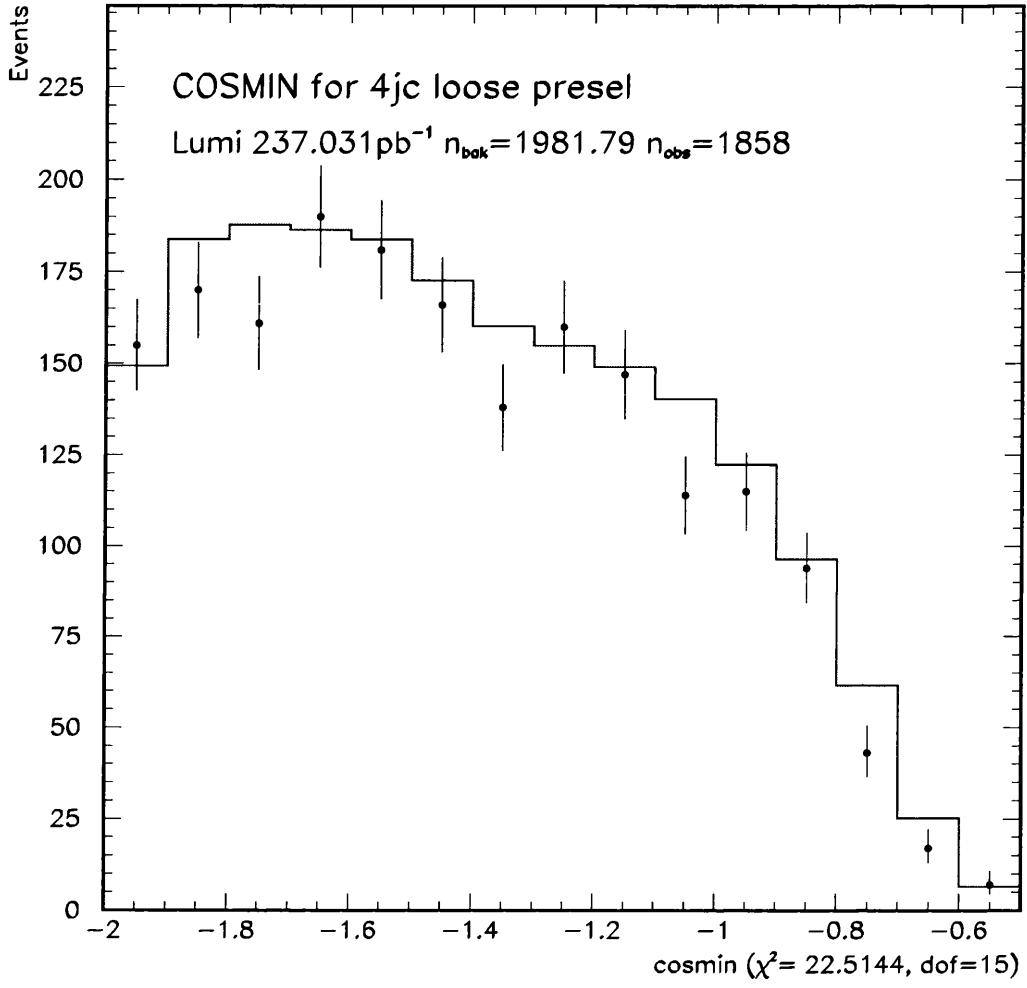
Figure 6.23: The distribution of γ in the data (points) and simulated background components (solid).
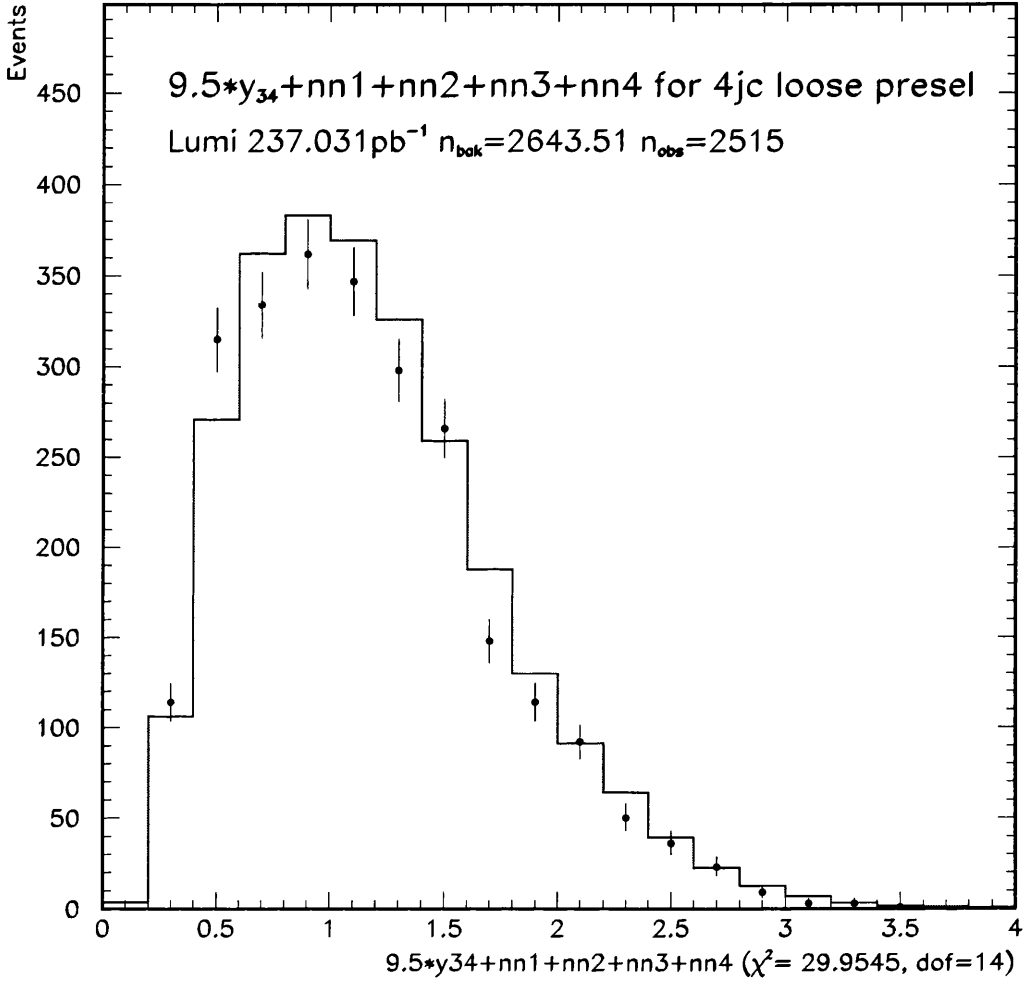
Figure 6.24: The distribution of '4b' branch discriminant, $9.5y_{34} + \sum_{i=1}^{4} \eta_i$ in the data (points) and simulated background components (solid).
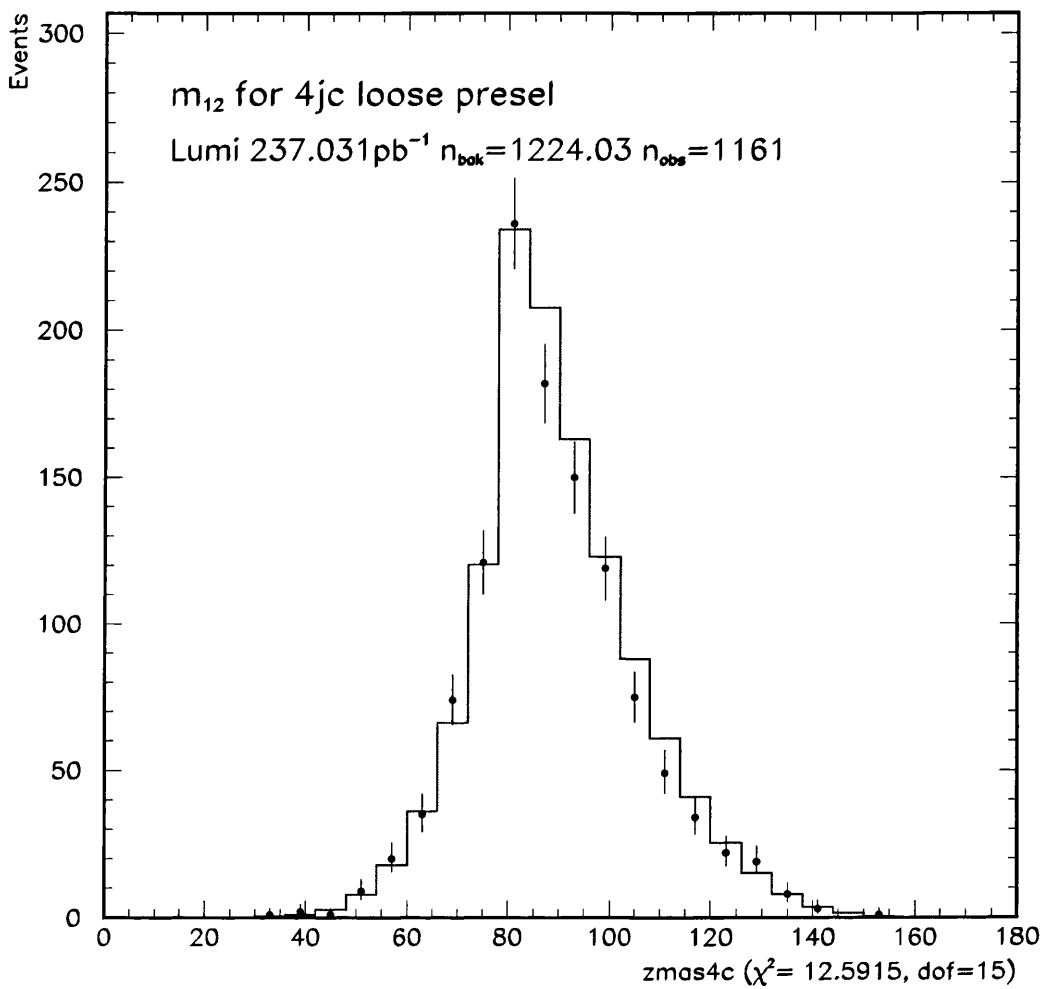
Figure 6.25: The distribution of m_{12} at the preselection level in the data (points) and simulated background components (solid).
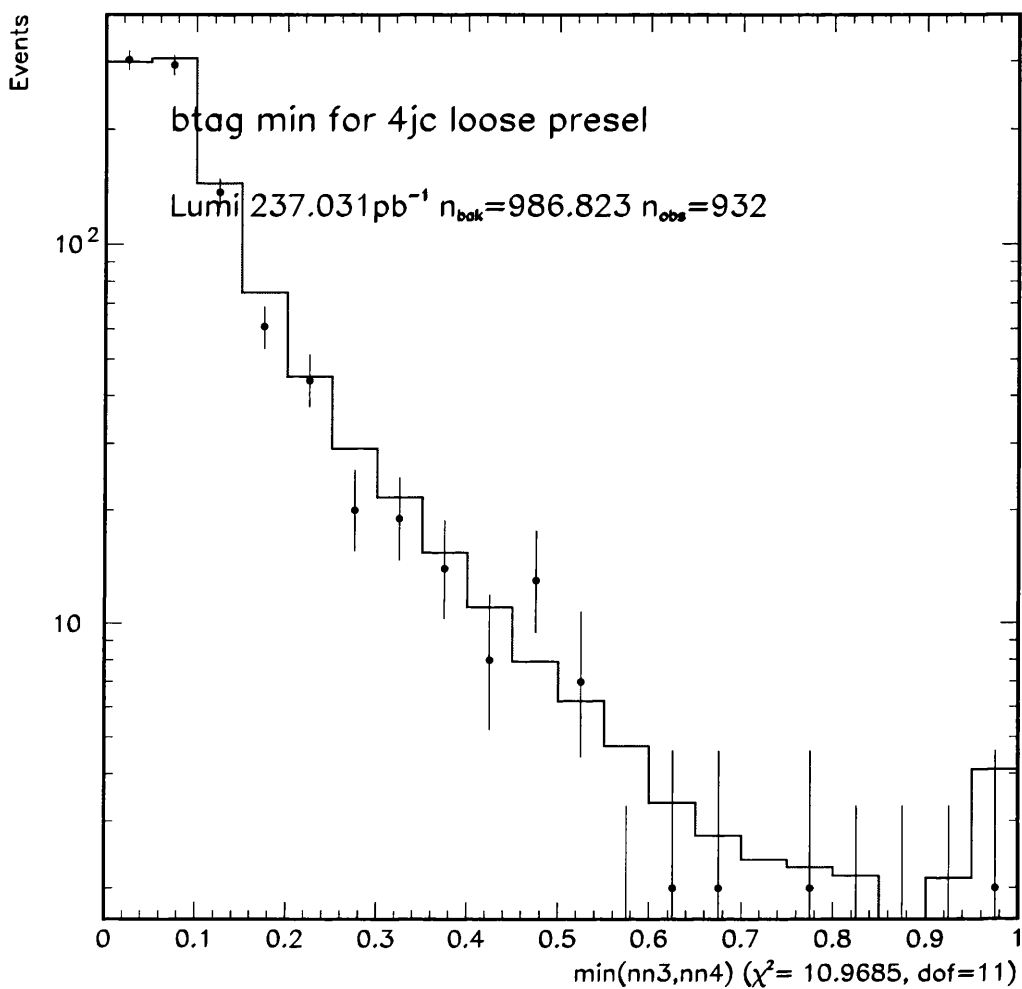
Figure 6.26: The distribution of b-tag value for the least b-like of the Higgs boson candidate jets, at the preselection level, in the data (points) and simulated background components (solid).
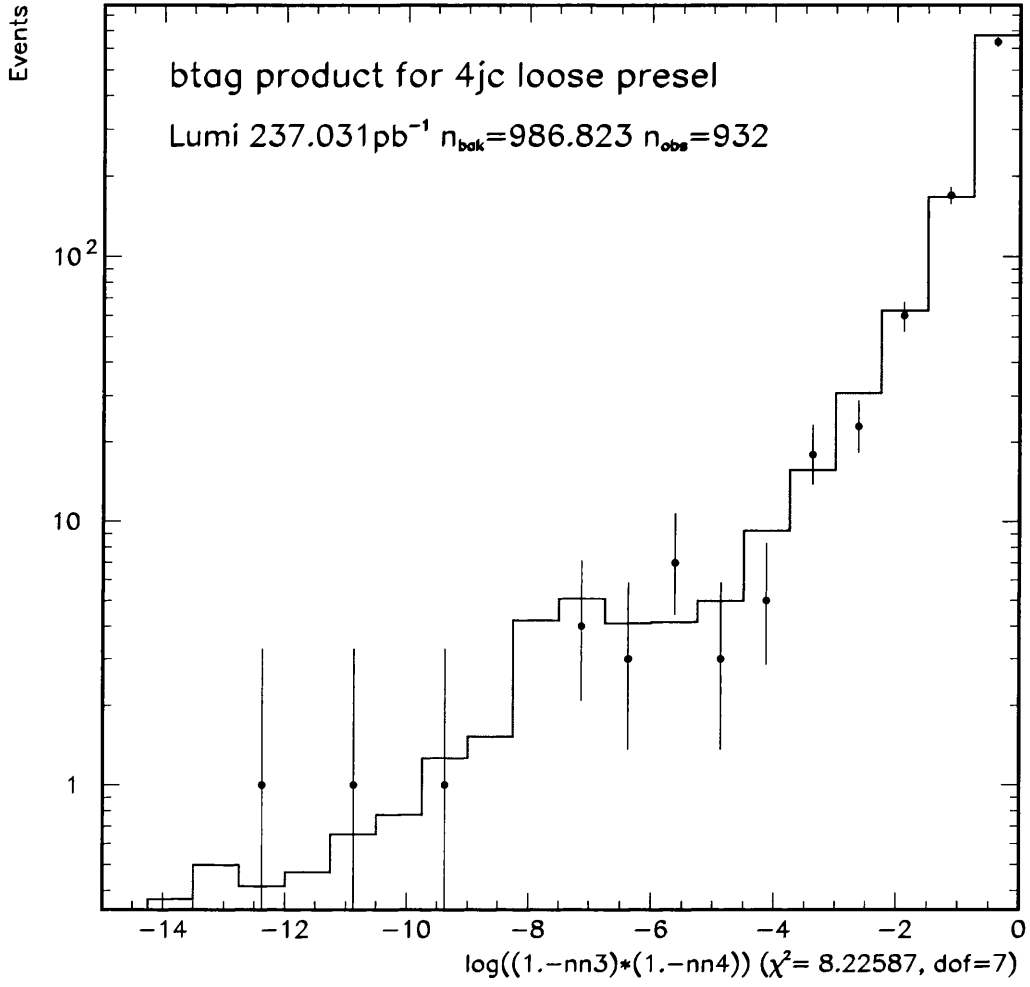
Figure 6.27: The distribution of $\ln(1 - \eta_3)(1 - \eta_4)$ at the preselection level, in the data (points) and simulated background components (solid).
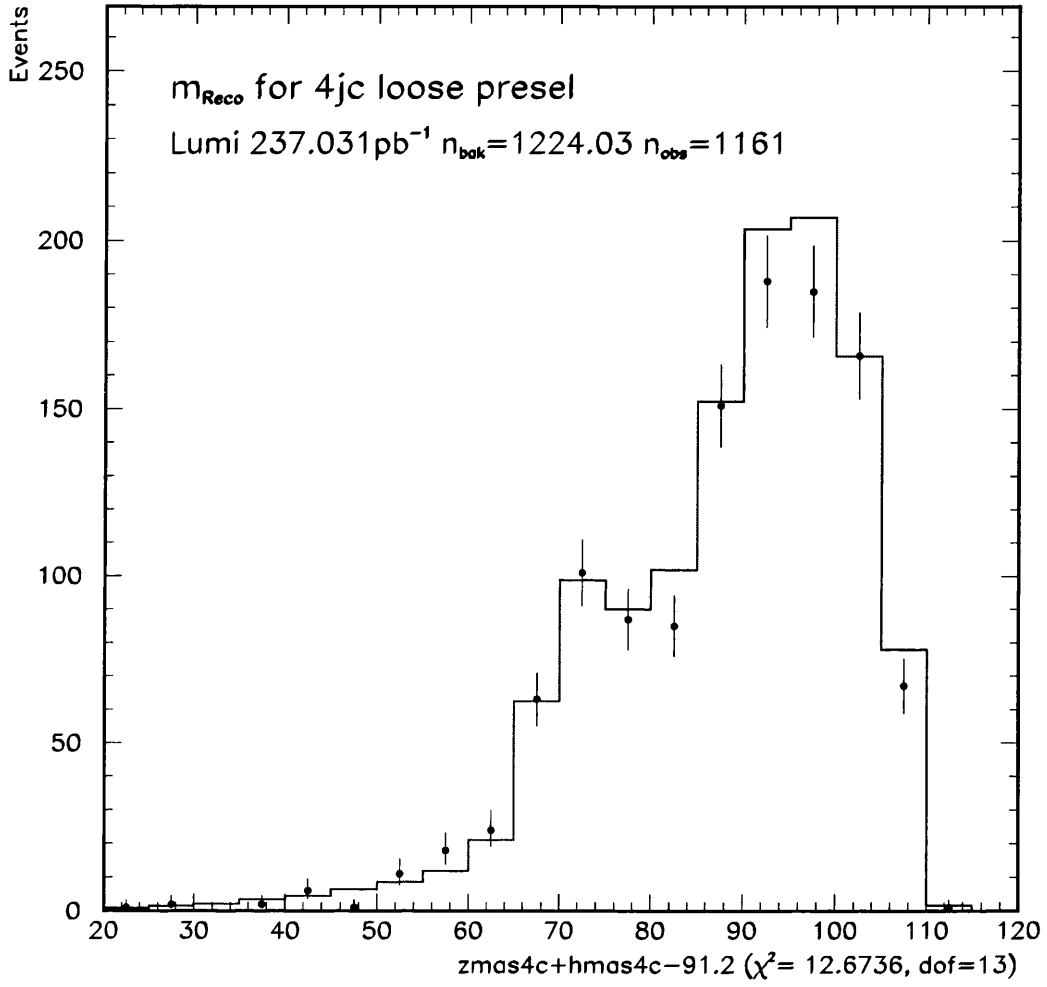
Figure 6.28: The distribution of m_{reco}, the reconstructed Higgs boson mass, at the preselection level. Shown are the data (points) and simulated background components (solid).
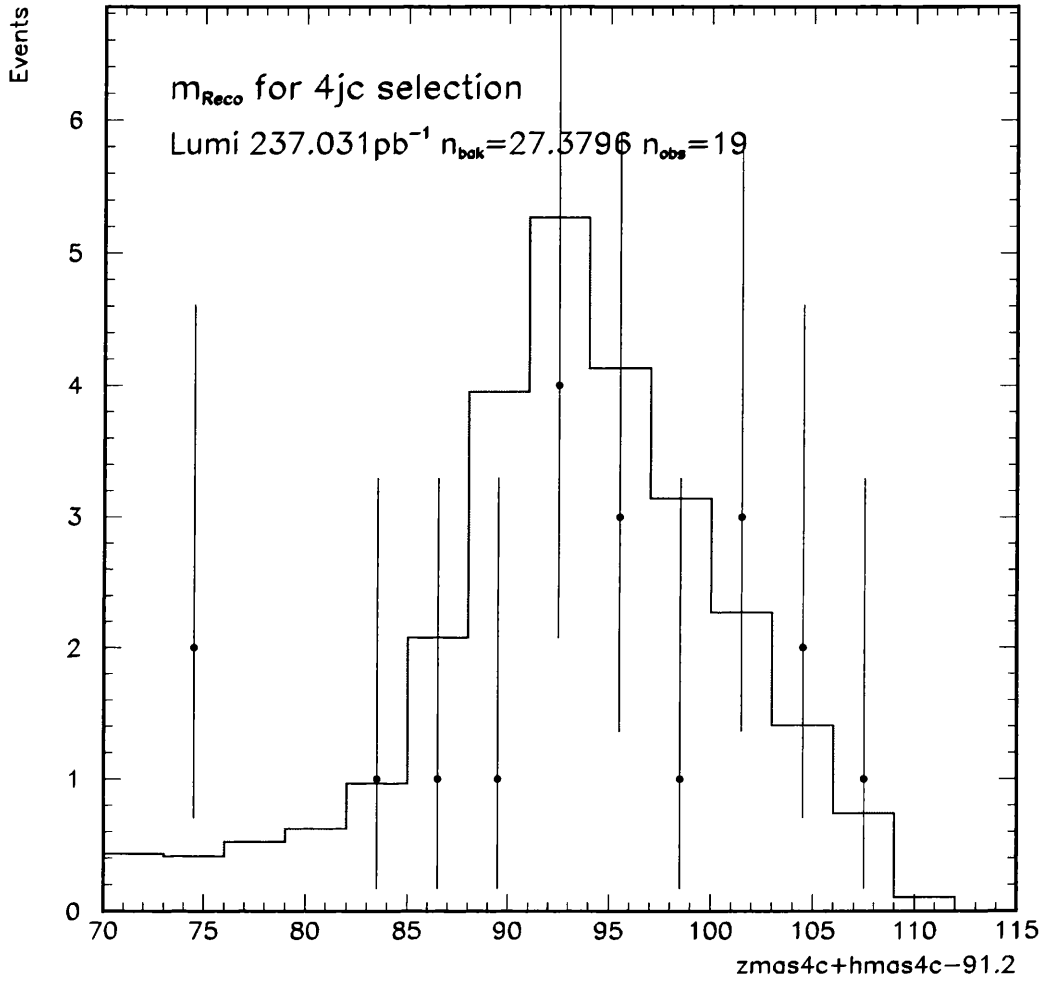
Figure 6.29: The distribution of m_{reco}, the reconstructed Higgs boson mass, at the end of the four-jet selection. Shown are data (points) and simulated background components (solid).

134

Chapter 7

Other Higgs boson search channels

While the four-jet channel is the single most important in the search for the Standard Model Higgs boson there are three other channels that can also be used in the search. When combined they are almost as powerful as the four-jet channel. Each of the three other channels has an associated selection. These other channels are hll (e, or μ leptons in the final state), h$\nu\bar{\nu}$ (the so-called *missing energy* final state) and X$\tau^+\tau^-$ (tau final states).

In addition, hA production is expected in the context of the MSSM. The h and A bosons of the MSSM are expected to decay mostly to b quarks or τ leptons, similar to the SM Higgs boson. Therefore there is also a hA $\rightarrow b\bar{b}b\bar{b}$ selection which is dedicated to a four b final state from hA decays. For hA signal decays to taus, the SM X$\tau^+\tau^-$ selection is used.

These other final state selections are briefly described here. The cuts based, rather than the neural network based, analyses are described where one exists.

7.1 Leptonic channel

The hll final state selection[49, 50] is designed to select events from the reaction hZ $\rightarrow$ X$\ell^+\ell^-$ where ℓ is an e or μ lepton and X is b$\bar{b}$ or $\tau^+\tau^-$. The hll final state accounts for 6.7% of the Higgsstrahlung decays. The ZZ-fusion process also contributes to this final state, although it makes only a small contribution compared to the hZ process.

Despite the small hll branching fraction the leptonic final state is distinctive, allowing a high selection efficiency to be achieved. It is also possible to reconstruct the Higgs

boson with better mass resolution than in the other channels, due to the presence of the well measured leptons.

The hll analysis locates the two leptons from the Z boson decay and calculates the recoiling mass, given the known centre of mass energy and the measured lepton momenta and energy. In order to achieve high selection efficiency and good mass reconstruction care must be taken to identify the correct leptons, account for possible bremsstrahlung from electrons and attempt to identify final state radiation (FSR) photons from the e or μ. Two jets are also formed from the particles in the event, excluding the two leptons. A b-tag is made on the jets and the result is used as a discriminating variable, in addition to the recoil Higgs boson mass. The event selection itself does not use the b-tag information.

7.1.1 Leptonic channel selection

The hll selection is cut based only. Events are required to have at least four good tracks entering the detector away from the beam line, i.e., $|\cos\theta| < 0.95$. The total energy of charged tracks must be larger than $0.1\sqrt{s}$. To choose the leptons from the Z boson decay, pairs of oppositely charged leptons are considered and their consistency with the m_Z hypothesis is checked. Here leptons are pairs of identified electrons or muons, or one identified lepton and any unidentified, isolated charged track. The isolation of a track is the half-angle of the cone around the track that contains 5% of the energy of the other particles in the event. To be considered isolated a track must have an isolation angle larger than 10°.

Further refinements are used to improve the m_Z reconstruction. Firstly the possibility of bremsstrahlung photons from the leptons is taken into account. Any neutral track within 2° of a lepton is not counted in the isolation calculation. In addition if the lepton is an identified electron the four vectors of the nearby neutral tracks are added to that of the lepton. Secondly a search for FSR photons from the Z boson decay is made. An FSR photon candidate must be a neutral, isolated track with at least 2 GeV energy. For the FSR photon the leptons are ignored in the isolation calculation. To reduce background from radiative Z returns the most energetic isolated photon must have an energy less than 75% of the most probable energy for the ISR

photon in $q\bar{q}(\gamma)$ events, which is 57 GeV for $\sqrt{s} = 196$ GeV.

The $\ell^+\ell^-(\gamma)$ system which gives the invariant mass closest to m_Z is chosen as the Z boson decay system. The reconstructed Z mass must be larger than 77 GeV/c^2. If there are four good tracks in the event it is considered to be a candidate for hZ $\rightarrow \tau^+\tau^-\ell^+\ell^-$ and the missing energy has to be at least $0.1\sqrt{s}$. The Higgs boson mass is then computed as the recoil mass to the Z boson decay:

$$m_{reco} = \sqrt{(s - E_Z^2) - P_Z^2} \tag{7.1}$$

where E_Z and P_Z are the measured energy and momentum of the Z boson. See figure 7.1.
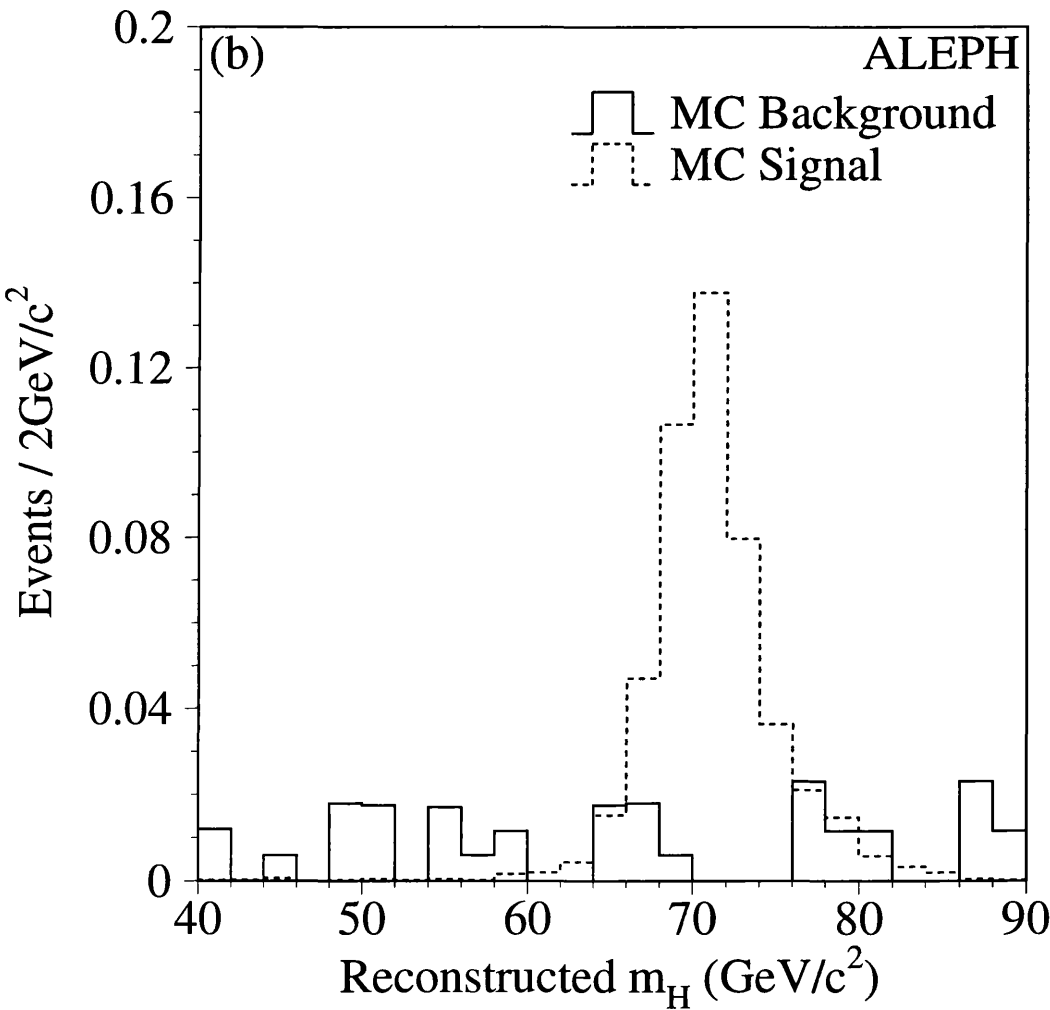
Figure 7.1: The distributions of the mass recoiling to the lepton pair for the hll analysis, for simulated events. The solid histogram is the background and the dashed histogram a Higgs boson signal. Taken from [51].

To reduce the background contamination from the semileptonic W decay, WW $\rightarrow$ $q\bar{q}\ell\nu$, an explicit reconstruction of events with only one identified lepton is performed, assuming WW kinematics. The identified lepton and missing momentum vector are used to calculate m_{W_1}, and the remaining hadronic dijet system is used to calculate m_{W_2}. If $m_{W_1} + m_{W_2} > 150$ GeV/c^2 and $|m_{W_1} - m_{W_2}| < 20$ GeV/c^2 then the event is classified as a semileptonic WW decay and is rejected.

To remove background from the processes $Z\gamma^*$, $e^+e^-\gamma^*$, $e^+e^- \rightarrow q\bar{q}$ and $\ell^+\ell^-\gamma\gamma$ further cuts are made. See reference [49] for details of the cuts.

The overall signal efficiency for a Higgs boson of 95 GeV/c^2 is 79.5%. The remaining contamination from background processes is mostly irreducible contributions from the ZZ and Zee processes.

7.2   Missing energy final state

Higgs boson production via Higgsstrahlung where the Z boson subsequently decays to two undetected neutrinos gives rise to a distinctive final state, h$\nu\bar{\nu}$, the so-called missing energy final state. The h$\nu\bar{\nu}$ final state is characterised by large missing energy, and mass, and the presence of two b-jets. Higgs boson production via the WW-fusion process also yields a similar final state. Although the production rate is smaller for the fusion processes the importance of the WW-fusion increases with Higgs boson mass. With a Higgs boson of 95 GeV/$c^2$the WW-fusion amounts to 20% of the total signal in the h$\nu\nu$ final state. The details of the ALEPH missing energy selection are covered in [49, 52], but the analysis is outlined here.

7.2.1   Missing energy preselection

Preselection is designed to find hadronic events consistent with missing momentum pointing away from the beam line, to avoid large contamination from qq(γ) returns to the Z.

An event is first required to have five or more reconstructed charged particles and the total energy of all charged particles to be at least $0.1\sqrt{s}$. The thrust axis is found and the event is divided into two hemispheres by the plane perpendicular to the thrust

axis, passing through the interaction point. There should be energy in both half halves of the event.

To reduce the selection of $\gamma\gamma$ events $E_{30°} > 0.25\sqrt{s}$ or $|p_T| > 0.05\sqrt{s}$, where $E_{30°}$ is the total energy deposited more than 30° away from the beam axis and p_T is the transverse component of the total momentum. Reduction of the qq(γ) selection rate in the cases where an energetic initial state radiation (ISR) photon is radiated along the beam axis is achieved by requiring that the longitudinal component of the total momentum must be small, $|p_Z| < 50$ GeV/c. The missing mass should be large, $\not{M} > 50$ GeV/c^2.

The resulting preselection is 85% efficient for a simulated Higgs boson signal of mass 95 GeV/c^2. The dominant backgrounds are pair production of W bosons and quarks.

7.2.2   Missing energy selection

The aim of the selection is to further reduce backgrounds from q$\bar{\text{q}}$, WW, Weν and Zee events.

In brief the $h\nu\bar{\nu}$ selection follows: To remove q$\bar{\text{q}}$ events remaining after preselection the angle of the missing momentum with respect to the beam axis, $\theta_{\not{p}} > 35°$. Many of the remaining q$\bar{\text{q}}$ events have an ISR photon pointing into the detector. To remove these events the *modified acoplanarity*, $\widetilde{A}$, is defined as

$$\widetilde{A} = (\hat{j}_1 \times \hat{j}_2) \cdot \hat{z} \tag{7.2}$$

where $\hat{j}_i$ are unit vectors along the total momentum in the ith hemisphere and $\hat{z}$ is beam direction. $|\widetilde{A}|$ must be greater than 0.08, which means the hadronic content of the two hemispheres must be acoplanar. See figure 7.2.

The remaining dominant background of WW pair production consists largely of semileptonic decays, where one W boson decays hadronicaly to two quarks and the other W boson decays to a τ lepton and neutrino. The tau decay can be rejected if it proceeds leptonicaly or is sufficiently energetic, by requiring $E_{iso} > 8$ GeV and $\alpha_{iso} < 25°$ where E_{iso} is the sum of the energy within 30° of the most energetic identified e or μ lepton, and the isolation angle α_{iso} is the angle from this track to its nearest
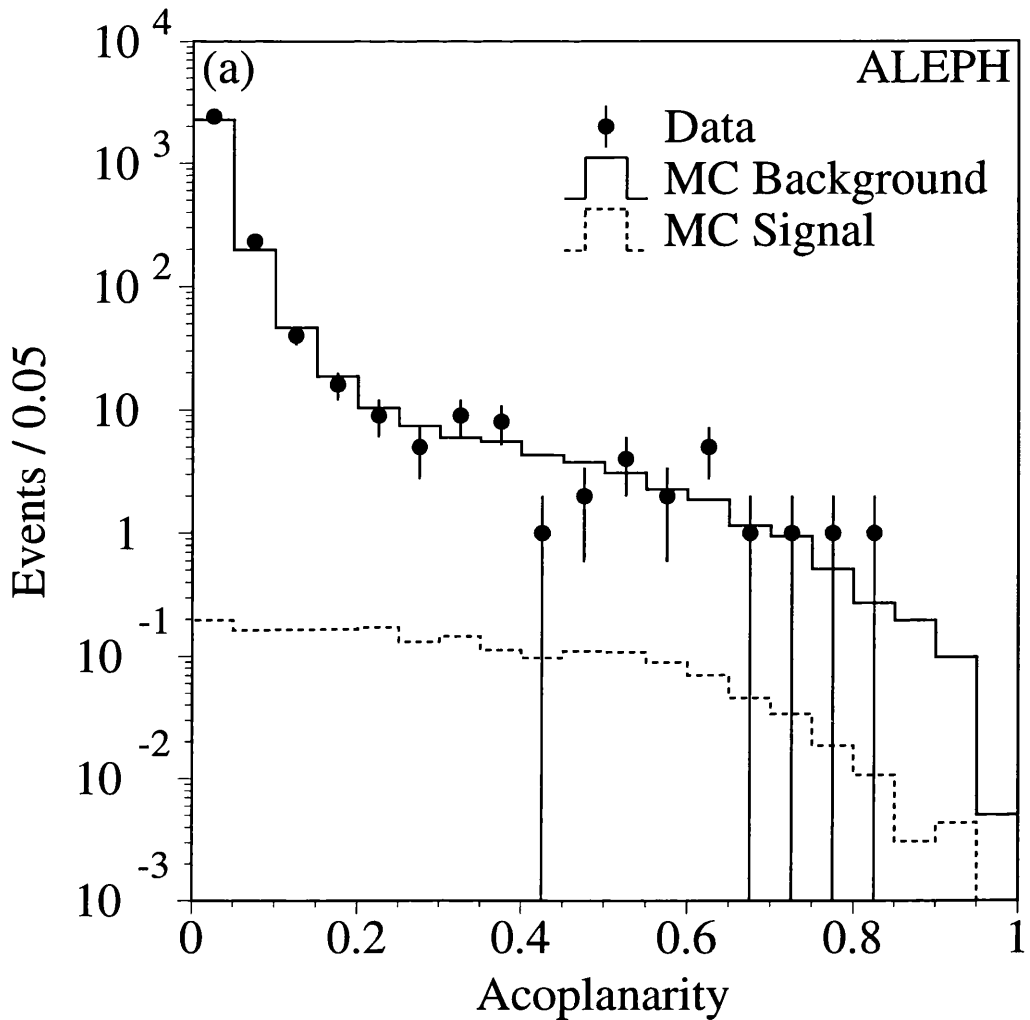
Figure 7.2: The event acoplanarity distribution for the data (points) and simulated events, background (solid histogram) and Higgs boson signal (dashed histogram). Taken from [51].

neighbour.

To reject Weν and Zee events with an energetic electron entering the detector at low angle, the energy deposited within a cone of 12° around the beam axis is required to be small, $E_{12} < 0.012\sqrt{s}$.

Finally, the cut on the missing mass is tightened to $M\!\!\!/ > 70$ GeV/c^2. The event is clustered into two or more jets using the DURHAM algorithm, $y_{cut} = 0.015$. The jets are then b-tagged. The two most b-like jets are taken as the Higgs boson decay products, and the b-tags are required to be sufficiently good. The most significant background comes from ZZ $\rightarrow$ b$\bar{\text{b}}\nu\bar{\nu}$, accounting for about 50% of the background events. For a simulated Higgs boson signal of 95 GeV/c^2 the typical $h\nu\bar{\nu}$ efficiency is

about 35%.

7.3 Tau final states

Final states with τ leptons may be produced by the hZ decay or the hA decay. The tau analysis[49, 53] is designed to select two τ leptons and two hadronic jets, denoted by $X\tau^+\tau^-$, although there is also efficiency for $X = \tau^+\tau^-$, i.e., for the four tau final state. The $X\tau^+\tau^-$ configuration may come from hZ $\to \tau^+\tau^- Z$ which accounts for 5.5% of the Higgsstrahlung decays. In the tau analysis the Z is considered to decay to quarks or τ leptons only, the leptonic states are included in the hll channel. In addition there is also hZ $\to h\tau^+\tau^-$, giving an additional 3.4%. The hA decay will yield a $b\bar{b}$, $\tau^+\tau^-$ system about 15.5% of the time.

The $X\tau^+\tau^-$ analysis is based upon neural networks only and does not have a cuts based version.

7.3.1 Tau preselection

Hadronic events are selected by requiring at least eight good charged tracks and the total energy of all charged particles to be greater than $0.2\sqrt{s}$. Events with an identified lepton with an energy greater than $0.25\sqrt{s}$ are rejected as semileptonic and leptonic decays of the WW or ZZ systems. Radiative returns to the Z peak, when the energetic ISR photon escaping detection along the beam pipe, are rejected by requiring $|p_z| + E <$ $1.8\gamma_{peak}$ and $|p_z| < 0.6\gamma_{peak}$ where $\gamma_{peak} = \sqrt{s}/2 - m_Z^2/(2\sqrt{s})$ is the expected energy of the photon to return to the Z peak.

A jet clustering is performed, yielding jets with an invariant mass smaller than 2.7 GeV$/c^2$, consistent with the τ hypothesis. The resulting jets are termed minijets. From the minijets, candidates for τ decays are chosen. The selection criteria are based upon minijet multiplicity, isolation and energy. See reference [54] for details of the selection process. A charge is assigned to each selected τ minijet candidate.

Events with two or more recognised τ minijets are processed further. Two oppositely charged τ minijets are considered at a time. The remaining tracks not in τ minijets are reclustered to two jets using the DURHAM algorithm. All four jets are then rescaled

in momentum and energy such that the mass of the τ minijets is set to the mass of the τ lepton. A χ^2 is calculated for each of the possible selections of two τ jets from the available candidate minijets. The analysis has three independent branches, hA $\rightarrow$ $\tau^+\tau^-$b$\bar{\text{b}}$, hZ $\rightarrow$ $\tau^+\tau^-Z$ or $h\tau^+\tau^-$. The χ^2 contains terms from energy-momentum conservation, hadronic jet resolutions and a term from a kinematic fit. The fit measures the compatibility of the appropriate dijet invariant masses according to assumed hA or hZ production. For the hA case a term is added to the χ^2 by comparing the hadronic masses to that of the $\tau^+\tau^-$ system. For hZ production two terms are added, one from fitting the $\tau^+\tau^-$ dijet masses to m_Z and one from fitting the hadronic jets to m_Z.

7.3.2 Tau selection
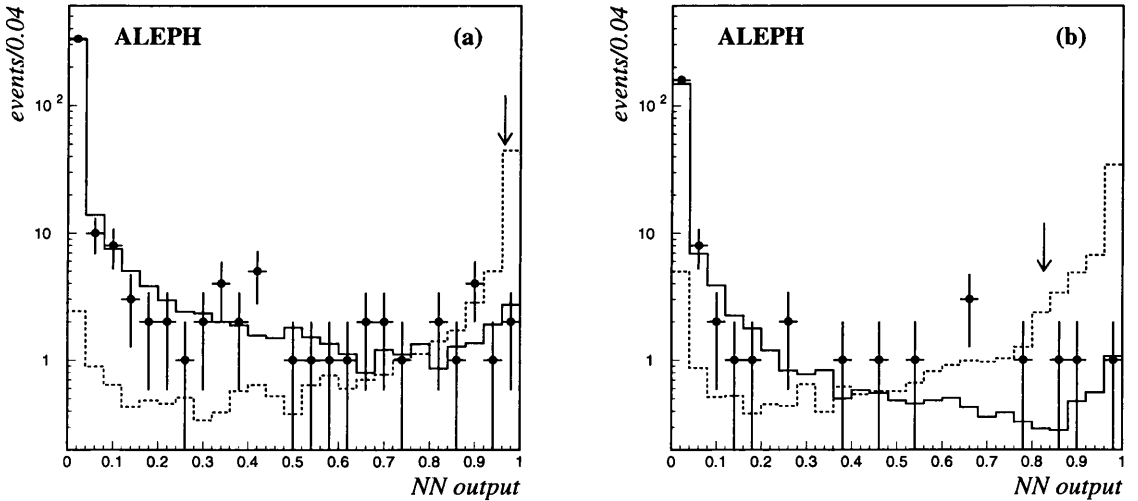
Figure 7.3: Distributions of the NN outputs (a) used in the selection of hZ candidates with τ leptons in the final state (b) used in the selection of hA candidates with $b\bar{b}\tau^+\tau^-$ final state. The arrows drawn in (a) and (b) indicate the value of the cut above which events are considered to be selected. Taken from [49].

The event selection is done by a combination of three neural networks. One five variable neural network, for hA selection, a four variable neural network for hZ $\rightarrow$ $\tau^+\tau^-Z$ and a five variable neural network for hZ $\rightarrow$ $h\tau^+\tau^-$. The inputs and architecture of the two five variable networks are identical, only the hA selection network is trained on hA $\rightarrow$ $\tau^+\tau^-b\bar{b}$ and the hZ selection network is trained on hZ $\rightarrow$ b$\bar{\text{b}}\tau^+\tau^-$. The five inputs are the kinematic χ^2 term, the event transverse momentum p_T, the sum of the

two τ minijet isolation angles, the fitted transverse momenta, P_T^{jet}, of the τ minijets with respect to the nearest hadronic jet and the sum of neural network b-tagging outputs of the two hadronic jets.

The four variable neural network is used for hZ $\to \tau^+\tau^- q\bar{q}$ selection. It has the same input variables as the five variable neural network with the exception of the b-tag sum.

For the hA selection the event is considered a candidate if the hA neural network output is larger than 0.826. A signal efficiency of 42.0% for $m_h = 85$ GeV/c^2 is obtained.

If an event is not selected as an hA candidate then it maybe selected as an hZ candidate, either $b\bar{b}\tau^+\tau^-$ or $\tau^+\tau^- q\bar{q}$. The event is processed by both the four and the five variable neural networks. If one neural network gives a much larger output than the other, the event is considered to be of the corresponding event type.

If the outputs of the hZ neural networks are similar, i.e., the sum is larger than 1.8, then the kinematic fit χ^2 is used. Assuming first the final state $b\bar{b}\tau^+\tau^-$, $\chi^2_{b\bar{b}\tau^+\tau^-}$ is found. In a similar way $\chi^2_{\tau\tau q\bar{q}}$ is found by assuming the final state $\tau^+\tau^- q\bar{q}$. The event is then classified according to $\chi^2_{b\bar{b}\tau\tau} - 1 > \chi^2_{\tau\tau q\bar{q}}$. The offset for the $\chi^2_{b\bar{b}\tau\tau}$ term introduces a bias towards classing the event more often as $b\bar{b}\tau^+\tau^-$. This is desired because for the $b\bar{b}\tau^+\tau^-$ neural network output to be large the event has a good b-tag sum, thus biasing it to more likely have originated from the b decay of the Higgs boson.

Finally once the event has been classified, in order to be selected as an hZ candidate the event is required to have the neural network output of the corresponding neural network in excess of 0.965. For a Higgs boson mass of $m_h = 95$ GeV/c^2, $h\tau^+\tau^-$ and $\tau^+\tau^- Z$ efficiencies of 29.5% and 17.4% are found respectively.

7.4 The hA $\to$ b$\bar{\text{b}}$b$\bar{\text{b}}$ final state

In hA pair decays the b$\bar{\text{b}}$b$\bar{\text{b}}$ final state accounts for about 80% of the possible decays. This is a similar topology to the hZ $\to$ four jets discussed in detail in chapter 6.

The principal differences between the hA and the hZ four-jet final state are:

- An enhanced b content and the absence of the Z boson, whose mass is known.

- In hA production it is assumed that $m_h \simeq m_A$, a fact that is exploited in a simplified pairing choice algorithm in this channel; The jet pairing chosen is the one which gives the smallest difference in the reconstructed mass for the h and A bosons.

- The sensitivity to an hA signal is such that the mass range where mass limits are typically set is further below production threshold than that which could be expected for hZ production. This leads to different kinematic considerations.

For detailed discussion of the hA four-jet analysis see [49, 55], here the selection is outlined.

7.4.1   hA to four-jets preselection

The preselection for the hA $\rightarrow$ b$\bar{\text{b}}$b$\bar{\text{b}}$ final state is very similar to the hZ four-jet preselection, namely the same multi-hadronic event selection is used. However with the extra b content the b-tagging cuts are even more powerful at rejecting background processes. The requirement of well separated jets, reflected in the y_{34} cut, is relaxed: $y_{34} > 0.001$.

7.4.2   hA to four-jets selection

The selection consists of cuts on topological variables and b-tag variables. The b-tagging is performed by a neural network. A four variable neural network is used. The inputs to the neural network are QIPBTAG, QVSRCH, the largest p_T of any identified leptons and X_E. X_E is defined as the fraction of the jet energy carried by the most energetic particles which have a total invariant mass smaller than 2.1 GeV/c^2.

A linear discriminant, $\mathcal{F}$, is used in the hA $\rightarrow$ b$\bar{\text{b}}$b$\bar{\text{b}}$ event selection:

$$\mathcal{F} = 300 \times \left(4 - \sum_{j=1}^{4} \eta_j\right) - \theta_{ij}^{min} \tag{7.3}$$

where η_j is the b-tag value of the jth jet and θ_{ij}^{min} is the minimum inter dijet angle, in degrees. A small value of $\mathcal{F}$ indicates an event with b-like jets which are well separated. The distribution of the $\mathcal{F}$ variable is shown in figure 7.4.
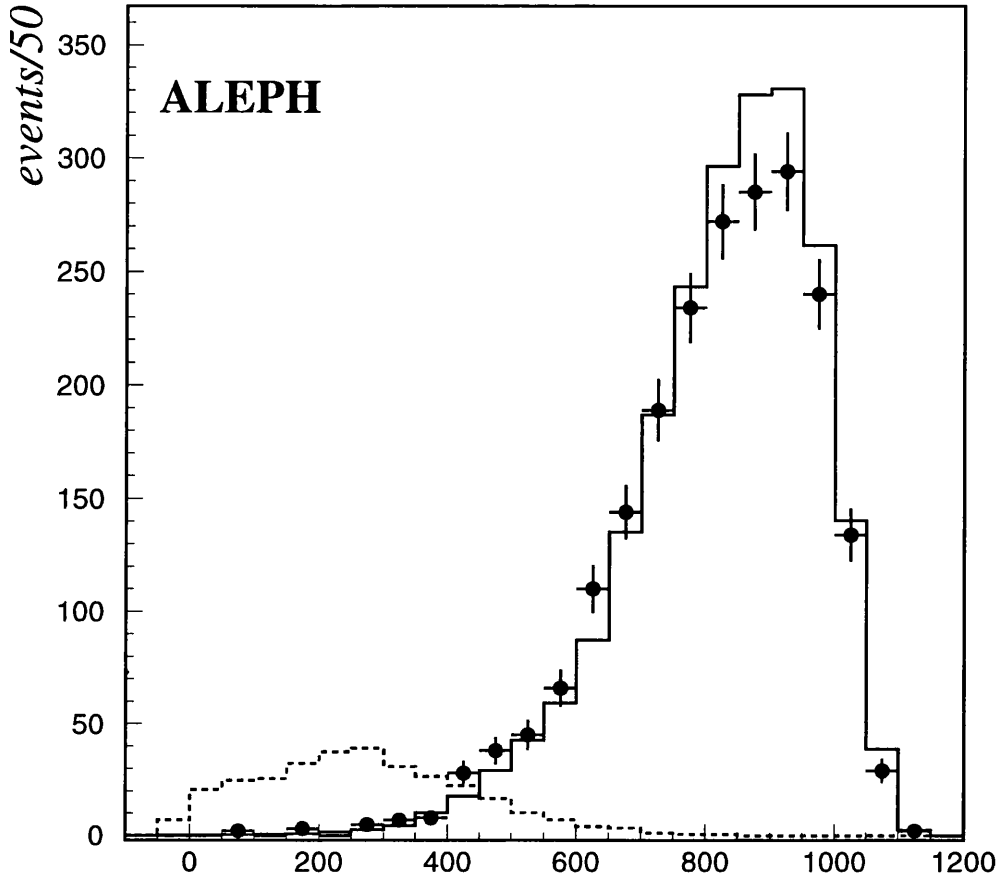
Figure 7.4: Distribution of the $\mathcal{F}$ variable for data (points with error bars), simulated background (solid histogram), and simulated Higgs boson signal for $m_h = 85$ GeV/c^2 (dashed histogram), at preselection level. Taken from [49].

In addition to a cut on the $\mathcal{F}$ variable it is also required that: $\theta_{ij}^{min} > 20°$ and $\Delta\theta_3 > 50°$. $\Delta\theta_3$ is a variable to reject $q\bar{q}g$ events. $\Delta\theta_3$ can take values in the range $0 < \Delta\theta_3 < 360$, and tends to zero for the topology of one jet recoiling against three others.

By optimising the working point of the hA selection (in a similar way to the hZ selection, section 6.7), it is found that $\mathcal{F} < 351$ yields the best sensitivity for the hA search. The hA four-jet analysis typically has an efficiency of 67% for $m_h = 90$ GeV/c^2.

7.5 Event classes within a final state

The possibility that an event could be selected by two or more analyses dealing with the same final state is a problem. A single event could contribute more than once which would invalidate the results of the search. For instance, there are two four-jet final state selections, hZ $\to b\bar{b}q\bar{q}$ and hA $\to b\bar{b}b\bar{b}$. As expected many events will be selected by both. If care is not taken when combining results from the four-jet analyses some of the background or signal will be counted more than once, thus artificially raising the selection efficiency. Any conclusions drawn from such a combination could be seriously flawed.
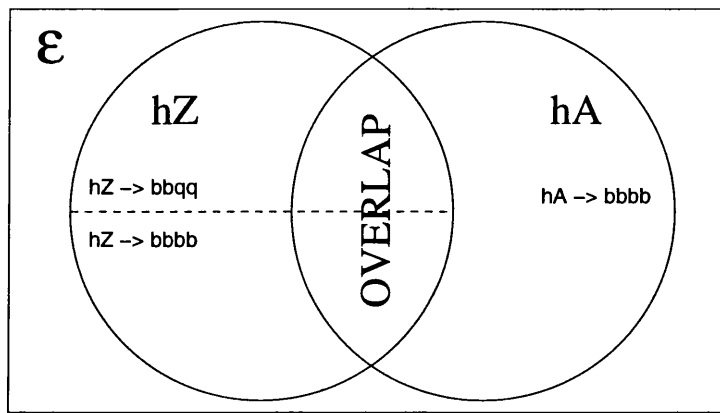
Figure 7.5: Venn-diagram showing the three classifications of an event by the four-jet final states. The dashed line shows that the classification is internal only to the hZ analysis. The three regions with solid borders are statistically independent, i.e., a single event may not reside in more than one of them. They are termed *hZ exclusive*, *Overlap* and *hA exclusive* selections.

For the four-jet final state analyses the selection of events is made statistically independent by assigning each event to one of three four-jet classifications. Figure 7.5 shows the three possible classes of selected four-jet event in a Venn-digram. The dashed line indicates that the hZ $\to b\bar{b}q\bar{q}$ selection has two internal streams corresponding to a $b\bar{b}b\bar{b}$ final state and, the more general, $b\bar{b}q\bar{q}$ final state. The distinction is made within the hZ analysis to gain efficiency because of the clear experimental signature of the four b-jets. It is to be expected that the hA and hZ analyses both have a large efficiency for the $b\bar{b}b\bar{b}$ final state.

The double counting problem is also present in the tau final state selection. The $X\tau^+\tau^-$ selection is comprised of three analyses (see section 7.3), an hZ $\to \tau^+\tau^- Z$, an

$hZ \rightarrow h\tau^+\tau^-$ and an $hA \rightarrow bb\tau^+\tau^-$ selection.

The $X\tau^+\tau^-$ final state is arranged so that a selected event is classified as either hA or else hZ. This is shown diagrammatically in fig 7.6.
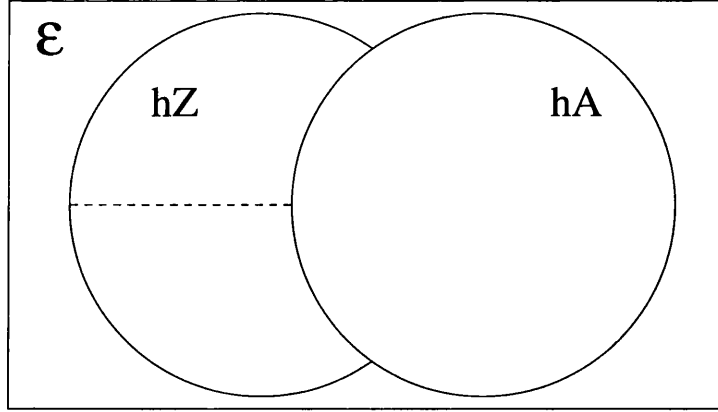
Figure 7.6: Venn-diagram showing the three classifications of an event by the $X\tau^+\tau^-$ analysis. The dashed line shows that the classification is internal to the channel. The two regions with solid borders are statistically independent, i.e., a single event may not reside in more than one of them. They are termed *hZ* or *hA* selections.

Chapter 8

Inputs to the Higgs boson search from the SM four-jets selection

8.1 Introduction

In this chapter the results of the four-jets search are given, when the search is applied to the 1999 ALEPH dataset, collected at approximately $192 < \sqrt{s} < 202$. In addition, the information required to generate a statistical interpretation of the results and combine them with the other search channels is also given.

8.1.1 Selection efficiency from simulated events

In order to compute the expected background and signal rates for a given selection, the analysis is performed on large quantities of simulated events. The simulated events classed in three broad types:

- Background $(\sqrt{s})$

- hZ signal $(\sqrt{s}, m_{\mathrm{h}})$

- hA signal $(\sqrt{s}, m_{\mathrm{h}}, \tan\beta)$

where there are samples of each type of event for several values of the parameters shown in parentheses. For each class of events the expected number of events n_{type} is:

$$n_{type}(\sqrt{s}, m_h, \tan\beta) = \mathcal{E}_{type}(\sqrt{s}, m_h, \tan\beta) \cdot \sigma_{type}(\sqrt{s}, m_h, \tan\beta) \cdot \mathcal{L}(\sqrt{s}) \qquad (8.1)$$

where $\mathcal{E}_{type}$ is the selection efficiency and σ_{type} is the production cross section. $\mathcal{L}$ is the integrated luminosity corresponding to the experiment.

The total expected number of four-jet events, n_{exp}, which is compared to the number observed by experiment, n_{obs}, is given by:

$$n_{exp}(m_h, \tan\beta) = \sum_{\sqrt{s}}^{energies} \sum_{t}^{types} n_{type}(\sqrt{s}, m_h, \tan\beta) \qquad (8.2)$$

where the sums are over all $\sqrt{s}$ at which data is collected and *types* are all types of signal event for which the four-jet selection has non zero selection efficiency. For example, for the background the expected number of events at a given energy is composed of contributions from 3 significant background processes, which are simulated as 7 separate samples. So selection efficiencies for all 7 samples are found and combined according to the relative production cross sections. The expected background rate is found separately at the four centre of mass energies at which data was collected.

The expected signal is somewhat more straight forward. A single simulated sample corresponding the process hZ $\rightarrow$ four-jets or hA $\rightarrow$ four-jets is available. However the efficiency is computed for a number of samples corresponding to a range of m_h and the four separate centre of mass energies.

Background components

For the background the three separate sources that are found to have significant selection efficiency by the four-jets selection are W^+W^- and ZZ pair decays and the QCD process $e^+e^- \rightarrow Z^* \rightarrow q\bar{q}(g)$, called the *QCD background*, where one or more gluons are radiated by quarks in the final state. The QCD background is simulated one flavour at a time, so there are five samples for the kinematically accessible quark flavours, u,d,s,c and b.

The handling of the QCD background is also complicated by the fact that the Monte Carlo simulation is known to be deficient in that the rate of $g \rightarrow q\bar{q}$, where

q is either c or b, is modelled poorly. While the effect is present in all the samples it has the most significant impact on the QCD background selection efficiency. For this reason the effect is corrected in the QCD background Monte Carlo by applying event-by-event weights. The selection efficiency then becomes the sum of the weights of selected events over the total of the weights for all events in the simulated sample. See section 8.2.1 for further discussion of the effect.

The simulated event samples used are:

Component	Final state	Generator	$\sqrt{s}/$ GeV	Number in sample	cross section/pb
CC03 WW	$W^+W^- \to f_1\bar{f}_1'f_2\bar{f}_2'$	KRLW02	192.0	250K	16.934
CC03 WW	$W^+W^- \to f_1\bar{f}_1'f_2\bar{f}_2'$	KRLW02	196.0	250K	17.222
CC03 WW	$W^+W^- \to f_1\bar{f}_1'f_2\bar{f}_2'$	KRLW02	200.0	500K	17.397
CC03 WW	$W^+W^- \to f_1\bar{f}_1'f_2\bar{f}_2'$	KRLW02	202.0	500K	17.465
ZZ	$ZZ \to f\bar{f}f'\bar{f}'$	PYTHIA04	191.6	50K	2.817
ZZ	$ZZ \to f\bar{f}f'\bar{f}'$	PYTHIA04	195.5	50K	2.860
ZZ	$ZZ \to f\bar{f}f'\bar{f}'$	PYTHIA04	199.5	50K	2.857
ZZ	$ZZ \to f\bar{f}f'\bar{f}'$	PYTHIA04	201.6	50K	2.837
QCD	$e^+e^- \to q\bar{q}$	KORLZ08	192.0	500K	95.820
QCD	$e^+e^- \to q\bar{q}$	KORLZ08	196.0	500K	91.014
QCD	$e^+e^- \to q\bar{q}$	KORLZ08	200.0	1000K	86.582
QCD	$e^+e^- \to q\bar{q}$	KORLZ08	202.0	1000K	84.537

Table 8.1: Event generator and sample size for the simulated background processes. The KORLZ08 samples are produced separately for each of the five quarks flavours, only the total is shown here.

8.1.2 Signal components

The Higgs boson signals are simulated with the HZHA03[29, 30] generator. Two types of event sample are generated, Standard Model hZ production and hA pair production in the context of the MSSM with $\tan\beta = 10$.

Efficiency for signal selection is considered only to come from the selection of the four-jet final state. Thus only events where the h,Z or A decay to gluons or quarks are included in the simulated signal events. Events are generated at many m_h reference masses and at the four energies corresponding to the experimental data.

Process	$\sqrt{s}/\mathrm{GeV}$	events	m_h mass ranges
hZ	191.6	6500	60 to 120 GeV/c^2 in 5 GeV/c^2 steps plus 97,98,99,100.4,100.7,101,102,103 GeV/c^2
	195.5	6500	60 to 120 GeV/c^2 in 5 GeV/c^2 steps plus 102,103,104,104.3,104.5, 104.7,106,108 GeV/c^2
	199.5	6500	60 to 120 GeV/c^2 in 5 GeV/c^2 steps plus 102,104,106,107,107.3,107.5,107.7,108, 108.3,108.5,108.7,109,111, 112,113,114,117,120 GeV/c^2
	201.6	6500	60 to 120 GeV/c^2 in 5 GeV/c^2 steps plus 106,107,108,109,109.2,109.4,109.6,109.8, 110.2,110.4,110.6,110.8,111,112, 113,114,117,118,119 GeV/c^2
hA($\tan\beta = 10$)	191.6	8000	60 to 90 GeV/c^2 in 5 GeV/c^2 steps plus 95.8 GeV/c^2
	195.5	8000	60 to 95 GeV/c^2 in 5 GeV/c^2 steps plus 97.75 GeV/c^2
	199.5	8000	60 to 95 GeV/c^2 in 5 GeV/c^2 steps plus 99.75 GeV/c^2
	201.6	8000	60 to 95 GeV/c^2 in 5 GeV/c^2 steps plus 100.8 GeV/c^2

Table 8.2: List of simulated signal events which were generated for the four-jet analysis using the HZHA03 generator. A set of samples of hZ, hA production were generated for each $\sqrt{s}$ at which data was collected. In the samples shown the h,Z,A bosons are allowed to decay to only gluons or quarks.

8.1.3 The four-jet cut based selections

The four-jet cut based analysis is divided into three statistically independent branches. These are known as the *hZ exclusive*, the *overlap* and the *hA exclusive* branches. As the names indicate they correspond respectively to the event subsamples selected exclusively by the hZ $\rightarrow$ four-jets selection, selected by both the hZ $\rightarrow$ four-jets selection and

the hA → four-jets selection, and selected by the hA → four-jets selection exclusively.

	hZ exclusive	Overlap	hA exclusive
Denoted by:	$hZ \cdot \overline{hA}$	$hZ \cdot hA$	$\overline{hZ} \cdot hA$

Table 8.3: The names of the three branches corresponding to the three statistically independent classifications of an event selected as a four-jet candidate. hZ and hA refer to the $hZ \rightarrow b\bar{b}q\bar{q}$ and the $hA \rightarrow b\bar{b}b\bar{b}$ analyses, together forming the four-jet selection.

8.1.4 Selection efficiency

Selection efficiency for signal events depends on the Higgs boson mass and the centre of mass energy. For an example the selection efficiencies of hZ and hA signals are shown in figure 8.1 for centre of mass energy $\sqrt{s} = 199.5$ GeV.
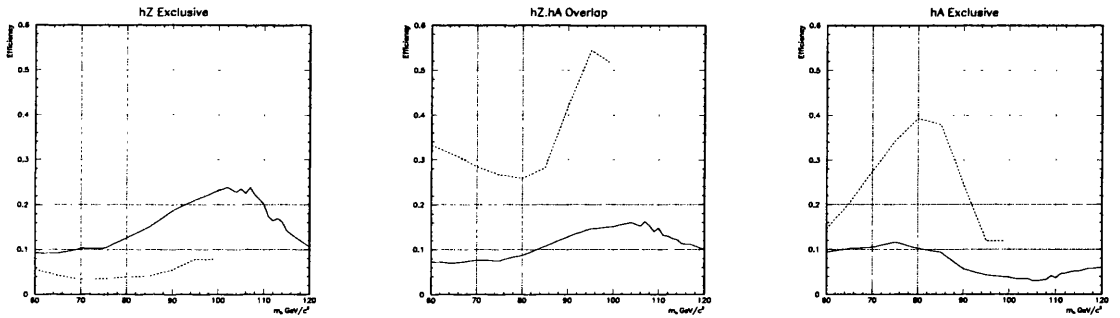
Figure 8.1: Examples of signal selection efficiency at $\sqrt{s} = 199.5$ GeV/c^2. Selection efficiency for hZ and hA signals are plotted against the mass of the h boson used in the simulation, m_h. The solid curve is hZ datasets and dashed the hA datasets. The three plots show the efficiency in each of the three four-jet branches.

It can be seen that the hA exclusive selection has a high selection efficiency for hA signal, and a low selection efficiency for hZ signal. Conversely the hZ exclusive selection has a high selection efficiency for the hZ signal and a smaller selection efficiency for the hA signal.

Background selection efficiencies are much lower than the signal selection efficiencies. The background selection efficiencies at $\sqrt{s} = 199.5$ GeV are summarised in table 8.4.

Process	hZ exclusive	hZ.hA overlap	hA exclusive
$q\bar{q}$	2.88×10^{-4}	1.13×10^{-4}	2.40×10^{-4}
W^+W^-	7.02×10^{-4}	0.660×10^{-4}	3.14×10^{-4}
ZZ	158×10^{-4}	72.8×10^{-4}	38.0×10^{-4}

Table 8.4: Background selection efficiencies at $\sqrt{s} = 199.5$ GeV.

8.1.5 Expected number of events

The signal selection efficiencies are used to calculate the expected number of signal events for any Higgs boson mass. The expected number of background events for each energy are also found. The total integrated luminosity at each energy is shown in table 8.5.

Energy/GeV	Integrated Luminosity/pb^{-1}
191.6	28.893
195.5	79.753
199.5	86.165
201.6	41.838

Table 8.5: Size of the data sets collected around the four central energies during the 1999 LEP run.

In addition, to calculate the expected number of events the cross sections for all processes and the decay branching ratio for the Higgs bosons are required. Plots of the production cross section and decay branching ratios are shown in figures 8.2 (for SM and MSSM) and 8.3 (for SM only) respectively. The decay branching ratio of the h and A bosons of the MSSM to jets is $\sim 91\%$ across the mass region considered, due almost entirely to b quarks.

To see the intrinsic selection power of each branch, for either hZ or hA signal the ratio of expected signal to background is computed and shown in table 8.7. The example masses used for the Higgs bosons are chosen to be close to the expected sensitivity found at the end of the analysis. It can be seen that the overlap has the largest s/b value for both the hZ and hA signals. The exclusive branches have the next
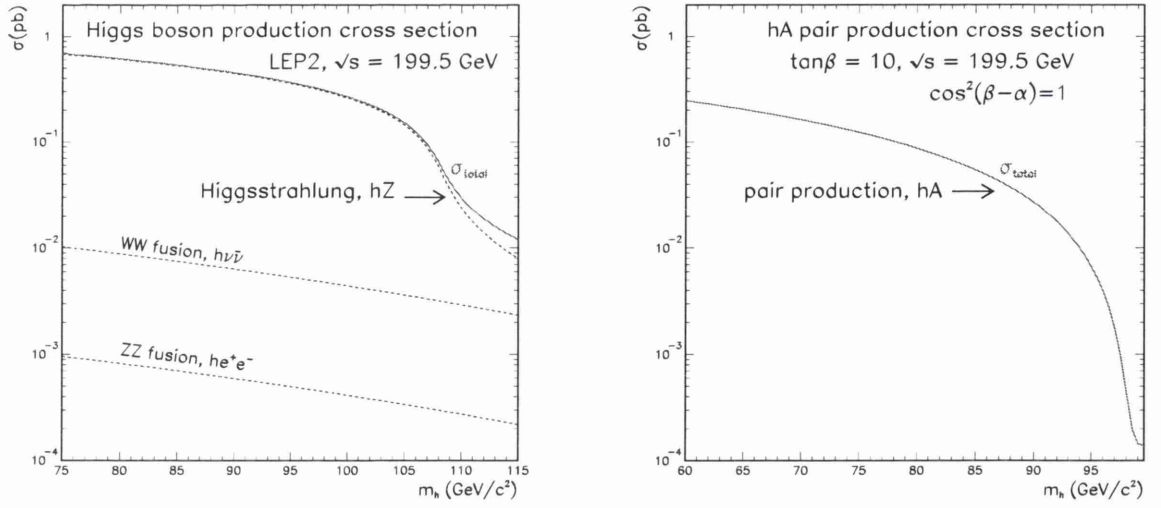
Figure 8.2: Production cross sections for hZ in the Standard Model and hA pair production in the MSSM in the case hA production is maximised with $\cos^2(\beta - \alpha) = 1$.
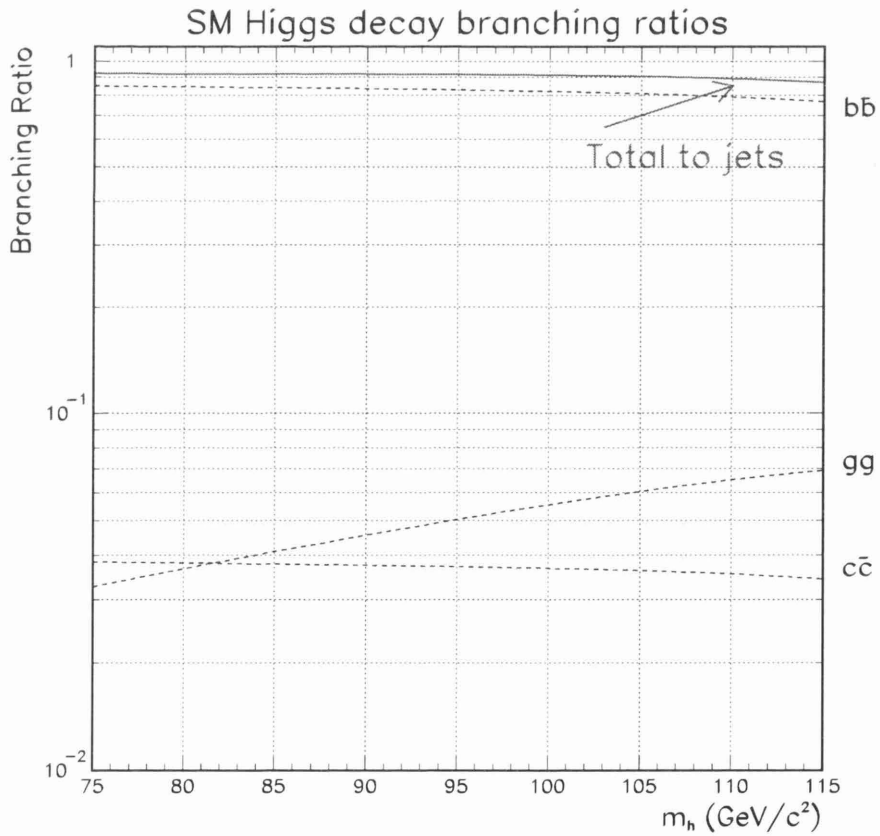
Figure 8.3: Decay fractions for the h boson of the standard model.

Type	hZ exclusive	Overlap	hA exclusive
Background	7.116	2.742	3.210
hZ ($m_h = 105$ GeV/c^2)	1.850	1.222	0.2338
hA ($m_h = 90$ GeV/c^2)	0.1231	0.9354	0.5509

Table 8.6: Number of background and signal events expected in the data collected at $\sqrt{s} = 199.5$. The background expected in the three branches of the four-jet analysis, together with the expected number of hZ and hA for two example masses are shown.

best s/b value for their corresponding signal. The case for hZ signal in hA exclusive and hA signal in hZ exclusive show the lowest s/b values.

Type	hZ exclusive	Overlap	hA exclusive
s/b hZ	0.260	0.446	0.0728
s/b hA	0.0173	0.341	0.172

Table 8.7: The s/b ratio for the three branches of the four-jet analysis. $\sqrt{s} = 199.5$, $m_{hZ} = 105$ GeV/c^2, $m_{h_{hA}} = 90$ GeV/c^2

8.1.6 Probability Density Functions of discriminating variables

In order to gain additional sensitivity to a possible signal, information about the selected candidates which show discrimination between background and signal events is used in addition to counting the number of selected candidates. For the four-jets analysis the reconstructed Higgs boson mass for each event is used as a discriminating variable. In order to incorporate the information a likelihood ratio is constructed (see chapter 5). The probability density function (pdf) of the reconstructed Higgs boson mass for any Higgs boson hypothesis mass is required for the computation of the likelihood.

The pdf is obtained from simulation. The selection is performed on the simulated data and the distribution of the reconstructed Higgs boson masses of selected candidates is obtained. To this a continuous function is fitted. When normalised to unity

the fitted function is taken to be the pdf of the reconstructed Higgs boson mass for the given event type.

Figure 8.4: The probability density functions for the reconstructed Higgs boson mass. The three functions in each plot correspond to three event types. Solid line is for an hZ signal, dashed line is for an hA signal, and dotted is the sum of the background processes. The four plots show the three separate selection branches, hZ exclusive, hA exclusive and hZ.hA overlap. The two plots shown for the overlap are derived from the same selected events, but the jet assignments in the events is chosen with two distinct methods labelled 'as hZ' and 'as hA'. The hZ sample is generated with $m_h = 105 \text{ GeV}/c^2$, while for the hA sample $m_h = 90 \text{ GeV}/c^2$.

For example in figure 8.4 the pdfs are plotted for each of the three branches. Since the hA and hZ analysis have different ways of selecting the choice of the jet pairs to

assign to each boson, the overlap branch has two plots. In one plot the choice is as in the hZ analysis and in the other it is as in the hA analysis. The reconstructed Higgs mass, m_{reco} is

$$m_{reco} = m_{12} + m_{34} - 91.2 \qquad (8.3)$$

In this way the reconstructed Higgs boson mass for the hA sample does not approximate m_h, but is rather centred at a different value. However the discrimination of signal is unaffected by scalings and shifts in the definition of the discriminating variable.

Figure 8.4 shows the probability density function for the reconstructed Higgs boson mass for hZ, hA and the total background. The signal samples have $m_h = 105$ GeV$/c^2$, for the SM sample and $m_h = 90$ GeV$/c^2$ for the MSSM sample. It can be seen that similar resolution on the hZ signal is achieved in the hZ exclusive and overlap branch when the overlap pairing choice is made by the hZ method. However in the hA exclusive selection it can be seen that the resolution on hZ signal is extremely poor. It is understood that the hA pairing, which is always used in the hA exclusive branch, frequently mixes the jets between the two bosons in the hZ signal. Therefore the mass resolution is expected to be poor. Likewise the hZ mass resolution in the overlap region when pairing is treated as in the hA analysis is degraded with the addition of a long tail to low masses.

Interestingly it can be seen that a visual comparison of hA signal pdfs in figure 8.4 do not show as large a variation in resolution between the hZ pairing and the hA pairing method. Indeed there is a larger probability for the hA signal to lie within the centre of the mass peak when the hZ pairing method is used in the overlap branch compared to when the hA pairing method is used.

The observed differences in resolution, seen in figure 8.4 on both the hA and hZ signals, between hA and hZ pairing methods may be understood by a consideration of the kinematics involved. Both the hZ and hA samples shown in figure 8.4 are close to the kinematic threshold. The centre of mass energy is 199.5 GeV, therefore the hZ sample is 3.3 GeV$/c^2$ below threshold and the hA sample is about 10 GeV$/c^2$ below. The hZ pairing choice fairs well in both cases, as in both topologies are comparable (recall that the hZ pairing is based upon decay angles, see section 6.2.2). Whereas the

hA pairing requires the selection of the pairing which yields the smallest mass difference between the two bosons, a bad assumption for the hZ signal where $m_Z = 91.2$ GeV/c^2, $m_h = 105$ GeV/c^2. Therefore as expected the hA pairing method does not achieve a good reconstructed mass resolution for this hZ signal.
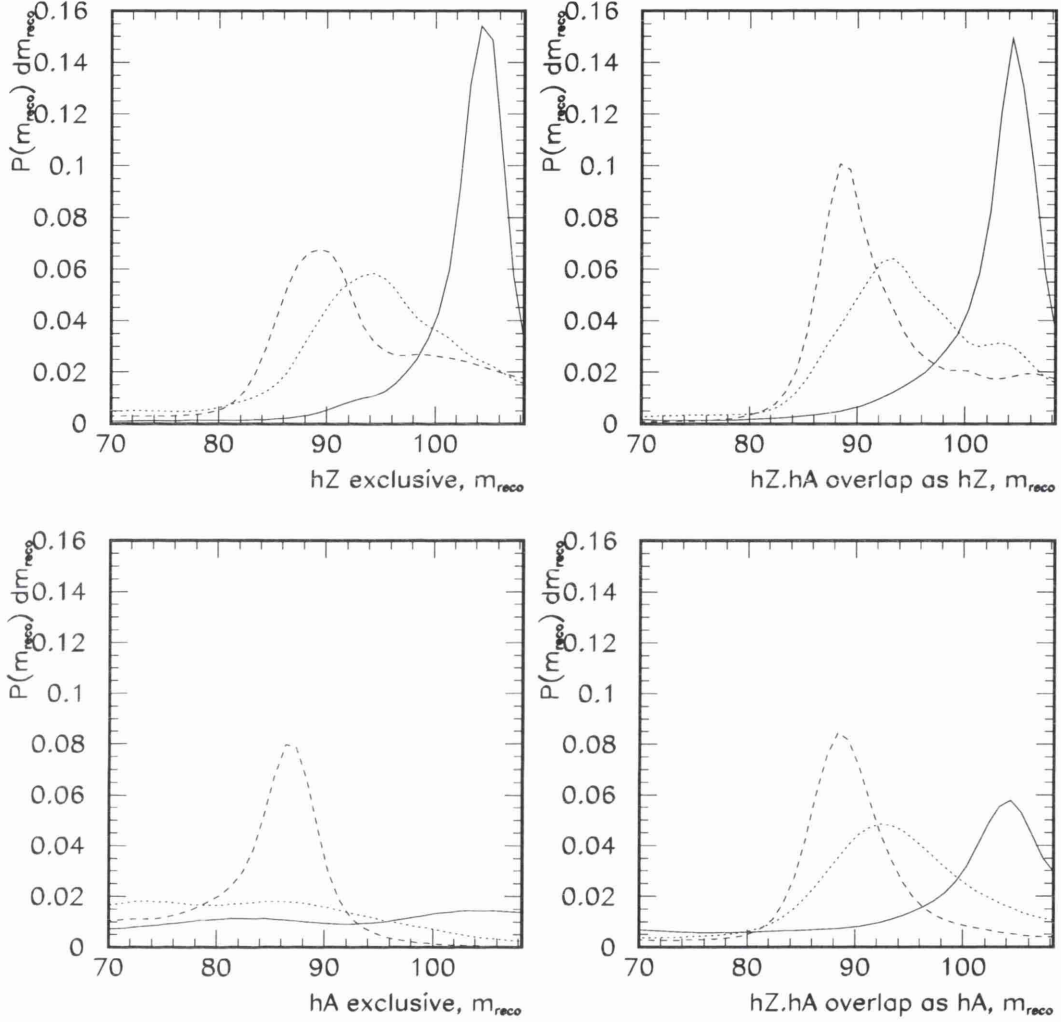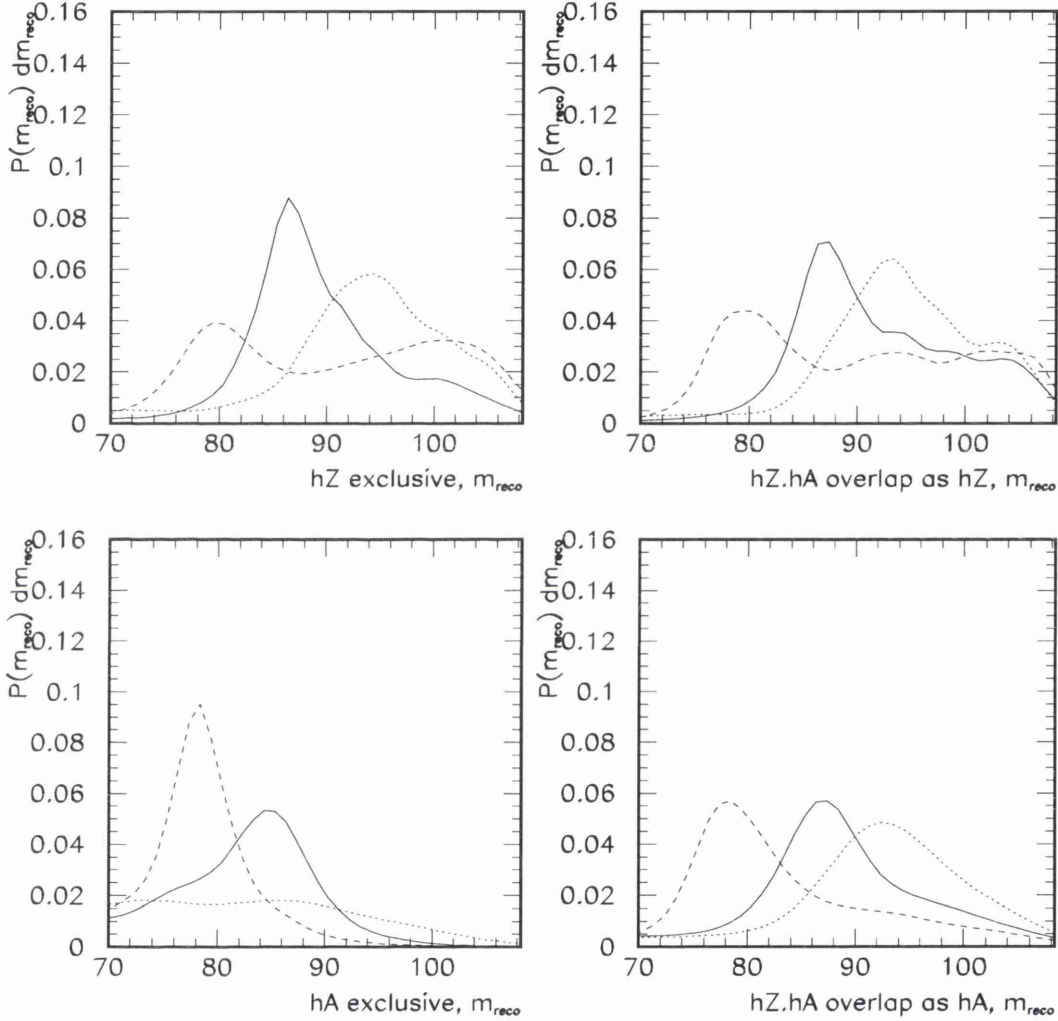

Figure 8.5: The probability density functions for the reconstructed Higgs boson mass. The three functions in each plot are for the three event types. Solid line is for an hZ signal, dashed line is for an hA signal, and dotted is the sum of the background processes. The four plots show the three separate selection, hZ exclusive, hA exclusive and hZ,hA overlap branch. The two plots shown for the overlap branch are derived from the same selected events, but the jet assignments in the events is chosen with two distinct methods labelled *as hZ* and *as hA*. The centre of mass energy is 199.5 GeV. The the SM and the MSSM Higgs boson samples were generated with $m_h = 85$ GeV/c^2.

The plots shown in figure 8.5 are similar to those in figure 8.4, but now with $m_h = 85$ GeV/c^2 for both the hZ and hA signal samples. The broadening of the hZ pdf compared to that of the sample closer to threshold shown in figure 8.4 is evident, together with a tail to high reconstructed mass. The peak of the hZ signal is also seen to be shifted from the expected peak at the simulated Higgs boson mass. This is understood to be due to the long tail of events at high reconstructed mass. In the case of hA signal it can be seen that when the hA pairing method is used in the hA exclusive and overlap branch an enhanced peak is now obtained with respect to the hZ pairing method.

The conclusion is that the hA pairing method results in good mass resolution for the hA signal but only gives a good resolution of the hZ signal when $m_h \sim m_Z$. The hZ pairing method tends to work well for a signal topology that is near kinematic threshold, and in that region may perform reasonably well on the hA signal. Away from kinematic threshold the hZ pairing method yields poorer mass resolution.

The region of greatest interest for the SM search is that where hZ signal is produced near kinematic threshold, but the same is not true for the MSSM hA search. This explains the need to have two alternative pairing methods for the two signal types.

The impact of a candidate event on the final likelihood ratio, for a given a signal scenario and Higgs boson mass hypothesis, is a multiplication by a factor:

$$1 + \frac{s_i S_i(m_h, m_{ij})}{b_i B_i(m_{ij})} \tag{8.4}$$

where s and b are the expected number of signal and background events, m_{ij} is the reconstructed mass of the candidate, m_h is the Higgs boson mass hypothesis and S_i and B_i are the functions described above. (See equation 5.7).

The likelihood ratio is often plotted as $-\ln(Q)$, in which case each candidate contributes a term of a sum. Hence to evaluate the impact of a candidate, one must consider a given Higgs boson mass hypothesis and a particular signal scenario, i.e., SM or MSSM, and then take the value of $\ln(1 + sS/bB)$. Figure 8.6 shows that quantity for the hZ signal, mass hypothesis of $m_h = 105$ GeV/c^2 or hA pair production with the hypothesis $m_h = 90$ GeV/c^2 and $\sin^2(\beta - \alpha) = 0$, for candidates at $\sqrt{s} = 199.5$ GeV.
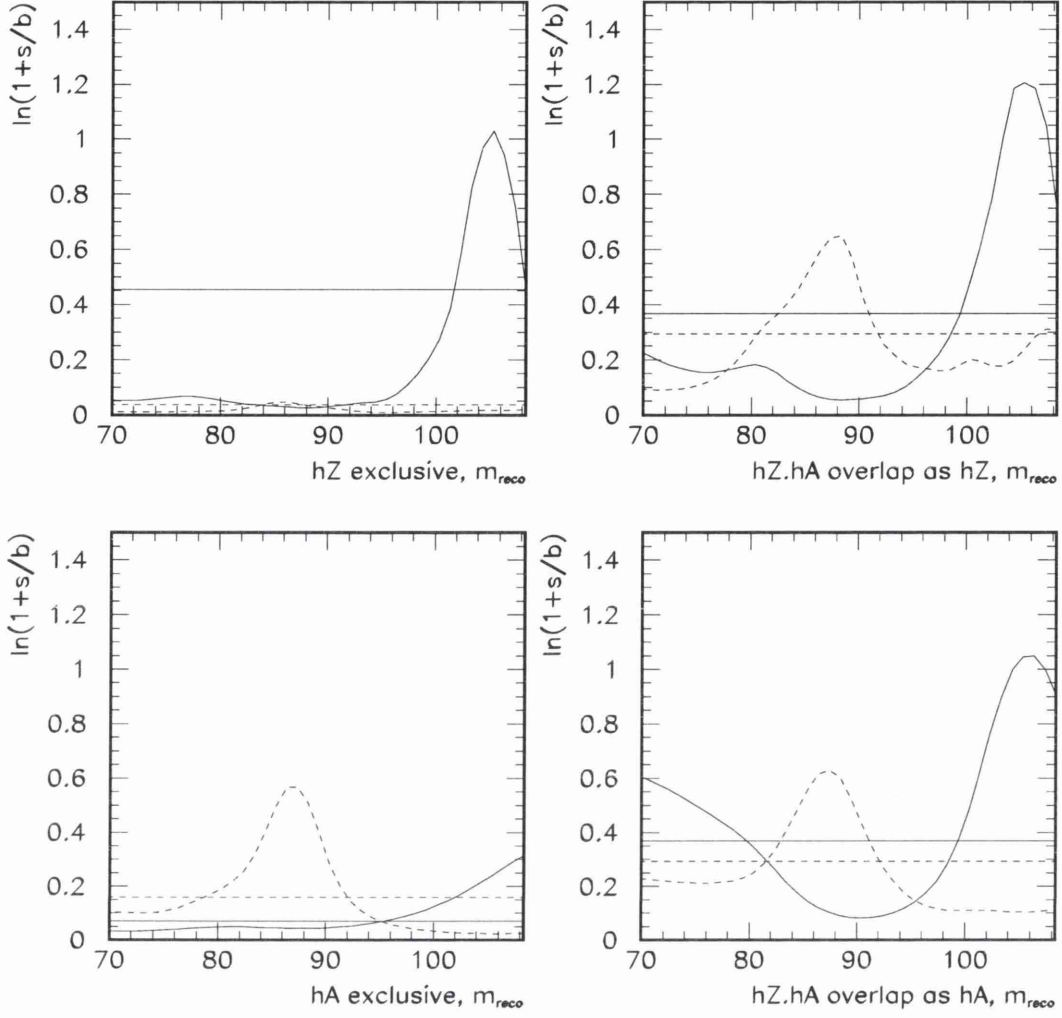
Figure 8.6: The contribution to the log likelihood ratio, $\ln(Q)$, for a candidate recorded at $\sqrt{s} = 199.5$ GeV in each of the selections and possible pairing methods. The two solid curves in each plot correspond to the hypothesis of an hZ signal only (i.e., a SM signal) with $m_h = 105$ GeV/c^2. The flat line is the value obtained without the use of the reconstructed Higgs boson mass as a discriminant. The dashed curves show the hypothesis of hA production (i.e., an MSSM signal with $\sin^2(\beta - \alpha) = 0$), with $m_h = 90$ GeV/c^2.

The value of:

$$\ln(1 + s/b) \tag{8.5}$$

is also shown. Equation 8.5 represents the contribution to $\ln(Q)$ by any candidate selected, if there are no extra event-by-event discriminating variables used. Equation 8.5 can be seen as giving a measure of the intrinsic performance of the selection analysis.

For instance, it can be seen that for SM hZ production, under the hypothesis that the Higgs boson mass $m_h = 105$ GeV/c^2, a candidate collected at $\sqrt{s} = 199.5$ GeV in the hZ.hA overlap branch could have the largest impact on $\ln(Q)$. The contribution is maximised when $m_{reco} \sim 105$ GeV/c^2, (when m_{reco} is found using the hZ pairing method), which can be understood since $m_{reco} \sim 105$ GeV/c^2 is the most likely reconstructed mass of a Higgs boson event under the hypothesis that the Higgs boson mass is 105 GeV/c^2.

8.2 Systematic studies

Simulated event samples are used extensively in the Higgs boson search. Both expected signal and background efficiencies are determined from the simulated samples. Therefore the selection efficiencies are subject to possible systematic biases arising from inaccuracies that may be present in the modelling of the underlying physics processes and detector response in the simulation. Sources of systematic error are identified and are varied within a range representative of the uncertainty on them. The size of systematic error on the selection efficiency is determined and included in the confidence level calculation necessary to interpret the final search results.

Sources of systematic error and the method used to estimate their size are discussed in the following subsections.

8.2.1 Gluon splitting

Gluon splitting refers to the process $g \to q\bar{q}$. Gluons in the final state of an e^+e^- annihilation may undergo gluon splitting, and where the $q\bar{q}$ are either c or b quarks these events will be more likely to be selected as Higgs boson candidates, due to the b-tagging requirement.

The gluon splitting systematic is due to the uncertainty in the frequency with which $g \to q\bar{q}$ where q is either c or b. It is known that the frequency of the process is modelled poorly in the simulated data[56], and it is corrected for in the case of the QCD background, where it has a significant effect on the selection rate. The correction weights are listed in table 8.8.

161

Process	Correction Factor
$g \rightarrow b\bar{b}$	1.9
$g \rightarrow c\bar{c}$	1.6

Table 8.8: The gluon splitting correction factors which are applied to the simulated events of the QCD background by event-by-event reweighting.

The systematic error comes about from the uncertainty on the correction. For the purposes of evaluating the systematic the reweighting factors are modified by $\pm 50\%$[56] and the systematic on the QCD background selection efficiency is taken to be the observed change in efficiency.

8.2.2 The Strong Coupling Constant

The uncertainty in the value of α_s[57]:

$$\alpha_s(m_Z) = 0.119 \pm 0.004 \tag{8.6}$$

is considered to propagate directly onto the production cross section for the QCD background process. The systematic is then taken to be a direct $\pm 5\%$ uncertainty on the expected number of background events from the QCD background.

8.2.3 b-tagging related systematics

Since the four-jet analysis relies heavily on b-tagging to reduce the background, it is vital to consider sources of systematic uncertainty in the b-tagging performance. There are four systematic sources considered.

• **B hadron lifetime** The B hadron lifetime determines the average length that a B hadron will travel for in the detector before decaying, i.e., the decay length. Two of the inputs to the neural net b-tagger (see section 4.3.6) are sensitive to the decay length. The impact parameter tag, $\mathcal{P}_{jet}$, from QIPBTAG and the secondary vertex fit,

$\Delta\chi^2$, from QVSRCH both rely on the measurable decay length of the B hadrons. Uncertainty in the decay length will lead to uncertainty in both QIPBTAG and QVSRCH performance.

The systematic is evaluated by reweighting events. With the known lifetime used in the Monte Carlo simulation and the particular decay length on an event-by-event basis, the simulated sample is reweighted to correspond to a sample with a different lifetime. The size of the systematic is taken to be the change in efficiency seen when the lifetime of the B hadrons are changed by $\pm 1\sigma$.

- **B hadron decay multiplicity** The average number of charged particles which result from the decay of a B hadron will also impact the b-tagging performance. The jet multiplicity is an explicit input to the neural net b-tagger and in addition a change in the average number of charged daughter products will also effect the performance of QIPBTAG and QVSRCH. The systematic is evaluated by event-by-event reweighting. The size of the systematic is taken to be the change in efficiency seen when the charged multiplicity of the B hadrons are changed by $\pm 1\sigma$.

- **b and c quark fragmentation parameters** ϵ_b, ϵ_c During confinement (see section 2.3) the colour carrying quarks are transformed into a several net colour neutral hadrons. In the case of a b quark the resulting hadrons will include a B hadron. The momentum of the B hadron is usually similar to that of the original b quark, but not exactly. Confinement is not rigorously understood so phenomenological models are used. The relationship between the momentum of the original b quark and the momentum component of the B hadron in the direction of the original b quark is modelled in the simulated samples using the Peterson fragmentation function[46].

$$D_Q^H(z) \propto \frac{1}{z}\left(1 - \frac{1}{z} - \frac{\epsilon_Q}{1-z}\right)^{-2} \tag{8.7}$$

where

$$z = \frac{(E + p_\parallel)_H}{(E + p)_Q} \tag{8.8}$$

and H and Q signify the hadron or quark, E is the energy of the hadron or quark, p the momentum of the quark and $p_\parallel$ is the momentum component of the hadron in the

direction of the original quark. D_Q^H is then the probability density function describing the distribution of z. Thus ϵ_Q is the tunable parameter in the Peterson function that characterises D_Q^H.

The simulated events are produced with $\epsilon_b = 0.0035$. Fits to data suggest a value for $\epsilon_b = 0.0045 \pm 0.0014$[58]. The systematic associated to the b quark fragmentation is then the efficiency change observed by reweighting the simulated events to $\epsilon_b = 0.0059$ and $\epsilon_b = 0.0031$.

In a similar way the c quark fragmentation into charmed mesons is also modelled by the Peterson fragmentation function. Since charmed mesons also posses significant lifetime (see table 4.1) they are a source of mis-tagged b-jets. Therefore there is also a systematic uncertainty associated with the ϵ_c parameter. In the simulated events $\epsilon_c = 0.040$. For the purpose of the evaluation of the systematic the uncertainty on ϵ_c was taken to be $\epsilon_c = 0.040 \pm 0.008$[59]. A systematic was assigned in the same way as for ϵ_b.

8.2.4 Selection variables

Systematic effects on selection efficiency are also assigned for five different four-jet selection variables. It is hypothesised that the modelling of variables may be deficient in the simulated events for an unknown reason. To determine the upper size of any possible modelling problems the combined expected background is compared to the observed dataset. Both the simulated data and the real data are selected at the pre-selection level. At the pre-selection level any signal content in the data would be negligible and in addition the larger number of data events reduces the impact of statistical fluctuations.

In each variable to be compared, binned distributions over representative ranges are prepared. In order to remove the overall event rate fluctuations both distributions are normalised to unit area. Bin-by-bin reweighting values are found for each variable by finding the ratio of the data distribution to simulated distribution.

The systematic associated with each selection variable for each type of simulated event is then found. The size of each systematic is evaluated in turn by reweighting the simulated events according to the prepared bin-by-bin reweighting values. Half of the

Systematic description	hZ	QQ	WW	ZZ
$\pm 50\%$ $g \to b\bar{b}/c\bar{c}$ correction	—	± 4.4	—	—
$\alpha_s \pm 5\%$	—	± 5.0	—	—
B lifetime +1 sigma	+0.55	+1.1	-0.0014	+0.60
B lifetime -1 sigma	-0.59	-1.1	-0.0054	-0.63
B mult +1 sigma	+1.5	+3.7	-0.64	+1.8
B mult -1 sigma	-1.4	-4.4	+0.77	-1.8
B frag ϵ_b=0.0031	+0.26	+1.3	—	+0.30
B frag ϵ_b=0.0059	-1.3	-4.9	—	-1.5
C frag ϵ_c=0.032	+0.21	-1.1	—	-0.03
C frag ϵ_c=0.048	-0.15	+0.91	—	+0.019
y_{34}	-0.81	-3.3	-2.5	-3.2
Θ	+0.013	-0.74	+0.93	-0.13
γ	+0.15	-3.4	-1.0	-1.1
m_{12}	-0.62	-2.5	-1.2	-0.66
m_{34}	+0.22	+0.29	+1.2	-0.28
Total	$\pm 1.83\%$	$\pm 8.94\%$	$\pm 1.80\%$	$\pm 2.72\%$

Table 8.9: Results of systematic studies, performed at 188.6 GeV. The size of the systematic effect associated to the event selection efficiency is shown in percent. The selection used was the hZ exclusive plus overlap branch. The signal shown is for a standard model Higgs boson mass of $m_h = 95$ GeV/c^2. The totals are the sum in quadrature of the components shown.

observed change in the selection efficiency is then taken to be the size of the associated systematic.

The five selection variables considered are y_{34}, Θ, γ, m_{12} and m_{34}. (See chapter 6 for an explanation of the variables).

Table 8.9 lists the sources of systematic error discussed together with an evaluation of the size of the effect on the Higgs boson selection efficiency and expected background rate.

The final systematic uncertainty on the signal and each background component from the study summarised in table 8.9 is taken to be the sum of the individual estimates in

quadrature, as the source of each is assumed to be independent of that of the others. The effect is assumed to be the same for each of the three branches of the analysis.

8.3   Further systematic effects

In addition to the sources already considered two more are evaluated. Due to their strong dependence on detector geometry, type of event and possibly their large value, the size of the systematic effects have been evaluated at the highest energy, ~ 202 GeV and found separately for each of the three branches of the four-jet cut analysis. Table 8.10 shows the result of the study. The sources of the systematic effects are described below, together with the method used to evaluate their size.

Event Type	hZ exclusive	Overlap	hA exclusive
B smearing			
QQ	-1.52	-10.49	-7.75
WW	-4.43	-19.05	-13.81
ZZ	+1.31	-4.97	+0.49
hZ	+0.87	-2.82	-1.55
hA	+2.81	-0.54	-1.20
Jet smearing			
QQ	-1.41	-0.44	+2.02
WW	-1.10	-5.56	+6.82
ZZ	-0.37	+0.65	+1.97
hZ	-0.065	+0.38	+1.55
hA	-1.29	+0.23	+0.31

Table 8.10: The systematic assigned to the uncertainty on selection efficiency due to b smearing and jet smearing and rescaling, determined using the 201.6 GeV simulated events. The numbers shown are half of the relative change in selection efficiency, in percent, when either correction is removed. The systematic is taken as a symmetric quantity with this magnitude. The sign in the table indicates the direction of the change found in the study. The signals are Standard Model hZ, $m_h = 107$ GeV/c^2 and hA pair production according to the MSSM, $m_h = 90$ GeV/c^2.

8.3.1 Jet smearing and rescaling

Jet smearing is a correction to the measured position of the clustered jets in simulated events. The jets have an extra, random, change in their direction added. This is done because the measured resolution of simulated events is better than that found in real data. Jet rescaling is when the energy and mass of a jet is rescaled by a factor, to improve agreement between simulated and real events. The smearing and rescaling parameters were determined[60] using real and simulated data at the Z peak.

The rescaling performed was a -0.1% change for jets which lie in the barrel of the detector, and a change of +0.9% for jets in the endcaps of the detector. Here the jet is considered to enter the detector endcaps if $|\cos\theta| > 0.8$.

The smearing of the position of the jet is done as:

$$\phi \to \phi + \frac{G(0.1)}{\sin(\theta)} \tag{8.9}$$

and

$$\theta \to \theta + G(0.2) \tag{8.10}$$

where the jet points in the direction (ϕ, θ) (measured in degrees) and $G(x)$ is a random variable distributed as Gaussian of width x and mean 0.

8.3.2 b smearing

b smearing refers to extra smearing of the track parameters $(D0, Z0)$ in simulated events, see section 6.1 and section 4.4.7 for a description of the two track parameters and an example of the smearing. The track parameters are relevant when calculating track impact parameters and so $\mathcal{P}_{jet}$, from QIPBTAG, is sensitive to problems in the modelling of the track parameters.

8.4 Total uncertainty on expected event rate

In addition to the total systematic uncertainty on the expected event rate, a statistical component is also present, due to the use of a finite number of simulated events. The sample size and the average selection efficiency (over all energies) for each type

of event was used to estimate the size of the statistical error. Table 8.11 lists the estimated statistical errors for each branch and event type. The total size of W^+W^- and QCD background simulated samples generated at 192 and 196 GeV and the samples generated at 200 and 202 GeV were different (see table 8.1). Hence these backgrounds have a statistical error which is different between energies.

Event Type	hZ exclusive	Overlap	hA exclusive	All branches
$QQ_{192,196}$	±8.3	±13.2	±8.9	±5.5
$QQ_{200,202}$	±5.9	±9.4	±6.3	±3.9
$WW_{192,196}$	±7.4	±23.5	±11.9	±6.1
$WW_{200,202}$	±5.2	±16.6	±8.4	±4.3
ZZ/energy	±3.5	±5.2	±7.7	±2.7
QQ total	±3.8	±6.1	±4.1	±2.5
WW total	±3.4	±10.8	±5.4	±2.8
ZZ total	±1.9	±2.8	±4.2	±1.5
$Bgd_{192,196}$	±3.4	±5.5	±5.9	±2.6
$Bgd_{200,202}$	±2.7	±4.5	±4.4	±2.1
Total Bgd	±1.6	±2.7	±2.8	±1.3
hZ/energy	±2.7	±3.1	±6.1	±1.9
hA/energy	±3.6	±1.3	±2.3	±1.1
hZ total	±1.7	±2.0	±3.7	±1.2
hA total	±2.0	±0.7	±1.3	±0.6

Table 8.11: The statistical component of the uncertainty in the expected number of events from background processes. The errors are quoted as relative fractions, in percent.

The systematics from table 8.9 and table 8.10 are combined together. The signs of the effects in the b smearing and jet smearing studies are taken into account when finding the total systematic effect.

- To obtain the total systematic for a given event type the three branches are combined according to the number of events expected in each branch of the analysis.

- To obtain the total systematic for each branch the event types are combined together in accordance with the total expected numbers of each type.

The results of the combinations are shown in table 8.12.

Event Type	hZ exclusive	Overlap	hA exclusive	All Branches
QQ	±9.2	±13.8	±12.0	±10.5
WW	±4.9	±19.9	±15.5	±8.1
ZZ	±3.0	±5.7	±3.4	±2.8
Total bgd	±4.5	±8.6	±9.4	±6.0
hZ	±2.0	±3.4	±2.9	±2.0
hA	±3.6	±2.0	±2.2	±1.9

Table 8.12: The relative estimated systematic uncertainty on the selection efficiency, in percent.

The final estimated uncertainty is taken to be the sum in quadrature of the statistical and systematic components.

8.4.1 Summary of expected events

The actual number of expected events of each type, and in each branch are shown in table 8.13.

8.4.2 Observations from experiment

The final information required to calculate the search results are the candidates observed in the data recorded the ALEPH detector. The results needed are the number of selected candidates for each of the three branches and the reconstructed Higgs boson mass of each candidate. In the overlap branch the Higgs boson mass may either be reconstructed using the hA or the hZ pairing method. Therefore two reconstructed masses are needed for candidates selected in the overlap branch. Table 8.14 shows the details of the Higgs boson four-jet candidates found in the ALEPH data.

Four-Jets Branch		Signal Events Expected		Background Events Expected				Events Observed
		hZ	hA	ZZ	WW	$f\bar{f}$	Total	
192	hZ and hA	0.024±0.001	0.208±0.005	0.539±0.042	0.039±0.012	0.271±0.052	0.850±0.087	0
	hA exclusive	0.0085±0.0006	0.055±0.002	0.208±0.017	0.119±0.023	0.74±0.11	1.07±0.12	0
	hZ exclusive	0.029±0.001	0.026±0.001	1.245±0.057	0.350±0.031	0.729±0.090	2.32±0.13	2
	Total	0.0615±0.0017	0.289±0.006	1.993±0.078	0.508±0.051	1.74±0.21	4.24±0.28	2
196	hZ and hA	0.14±0.01	0.747±0.017	1.73±0.13	0.077±0.024	0.94±0.18	2.75±0.28	1
	hA exclusive	0.041±0.003	0.280±0.009	0.667±0.056	0.406±0.079	1.75±0.26	2.83±0.31	2
	hZ exclusive	0.20±0.01	0.107±0.005	3.74±0.17	0.949±0.084	1.88±0.23	6.57±0.37	6
	Total	0.381±0.010	1.134±0.025	6.14±0.24	1.43±0.14	4.58±0.55	12.15±0.79	9
200	hZ and hA	0.76±0.04	0.935±0.021	1.79±0.14	0.099±0.026	0.85±0.14	2.75±0.27	1
	hA exclusive	0.14±0.01	0.551±0.018	0.937±0.079	0.471±0.083	1.81±0.24	3.21±0.33	6
	hZ exclusive	1.12±0.04	0.123±0.006	3.91±0.18	1.053±0.076	2.16±0.24	7.13±0.38	7
	Total	2.02±0.06	1.609±0.035	6.64±0.26	1.62±0.15	4.82±0.54	13.09±0.83	14
202	hZ and hA	0.59±0.03	0.460±0.011	0.910±0.070	0.062±0.016	0.412±0.069	1.38±0.13	1
	hA exclusive	0.10±0.01	0.341±0.011	0.484±0.041	0.196±0.034	0.96±0.13	1.64±0.17	0
	hZ exclusive	0.87±0.03	0.065±0.003	1.915±0.088	0.579±0.042	1.13±0.12	3.63±0.19	1
	Total	1.56±0.04	0.866±0.019	3.31±0.13	0.837±0.077	2.50±0.28	6.65±0.42	2
hZ and hA total		1.514±0.060	2.350±0.048	4.98±0.32	0.276±0.063	2.48±0.37	7.73±0.70	3
hA exclusive		0.290±0.014	1.227±0.032	2.30±0.12	1.19±0.20	5.26±0.67	8.75±0.86	8
hZ exclusive		2.219±0.059	0.321±0.013	10.81±0.39	2.93±0.18	5.91±0.59	19.65±0.94	16
Grand Total		4.023±0.093	3.898±0.077	18.09±0.56	4.40±0.38	13.65±1.47	36.13±2.20	27

Table 8.13: The expected background and observed candidates for the four-jet analyses. The expected number of signal events for Standard Model Higgs boson production with $m_h = 107$ GeV/c^2 and pair production of h and A Higgs bosons according to the MSSM with $m_h = 90$ GeV/c^2, $\cos^2(\beta - \alpha) = 1$. The quoted error is the sum in quadrature of the systematic and statistical uncertainties.

Selection	$\sqrt{s}$	KRUN	KEVT	m_{reco} as hZ	m_{reco} as hA
hZ exclusive	191.6	49476	930	91.45	–
	191.6	49531	7915	74.78	–
	195.5	50613	2366	82.37	–
	195.5	49885	13478	96.18	–
	195.5	50170	4182	93.57	–
	195.5	50368	8985	85.01	–
	195.5	50252	10525	94.02	–
	195.5	50440	6248	101.92	–
	199.5	50814	1257	90.18	–
	199.5	50829	12526	91.97	–
	199.5	51060	11639	101.31	–
	199.5	51093	3421	74.85	–
	199.5	51311	9998	94.70	–
	199.5	51555	2260	101.14	–
	199.5	52029	2878	97.53	–
	201.6	52094	14362	108.06	–
Overlap	195.5	50037	687	92.22	80.66
	199.5	50857	1323	104.99	64.89
	201.6	51806	5386	103.08	103.08
hA exclusive	195.5	50056	8762		-5.11
	195.5	50269	17538	–	42.83
	199.5	50699	11223	–	78.08
	199.5	51059	9020	–	77.95
	199.5	51111	5183	–	71.42
	199.5	51387	11839	–	67.11
	199.5	51582	15907	–	74.86
	199.5	52313	5381	–	-17.21

Table 8.14: The result of the four-jets cuts analyses on the ALEPH data.

Chapter 9

Higgs boson search results

The results of the four-jet cuts analyses, detailed in chapter 8 are combined with the results of the three final state analyses hll, $h\nu\bar{\nu}$ and $X\tau^+\tau^-$ (see chapter 7). The combination is used to test for Higgs boson production. In the absence of any indication of production, it is possible to set a lower limit on the Higgs boson mass.

9.1 Data recorded by **ALEPH** in 1998

In the case of the Standard Model Higgs boson search a dataset with a high centre of mass energy will quickly become more important to search sensitivity than other datasets collected at lower energies. However the searches for the hA pair production process in the context of the MSSM are most sensitive to the total integrated luminosity of the dataset collected. For this reason the 176 pb^{-1} of data recorded by the ALEPH Collaboration during 1998 at $\sqrt{s} = 188.6$ GeV are also incorporated into the combination.

A summary of the number of expected and observed candidate events from the analysis of ALEPH data at $\sqrt{s} = 188.6$ GeV can be found in table 9.1.

9.2 Mass distributions

For completeness the distribution of the expected and observed events in reconstructed mass are shown here. The total mass plot for the combination is shown in 9.1.

However, it should be noted that the mass plot does not convey all the information

Channel	Expected background	Observed
Four jets	4.8	7
$h\nu\bar{\nu}$	7.2	8
hll	14.2	14
$X\tau^{+}\tau^{-}$	3.6	4

Table 9.1: Summary of the 1998 ALEPH SM Higgs search, for $\sqrt{s} = 188.6$ GeV.
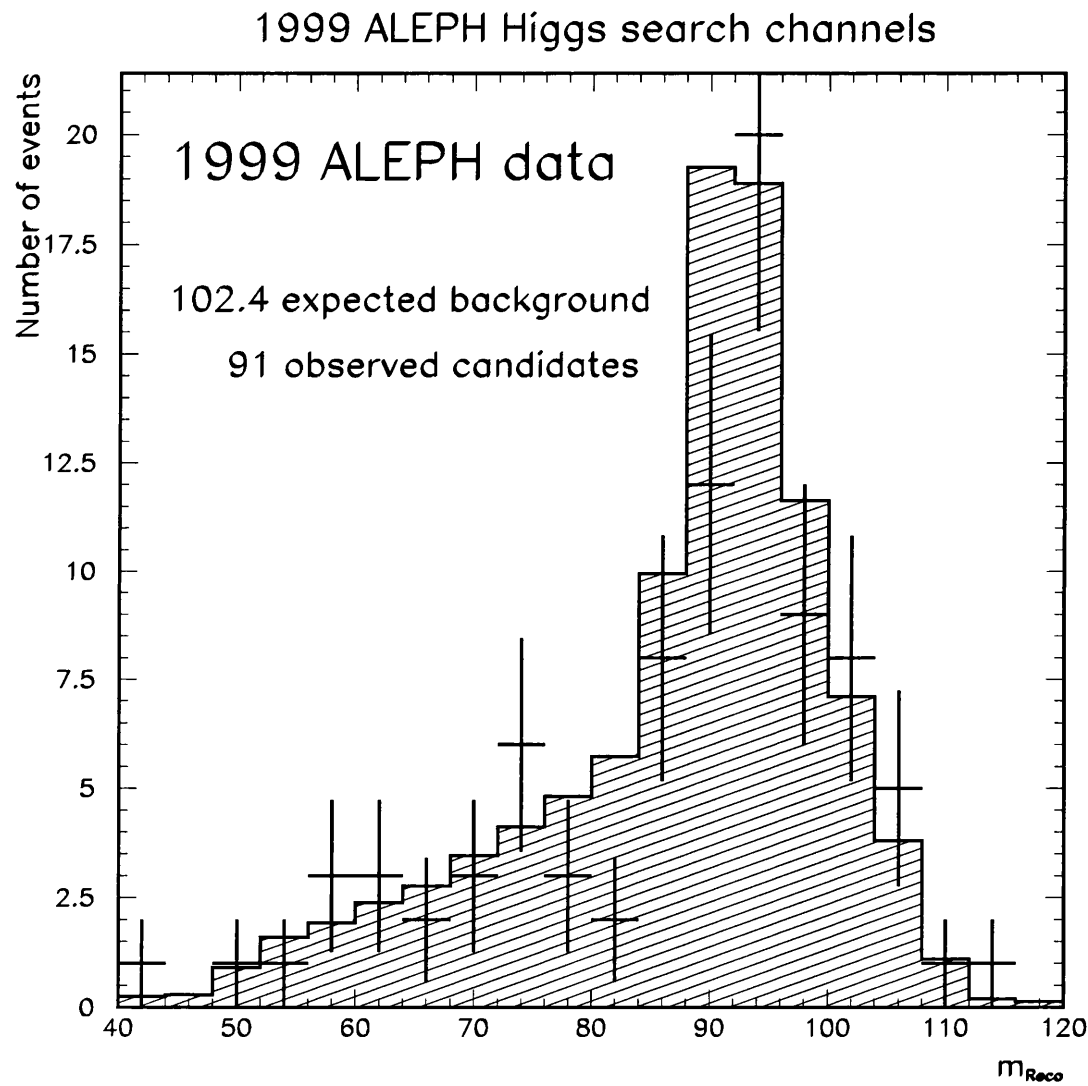

Figure 9.1: Mass plot of all candidates selected from the 1999 ALEPH data in the cuts based neutral Higgs boson search. The crosses are the recorded events while the hatched histogram shows the expected background.

used in the combination. In particular events within a given bin do not necessarily carry equal weight in the combination. The sensitivity depends on search channel, $\sqrt{s}$ and, in the case of the hll analysis, the b-tag.
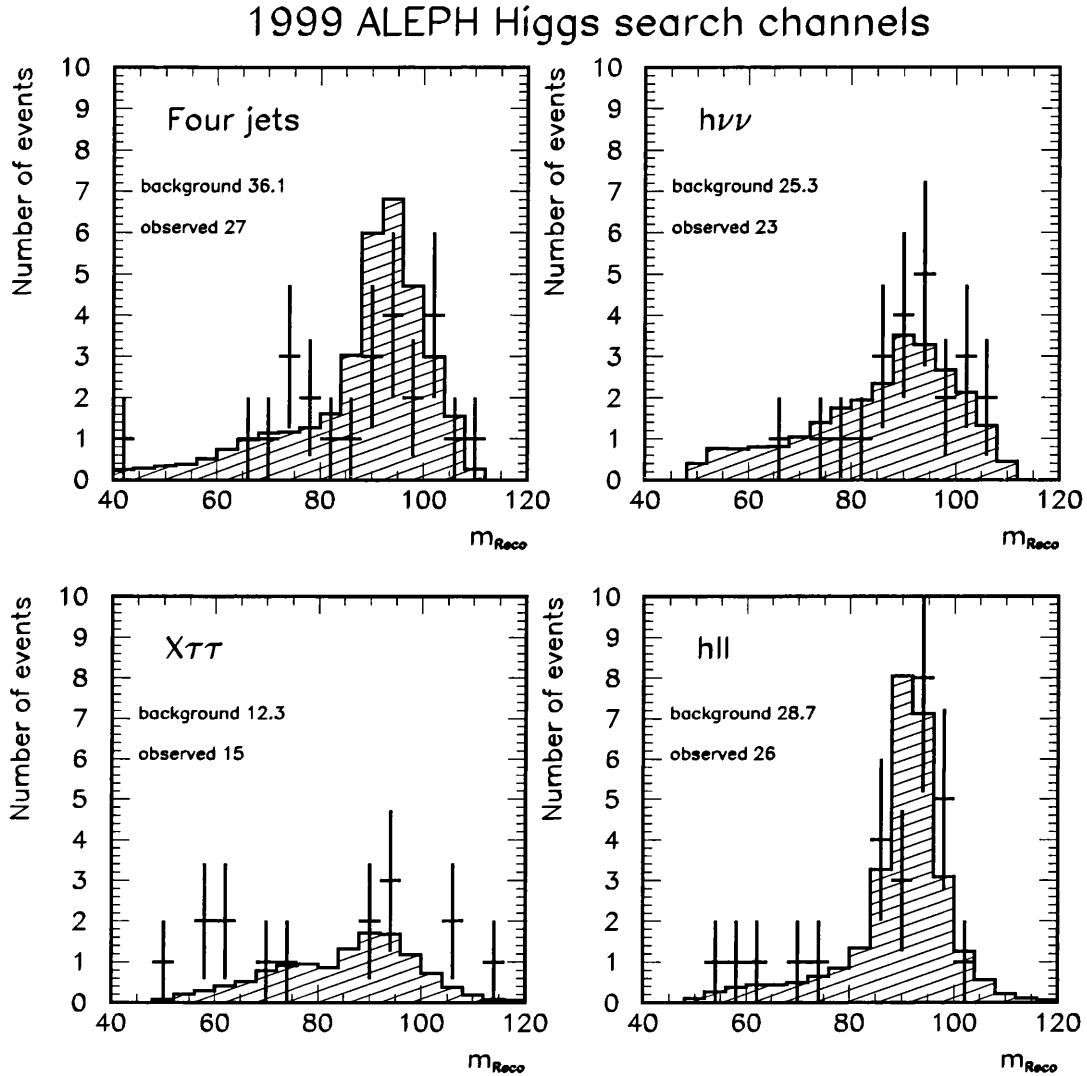
Figure 9.2: Mass plot of all candidates selected from the 1999 ALEPH data, separated into the four final state selections. For the hll analysis a second, b-tag, discriminant is used *(not shown here)*, in addition to the reconstructed Higgs boson mass.

The reconstructed mass distributions for each channel are shown in figure 9.2. The hll analysis uses two discriminating variables, a b-tag as well as the reconstructed Higgs boson mass. However, only the reconstructed Higgs boson mass is shown in figure 9.2, irrespective of the b-tag associated with hll candidates.

In figure 9.3 the four-jet 1999 ALEPH candidates are shown branch-by-branch. The

1999 ALEPH four jets cuts
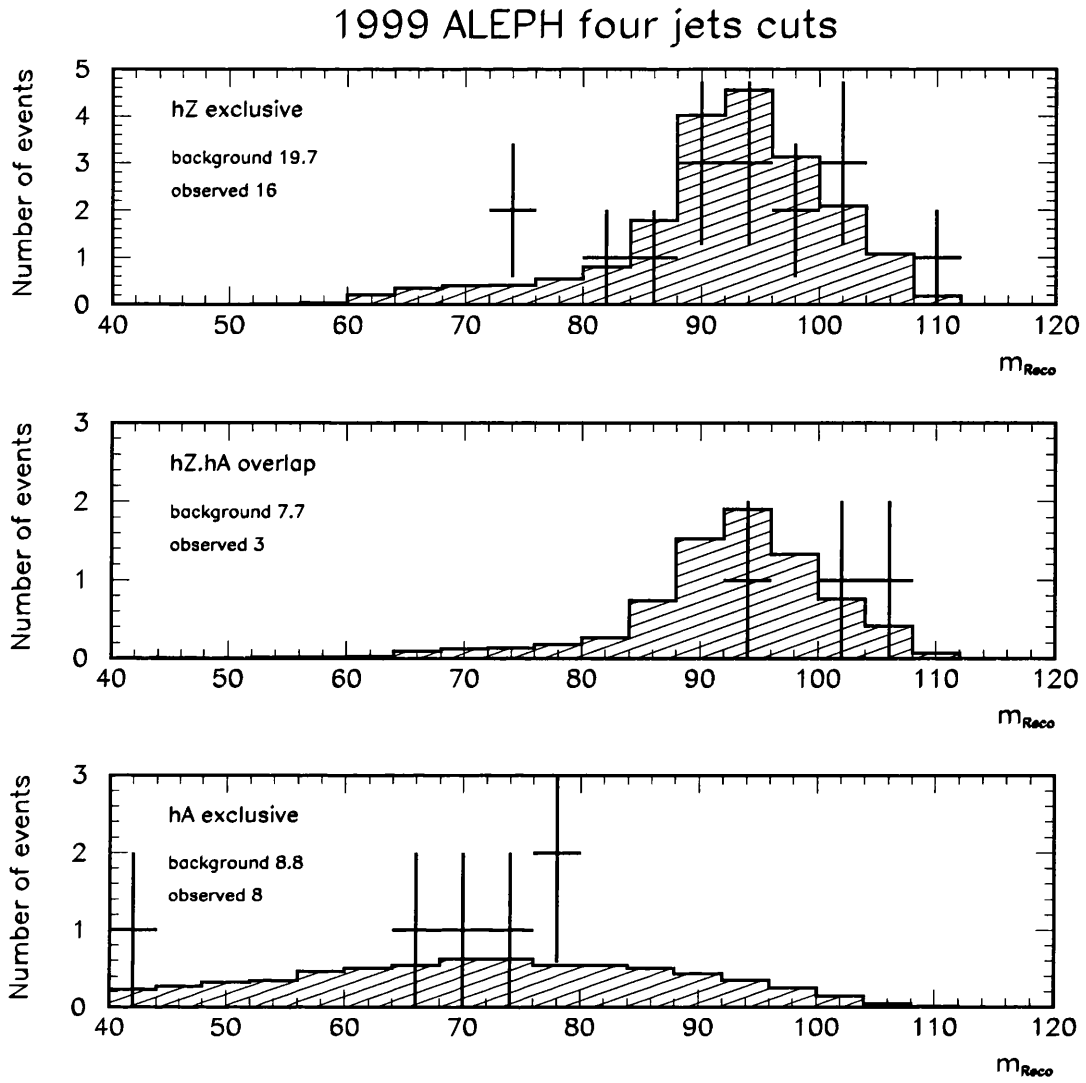
Figure 9.3: The distribution of candidates selected from the 1999 ALEPH data by the four jets cuts based analyses. Each of the three branches are shown separately along with the background only prediction from simulated events.

events which carry the most weight in the four-jet analyses fall in the overlap branch where they are selected both as hZ and hA candidates. Since the hA four-jet analysis requires good b-tagging, with the expectation of four b quarks in the final state, the overlap candidates have clear b signatures and consequently lower background. In this way even for the Standard Model Higgs boson search the combination will weight overlap candidates more than a candidate of equal mass which falls into the hZ exclusive branch.

A subset of the data are shown in figure 9.4. The selection corresponds to the
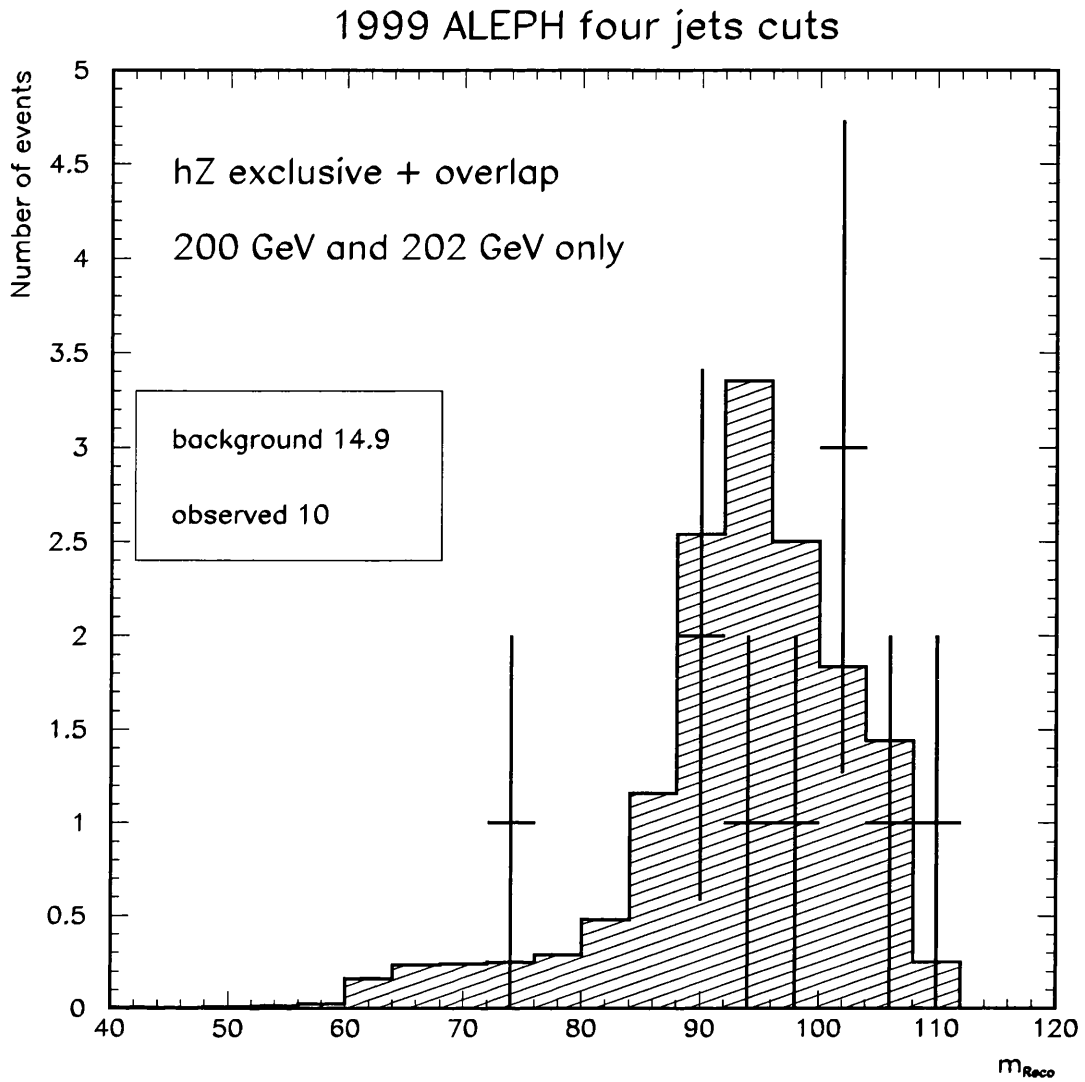
Figure 9.4: The distribution of candidates selected by the four-jet analyses from the highest energy 1999 ALEPH data, recorded at 200 and 202 GeV. The hZ exclusive and overlap are shown, this subset of the data bringing much of the total sensitivity for the Standard Model Higgs boson.

four-jet hZ exclusive and overlap branches, at $\sqrt{s} = 200$ and 202 GeV. It is found that this subset of data are the most powerful components of the four-jet dataset. (A lower mass limit of 105.2 GeV/c^2 at 95% CL would be expected from this sample, in the case that only background events were seen in the data).

9.3 The Standard Model Higgs boson search results

To search for Standard Model Higgs boson production all the analyses are combined. The likelihood ratio is calculated assuming Standard Model production cross section and decay branching ratios. The hA production is given zero production cross section. However, the hZ and hA exclusive and overlap classifications are retained for the four-jet and $X\tau^+\tau^-$ analyses. Although there is no hA production possible the combination still benefits in sensitivity by classing candidates into the statistically independent branches. For the overlap branch the pairing choice and mass reconstruction are done according to the hZ method.

The combination is performed for many Higgs boson hypothesis, for each the corresponding signal component in the likelihood ratio and the signal discriminating pdfs $S_i(m_h, m_{ij})$ are used. The result are the confidence levels on the background-only and background + signal hypothesis, CL_b, CL_{s+b} and derived quantities CL_s and CL_{SE}, as a function of Higgs boson mass hypothesis.

9.4 Sensitivity of the combination components

To understand the sensitivity to Higgs boson production, each of the component analyses in the combination were tested individually. For each the median expected mass limit at the 95% confidence level is calculated. The expected limit is the lower limit on the Higgs boson mass that can be expected in the case that only background is present in the experiment. It is the value of the Higgs boson mass hypothesis for which $\langle CL_{SE} \rangle$ exceeds 5%.

Table 9.2 shows the expected limits at the 95% confidence level obtained with various sets of analyses in the combination. The uncertainty on the expected limit is of the order of $100 \text{MeV}/c^2$ due mainly to systematic uncertainties in the discriminating pdfs. None the less it is instructive to compare the expected limits to the MeV/c^2 level.

From the 1st and 2nd columns in table 9.2 it can be seen that including all search channels at 188.6 GeV gives only a 10.6 MeV/c^2 increase in the expected limit on the SM Higgs search. This supports the hypothesis that, for the Standard Model search,

Component	Included Channels							
$\sqrt{s} = 188.6$ GeV	X							
$\sqrt{s} = 192 - 202$ GeV :								
Four jet	X	X	X$^-$	X				
$h\nu\bar{\nu}$	X	X	X		X			X
hll	X	X	X			X		X
$X\tau^+\tau^-$	X	X	X$^-$				X	X
Expected Limit/ GeV/c^2	107.2555	107.2449	107.2292	105.5530	98.8448	90.0449	85.4619	104.4181
no discriminants	*104.0928*	*104.0732*	*104.0083*	*102.9768*	*94.0915*	*$\sim$ 73*	*$\sim$ 65*	*97.7100*

Table 9.2: Median expected limits for different components in the search for the Standard Model Higgs boson. The limit is lower limit that could be expected to be set on the Higgs boson mass at 95% from an experiment which contains only background. The indication X$^-$ on components from the four jet or $X\tau^+\tau^-$ analyses means that the hA exclusive branches of those selections are *not* included. The last row gives the expected limit if no discriminating variables are used.

the highest energy data tends to dominate the total sensitivity. Interestingly even in this case, when there is no expected hA production, it can be seen from the 2nd and 3rd columns that including the hA exclusive branches in the four jet and $X\tau^+\tau^-$ analyses yields a gain in the sensitivity of 15.7 MeV/c^2. In columns 4 to 7 the four 1999 final states are then tested one by one to check the expected sensitivity of each. It can be seen that the expected limit each can set in isolation is in approximately the order expected from the hZ decay branching ratio. Four jets is seen to be the most sensitive. The addition of the other final state selections yield an extra 1.69 GeV/c^2 on the expected limit. The four-jet analysis is followed by the $h\nu\bar{\nu}$ selection in terms of sensitivity. This agrees intuitively with $\sim$ 60% and 20% signal branching ratio to the two final states.

The hll and $X\tau^+\tau^-$ analyses, with 6.7% and 8.9% respectively of the branching ratio are seen to be reversed in terms of sensitivity. The hll analysis by itself yields a better expected limit than the $X\tau^+\tau^-$ analysis. This is understood to be due to the nature of the τ lepton. The τ lepton decays weakly inside the detector and leads to an experimentally more challenging signature, whereas the *hll* topology has a clearer experimental signature. For $h\tau^+\tau^-$ and $\tau^+\tau^- Z$ the tau selection has typically 30% and 20% signal selection efficiency, respectively. The hll analysis attains 80% efficiency at its working point.

Since it seems that the four jet analysis is bringing almost all of the power to the

combination it is important to note that the other three analyses combined are almost as powerful as the four jet. It can be seen from table 9.2 by comparing columns 4 and 8 that indeed the three combined analyses yield a limit only 1.1 GeV/c^2 below that of the cuts analysis, confirming that as expected from the branching ratios the four jets is only slightly more powerful than the other three searches combined.

To understand the impact of using discriminating variables, in addition to the expected signal and background numbers an explicit test was made. By setting all discriminants to a uniform flat distribution the analyses were reduced to number counting. The likelihood ratio becomes the ratio of Possion terms. When this is done the analyses are seen to retain their order of significance. This implies that the order is determined only by the relative numbers of signal and background events expected. However the individual power of each analysis drops, the four jet sensitivity drops by ~ 2.6 GeV/c^2 and the total of all combined data by ~ 3.2 GeV/c^2.

It is also noticeable that the size of the gain seen by each analysis when making use of event discriminants is larger for the less powerful analyses. All the analyses are limited by the very fast drop in hZ production cross section near the kinematic threshold. As the combined sensitivity of the analyses approaches this region the gains possible by using extra discriminants, or collecting more luminosity, fall quickly.

9.5 Compatibility of observation with background production

The combined data set is checked for compatibility with the background only hypothesis. If no significant excess is seen, a lower limit may be set on the Higgs boson mass. If a significant excess is seen (i.e., incompatible with a background fluctuation) it is an indication of discovery. To check the data to expected background compatibility, the confidence level on the background hypothesis, CL_b, is computed. The result for the full combination is shown in figure 9.5. The solid horizontal line in the figure indicates the expected value of CL_b and takes the value ~ 0.5. Small deviations away from the value 0.5 may occur due to the inclusion of estimates of the effects of systematic errors.

The observed CL_b shows no significant deviation away from 0.5. Table 9.3 shows
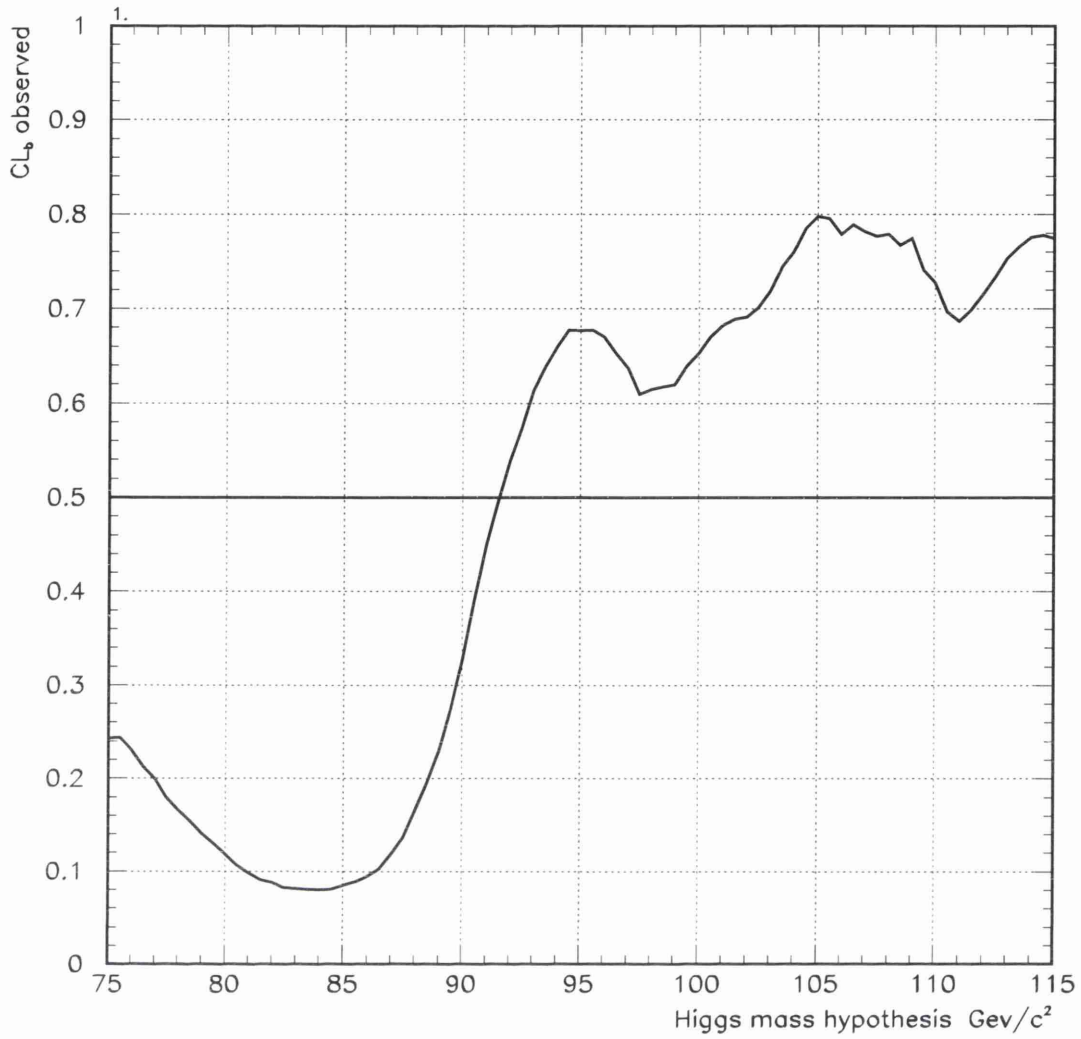
Figure 9.5: The confidence level on the background only hypothesis, CL_b. Deviation of CL_b above (below) 0.5 indicated an excess (deficit) with respect to the Standard Model background expectation.

how the CL_b value may be translated into a Gaussian standard deviation. These tables are for a one sided confidence level, since CL_b distinguishes between excess and deficit. Expressing the extremes of CL_b as a significance it can be seen the data is compatible with data to about $\pm 1\sigma$. The most significant excess occurs at a Higgs boson mass hypothesis of ~ 105 GeV/c^2 and has a small significance of $\sim 0.84\sigma$.

Standard Deviations	Confidence Level	Standard Deviations	Confidence Level
+2.45 sigma	0.993	+6 sigma	0.999999999
+2.41 sigma	0.992	+5 sigma	0.99999971
+2.36 sigma	0.991	+4 sigma	0.9999685
+2.33 sigma	0.990	+3 sigma	0.99865
+2.05 sigma	0.980	+2 sigma	0.97725
+1.88 sigma	0.970	+1 sigma	0.84135
+1.75 sigma	0.960	0 sigma	0.50000
+1.64 sigma	0.950	-1 sigma	0.15865
+1.28 sigma	0.900	-2 sigma	0.02275
+0.84 sigma	0.800	-3 sigma	0.00135
+0.52 sigma	0.700	-4 sigma	0.0000315
+0.25 sigma	0.600	-5 sigma	0.000000285
0 sigma	0.500	-6 sigma	0.000000001

Table 9.3: Conversion of a one sided confidence level to a Gaussian standard deviation.

9.6 Setting a limit

In the absence of significant excess in the data a limit is set on the SM Higgs boson mass. To do this the confidence level CL_{SE} is calculated. The expected and observed CL_{SE} are shown in figure 9.6.

A lower limit is set on the Higgs boson mass at 95% confidence level. The limit is the lowest mass hypothesis for which CL_{SE} exceeds 0.05. The median expected limit was calculated to be 107.3 GeV/c^2 while the observed limit from the ALEPH data was 105.2 GeV/c^2.

9.7 The h and A bosons of the MSSM

The search strategy for the h and the A neutral Higgs bosons of the MSSM is very similar to that for the pure Standard Model Higgs boson. The background is unmodified, but for each Higgs mass hypothesis there are two signal components which are added together. The first component is the hZ signal with the SM Higgs production cross section multiplied by the additional suppression factor $\sin^2(\beta - \alpha)$.

The branching ratio of hZ to the four-jet final state is taken to be the same of the Standard Model hZ decay. In fact at $m_h = 90$ GeV/c^2 the hZ to four-jet final state branching ratio is about $\sim 0.18\%$ less than that of the Standard Model. But the b
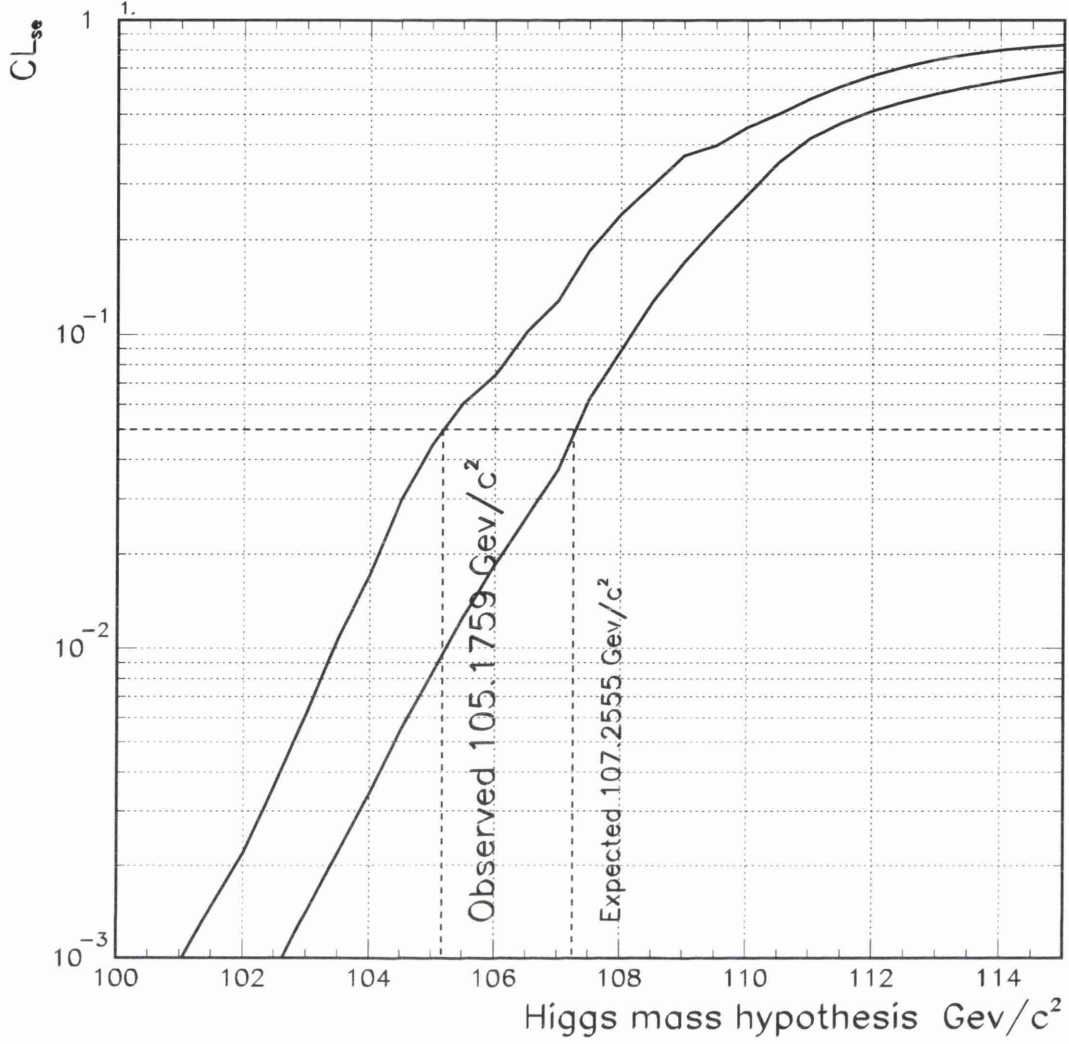
Figure 9.6: The confidence level CL_{SE}. The lowest mass hypothesis for which CL_{SE} exceeds 0.05 gives the lower Higgs boson mass limit at the 95% confidence level.

content will be slightly higher as the decay branching ratio for the MSSM h boson to b quarks is 7.85% higher than that of the Standard Model Higgs boson at this mass. Consequently the selection efficiency for four-jet events within the MSSM could be $\sim 3.8\%$ higher at the working point than expected, assuming the selection had zero efficiency for $h \rightarrow c\bar{c}, gg$. In the event of setting an exclusion limit this leads to a slightly conservative limit.

Assuming that the four jet analysis only has efficiency for the $h \rightarrow b\bar{b}$ events in the four jet final state the effect may be assessed quantifiably by increasing the efficiency accordingly. It was found that the expected 95% CL limit is increased by 222 Mev/c^2

for $\sin^2(\beta - \alpha) = 1$, which should be considered the upper limit on the size of the effect.

The other component in the expected signal for the MSSM search is the hA pair production. The production cross section for hA includes a factor of $\cos^2(\beta - \alpha)$ and is therefore complimentary to hZ production. The mass of the A boson is related to that of the h boson by $\tan \beta$. In the simulation, production and decay calculations this is assumed to be 10, yielding $m_h \simeq m_A$.

The combination is performed over a range of Higgs boson mass hypothesis, $m_{\rm h}$, as in the case of the Standard Model. In addition the procedure is also repeated for steps in $\sin^2(\beta - \alpha)$ over the range 0 to 1. For each value of $\sin^2(\beta - \alpha)$ two expected limits may be derived. The extra degree of freedom comes from the overlap branches, present in the four-jets and $X\tau^+\tau^-$ analyses. The overlap branches may either treat events as hA or hZ. The treatment is always chosen to be the same in both overlaps, but this still leaves a degrees of freedom. In order to optimise the sensitivity the treatment which gives the highest expected limit for each $\sin^2(\beta - \alpha)$ point is chosen. See table 9.4 for the limits found when performing a scan in $\sin^2(\beta - \alpha)$.

$\sin^2(\beta - \alpha)$	Expected as hZ GeV/c^2	Expected as hA GeV/c^2
1.0000	107.2555	107.1458
0.9000	106.9807	106.7670
0.8000	106.4024	106.1635
0.7000	105.6678	105.4508
0.6000	104.7361	104.4985
0.5000	103.4331	103.1055
0.4000	101.1406	100.7169
0.3000	96.2075	95.9394
0.2000	91.9037	91.8297
0.1000	89.7119	89.7048
0.0000	88.5947	88.5948

Table 9.4: Expected limit obtained for each point in a scan of $\sin^2(\beta - \alpha)$, using either hA or hZ treatment in the overlap branches.

It can be seen from table 9.4 that treating the overlap branches as hZ gives a better expected limit for $0.1 < \sin^2(\beta - \alpha) < 1.0$. For the case of pure hA production at $\sin^2(\beta - \alpha) = 0.0$ it is seen that treating the overlap as hA does indeed result in a

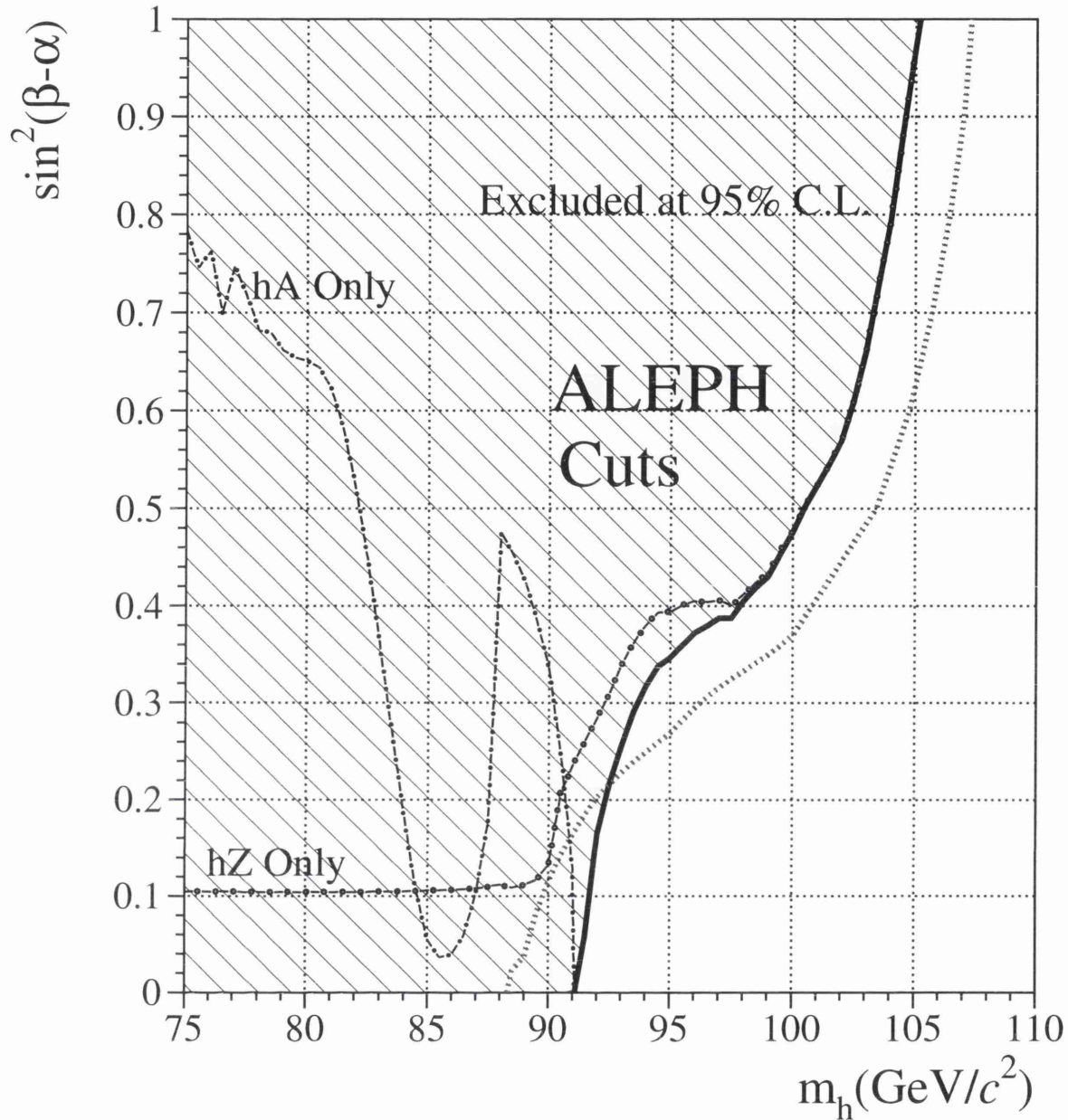slightly better expected limit.

Figure 9.7:   MSSM results in the $\sin^2(\beta - \alpha)$ plane, taken from [61].

The final exclusion plot obtained by the MSSM scan is shown in figure 9.7.

Chapter 10

Summary and conclusions

The existence of one (or more) Higgs bosons is of great importance to our understanding of Nature. The Higgs mechanism is the process whereby the Standard Model is able to account for the observed mass of all the matter that we see. A consequence of the Higgs mechanism would be the existence of at least one Higgs boson.

Although the Higgs boson mass is a free parameter in the Standard Model, fits of the Standard Model to precision electroweak data are able to yield information about the Higgs boson mass. Fits have been found to suggest that the Higgs boson mass should be light, perhaps detectable at the LEP accelerator.

In this thesis, work was detailed which improves the performance of Higgs boson selections by applying modifications to the impact parameter based b-tag. The modifications were adopted by the Higgs group in ALEPH. Also detailed was the search for neutral Higgs bosons in the four-jets channel in ALEPH. The procedure to combine all the Higgs boson search channels was carried out and was described here. Results of the search for neutral Higgs bosons of either the Standard Model or the Minimal Supersymmetric extension of the Standard Model were shown. No evidence was found that the Standard Model Higgs boson had been produced in ALEPH and recorded in the 1999 dataset. The absence of signal allowed a lower mass limit to be placed on the Standard Model Higgs boson. At the 95% confidence level it was found that $m_h > 105.2$ GeV/c^2. The results shown form part of the ALEPH Collaboration's results for searches for neutral Higgs bosons, available in [61].

The search for Higgs bosons will continue. LEP has now closed and the results from

the datasets collected in 2000 (at $200 < \sqrt{s} < 209$ GeV) showed no evidence of Higgs boson production, although there was an excess of Higgs boson like events seen with $m_{\rm h} \simeq 115$ GeV$/c^2$[62, 63]. Future searches will be done at the Tevatron, at Fermilab and later at the LHC at CERN.

Bibliography

[1] ALEPH Collaboration, *ALEPH: A Detector for electron-positron annihilations at LEP*, Nucl. Instrum. Meth. **A294** (1990) 121.

[2] DELPHI Collaboration, *The DELPHI detector at LEP*, Nucl. Instrum. Meth. **A303** (1991) 233-276.

[3] L3 Collaboration, *The Construction of the L3 Experiment*, Nucl. Instrum. Meth. **A289** (1990) 35.

[4] OPAL Collaboration, *The OPAL detector at LEP*, Nucl. Instrum. Meth. **A305**(1991) 275-319.

[5] J. J. Thomson, *Cathode Rays*, Phil. Mag. **44** (1897) 293.

[6] J. D. Bjorken and E. A. Paschos, *Inelastic Electron-Proton and γ-Proton Scattering and the Structure of the Nucleon*, Phys. Rev. **D185** (1969) 1975.

[7] F. Halzen and A. D. Martin, *Quarks and Leptons*, John Wiley and Sons, New York USA, 1984.

[8] ALEPH Collaboration, *A Precise Determination of the Number of Families With Light Neutrinos and of the Z Boson Partial Widths*, Phys. Lett. **B235** (1990) 399-411.

[9] E. Noether, Nachr. Kgl. Ges. Wiss. Göttingen (1918) 235.

[10] The LEP collaborations ALEPH, DELPHI, L3 and OPAL Collab., The LEP electroweak working group *et al.*, *A Combination of Preliminary Electroweak Measurements and Constraints on the Standard Model*, CERN-EP/2001-021.

[11] ALEPH Collaboration, *Measurement of the Z Resonance Parameters at LEP*, European Physical Journal **C14** (2000) 1.

[12] P. W. Higgs, *Broken Symmetries, Massless Particles and Gauge Fields*, Phys. Lett. **B12** (1964) 132.

[13] P. W. Higgs, *Spontaneous Symmetry Breakdown Without Massless Bosons*, Phys. Rev. **D145** (1966) 1156.

[14] J. Goldstone, Nuovo Cimennto **19** (1961) 15.

[15] S. Glashow, *Partial Symmetries of Weak Interactions*, Nucl. Phys. **B22** (1961) 579.

[16] A. Salam, *Elementary Particle Theory*, Ed. N. Svaratholm, Stockholm: Almquist and Forlag (1968) 367.

[17] S. Weinberg, *A Model of Leptons*, Phys. Rev. Lett. **19** (1967) 1264.

[18] S. L. Wu and G. Zobernig, Z. Phys. **C2** (1979) 107.

[19] S. L. Wu and G. Zobernig, TASSO Note 84 (1979).

[20] TASSO collaboration, Phys. Lett. **B86** (1979) 243.

[21] C. Caso *et al.*, (PDG Group) European Physical Journal **C3** (1998) 1.

[22] C. Quigg, B. W. Lee and H. B. Thacker, Phys. Rev. **D16** (1977) 1519.

[23] F. Abe *et al.*, *Evidence for Top Quark Production in pbar-p Collisions at sqrt(s)=1.8Tev*, Phys. Rev. Lett. **73** (1994) 225, Phys. Rev. **D50** (1994) 2966.

[24] F. Abe *et al.*, *Observation of Top Quark Production in p anti-p Collisions with the Collider Detector at Fermilab*, Phys. Rev. Lett. **74** (1995) 2626.

[25] G. Cowan *Statistical Data Analysis*, Oxford University Press, Oxford. (1998) 51.

[26] The LEP collaborations ALEPH, DELPHI, L3 and OPAL Collab., The LEP working group for Higgs boson searches, *Searches for Higgs bosons: Preliminary combined results using LEP data collected at energies up to 202 Gev*, CERN-EP/2000-055.

[27] S. Jin and P. McNamara *The Signal Estimator Limit Setting Method*, hep-ph/9812030, submitted to Nucl. Instrum. Meth. A.

[28] G. L. Kane, J. F. Gunion, H. E. Haber and S. Dawson, *The Higgs Hunter's Guide*, Perseus Publishing, Cambridge, Massachusetts (2000).

[29] P. Janot, *The HZHA Generator* Physics at LEP2 (edited by G. Altarelli, T. Sjöstrand and F. Zwirner), CERN 96-01, (1996) 309.

[30] P.Janot, http://alephwww.cern.ch/~janot/Generators.html

[31] ALEPH Collaboration, *The ALEPH handbook*, Vol. 1 and 2 are available from the ALEPH secretariat at CERN, 1995.

[32] ALEPH Collaboration, *Performance of the ALEPH detector at LEP*, Nucl. Instrum. Meth. **A360** (1995) 481-506.

[33] T. Sjöstrand, *High-Energy Physics event generation with PYTHIA 5.7 and JET-SET 7.4*, Comp. Phys. Commun. **82** (1994) 74.

[34] G. Marchesini *et al.*, *HERWIG: A Monte Carlo event generator for simulating hadron emission reactions with interfering gluons Version 5.1 - April 1991*, Comp. Phys. Commun. **67** (1992) 465.

[35] B. Bloch-Devaux *et al.*, *KINGAL Users Guide*, Tech. Rep. ALEPH 87-53, ALEPH internal report, 1987.

[36] F. Ranjard, *GALEPH - Monte Carlo Program for ALEPH*, Tech. Rep. ALEPH 88-119, ALEPH internal report, 1988.

[37] Application Software Group, Computing and Networks Division, CERN. *GEANT: Detector Description and Simulation Tool*, CERN Program Library Long Writeup W5013.

[38] J. Knobloch, *JULIA Users and Programmers Guide*, Tech. Rep. ALEPH 90-11, ALEPH internal report, 1990.

[39] E. B. H. Albrecht and J. Boucrot, *ALEPH Physics Analysis Package - ALPHA User's guide - versions > 124*, Tech. Rep. ALEPH 99-087, ALEPH internal report, 1999.

[40] D. Brown, M. Frank, *Tagging b-hadrons using track impact parameters*, ALEPH Note 92-135.

[41] D. Brown, *QFNDIP, a primary vertex finder*, ALEPH Note 92-047.

[42] T. Mattison, *QVSRCH A Tool for Inclusive Secondary Vertex Finding*, ALEPH Note 92-173.

[43] S. Armstrong *et al.*, University of Wisconsin-Madison, *Identification of b-jets in Higgs Searches Using a Neural Network*, ALEPH Note 96-100.

[44] S. Bethke, Z. Kunszt, D.E. Soper and W.J. Stirling, *New jet cluster algorithms: Next-to-leading order QCD and hadronization corrections*, Nucl. Phys. **B370** (1992) 310.

[45] S. Catani, Yu.L. Dokshitzer, M. Olsson, G. Turnock and B.R. Webber, *New clustering algorithm for multi - jet cross-sections in* e^+e^- *annihilation*, Phys. Lett. **B269** (1991) 432.

[46] C. Peterson, D. Schlatter, I. Schmitt, and P.M. Zerwas, *Scaling violations in inclusive* e^+e^- *annihilation spectra*, Phys. Rev. **D27** (1983) 105.

[47] D. Buskulic *et al.*, ALEPH Collaboration, *Measurement of the effective b-quark Fragmentation Function at the Z Resonance*, Phys. Lett. **B357** (1995) 699.

[48] ALEPH Collaboration, *Search for the Neutral Higgs Bosons of the Standard Model and the MSSM in* e^+e^- *Collisions at* $\sqrt{s}$ = 188.6 GeV., ALEPH 99-053 (CONF 99-029) available from http://alephwww.cern.ch/.

[49] ALEPH Collaboration, *Search for neutral Higgs bosons of the Standard Model and the MSSM in* e^+e^- *collisions at sqs* = 189 GeV , European Physical Journal **C17** (2000) 223-240.

[50] T. Greening, *Search for the Standard Model Higgs boson in the electron and muon channels at* $\sqrt{s} = 183$ GeV, ALEPH Note 98-003.

[51] ALEPH Collaboration, *Search for the Standard Model Higgs boson in* e$^+$e$^-$ *collisions at* $\sqrt{s} = 161, 170$ *and* 172 GeV, Phys. Lett. **B412** (1997) 155.

[52] C. Loomis *et al.*, *Search for Standard Model Higgs boson in* e$^+$e$^-$ *collisions at* $\sqrt{s} = 183$ GeV *using the* hZ $\rightarrow$ h$\nu\bar{\nu}$ *channel*, ALEPH Note 98-009.

[53] The ALEPH Higgs Taskforce, *Search for neutral Higgs bosons in the* $\tau^+\tau^-$q$\bar{q}$ *final states at 183 GeV*, ALEPH Note 98-010.

[54] ALEPH Collaboration, *Search for the Standard Model Higgs Boson at the LEP2 collider near* $\sqrt{s} = 183$ GeV , Phys. Lett. **B447** (1999) 336.

[55] The ALEPH Higgs Taskforce, *Search for neutral Higgs bosons of the MSSM in the channel* hA $\rightarrow$ b$\bar{\text{b}}$b$\bar{\text{b}}$ *at* $\sqrt{s} = 183$ GeV, ALEPH Note 98-002.

[56] ALEPH Collaboration, *A Measurement of the Gluon Splitting Rate into* b$\bar{\text{b}}$ *pairs in Hadronic Z decays*, Phys. Lett. **B434** (1998) 437.

[57] D. E. Groom *et al.*, European Physical Journal **C15** (2000) 1.

[58] ALEPH Collaboration, ALEPH Note 97-027.

[59] G. Rudolph, Private Communication.

[60] M. Kado, Private Communication.

[61] ALEPH Collaboration, *Searches for neutral Higgs bosons in* e$^+$e$^-$ *collisions at centre-of-mass energies from 192 to 202 GeV*, CERN-EP/2000-131.

[62] ALEPH Collaboration, *Observation of an excess in the search for the Standard Model Higgs boson at ALEPH*, Phys. Lett. **B495** (2001) 1.

[63] J. Kennedy, *Observation of an Excess in the Search for the Standard Model Higgs Boson using Cuts Based Analyses at ALEPH*, PhD Thesis, The University of Glasgow, 2001.